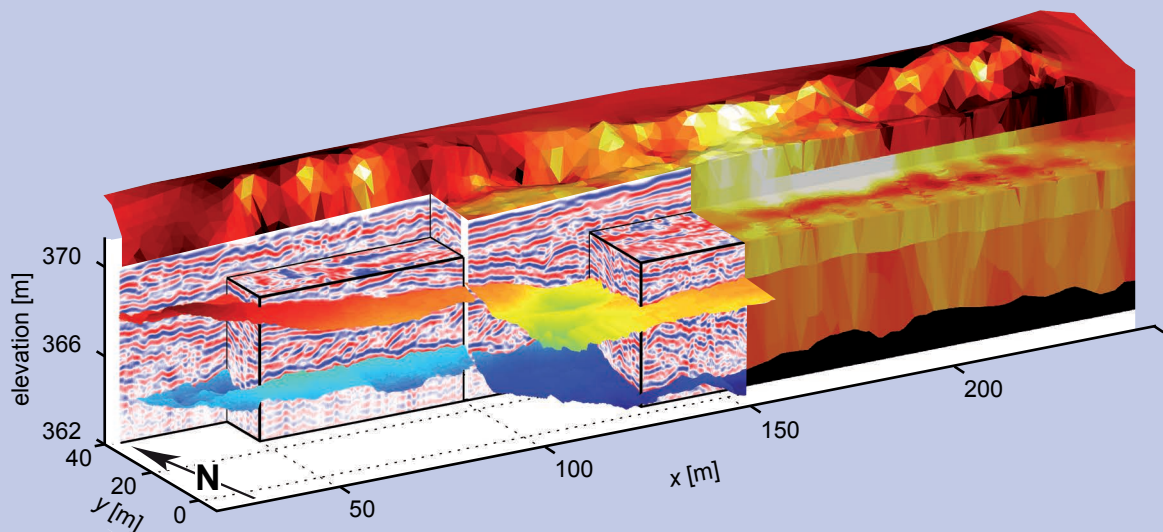


Diss. ETH
No. 19762

Joint and Constrained Inversion of Geophysical Data for Improved Imaging of Aquifer Structure and Processes



2011

Joseph Doetsch

DISS. ETH NO. 19762

**JOINT AND CONSTRAINED INVERSION OF GEOPHYSICAL DATA FOR
IMPROVED IMAGING OF AQUIFER STRUCTURE AND PROCESSES**

A dissertation submitted to
ETH ZURICH

for the degree of
DOCTOR OF SCIENCES

presented by
JOSEPH ANDREAS DOETSCH

Dipl. Phys., ETH Zurich
born August 25th, 1981
citizen of Germany

accepted on the recommendation of
Prof. Dr. Alan G. Green, examiner
Prof. Dr. Niklas Linde, co-examiner
Prof. Dr. Stewart A. Greenhalgh, co-examiner
Prof. Dr. Andreas Kemna, co-examiner

2011

CONTENTS

Zusammenfassung	v
Abstract	vii
1 Introduction	1
1.1 Introduction to hydrogeophysics	2
1.2 Geophysical methods for aquifer characterization	3
1.3 The record project and the Thur River field sites	5
1.4 Data integration	8
1.5 Time-lapse inversion	12
1.6 Objectives and structure of this thesis	15
2 Aquifer zonation based on joint inversions	17
Abstract.....	18
2.1 Introduction	18
2.2 Methodology.....	21
2.3 Field site, parameters, and procedures common to the synthetic and field examples.	26
2.4 Synthetic example.....	30
2.5 Field example	34
2.6 Hydrogeophysical interpretation	38
2.7 Discussion.....	41
2.8 Conclusions	42
3 Structural time-lapse joint inversion	43
Abstract.....	44
3.1 Introduction	44
3.2 Methods	45
3.3 Results	47
3.4 Concluding remarks.....	53

4	The borehole-fluid effect in ERT	55
	Abstract.....	56
4.1	Introduction	56
4.2	Modeling the borehole-fluid effect.....	60
4.3	Multi-hole 3-D ERT data set	63
4.4	3-D inversion results with and without boreholes.....	66
4.5	The inadequacy of correction factors	68
4.6	Conclusions	71
5	Constraining 3-D ERT with GPR reflection data	73
	Abstract.....	74
5.1	Introduction	74
5.2	Thur River field site.....	77
5.3	GPR data acquisition, processing and interpretation.....	78
5.4	ERT data acquisition and inversion.....	81
5.5	Interpretation and discussion	89
5.6	Conclusions	91
6	Imaging salt tracer transport by means of 3-D ERT monitoring.....	93
	Abstract.....	94
6.1	Introduction	94
6.2	Outline of the methodology.....	96
6.3	Thur River study site	99
6.4	Salt tracer experiment.....	101
6.5	ERT inversion.....	104
6.6	Groundwater transport modeling.....	107
6.7	Results	109
6.8	Discussion.....	112
6.9	Conclusions	113
7	Conclusions & Outlook.....	115
7.1	Summary of conclusions	116
7.2	Outlook.....	118

Appendix A: Hydrogeophysical studies at the Thur River	121
Abstract.....	122
A.1 Introduction.....	122
A.2 Site descriptions and instrumentation.....	125
A.3 Investigations at the unrestored channelized site.....	127
A.4 Investigations at the restored site.....	130
A.5 Discussion.....	131
A.6 Conclusions.....	132
Appendix B: 3-D ERT for monitoring of infiltrating river water	133
Abstract.....	134
B.1 Introduction.....	134
B.2 Widen field experiment.....	138
B.3 Full 3-D crosshole static inversion	143
B.4 Discussion.....	149
B.5 Conclusions.....	153
Appendix C: Full-waveform inversion of GPR data from the Thur River aquifer.....	155
Abstract.....	156
C.1 Introduction.....	156
C.2 Full-waveform inversion methodology.....	158
C.3 Case study: Thur River hydrogeophysical test site.....	163
C.4 Conclusions and Outlook.....	177
Appendix D: Instrumentation of a restored river corridor.....	181
Abstract.....	182
D.1 Introduction.....	182
D.2 Thur catchment and test site selection	186
D.3 Preliminary investigations	190
D.4 Design of continuous monitoring and instrumentation	197
D.5 Results.....	202
D.6 Discussion and conclusions	205
Appendix E: Self-potential investigations in the Thur River corridor	211
Abstract.....	212
E.1 Introduction	212
E.2 Methods.....	215

E.3	Results	221
E.4	Discussion	232
E.5	Conclusions	233
Appendix F: Joint inversion of crosshole GPR and seismic traveltime data.....		235
	Abstract.....	236
F.1	Introduction	236
F.2	Method.....	238
F.3	Results	244
F.4	Discussion	255
F.5	Conclusions	257
F.6	Appendix: stochastic regularization operators	258
Appendix G: Fracture imaging using single- and crosshole GPR reflection data		261
	Abstract.....	262
G.1	Introduction.....	262
G.2	General setting of the crystalline aquifer.....	264
G.3	Multifold data acquisition.....	265
G.4	Data processing.....	266
G.5	Results.....	275
G.6	Discussion.....	278
G.7	Conclusions.....	279
References		281
Acknowledgments.....		305

ZUSAMMENFASSUNG

Um die Verfügbarkeit von Grundwasser, dessen Anfälligkeit für Kontaminierung und eventuell Maßnahmen zur Sanierung im Falle von Verschmutzung zu beurteilen, kann eine prognostische Grundwassermodellierung wesentliches beitragen. Leider sind genaue Informationen über die Eigenschaften der Grundwasserleiter, welche für die Modellierung wichtig sind, schwer abzuschätzen. Geophysikalische Bildgebungsverfahren können die Struktur von Grundwasserleitern und deren Eigenschaften abschätzen, allerdings sind die Ergebnisse nicht eindeutig. Dieser Nachteil kann teilweise behoben werden, indem Daten verschiedener geophysikalischer Methoden in einer gemeinsamen Inversion (*joint inversion*) oder einer Inversion mit strukturellen Randbedingungen (*constrained inversion*) kombiniert werden. Fünf Beispiele für solche Datenintegrationsansätze für statische und zeitabhängige Daten sind Bestandteil dieser Dissertation und werden im Folgenden zusammengefasst.

Ein viel versprechender Ansatz zur Charakterisierung von Grundwasserleitern ist die strukturelle gemeinsame 3-D Inversion verschiedener geophysikalischer Daten, gefolgt von einer Einteilung in hydrologische Zonen und Zonenparameterschätzung. Anhand einer Studie mit synthetischen Daten wird gezeigt, wie die gemeinsame Inversion von Seismik- und Georadar-Laufzeiten, sowie Geoelektrik-Daten, die Klassifizierung von Zonen gegenüber getrennten Inversionen verbessert (3.7% anstatt 21.3% falsch klassifizierte Zellen). Dadurch werden auch die Zonenparameter genauer bestimmt (0.3% anstatt 1.8% Fehler). Daten eines Grundwasserleiters in der Nähe der Thur (Nordostschweiz) zeigen drei verschiedene Zonen mit ~30% unterschiedlicher Porosität und einem erhöhten Lehmanteil in der Tiefe.

Die Erweiterung der strukturellen gemeinsamen Inversion für zeitabhängige Daten wurde erfolgreich auf Georadar- und Geoelektrik-Daten eines Wasserinjektionsversuchs in ungesättigtem Sandstein angewandt. Die Ergebnisse einer Modellstudie und eines Feldversuchs zeigen, dass die zeitabhängige gemeinsame 3-D Inversion die Bilder des injizierten Wassers im Untergrund deutlich verbessert.

Durch die Inversion mit Randbedingungen kann die Uneindeutigkeit der Inversionsmodelle durch zusätzliche strukturelle Information vermindert werden. Die strukturellen Randbedingungen können entweder von hochauflösenden geophysikalischen

Methoden oder aus detailliertem Vorwissen stammen. Zum Beispiel konnten Geoelektrikmessungen zwischen Bohrlöchern nahe der Thur nur sinnvoll ausgewertet werden, nachdem die physikalischen Eigenschaften der wassergefüllten Bohrlöcher explizit berücksichtigt wurden.

Bei Oberflächengeoelektrikmessungen auf einer Kiesbank im Flussbett der Thur konnten Unterschiede innerhalb des Grundwasserleiters nur unter Berücksichtigung von Schichtgrenzen aus Georadarreflexionsdaten interpretiert werden. Ohne die Schichtgrenzen zwischen dem Kiesgrundwasserleiter und dem darunter liegenden Lehm wurden die Widerstandsmodelle durch die starken Kontraste verschmiert. Eine Entkopplung der Schichten in der Inversion konnte dieses Problem beheben.

Ein Salzmarkierungsversuch (*tracer test*) an der gleichen Messstelle an der Thur wurde mit Oberflächengeoelektrik beobachtet. Die Salzfahne konnte über 35 m verfolgt werden, bis sie das Messgebiet verließ. Die hydraulische Leitfähigkeit von 4×10^{-4} m/s wurde durch Vergleiche mit einer Simulation des Transports im Grundwasser bestimmt. Der Vergleich von synthetischen Geoelektrikinversionen basierend auf dem Grundwassermodell mit den Feldtestergebnissen zeigt, dass die Bewegung der Salzfahne anfänglich durch ein homogenes Modell beschrieben werden kann. Nach 6 Stunden wird aber der starke Einfluss der Heterogenität des Grundwasserleiters sichtbar.

Diese fünf Beispiele zeigen, dass das Kombinieren verschiedener geophysikalischer Messungen die Charakterisierung von flachen Grundwasserleitern gegenüber der einzelnen Datenbehandlung deutlich verbessert. Die hier gezeigten Ansätze können auf andere Methoden und Situationen erweitert werden. Die direkte Einbindung von hydrogeologischen Messungen in die Inversion wäre eine wichtige Neuerung.

ABSTRACT

Predictive groundwater modeling can help to assess groundwater supplies, their vulnerability to contamination, and the design of remediation schemes in cases of pollution. Unfortunately, accurate information on aquifer characteristics required for groundwater modeling is generally difficult to obtain. Geophysical imaging is a powerful tool for delineating aquifer structure and physical properties at an appropriate scale and resolution, but it suffers from problems of ambiguity and yields only indirect information on hydraulic properties. These limitations can be partly overcome by combining data from multiple geophysical techniques in joint or constrained inversion strategies. Five such data integration approaches for static and time-lapse data constitute the subject matter of this thesis and are summarized in the following.

One promising approach for aquifer characterization is structural 3-D joint inversion of multiple geophysical data sets, followed by clustering to form zones and subsequent inversion for zonal parameters. A synthetic study demonstrates how joint inversion of seismic and ground-penetrating radar (GPR) traveltimes and electrical resistance tomography (ERT) data greatly reduces misclassification of zones (down from 21.3% to 3.7%) and improves the accuracy of retrieved zonal parameters (from 1.8% to 0.3% error) compared to individual inversions. Application of the scheme to a data set collected close to the Thur River in northeastern Switzerland shows that the inversion models resolve three principal sub-horizontal units distinguished by a ~30% variation in porosity within the gravel aquifer and an increasing fraction of finer sediments with depth.

The extension of the structural joint inversion technique to time-lapse data is successfully applied to crosswell GPR traveltimes and ERT monitoring data of a water injection experiment in unsaturated sandstone. The results from a synthetic and companion field study show that joint 3-D time-lapse inversion significantly improves the imaged features of the point-injected plume, such as lateral spreading and center of mass, as well as the overall consistency between models.

Constrained inversion is an effective means of reducing ambiguity in a single inversion, particularly if additional structural information is available. Structural constraints critical for

meaningful inversions can be either derived from complementary high-resolution geophysical surveys or based on detailed prior knowledge. For example, meaningful inversions of crosshole ERT data collected in the vicinity of the Thur River are only possible once the boreholes and their fluids are properly taken into account.

In using surface ERT to resolve aquifer properties below a gravelbar within the active channel of the Thur River, the imposition of interfaces delineated by reflection GPR were crucial to a meaningful interpretation of subtle changes within the aquifer. If GPR-defined boundaries between the shallow gravel aquifer and an underlying clay layer, and between two units within the aquifer, are not included in the inversion, then strong smearing in the resistivity model results from the large resistivity contrasts and regularization effects. Decoupling the regularization between the layers resolved this issue.

A salt tracer injection experiment at the same Thur River field site was monitored using surface ERT. The tracer plume could be tracked for 35 m until it moved beyond the ground covered by the electrode array. An effective 4×10^{-2} m/s hydraulic conductivity within the aquifer was determined by constraining a groundwater flow and transport model by the positions of the plume's center of mass determined in the time-lapse ERT images. Comparison of synthetic ERT inversions based on transport simulation with ERT inversions of the field experiment demonstrates that the tracer movement is initially consistent with a homogeneous aquifer, but that heterogeneity has a very strong influence on the plume transport 6 hours after the injection.

These five examples show that integration of multiple geophysical data sets can improve the characterization of shallow aquifers compared to separately treated data sets. The approaches presented here can be extended to other methods and situations. Including hydrogeological measurements directly in the modeling and inversion would be an important development.

1 INTRODUCTION

In this introduction, I provide an overview of selected aspects of hydrogeophysics, introduce the field sites, discuss various ways of integrating data from different geophysical methods, and present some concepts of time-lapse monitoring. Finally, I summarize the content of my thesis.

The introduction to hydrogeophysics and hydrogeophysical methods concentrates on themes relevant to my thesis and is not an attempt of a general overview; this can be found in the relevant references to journal articles and textbooks. One of the objectives of this introduction is to provide a framework for my published and submitted papers.

1.1 INTRODUCTION TO HYDROGEOPHYSICS

The subdiscipline of hydrogeophysics has emerged over the past 20 years as a multidisciplinary effort to use geophysical methods for resolving hydrogeological problems; good overviews, including case studies, can be found in *Rubin and Hubbard* [2005], *Vereecken et al.* [2006], *Binley et al.* [2010] and *Hubbard and Linde* [2011]. Whereas the development and application of geophysical techniques for oil and gas exploitation, as well as mining are widespread, quantitative hydrogeological applications of geophysics are relatively scarce and mostly found in the scientific community. Applying geophysical methods in hydrogeological studies is not new, but earlier applications were restricted to supplying lithological boundaries without attempting quantitative estimations of physical properties.

Traditional hydrogeology is based on point measurements (e.g., hydraulic head) and methods that average over a certain volume assuming constant effective properties (e.g., pumping tests). In the saturated zone, hydraulic head and other parameters are typically measured in screened boreholes, whereas in the unsaturated zone, water content can be monitored at single locations using time-domain reflectometry (TDR; *Topp et al.* [1982]). To interpolate between these point measurements, there is a wide range of geostatistical tools [*Deutsch and Journel*, 1998], but the quality of interpolated values is inherently limited when few data are available and the subsurface is highly heterogeneous. In addition, the geostatistical model parameters, such as the integral scales, are usually not well known and are thus estimated based on prior knowledge of the field site and the spacing between measurements. Interpolating point measurements gives reasonable results for some quantities like hydraulic head, whereas for others (e.g., water content in the unsaturated zone) local variations are too strong for such an approach [e.g., *Western et al.*, 2002]. For monitoring contaminant or tracer concentrations, point measurements are important as they can give precise concentrations at certain locations, but the contaminant or tracer can easily bypass the loggers and thus not provide any signal [e.g., *Boggs et al.*, 1992]. For tracer tests, even when tracer breakthrough is observed, it is difficult to assess which part of the plume was sampled.

Relatively scarce data based on point measurements are in strong contrast to the possibilities offered by groundwater modeling. The development of versatile flow and transport modeling codes such as MODFLOW [*Harbaugh*, 2005], TOUGH2 [*Pruess et al.*, 1999] and FEFLOW [*Trefry and Muffels*, 2007], along with a strong increase in computational power over the recent past allows detailed simulation of complex groundwater systems. Flow and transport that includes multiple compounds and chemical reactions can be

modeled on very fine meshes. These fine meshes enable large-scale subsurface features as well as small-scale heterogeneity to be modeled. Unfortunately, even large subsurface features might not be resolved by point measurements alone [e.g., *Oreskes et al.*, 1994], such that many different models can reproduce the data equally well [e.g., *Beven and Binley*, 1992].

Hydrogeophysics can help to close this information gap by contributing structural knowledge as well as hydrogeologically important properties (e.g., porosity) on an intermediate scale. Current hydrogeophysical research offers a substantially improved ability compared to earlier geophysical applications in hydrogeology in (1) imaging the subsurface in greater detail, (2) providing quantitative estimates of hydrologically important properties, (3) combining different geophysical methods, and (4) integrating geophysical and hydrogeological measurement and modeling techniques.

1.2 GEOPHYSICAL METHODS FOR AQUIFER CHARACTERIZATION

The most common geophysical methods for aquifer characterization are electrical resistance tomography (ERT) and ground-penetrating radar (GPR). Especially in combination, these two methods can be used to obtain quantitative estimates of subsurface physical properties [e.g., *Binley et al.*, 2002b]. Other methods like induced polarization, electromagnetic induction, self-potential, seismic, surface nuclear magnetic resonance, magnetics, gravity and wellbore logging techniques have been successfully applied in hydrogeophysical studies. These methods are not the focus of this thesis and an overview of their physical principles and applicability in hydrogeophysics is given by *Hubbard and Linde* [2011].

1.2.1 Electrical resistance tomography (ERT)

The popularity of ERT in hydrogeophysics is due to the direct dependence of electrical resistivity on water content, pore-fluid resistivity (or conductivity) and the amount of clay minerals in the subsurface. ERT measurements involve a number of electrodes (typically stainless steel) that are deployed either at the earth's surface or inside boreholes within formations. The resistance is measured by injecting a current between two electrodes and measuring the resulting potential difference between another two electrodes [e.g., *Daily et al.*, 2005; *Zonge et al.*, 2005]. Many (some thousands) such ERT configurations are measured automatically to create one data set. Models of subsurface electrical resistivity can be

obtained from these measurements using inversion algorithms [e.g., *Ellis and Oldenburg, 1994; Loke and Barker, 1996; Günther et al., 2006; Blome et al., 2009*].

In many formations, the subsurface electrical resistivity – or its inverse, the electrical conductivity σ_{eff} – depends on the electrical formation factor F , water saturation S_w , electrical conductivity of the pore water σ_w and surface conduction σ_s as given, for example, by the following equation [*Linde et al., 2006a*]:

$$\sigma_{eff} = \frac{1}{F} \left[S_w^n \sigma_w + (F-1) \sigma_s \right], \quad (1.1)$$

where n is Archie's saturation index with typical values of 1.5 – 2, which is usually assumed to be constant for a given aquifer. The electrical formation factor is defined as $F = \sigma_w / \sigma_{eff}$ in the case of full saturation ($S_w = 1$) and no surface conduction ($\sigma_s = 0$). F can be related to porosity ϕ through $F = \phi^{-m}$, where m is Archie's cementation index. Equation 1.1 is only strictly valid in the high-salinity limit at which the current flow path is completely governed by the configuration of the pore space. Other petrophysical models are summarized in *Lesmes and Friedman [2005]*.

Under saturated conditions (i.e., $S_w = 1$) and constant σ_w , electrical conductivity only depends on F and σ_s . Combining ERT with GPR, which also depends on F , can therefore yield estimates of σ_s (see Chapter 2). When σ_s is negligible (e.g., in clean gravelly aquifers or sandstone), ERT can be used to monitor changes in S_w (Chapter 3) and σ_w (Chapter 6), given that the other property doesn't change.

1.2.2 Ground-penetrating radar (GPR)

GPR is sensitive to the effective permittivity κ_{eff} of the subsurface, as, for example, described by the following equation [*Linde et al., 2006a*]:

$$\kappa_{eff} = \frac{1}{F} \left[S_w^n \kappa_w + (1 - S_w^n) \kappa_a + (F-1) \kappa_s \right], \quad (1.2)$$

where κ_w , κ_a and κ_s are the relative permittivities of water, air and the minerals forming the rock matrix, respectively. GPR transmission experiments between boreholes are sensitive to κ_{eff} along a ray path, whereas GPR reflection surveys record radar waves reflected at interfaces of changing κ_{eff} . Generally, $\kappa_w = 81$ and $\kappa_a = 1$ are known constants (although κ_w is known to be temperature dependent, see *Eisenberg and Kauzmann, [1969]*) and κ_s can usually be assumed to be constant within an aquifer. Making the assumption of constant n , under fully saturated conditions, the only variable is F . GPR transmission data are used to

estimate differences in ϕ between three zones of an aquifer in Chapter 2 and reflections from interfaces between units of different porosity are used to image aquifer structure in Chapter 5. In the unsaturated zone, S_w usually controls the value of κ_{eff} and this effect is used to follow a water tracer injection in unsaturated sandstone in Chapter 3.

1.3 THE RECORD PROJECT AND THE THUR RIVER FIELD SITES

The Thur River is the largest Swiss river without natural or artificial reservoirs. It is a peri-alpine tributary of the River Rhine with a catchment area of $\sim 1750 \text{ km}^2$ (Figure 1.1). Water level and discharge variations in the Thur are similar to those of unregulated alpine rivers, and river discharge can vary in the $3 - 1000 \text{ m}^3/\text{s}$ range, with a mean discharge of $20 - 50 \text{ m}^3/\text{s}$ (Figure 1.2; *BAFU* [2010]). Like many other rivers, the meandering Thur was channelized towards the end of the 19th century for flood protection and to gain arable land. In an attempt to combine flood protection with ecological objectives, a more natural environment was restored along a 2.5 km long reach of the Thur River, starting in 2000. The effects of this restoration effort are currently being investigated through a large multidisciplinary research initiative [*RECORD*, 2011] concerned with coupled hydrological, biogeochemical and ecological processes. Hopefully, the new knowledge can be transferred to other river systems undergoing restoration. The research within the RECORD project is concentrated at two field sites along the Thur River: the Widen site near Frauenfeld, where the Thur is channelized and a restored site between Altikon and Neunforn (see Figure 1.1).

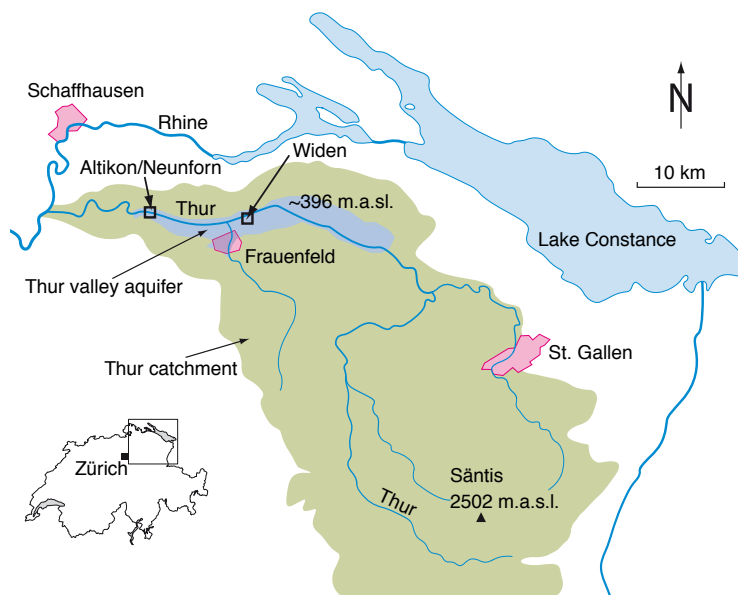


Figure 1.1. Catchment of the Thur River in northeastern Switzerland, with the two investigation sites at Widen and Altikon / Neunforn.

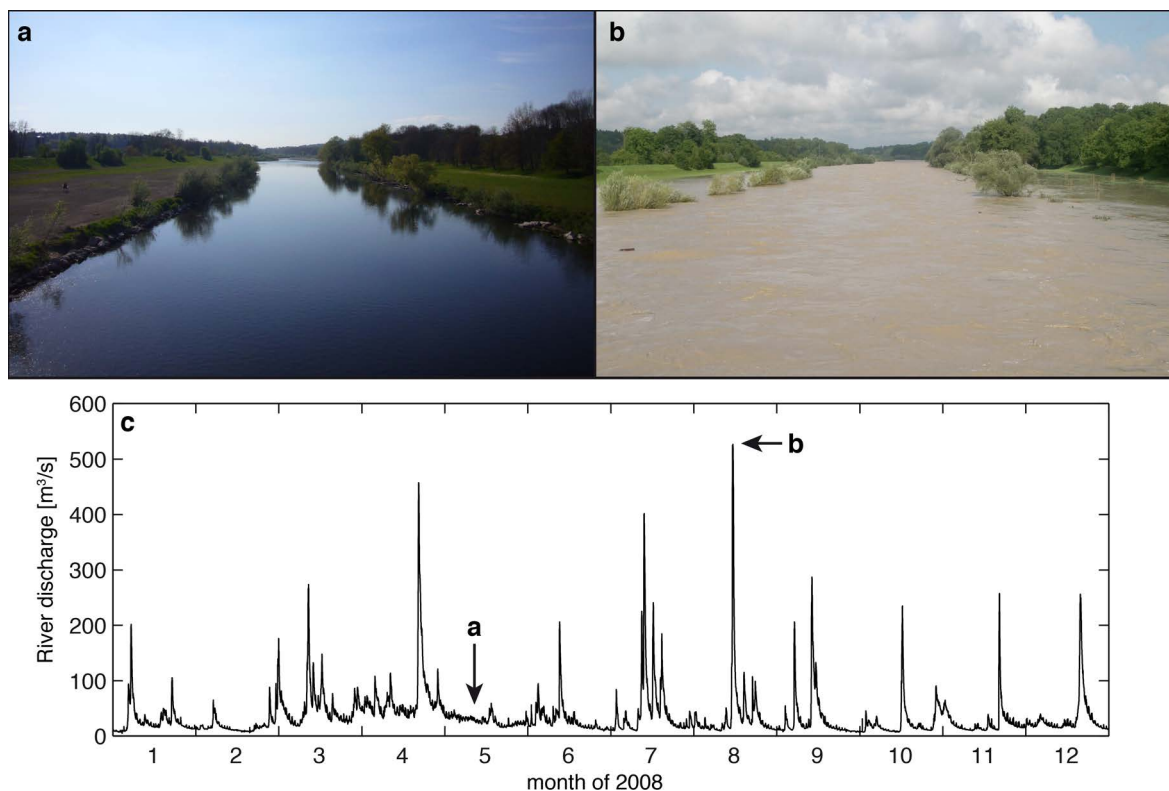


Figure 1.2. Photos of the Thur River at Altikon / Neunforn at discharge rates of (a) 20 m³/s and (b) 500 m³/s. The strong variations in river discharge can also be appreciated in the hydrograph of the year 2008 shown in (c). The recording times of the pictures (a) and (b) are marked in (c).

1.3.1 Widen field site

Investigations at the unrestored Widen field site (see Figure 1.1 for the location) concentrate on a 10 × 20 m area, 5 – 25 m from the Thur River channel. This site is part of a flat overbank (Figure 1.3) that is elevated ~4 m above the riverbed and is flooded during high flow events (i.e., river discharge > 800 m³/s). The geology at this location comprises a ~3-m-thick soil layer of alluvial sandy loam successively underlain by ~1 m of unsaturated gravel, ~6 m of water-saturated gravel, and lacustrine clay of considerable thickness (>30 m). The top 10 m down to the clay-rich aquitard are penetrated by 18 boreholes placed at the corners of 3.5 × 3.5 m squares [Coscia *et al.*, 2011a]. The focus of all studies at the site is the 6-m-thick saturated aquifer.

Bank filtration on a scale of 200 m was investigated by Cirpka *et al.* [2007]. The general aim of current research at the site is to characterize the aquifer and gain a detailed understanding of bank filtration and mixing of the infiltrating water with groundwater on a smaller scale. Chapter 2 presents a zonation approach to the interpretation of crosshole ERT, GPR and seismic data acquired within a 5 × 5 m region of the field site, and Chapter 4 deals

with the unwanted effects of the borehole fluids on ERT inversions. A 3-D model of the aquifer between all 18 boreholes based on crosshole ERT was developed by *Coscia et al.* [2011a], and *Coscia et al.* [2011b] developed a deconvolution approach for correcting time-lapse ERT data for water-table fluctuations and for improving the imaging of natural aquifer dynamics. Hydraulic conductivity of the gravel aquifer was estimated by *Diem et al.* [2010] using pumping and slug tests, sieve analysis and flowmeter logs. Currently a numerical flow and transport model of the site is being designed, which will integrate the results of the above mentioned studies.



Figure 1.3. Crosshole GPR acquisition at the Widen field site.

1.3.2 Restored site at Altikon / Neunforn

At the restored field site near Neunforn / Altikon (see Figure 1.1 for the location) the riverbed morphology is constantly changing, especially in response to high discharge events. Within the river channel, several gravelbars have developed. Most research is concentrated on a gravelbar at the northern side of the river and an adjacent forest (Figure 1.4). This site was instrumented with numerous boreholes that penetrate the aquifer. It is permanently instrumented with a meteorological station and several hydrological loggers placed in the boreholes [*Schneider et al.*, 2011]. Changes in river morphology are continuously monitored with cameras from two towers to gain an improved understanding of the morphodynamic evolution of restored river corridors [*Pasquale et al.*, 2011]. Hydrogeological studies at the site include mapping and monitoring the hydraulic head distribution. The aim is to better understand groundwater flow directions [*Schneider et al.*, 2011] and to investigate river water – groundwater interactions in this environment, where the Thur River mainly loses water to the aquifer. Seepage rates and bank filtration characteristics are derived from vertical fiber-optic temperature profiling [*Vogt et al.*, 2010a] and time-series of natural variations in

electrical conductivity of water in the river and within a number of boreholes [Vogt *et al.*, 2010b]. The gravel aquifer and depositional patterns within the aquifer are investigated using surface GPR and ERT (Chapter 5), and the dynamics of groundwater flow and transport below the gravelbar are investigated using ERT monitoring of a salt tracer test (Chapter 6).



Figure 1.4. Gravelbar at the restored Thur River field site near Altikon / Neunforn showing upstream (a) and downstream (b) views.

1.4 DATA INTEGRATION

Integration of data obtained from different geophysical techniques, as combining geophysical data with other information such as borehole logs or hydrogeological data, is of growing importance [e.g., Gallardo and Meju, 2011]. Significant progress in the design of data acquisition systems over the past 20 years has led to relatively easy and inexpensive acquisition of large data sets [e.g., Annan, 2005; Blome *et al.*, 2011], often resulting in different types of geophysical data being available over the same target area. At the same time, computing power and versatile processing / inversion codes have substantially increased to make joint- or constrained-inversion of large data sets feasible.

Figure 1.5 indicates three approaches of integrating different geophysical data types for a hydrogeological interpretation of a field site: individual processing and inversion of disparate data sets (Section 1.4.1), joint inversion of such data sets (Section 1.4.2) and constrained inversion of one data set using structural information from a second data set (Section 1.4.3).

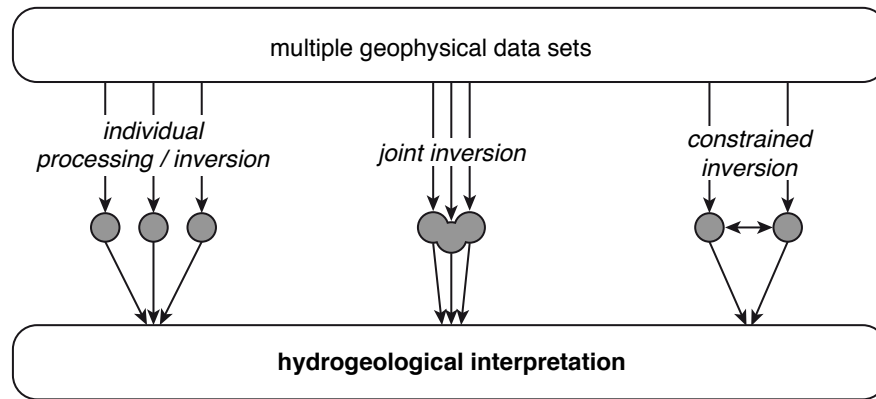


Figure 1.5. Illustration of different approaches for integrating multiple geophysical data sets for a hydrogeological interpretation.

1.4.1 Individual processing and inversion

By far the most common way of data integration is to process and invert data obtained using different geophysical techniques separately and bring the information together in an interpretation step [e.g., Lanz *et al.*, 1998; Binley *et al.*, 2002b; Sandberg *et al.*, 2002; Bowling *et al.*, 2005; Looms *et al.*, 2008; Bélanger *et al.*, 2010]. For projects aimed at mapping different lithological units in the subsurface, the results of the individual inversions may answer the posed questions, such that there is not necessarily a need for more elaborate approaches. Because the integration of the different methods happens as a final step, processing and inversion schemes for the different data sets can be individually tested and adjusted. This is a major advantage, because there are no restrictions to use the same mesh or grid, have co-located measurements or record data under the same conditions of the investigated system.

The inversion and imaging results from the different methods can either be qualitatively integrated for a hydrogeological interpretation or they can be used for further analysis using, for example, clustering algorithms to identify lithological zones [e.g., Avseth *et al.*, 2001; Bedrosian *et al.*, 2007]. Quantitative analysis of inversion results in terms of physical parameters of the system (e.g., porosity, water content) is however difficult. Applying petrophysical relationships on tomograms can lead to misinterpretation, because tomograms represent blurred models of the subsurface physical property distribution. The effects of regularization and limited data coverage can lead to unresolved areas in the tomograms. Even in the well-resolved parts of the model, the natural variability of the subsurface parameters may not be accurately recovered [e.g., Friedel, 2003]. Figure 1.6 illustrates the loss of

resolution and variance for a comparatively well-resolved synthetic crosshole seismic experiment [Day-Lewis and Lane, 2004]. In addition, petrophysical relationships are often site-specific, so that they cannot be easily extrapolated to other locations or geologic conditions.

Careful individual inversion of each data set should be the starting point for any type of joint inversion. Individual inversions allow for the assessment of data quality, error sources and magnitude of the data errors. Possible links and correlation between the different geophysical parameters should be evaluated on the tomograms from individual inversions before imposing relationships in a joint inversion.

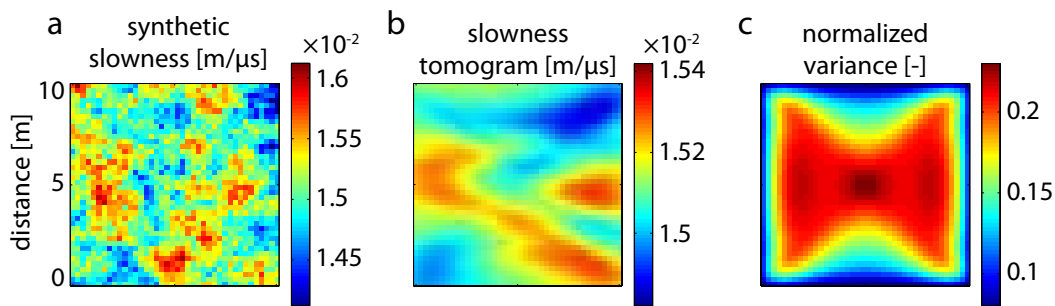


Figure 1.6. (a) Model of synthetic seismic slowness and (b) tomogram of seismic slowness from a crosshole travelt ime inversion experiment. The loss of resolution and variance is illustrated in (c), which shows the variance of (b), normalized by (a). Modified from Day-Lewis and Lane [2004].

1.4.2 Joint inversion

Coupling different types of co-located geophysical data in a joint inversion can help to reduce model uncertainties and help to obtain a consistent hydrogeophysical interpretation [Gallardo and Meju, 2011, and references therein]. The power of this approach lies in the complementary nature of the data and models that can be exploited to constrain the range of plausible hydrogeologic interpretations. Because different geophysical methods (e.g., seismic and radar transmission and ERT) are sensitive to different physical properties of an aquifer, joint inversion is traditionally achieved by imposing petrophysical relationships; multiple models are linked during the inversion by petrophysical equations with known parameter values [e.g., Tryggvason *et al.*, 2002]. For example, because resistivity and dielectric permittivity depend on porosity [e.g., Pride, 1994; Revil *et al.*, 1998; Linde *et al.*, 2006a], this style of joint inversion could directly yield porosity estimates. A drawback of such schemes is

that general petrophysical models typically involve many parameters that are likely to vary spatially and are usually poorly known.

A less restrictive approach to joint inversion, presented independently by *Haber and Oldenburg* [1997] and *Zhang and Morgan* [1997], is to impose structural similarity between models during the inversion process without any explicit assumptions about petrophysical relationships except that the geophysical parameters are assumed to vary at common locations. By advocating that the gradients of a model could be used to quantify structure, *Gallardo and Meju* [2003; 2004] further develop this structural approach into a robust methodology for joint inversion. They introduce the idea that the vector cross-product:

$$\boldsymbol{\tau} = \nabla \mathbf{m}_1 \times \nabla \mathbf{m}_2 \quad (1.3)$$

of the gradients of two models \mathbf{m}_1 and \mathbf{m}_2 should be forced to zero (implying similar directions of the gradient vectors) at each iterative step of a joint inversion. Figure 1.7 illustrates that changes in the two parameters \mathbf{m}_1 and \mathbf{m}_2 at a given location must then be either zero, parallel, or antiparallel to ensure $\boldsymbol{\tau} = 0$.

The cross-gradient joint inversion approach is today a well-established method that has been further developed and applied by several researchers (see references in *Gallardo and Meju* [2011]). Chapter 2 introduces an extension of this method to three geophysical methods in 3-D and presents new possibilities for further analyzing joint inversion tomograms. The analysis includes a classification scheme to find zones of similar physical parameters and determine petrophysical relationships on the scale of these zones. Chapter 3 describes the first time-lapse joint inversion for monitoring the injection of a tracer plume in the subsurface (see Section 1.5 for an introduction of time-lapse inversion).

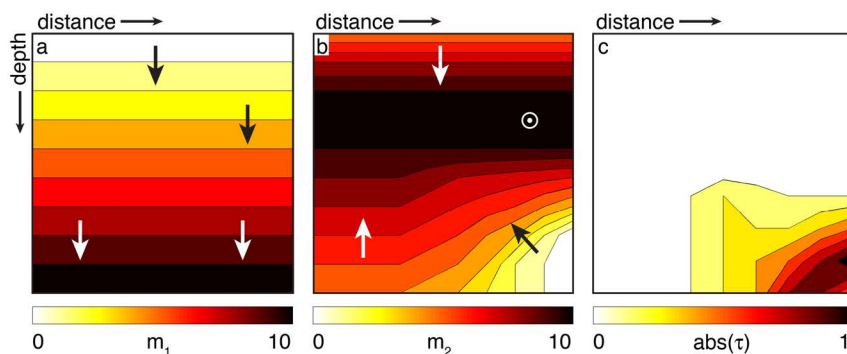


Figure 1.7. (a) and (b) Display models of two different geophysical properties. The magnitude of the normalized cross-gradient function for the two models in (a) and (b) is shown in (c). The normalization in (c) was made with respect to the maximum value of the cross-gradient function.

1.4.3 Constrained inversion

Instead of structurally coupling multiple models in a joint inversion, the inversion process can also be constrained by information from other geophysical techniques or other detailed prior knowledge. Constrained inversion is particularly useful when one wants to combine geophysical data that are mainly sensitive to structure (e.g., seismic and GPR reflection data) with data that are primarily sensitive to bulk properties (e.g., ERT data). As examples, *Favetto et al.* [2007], *Jegen et al.* [2009] and *Li et al.* [2003] improved the inversion results of gravity and magnetotelluric data by constraining the inversions using interfaces defined in seismic reflection models.

Chapter 4 demonstrates that the boreholes in which the ERT electrodes are installed might have to be included in modeling and inversion procedures. Meaningful inversions of crosshole ERT data were only possible once the water that filled the boreholes was accounted for.

In chapter 5, I investigate the extent to which GPR-derived interfaces can improve ERT inversion and subsequent aquifer characterization. The constraints are implemented by conditioning an unstructured inversion mesh using these interfaces and by not imposing any smoothness constraints across these interfaces during the inversion. An unstructured mesh is essential to accurately include surface topography [*Günther et al.*, 2006], arbitrary electrode positions and prior structural information. The time-lapse inversion in Chapter 6 uses the same type of constraints as used in Chapter 5.

1.5 TIME-LAPSE INVERSION

Acquiring data before and during a transient process such as a tracer test can help to understand the dynamics of a system. For example, in hydrogeology one is mostly interested in the movement of the water and substances carried with it. The easiest way of performing time-lapse inversion is to treat the different data sets acquired during an experiment as static independent entities, perform the inversions and then compare the resultant models for the different times [e.g., *Miller et al.*, 2008]. This imaging of the transient process can be significantly improved, however, by considering the correlation of the data acquired at the different times and by solving for the time-lapse changes instead of for the full model [e.g., *Daily et al.*, 1992; *LaBrecque and Yang*, 2001].

1.5.1 Time-lapse data

Variation of time-lapse data due to a transient process (e.g., salt tracer test) may be smaller (<1% variation of e.g., apparent resistivity) than the total error of the data set. Inverting each such data set independently would not resolve the transient changes. Considering different types of error sources and the correlation between errors of the different time-lapse data sets can help to improve significantly time-lapse inversion results. We express a data set \mathbf{d}_i recorded at time step i as:

$$\mathbf{d}_i = g(\mathbf{m}_i) + \boldsymbol{\epsilon}_s + \boldsymbol{\epsilon}_n + \boldsymbol{\epsilon}_{ri}, \quad (1.4)$$

where g is the forward operator that calculates the response of the model \mathbf{m}_i with errors being distributed as static $\boldsymbol{\epsilon}_s$, numerical $\boldsymbol{\epsilon}_n$ and random $\boldsymbol{\epsilon}_{ri}$ contributions. We assume $\boldsymbol{\epsilon}_s$ to be the same for all time-lapse data. The numerical errors $\boldsymbol{\epsilon}_n$ refer to errors introduced due to an imperfect forward operator. They can be assumed to be similar for all models, as long as the models do not change significantly during the time-lapse inversion process. The random errors $\boldsymbol{\epsilon}_{ri}$ correspond to the random observational errors that vary between time-lapse data sets. The relative size of the different errors depends on the geophysical method, acquisition type and field conditions.

For crosshole GPR measurements, the data acquisition error is mainly due to inaccurate positioning of the antennas within the boreholes and uncertainties of the time zero [e.g., *Alumbaugh et al.*, 2002]. These errors vary with each time-lapse acquisition so that $\boldsymbol{\epsilon}_s$ and $\boldsymbol{\epsilon}_n$ are much smaller than $\boldsymbol{\epsilon}_{ri}$. In contrast, for ERT measurements made with (semi) permanently installed electrodes, $\boldsymbol{\epsilon}_s$ is significant due to coupling conditions of the electrodes and positioning errors that do not change over time [e.g., *LaBrecque and Yang*, 2001]. The $\boldsymbol{\epsilon}_n$ errors can be >1 % for some ERT configurations, depending strongly on the mesh quality, the type of configuration and the forward solver. From my experience, $|\boldsymbol{\epsilon}_s + \boldsymbol{\epsilon}_n|_2$ for ERT data is usually ~ 10 times larger than $|\boldsymbol{\epsilon}_{ri}|_2$, so that removing $\boldsymbol{\epsilon}_s$ and $\boldsymbol{\epsilon}_n$ from the data reduces the error level by one order of magnitude. The $\boldsymbol{\epsilon}_s$ and $\boldsymbol{\epsilon}_n$ contributions are, in general, difficult to separate, but as long as $\boldsymbol{\epsilon}_n$ does not change with time, they can be considered as a single static error.

One common means of removing the effects of $\boldsymbol{\epsilon}_s$ and $\boldsymbol{\epsilon}_n$ is the difference inversion approach of *LaBrecque and Yang* [2001], which has been successfully applied by *Kemna et al.* [2002]. It uses as input data:

$$\hat{\mathbf{d}}_i = \mathbf{d}_i - \mathbf{d}_0 + g(\mathbf{m}_0) = g(\mathbf{m}_i) + \boldsymbol{\epsilon}_{ri} - \boldsymbol{\epsilon}_{r0}, \quad (1.5)$$

where $\boldsymbol{\varepsilon}_s$ and $\boldsymbol{\varepsilon}_n$ from the two data sets cancel. Another way to remove the effect of $\boldsymbol{\varepsilon}_s$ and $\boldsymbol{\varepsilon}_n$ is the ratio inversion technique of *Daily et al.* [1992], in which the ratios of data \mathbf{d}_i acquired during and data \mathbf{d}_0 acquired prior to an experiment are inverted. The input data for the i -th time step is:

$$\tilde{\mathbf{d}}_i = \frac{\mathbf{d}_i}{\mathbf{d}_0} g(\mathbf{m}_{bg}), \quad (1.6)$$

where \mathbf{m}_{bg} is a background model. To compare the difference and ratio inversion approaches, Equation 1.6 can be expanded and rearranged to look similar to Equation 1.5

$$\tilde{\mathbf{d}}_i = \frac{\mathbf{d}_i}{\mathbf{d}_0} g(\mathbf{m}_{bg}) = (\mathbf{d}_i - \mathbf{d}_0) \frac{g(\mathbf{m}_{bg})}{\mathbf{d}_0} + g(\mathbf{m}_{bg}). \quad (1.7)$$

After substituting the result \mathbf{m}_0 of the background inversion for \mathbf{m}_{bg} and assuming the background data \mathbf{d}_0 to be perfectly explained by the forward model (i.e., $g(\mathbf{m}_0)/\mathbf{d}_0 = 1$), Equations 1.5 and 1.7 become identical. In most realistic cases, in which $g(\mathbf{m}_0)$ is only approximately equal to \mathbf{d}_0 , the difference between $\hat{\mathbf{d}}_i$ and $\tilde{\mathbf{d}}_i$ will be practically negligible.

1.5.2 Time-lapse models

In the difference inversion approach of *LaBrecque and Yang* [2001], starting from the background model \mathbf{m}_0 , one typically uses the data difference $\hat{\mathbf{d}}_i$ (Equation 1.5) to invert for the model update. This approach is used in Chapter 3 of this thesis.

When using the ratio inversion technique of *Daily et al.* [1992], what is solved for depends on the background model \mathbf{m}_{bg} . It is common practice to use a homogeneous starting model as \mathbf{m}_{bg} [e.g., *Daily et al.*, 1992; *Slater et al.*, 2000; *Binley et al.*, 2002b; *Cassiani et al.*, 2006], such that the forward response of all data points is simply the homogeneous resistivity \mathbf{m}_{bg} . The value of \mathbf{m}_{bg} is often chosen to be 100 Ωm , so that the reconstructed difference model shows the percentage change in resistivity. This approach might lead to sub-optimal inversion results for two reasons. First, $\boldsymbol{\varepsilon}_n$ can be significant compared to $\boldsymbol{\varepsilon}_{ri}$, so $g(\mathbf{m}_{bg})$ should be calculated numerically to remove the associated numerical errors from the ratio inversion. Second, the choice of \mathbf{m}_{bg} affects the time-lapse inversion through the sensitivity kernel. If the resistivity variations in the subsurface are small compared to the time-lapse changes, then the initial sensitivities based on a homogeneous subsurface yield good results [e.g., *Binley et al.*, 2002b], but for cases in which resistivity variations are large, the imaged changes in resistivity might be unreliable.

Instead of assuming a homogeneous background model in the ratio inversion, I propose to use \mathbf{d}_0 to invert for the background model $\mathbf{m}_{bg} = \mathbf{m}_0$. In the time-lapse inversion in Chapter 6, the algorithm solves for updates to this model. This approach practically removes $\boldsymbol{\epsilon}_s$ and $\boldsymbol{\epsilon}_n$ and ensures reliable sensitivity patterns. Note that the difference approach of Equation 1.5 is equal to the general ratio inversion approach if $\hat{\mathbf{d}}_i$ is calculated as the difference between the logarithms of \mathbf{d}_i and \mathbf{d}_0 .

1.6 OBJECTIVES AND STRUCTURE OF THIS THESIS

The main goals of this thesis are to investigate how different geophysical methods can be integrated for characterizing shallow aquifers. All chapters have both a methodological aspect, thus introducing new processing and inversion techniques, as well as an applied component, in which the new methods help to understand better the subsurface at a field site. The data used in the Chapters 2, 4, 5 and 6 were acquired as part of this thesis at the two field sites at the Thur River (see Section 1.3). A team from University of Lancaster acquired the data used in Chapter 3 in 1998 under the leadership of Prof. A. Binley, who kindly provided the data.

Chapter 2 introduces a methodology for aquifer characterization based on structural joint inversion of multiple geophysical data sets followed by clustering to form zones and subsequent inversion for zonal parameters. The methodology is applied to a synthetic example and a field example of crosshole seismic and GPR traveltimes and ERT data.

The extension of the structural joint inversion approach to time-lapse data is described in Chapter 3. The time-lapse joint inversion is tested on crosshole ERT and GPR traveltimes data, acquired during a tracer test in unsaturated sandstone. I attempt to determine if time-lapse joint inversion can enhance the contrast of the tracer plume in the model and thus help to retrieve the spatial moments of the plume more accurately.

Chapter 4 investigates the importance of including the water-filled boreholes in the inversion of crosshole electrical resistance data. Not including this effect may lead to strong inversion artifacts that make interpretation very difficult. The idea of including structural constraints in an ERT inversion is further developed in Chapter 5, where I include GPR-derived interfaces in a 3-D inversion of surface ERT data. This concept is applied to data acquired on a gravelbar within the Thur River channel. These data are intended to detect zones of different depositional character.

To investigate the dynamics of the aquifer imaged in Chapter 5, I monitor a salt tracer using surface ERT in Chapter 6. The time-lapse ERT results are used to constrain hydraulic conductivity in a groundwater-flow and transport model. The results of the transport simulation are used to synthesize ERT images that are compared to results of the field experiment.

Finally in Chapter 7, I draw some conclusions and indicate some areas of future research.

The Appendices include other hydrogeophysical studies that I was involved in during my thesis. Appendix A gives an overview of preliminary hydrogeophysical results at the two Thur River field sites and Appendix B investigates the Widen field site using 3-D ERT based on data acquired between 18-boreholes. Appendix C uses GPR crosshole data from the Widen site for a full-waveform inversion. The resultant images resolve small-scale features in the permittivity and resistivity distribution of the aquifer. Appendix D provides an overview of studies in the restored Thur River section. Self-potential investigations at this field site are described in Appendix E. A detailed formulation of the inverse problem for cross-gradient joint inversion is included in Appendix F. A study where single- and crosshole GPR reflection data is used to image fractures in granitic rock is introduced in Appendix G.

2 AQUIFER ZONATION BASED ON JOINT INVERSIONS

Published in *Geophysics*:

Doetsch, J., Linde, N., Coscia, I., Greenhalgh, S. A., and Green, A. G., 2010. Zonation for 3D aquifer characterization based on joint inversions of multimethod crosshole geophysical data, *Geophysics*, **75**, G53-G64.

ABSTRACT

Predictive groundwater modeling requires accurate information on aquifer characteristics. Geophysical imaging is a powerful tool for delineating aquifer properties at an appropriate scale and resolution, but it suffers from problems of ambiguity. One way to overcome such limitations is to adopt a simultaneous multitechnique inversion strategy. We have developed a methodology for aquifer characterization based on structural joint inversion of multiple geophysical data sets followed by clustering to form zones and subsequent inversion for zonal parameters. Joint inversions based on structural cross-gradient constraints require less restrictive assumptions than, say, applying predefined petrophysical relationships, and generally yield superior results. This approach has, for the first time, been applied to three geophysical data types in three dimensions. A classification scheme using maximum likelihood estimation is used to determine the parameters of a Gaussian mixture model that defines zonal geometries from the joint inversion tomograms. The resulting zones are used to estimate representative geophysical parameters of each zone, which are then used for field-scale petrophysical analysis. A synthetic study demonstrates how joint inversion of seismic and radar traveltimes and electrical resistance tomography (ERT) data greatly reduces misclassification of zones (down from 21.3% to 3.7%) and improves the accuracy of retrieved zonal parameters (from 1.8% to 0.3%) compared to individual inversions. We applied our scheme to a data set collected in northeastern Switzerland to delineate lithological subunits within a gravel aquifer. The inversion models resolve three principal sub-horizontal units along with some important 3-D heterogeneity. Petrophysical analysis of the zonal parameters indicates ~30% variation in porosity within the gravel aquifer and an increasing fraction of finer sediments with depth.

2.1 INTRODUCTION

Aquifer characterization is a prerequisite for predictive groundwater modeling. Traditionally, small-scale aquifer properties are derived from geological and hydrological investigations at a limited number of boreholes. These investigations may include simple lithological interpretations of drill chips/cuttings and laboratory determinations of physical properties (e.g., hydraulic conductivity) of retrieved cores. The sampling volume for such measurements is very limited, being restricted to the actual borehole positions. Furthermore, the assumption that laboratory-determined physical properties represent in-situ conditions may not be valid because of significant scaling effects, differences in confining pressure,

strain, and fracturing, and a natural sampling bias towards intact specimens. Geophysical well logging overcomes some of these problems and extends the sampling distance up to a maximum of approximately 1 m from the borehole. Nevertheless, upscaling information derived from laboratory measurements and well logs to help construct fluid-flow and transport models of heterogeneous formations does not always lead to accurate predictions [Scheibe and Chien, 2003].

Hydrologists often perform in situ pumping tests, which together with certain assumptions about aquifer homogeneity and isotropy, enable the aquifer to be characterized on a much broader scale. This constitutes the other extreme end member solution to the spatial scaling problem.

An intermediate scaling approach involves constraining hydrological models using appropriate crosshole and/or surface geophysical data. Geophysical imaging is particularly useful (and complementary) because it interrogates a much greater volume of the aquifer than simple drilling and logging, provides almost continuous subsurface sampling, and is capable of delineating heterogeneity. For example, Scheibe and Chien [2003] produce accurate predictions of bromide breakthrough curves using a combination of crosshole radar tomograms and flow-meter and slug-test data, whereas traditional hydrological data alone yield poor predictions. The success of this approach is attributed to the large spatial coverage and 0.1 – 1 m resolution of the radar tomograms combined with a strong correlation between radar wavespeed and effective porosity. For such approaches to produce meaningful results, there must be a strong empirical relationship between the tomographic (geophysical) parameter and the hydrological properties [Day-Lewis and Lane, 2004; Linde et al., 2006b]. Unfortunately, petrophysical relationships are often site-specific, such that they cannot be easily extrapolated to other locations or geologic conditions. Likewise, simplified theoretical relationships between geophysical parameters and hydrological properties have limited ranges of applicability and cannot always be directly applied to geophysical tomograms based on standard inversions [Day-Lewis and Lane, 2004].

Although tomograms obtained from a single geophysical data type may help to improve hydrological models, ambiguity often remains. The conventional way to reduce such nonuniqueness is to introduce external constraints, such as a priori geological information, smoothing, stochastic regularization, or inversion for a specific model type. An alternative approach for reducing model ambiguity is joint inversion of two or more different types of co-located geophysical data to produce a single integrated model. The power of this approach lies

in the complementary nature of the data and models that can be exploited to constrain the range of plausible hydrological interpretations. Since different geophysical methods (e.g., seismic and radar transmission and electrical resistance tomography [ERT]) are sensitive to different physical properties of an aquifer, joint inversion is traditionally achieved by imposing petrophysical relationships; multiple models are linked during the inversion by petrophysical equations with known parameter values [e.g., *Tryggvason et al.*, 2002]. For example, since resistivity and dielectric permittivity both depend on porosity [e.g., *Pride*, 1994; *Revil et al.*, 1998; *Linde et al.*, 2006a], this style of joint inversion could directly yield porosity estimates. A drawback of such schemes is that general petrophysical models typically involve many parameters that are likely to vary spatially and are usually poorly known.

A less restrictive approach to joint inversion, presented independently by *Haber and Oldenburg* [1997] and *Zhang and Morgan* [1997], is to impose structural similarity between models during the inversion process without any explicit assumptions about petrophysical relationships, except that the geophysical parameters are assumed to vary at common locations. *Gallardo and Meju* [2003; 2004] developed this structural approach into a methodology for joint inversion by advocating that the gradients of a model could be used to quantify structures. They introduced the idea that the vector cross product of the gradients of two models should be forced to zero (implying similar directions of the gradient vectors) at each iterative step of a joint inversion. Changes in the two parameters at a given location must then be either zero, parallel, or anti-parallel. *Gallardo and Meju* [2003] applied this approach to field data and used the final models for visual zonation and interpretation. One key advantage of the structural approach to joint inversion is that scatter plots between different models provide less biased information about petrophysical parameters than those obtained using direct petrophysical approaches to joint inversion [*Tryggvason and Linde*, 2006]. Several researchers have further modified and applied the cross-gradients joint inversion approach [e.g., *Gallardo and Meju*, 2007; *Linde et al.*, 2008], and it has recently been applied to more than two data types [*Gallardo*, 2007] and to 3-D data sets [*Linde et al.*, 2006a; *Tryggvason and Linde*, 2006; *Fregoso and Gallardo*, 2009]. We extend here the methodology developed by *Linde et al.* [2006a] to three different types of 3-D data.

Rather than using inverted tomograms to delineate the detailed structure of an aquifer [e.g., *Hubbard et al.*, 1999], it is often useful to integrate the information to define zones on a scale significantly larger than the inherent resolution of each tomogram. This allows us to

determine “effective” geophysical parameters that are only weakly affected by the original regularization constraints. The zones thus identified are assumed to have similar petrophysical characteristics [Hyndman and Gorelick, 1996; Hyndman and Harris, 1996; Eppstein and Dougherty, 1998] and hence are more useful in flow and transport modeling. Whereas applications of zonation and classification techniques are common in medical imaging and remote sensing, they are still in their infancy in geophysics [Avseth *et al.*, 2001; Bedrosian *et al.*, 2007]. In near-surface investigations, Tronicke *et al.* [2004] and Paasche *et al.* [2006] have applied K-means and fuzzy c-means clustering techniques to crosshole traveltime and attenuation tomograms. Neither method is well suited for zone identification and classification of strongly correlated parameters, which is a fundamental requirement when applied to structurally constrained joint inversions. By using maximum likelihood estimation to find the parameters of a Gaussian mixture model, our preferred clustering approach incorporates the covariance between the various parameters [Dempster *et al.*, 1977; Mitchell, 1997]. As a consequence, this approach is explicitly aimed at determining zones for which there are strong correlations between the various parameters (e.g., Figure 4 in Gallardo and Meju [2003]).

In this contribution, we begin by explaining our inversion and clustering techniques and introducing the field test site in northern Switzerland. We then determine zonal models based on parameters estimated from structurally constrained joint inversions of comparable synthetic and field data sets, each comprising three different types of 3-D geophysical data (crosshole seismic, radar, and ERT). By fixing the zone boundaries defined by the joint inversion and clustering algorithms and re-inverting the same three data sets for uniform zonal parameter values (i.e., seismic and radar wavespeed and electrical resistivity), the effective parameters of each zone are established. As a final step, we use the estimated zonal parameters for the field example to infer hydrologically relevant properties, such as formation factor and relative variations in the distributions of fine materials (silts and clays).

2.2 METHODOLOGY

In this section we describe the main components of our scheme (i.e., joint inversion, cluster analysis and zonation, and zonal inversion). Figure 2.1 shows a flow-chart of the entire process from raw field data and *a priori* information to the final petrophysical properties of the aquifer.

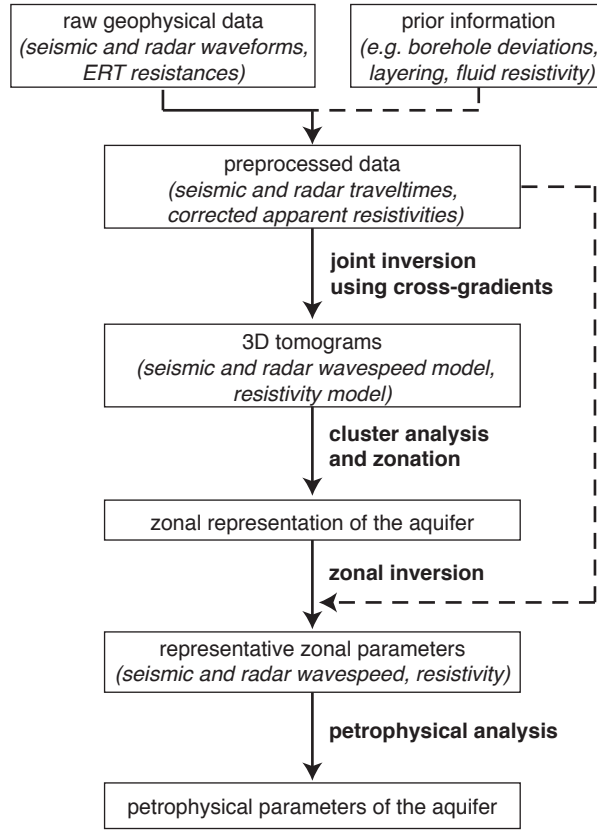


Figure 2.1. Workflow designed to locate aquifer zones and determine their petrophysical properties. Crosshole geophysical data - seismic, radar and ERT - are used as input to this scheme.

2.2.1 Joint inversion

Our formulation and implementation of the inverse problem is illustrated in Figure 2.2 and follows closely the scheme outlined by *Linde et al.* [2006a; 2008]. Forward solvers are used to calculate seismic and radar traveltimes, electrical resistances, and the corresponding sensitivities. The traveltimes and raypaths are calculated in the high frequency limit using a finite-difference algorithm [*Podvin and Lecomte*, 1991; *Tryggvason and Bergman*, 2006], and the electrical responses and related sensitivities are computed using a finite-element solver implemented by *Rücker et al.* [2006].

The objective function Φ for K different data sets is defined as

$$\Phi = \sum_{k=1}^K w_k (\Phi_{d(k)} + 10^\epsilon \Phi_{m(k)}) + \lambda \sum_{k=1}^K \sum_{l < k} T_{kl} \quad (2.1)$$

with $\Phi_{d(k)}$ and $\Phi_{m(k)}$ being the data misfit and regularization term for data set k , and T_{kl} is the sum of the absolute values of the cross-gradient function \mathbf{t}_{kl} between the models corresponding to data sets k and l (see below). The parameters w_k , ϵ and λ are the weighting factors for each data set, the regularization term, and the cross-gradients term, respectively.

When individually inverting a single data set, only $\Phi_{d(k)}$ and $\Phi_{m(k)}$ contribute to the objective function (Equation 2.1 and Figure 2.2): $\Phi_{d(k)}$ is the misfit between the observed data and the data predicted by the wavespeed or resistivity-models and $\Phi_{m(k)}$ quantifies the model regularization that penalizes model structure in some sense. We use a stochastic regularization operator (having weight 10^e relative to the data fit term) based on an exponential geostatistical model that penalizes model complexity and deviations from the initial input model [*Linde et al.*, 2006a].

Joint inversion of two colocated data sets (e.g., radar and ERT) using a structural approach adds the third component to the objective function that enforces structural similarity [*Haber and Oldenburg*, 1997]. The structural similarity of two models \mathbf{m}_k and \mathbf{m}_l is quantified by calculating a normalized version of the cross-gradients function introduced by *Gallardo and Meju* [2003] at each location as [*Linde et al.*, 2008]

$$\mathbf{t}_{kl}(x, y, z) = \frac{\nabla \mathbf{m}_k(x, y, z) \times \nabla \mathbf{m}_l(x, y, z)}{\mathbf{m}_{k_apriori}(x, y, z) \cdot \mathbf{m}_{l_apriori}(x, y, z)}. \quad (2.2)$$

The normalization of Equation 2.2 is with respect to the à priori models $\mathbf{m}_{k_apriori}$ and $\mathbf{m}_{l_apriori}$. Note that the denominator never goes to zero. By normalizing the cross-gradients function, the constraints for each model combination have, for a given relative change in the model properties, the same weight in the optimization. The linearized normalized cross-gradients function of \mathbf{m}_k and \mathbf{m}_l is added as a constraint at each iterative step by giving it a large weight in the linear system of equations [*Linde et al.*, 2006a]. *Paige and Saunders* [1982] iterative conjugate gradient algorithm LSQR is used to minimize the objective function in a least-squares sense.

For three-method joint inversion, we calculate the cross-gradients function for every possible model combination to give three cross-gradients fields. These linearized cross-gradients constraints are imposed at each iterative step. *Gallardo* [2007] introduced an alternative approach that is based on the cross-product of a reference gradient (defined at each location as the strongest model gradient of all models in the previous iteration) and the gradients of each of the models being inverted for in the process.

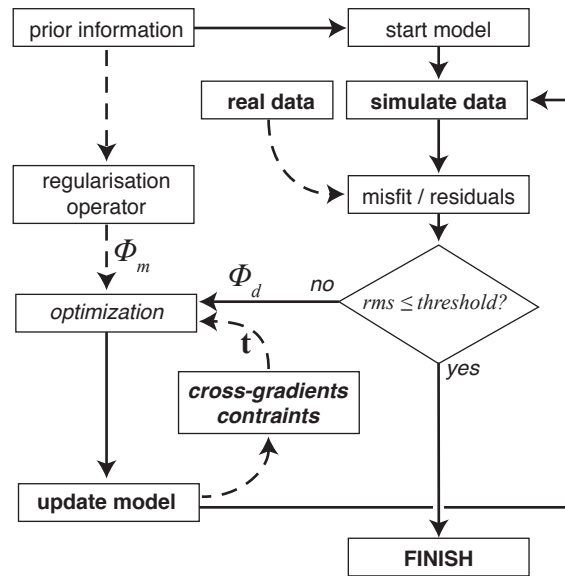


Figure 2.2. Flowchart of the joint inversion scheme using cross-gradients constraints. Φ_d and Φ_m represent the sole contributions to the objective function Φ (Equation 2.1) in individual inversions. For joint inversion, coupling between the models is introduced by penalizing deviations of the cross-gradient function \mathbf{t} from zero during model optimization.

2.2.2 Zonation

We employ an unsupervised zonation algorithm to group model cells into zones distinguished by common physical characteristics, such that two or more zones with uniform properties are used to describe the distribution of geophysical parameters in a region of interest (e.g., an aquifer).

Defining the zones is a four-step process:

1. Preprocessing: The values of each input model (3-D tomogram) are scaled to a mean of 1 to avoid effects associated with the model units (e.g., km/s). The logarithm of electrical resistivity is used to compress the typically large range of values for this parameter. Classification needs reliable information from at least two methods for each cell and only model cells with ray coverage in either the seismic or radar forward models are used for the classification. This is guaranteed by sufficient ray coverage in one or both of the ray-based models plus the non-zero sensitivity of the ERT throughout the entire inversion domain. The decision of which cells to use for the cluster estimation could probably be improved by model appraisal (e.g., using the model covariance matrix) and might have to be adapted for surface-based data with generally coarser data coverage.

2. Cluster estimation: The clusters are modeled as a mixture of Gaussian functions with parameters that are automatically estimated on the basis of an expectation maximization

algorithm [Bouman, 1997]. This algorithm maximizes the probability of each cell belonging to a given set of clusters with optimized cluster parameters. The probability p_n that a cell n with model values \mathbf{x}_n belongs to the k^{th} cluster is given by

$$p_n(k) = \frac{1}{(2\pi)^{M/2}} |\mathbf{R}_k|^{-1/2} \exp\left\{-\frac{1}{2}(\mathbf{x}_n - \boldsymbol{\mu}_k)' \mathbf{R}_k^{-1} (\mathbf{x}_n - \boldsymbol{\mu}_k)\right\}, \quad (3)$$

where $\boldsymbol{\mu}_k$ is the M - dimensional spectral mean and \mathbf{R}_k is the covariance matrix of cluster k .

The cluster parameters are optimized as follows:

- a) begin with a large number of clusters (e.g., 100);
- b) classify all model cells and update statistics of the clusters;
- c) combine the two statistically nearest neighbor clusters;
- d) perform expectation maximization to update the mean and covariance of each cluster.

Steps b-d are repeated until a user-defined number of clusters is reached.

3. Classification: Each aquifer zone is represented by a single cluster and each cell is assigned to the zone for which $p_n(k)$ is maximal (Equation 2.3).

4. Zone interpolation: All poorly resolved cells not classified in step 3 are assigned to a zone based on interpolation/extrapolation of the well-resolved cells. The indicator kriging routine of the geostatistical software library GSLIB [Deutsch and Journel, 1998] is used for this purpose. The output of the indicator kriging is a zonal model of the entire model domain.

2.2.3 Zonal inversion

After obtaining a geometrical model of the zones, we perform an overdetermined inversion to find the optimum parameter values (i.e., the seismic and radar wavespeeds and electrical resistivity) of each zone. The zonal inversion uses the same forward operators and preprocessed data as used for the joint inversion (shown by the dashed arrow in Figure 2.1), but instead of inverting for many thousands of model parameters it only inverts for one parameter value of each geophysical method in each zone. Starting from a homogeneous initial model, a linearized iterative inversion scheme is used to optimize the zonal parameters. There is no need for additional regularization, because the inverse problem is strongly overdetermined (e.g., 5000 data points to define 3 parameters). The parameter update is slightly reduced at each iterative step to stabilize the non-linear inverse process.

Convergence of this inversion process is both fast and robust. The final data misfit can be used as an indicator of how well the zonal model can explain the geophysical data. If only a few model parameters in the zonal model can describe the data almost as well as relatively

complex seismic, radar and ERT models with many thousands of parameters, then a zonal model is justified.

The inverted zonal parameters and any derived petrophysical properties are effective values on the scale of the zones, thereby providing a simple form of upscaling for use in future hydrological modeling. In most applications, it is highly unlikely that the underlying physical property distribution is made up of zones with uniform properties or overly smooth distributions. Constructing two end members of inversion models can help to understand the characteristics of the system under study.

2.3 FIELD SITE, PARAMETERS, AND PROCEDURES COMMON TO THE SYNTHETIC AND FIELD EXAMPLES

We have applied our methodology to a field site beside the Thur River in northern Switzerland, where the hydrological, ecological and biochemical effects of river restoration are currently being investigated [*RECORD*, 2011]. Our experiment is one component of a hydrogeophysical pilot study that targets a gravel aquifer in direct contact with an unrestored section of the river. We wish to estimate the spatial variability of geophysical and hydrogeological properties of the ancient river sediments forming the aquifer and to derive a 3-D zoned representation of the subsurface as a basis for future hydrogeophysical inverse modeling.

In this section we describe the following details that are common to the synthetic and field examples: geological/geophysical model, borehole geometry, recording configurations and processing parameters. The synthetic example helps to validate our new approach and guide the interpretation of the field data and associated models.

2.3.1 Experimental setup

Cores from boreholes across the field site reveal a laterally extensive three-layer structure with a 3-m-thick silty sand layer at the top, an intermediate-depth 7-m-thick gravel aquifer, and a thick impermeable clay aquitard at the base. The water table is normally at 4 m depth except during river flood events. For our experiment, the aquifer is accessed by four 11.4-cm-diameter fully-slotted PVC-cased boreholes located at the corners of a 5×5 m square, approximately 10 m from the river (Figure 2.3). Our analysis is concerned with this 5×5 m section of the 6-m-thick saturated part of the aquifer.

For the inversion of all three data sets, the area of interest is represented by a $7 \times 7 \times 6$ m volume containing a cubic mesh with 0.25 m edge lengths. The ERT model includes additional layers above and below this volume, but no regularization is applied across the boundaries to these layers. This is done because the boundaries are known to be sharp and because continuous regularization across these boundaries causes inversion artifacts within the gravel unit. A finer cubic mesh with 0.0625-m edge lengths is employed for the forward modeling of the seismic and radar traveltimes, whereas tetrahedra with 0.25-m edge lengths are used for the ERT forward modeling. Boundary effects in the ERT forward modeling were avoided by using a much larger domain than for the inversion and by using mixed type boundary conditions [Rücker *et al.*, 2006].

Crosshole seismic, radar, and ERT data were acquired across all six planes between the four boreholes. Seismic data were recorded using source and receiver spacings of 0.25 m, whereas radar data were collected with source and receiver spacings of 0.5 m and 0.1 m, respectively. To ensure full symmetric radar coverage, the source and receiver antennas were interchanged and the experiment repeated for each plane. For the ERT survey, 9 electrodes at 0.7-m intervals were deployed in each borehole. We used two different types of electrode configuration [Bing and Greenhalgh, 2000]: the AB-MN configuration with two current electrodes (A, B) in one borehole and two potential electrodes (M, N) in a second borehole, and the AM-BN configuration with one current and one potential electrode in a common borehole and the other two electrodes in a second borehole. Data using all possible combinations of bipole size and position were acquired in each plane, resulting in a total of 2464 AB-MN and 7776 AM-BN measurements. To speed up the inversions, the 10240 measurements were reduced to the 5000 most information-rich values using an experimental design procedure (for details see Chapter 4).

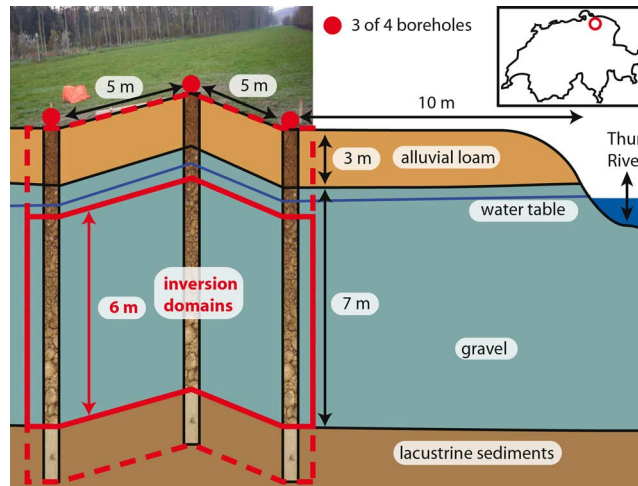


Figure 2.3. Cross section of the field site located close to the Thur River in northeastern Switzerland (see inset). The gravel aquifer is intersected by four boreholes located at the corners of a 5 m x 5 m square approximately 10 m from the river. Our inversion domain has horizontal dimensions of 7 m x 7 m for all data and a vertical extent of 6 m for the seismic and radar data (solid red rectangle) and 12 m for the ERT data (dashed red rectangle).

2.3.2 Inversion parameters

During inversion, stochastic regularization was used with an exponential model [Deutsch and Journel, 1998]. To honor the subsurface layering evident in the borehole cores, without imposing excessive constraints, we used 1.5- and 0.75-m integral scales in the horizontal and vertical directions, respectively. Because no detailed geostatistical analysis had been carried out at this site, the integral scales were chosen in a pragmatic manner to be comparable to the resolving capabilities of the geophysical data but smaller than the borehole spacing. The integral scales were varied about the chosen values without significant changes in the final inversion results. The same geostatistical model was used for the indicator kriging.

Initial homogeneous input models were seismic wavespeed $\alpha = 2.05 / 2.05$ km/s, radar wavespeed $v_r = 76 / 76$ m/ μ s and electrical resistivity $\rho = 250 / 180$ Ω m for the synthetic / field examples. The standard deviation of the stochastic regularization was 10% of the input models for the seismic and radar experiments, corresponding to the expected variations in the field example and the variations used in the synthetic model. The ERT data were inverted for the logarithm of the resistivity, assuming a 20% standard deviation for the stochastic regularization.

Strong regularization (high ε , see Equation 2.1) was employed for the initial inversion step and then progressively decreased with a specified step length after each iteration until the normalized root mean squared (RMS) misfit reached a predefined threshold (see Figure 2.2).

Successively decreasing ε stabilizes the linearized inversion compared to using the final ε throughout the inversion process. To compare the results between individual and joint inversion as well as between the different methods, the target normalized RMS misfit was set to a uniform 1.2. It was possible to invert for a normalized RMS misfit of 1.0, corresponding to the actual error level in the synthetic example, but this led to inversion artifacts that adversely affected the subsequent cluster classification.

All inversions reached the target misfit after 10-19 iterations. Convergence could be achieved with fewer iterations by decreasing ε at a higher rate, but this resulted in higher values of the cross-gradients function in the final model [see *Linde et al.*, 2008]. The value of the ε was the same for all data sets during joint inversion, but each data set was weighted differently in the objective function and when calculating the model updates. The data set weights $w_1 - w_3$ were applied to the data misfit and the regularization of the corresponding model (Equation 2.1). They were initialized to compensate for the different number of measurements in each data set (in inverse proportion) and varied until the 3-D tomograms of all methods predicted the data equally well. Figure 2.4 illustrates the process we used to determine $w_1 - w_3$ and Table 2.1 shows the final inversion parameters for the synthetic and field examples. Tests using all possible combinations of two-method joint inversions and varying the inversion parameters gave very similar results to what is presented below for the three-method joint inversion, thus demonstrating the robustness of the methodology and each sequential part of it.

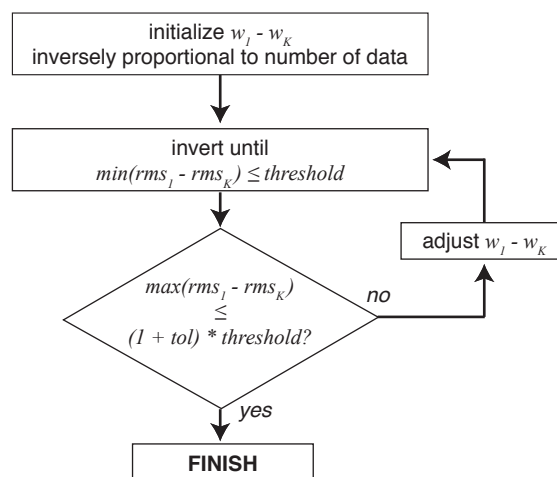


Figure 2.4. Flow chart of the procedure to determine the relative weights $w_1 - w_K$ of the K different data sets for joint inversion. The threshold of the normalized RMS was set to 1.2 and the tolerance between the methods was chosen as $\text{tol} = 0.04$.

Table 2.1. Inversion parameters for the synthetic and field examples. In the column and row headers: *S* - seismic; *R* - radar; *E* - ERT individual inversions; *SRE* - joint inversion of all three methods.

Data set	geophys. method	weight w_k			ϵ	iterations	RMS misfit			
		<i>S</i>	<i>R</i>	<i>E</i>			<i>S</i>	<i>R</i>	<i>E</i>	mean
synthetic example	<i>S</i>	1			1.10	10	1.19			1.19
	<i>R</i>		1		1.20	10		1.18		1.18
	<i>E</i>			1	1.08	10			1.20	1.20
	<i>SRE</i>	1.3	1.0	1.0	0.98	16	1.17	1.17	1.20	1.18
field example	<i>S</i>	1			1.15	10	1.20			1.20
	<i>R</i>		1		1.20	10		1.21		1.21
	<i>E</i>			1	1.12	10			1.21	1.21
	<i>SRE</i>	1.5	1.2	1.0	0.88	19	1.20	1.16	1.20	1.19

2.4 SYNTHETIC EXAMPLE

The synthetic input model (Figure 2.5) was chosen to mimic the field situation. It consists of three sub-horizontal layers, of which the middle layer has the highest seismic and radar wavespeeds and resistivity. Its thickness varies from 2.5 m in one corner to 1 m in the opposite corner. The seismic wavespeed α and resistivity ρ are lowest in the bottom layer, whereas the radar wavespeed v_r is lowest in the top layer. For the ERT modeling, an additional top layer with a resistivity of $\rho = 1000 \Omega\text{m}$ representing the unsaturated zone, and a bottom layer with a resistivity of $\rho = 25 \Omega\text{m}$ representing the clay aquitard, are added.

Source, receiver, and electrode positions, as well as the measuring configurations were identical to the field example. The synthetic data were created with the same forward solvers and grid as used for the inversions. The 2661 seismic and 5584 radar traveltimes were contaminated with 1% and the 5000 apparent resistivities with 3% uncorrelated Gaussian noise prior to inversion.

2.4.1 Individual and joint inversion results

The three data sets are inverted separately and jointly. All resulting 3-D tomograms (Figure 2.6) recover the main features of the synthetic input models (Figure 2.5), albeit with somewhat gradual rather than abrupt transitions between the layers. The seismic and radar models obtained by individual inversion (Figure 2.6a and b) clearly resolve the high wavespeed center region. Low wavespeed parts are less well resolved, especially for the radar model. This is mainly due to the limited ray coverage, particularly crossing rays, in the top

and bottom regions of the model. The individual ERT inversion (Figure 2.6c) resolves the two low resistivity zones, but the high resistivity layer in the middle is not continuous, as it should be. This poor performance in the center is attributed to current channeling in the high conductivity zones above and below and to the much higher sensitivities around the electrodes.

The 3-D seismic and radar tomograms resulting from joint inversion (Figure 2.6d and e) are very similar to the individual inversion tomograms, but the values of the low wavespeed regions are closer to the true values. The improvement in the joint inversion ERT tomogram (Figure 2.6f) is more pronounced, because the radar and seismic data help to constrain the geometry of the more resistive middle layer. Despite the restriction of rays to the acquisition planes and the concentration of ERT sensitivities around the boreholes, the homogeneous layers are well retrieved in 3-D, including the regions between the acquisition planes. The values of the cross-gradients function between the models were decreased by more than a factor of 100 compared to the individual inversions.

An informative view of the difference between models obtained from the individual and joint inversions is supplied by the scatter plots of Figure 2.7a-c and e-g. Whereas the scatter plots derived from the individual inversion show no evidence of clustering (Figure 2.7a-c), those from the joint inversion are sharply defined and relatively easy to classify (Figure 2.7e-g).

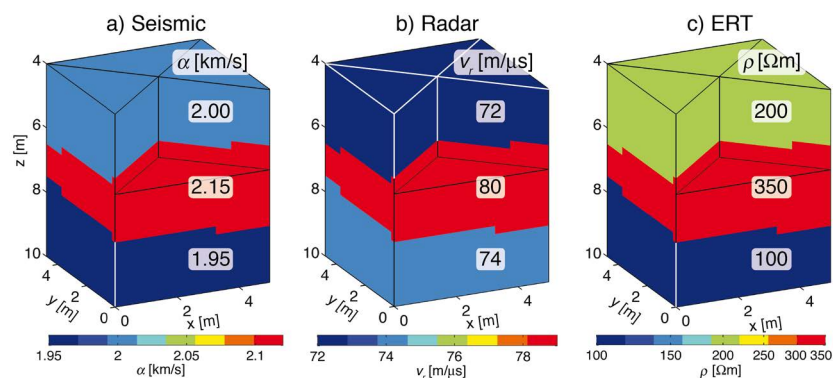


Figure 2.5. Input model used to create the synthetic data. It consists of three layers, the middle one of which has high seismic and radar wavespeeds α and v_r , and a high resistivity ρ relative to the others. The thickness of this middle layer varies between 1 and 2.5 m at opposite corners. The synthetic data were contaminated with Gaussian noise (1% for seismic and radar traveltimes, 3% for apparent resistivities) before inversion. The boreholes used for the measurements are located at the four corners of the input model.

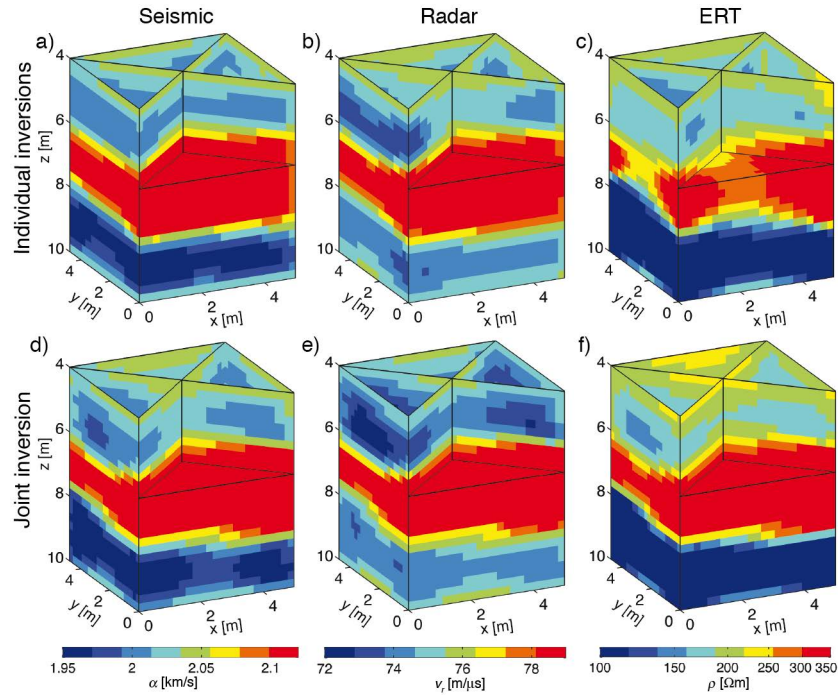


Figure 2.6. Results of (a-c) individual and (d-f) joint inversions of the synthetic data sets. All models fit the data with a normalized RMS misfit of 1.2 (1.0 corresponds to the error level). The main layering of the input model (see Figure 3) is observed in all models. The two seismic (a and d) and two radar (b and e) models are very similar, but a clear improvement is observed in the ERT model obtained by joint inversion (f) compared to the individual inversion model (c).

2.4.2 Classification

The scatter plots are now used for cluster estimation and zonation. The final number of zones was set to the true value of three for the synthetic study. Differences in the scatter plots are reflected in the classifications. The 50% confidence ellipsoids for each cluster are much smaller and more needle-like for the joint inversion (Figure 2.7h) than for the individual inversion results (Figure 2.7d). Outputs of the classification algorithm are the zonal models shown in Figure 2.8. The zonation based on the joint inversion tomograms (Figure 2.8c) is a much better reconstruction of the input model (Figure 2.8a) than that based on the individual inversion models (Figure 2.8b). Misclassification is only 3.7% for Figure 2.8c compared with 21.3% for Figure 2.8b. It is remarkable that the zones defined from the joint inversion tomograms are geometrically continuous, even though the positions of the cells are not considered during classification.

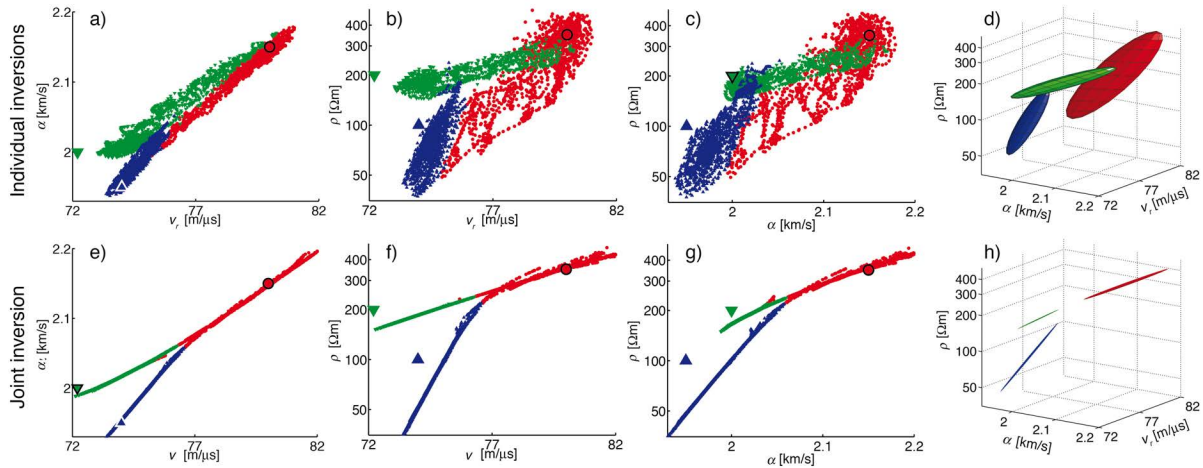


Figure 2.7. Scatter plots for the models obtained by (a-c) individual and (e-g) joint inversion together with visualizations of the automatically determined clusters used for zonation of the models obtained by (d) individual and (h) joint inversion. The larger triangles and circles in (a-c) and (e-g) show the true parameter values of each zone in the input model. The colors of the symbols in the scatter plots and cluster representation correspond to the respective zonal model in Figure 2.8.

2.4.3 Zonal inversion

The inverted zonal parameters and RMS misfits are shown at the base of Figure 2.8. The parameter values for each zone are much better retrieved through zonal inversion than by averaging the models in Figure 2.6 for each zone. The zonal model from joint inversion predicts the data with similar RMS misfits as for the 3-D tomograms (1.1-1.5), but the zonal model from individual inversions fails to do so (RMS misfits of 1.6-3.0).

The inverted zonal parameters reproduce the true values with a deviation of only 0.3% when using the zones derived from the joint inversion tomograms, whereas the deviation is 1.8% when using the zones derived from the individual inversion tomograms. A deviation of almost 2% in the parameter estimation is quite significant when compared to the 10-20% variation in the parameters of the synthetic input models (Figure 2.5).

The misclassification rates and matches of the geometry and parameter values (see images and tables in Figure 2.8) for the synthetic study demonstrate the superior performance of the joint inversion scheme vis-à-vis the individual inversion approach. For field data with unknown zone geometries and parameters, the zonation has to be judged on the basis of the RMS data misfit and by visual inspection. The performance of the method applied to field data is investigated in the next section.

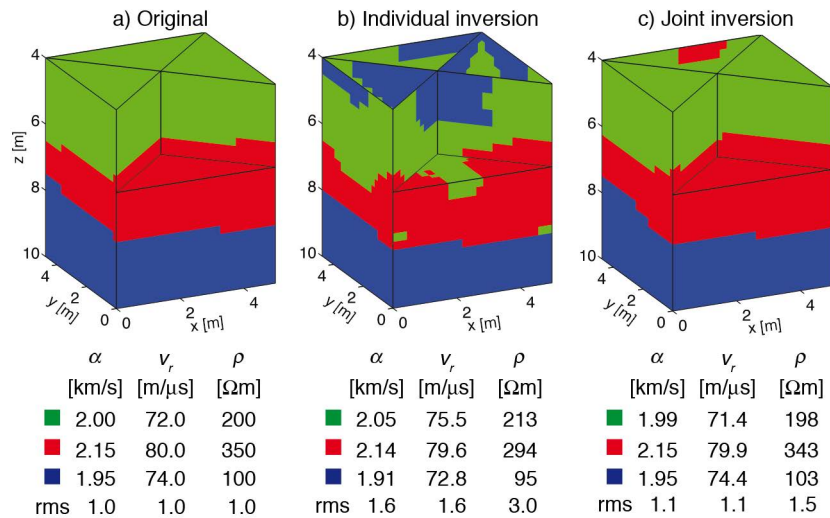


Figure 2.8. The (a) true zonal model (see Figure 5) and those derived by (b) individually and (c) jointly inverting the synthetic data. The zonal models derived from the individual and joint inversions have misclassification rates of 21.3% and 3.7%, respectively.

2.5 FIELD EXAMPLE

2.5.1 Measurements

Our field data were acquired with state-of-the art equipment. A sparker source was used to generate seismic waves with a center frequency of about 1 kHz, and hydrophones and a GEODE system were used to record the seismic data at a sampling rate of 21 μ s. Very strong signals caused the seismic waveforms to be clipped, but the first arrivals could clearly be identified (e.g., Figure 2.9a). Crosshole radar data at a 0.4 ns sampling rate were acquired using a RAMAC 250 MHz system, which at our site had a center frequency of \sim 100 MHz with energy in the 50-170 MHz frequency range (e.g., Figure 2.9b). ERT resistances were recorded using a Syscal Pro resistivity meter. Borehole deviations were measured with a deviation probe using a three-axis fluxgate magnetometer for bearing and a three-axis accelerometer for inclination. Corrections for the borehole deviations were critical for the traveltimes inversions.

Preprocessing of the seismic and radar data included manual traveltimes picking and assignment of the correct source-receiver positions in the deviated boreholes. A total of 2661 seismic and 5584 radar traveltimes could be reliably picked. Seismic traveltimes ranged between 2.2 and 4.3 ms and radar traveltimes ranged between 60 and 116 ns, with estimated picking errors for both data sets of \sim 1%.

The ERT data were strongly influenced by the resistivity contrast between the borehole fluid and the formation, such that correction factors derived from modeling with and without the boreholes had to be applied (for details see Chapter 4). A 2.5% error in the apparent resistivity data was assumed in the subsequent inversions. A frequency polygon plot of apparent resistivities before and after application of the borehole-fluid corrections is displayed in Figure 2.9c.

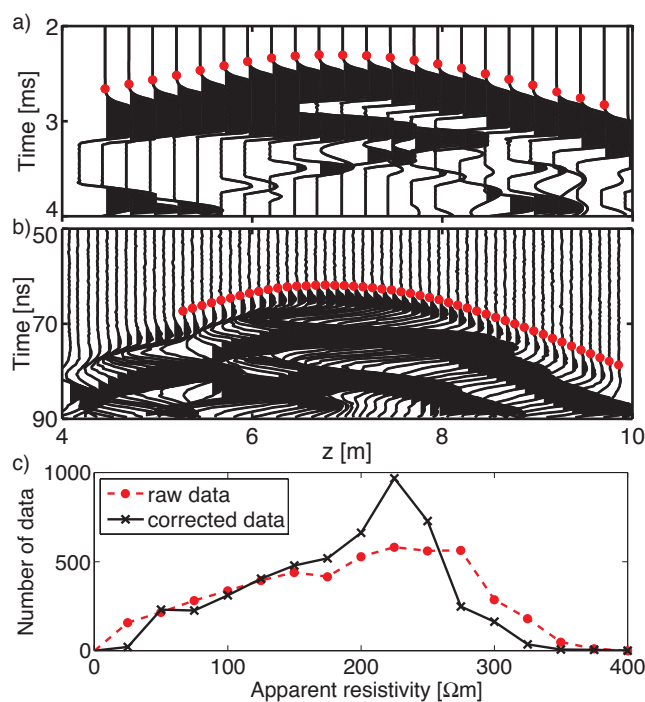


Figure 2.9. Typical raw (a) seismic and (b) radar source gathers for a source depth of 6.75 m. Red dots in (a) and (b) represent calculated forward responses of the final models obtained by joint inversion (see Figure 2.10d and e). (a) Although the seismic data were clipped, first arrivals could be reliably picked. (b) Picked first arrivals in the radar data do not include refracted waves through the unsaturated high wavespeed layer above 4 m; for the displayed source gather this means neglecting data collected above 5 m depth. (c) Frequency-polygon (histogram) of apparent resistivities plotted for raw and borehole-effect-corrected data.

2.5.2 Individual and joint inversion results

The models for the three parameter types obtained from the individual inversions contain very similar features, the most prominent being the high wavespeed and high resistivity layer in the middle of the domain (Figures 2.10a-c and 2.11a-c). Correlations between the models are relatively high (correlation coefficients > 0.6), even though each inversion is fully independent. This strong correlation indicates that all three methods sense the same geological/hydrological units, thus justifying the application of joint inversion to these data sets.

Seismic and radar tomograms from the three-method joint inversion (Figures 2.10d-e and 2.11de) are very similar to the individually inverted ones (Figures 2.10a-b and 2.11a-b), whereas resistivities in the jointly inverted ERT tomogram (Figures 2.10f and 2.11f) are noticeably more continuous than in the individually inverted one (Figures 2.10c and 2.11c). In similar fashion to the synthetic case, the magnitude of the cross-gradients between the models were reduced by more than a factor of 100 compared to the individual inversions. Although the images in Figure 2.10 are layered, when viewed from different directions (e.g., Figure 2.11) some pronounced 3-D heterogeneity is apparent. This heterogeneity is evident in all individual inversion tomograms (see Figure 2.11a-c), even though the sensitivity patterns of the traveltime and ERT data are fundamentally different with respect to location relative to the borehole.

The field example scatter plots in Figure 2.12 reveal the same variations between individual and joint inversion results as seen in the synthetic example (Figure 2.7). Although the scatter plots in Figure 2.12a-c show a general positive correlation between the geophysical parameters, the evidence for clusters is weak. By contrast, the joint inversion scatter plots in Figure 2.12e-g reveal distinct linear features.

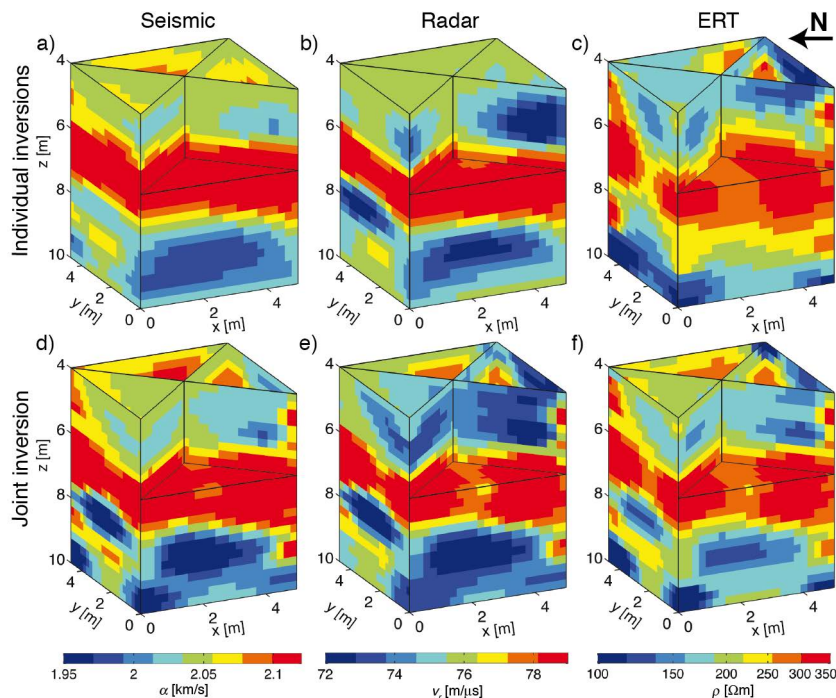


Figure 2.10. Results of (a-c) individual and (d-f) joint inversions of the field data set. All models fit the data with a normalized RMS misfit of 1.2 (1.0 corresponds to the error level). Note how the middle layer in the resistivity model obtained by joint inversion is more continuous than for the individual inversion.

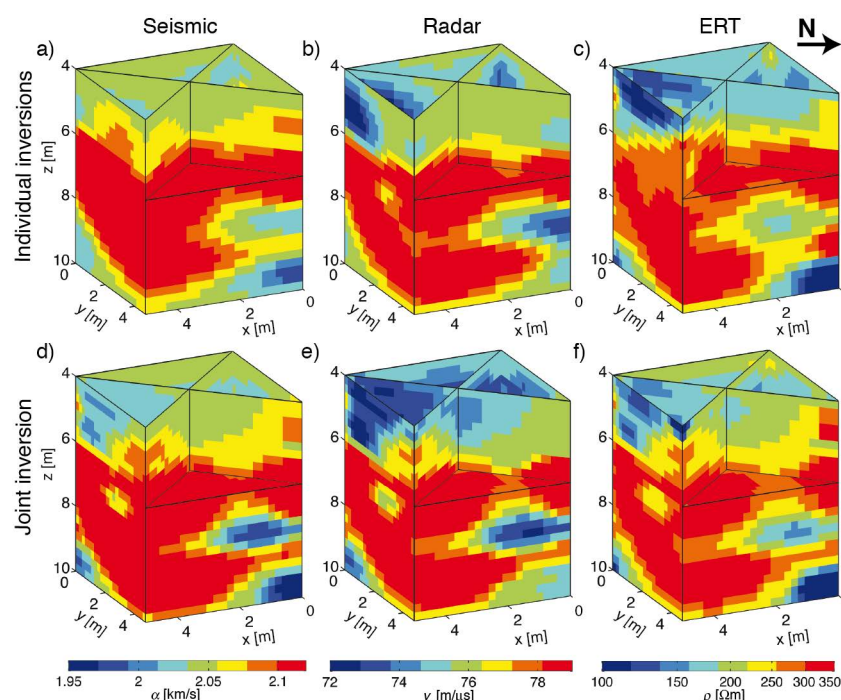


Figure 2.11. As for Figure 10, but viewed from a different direction. There are clear 3D structures and the individual inversions (a-c) show that all main features are detected independently by the three methods.

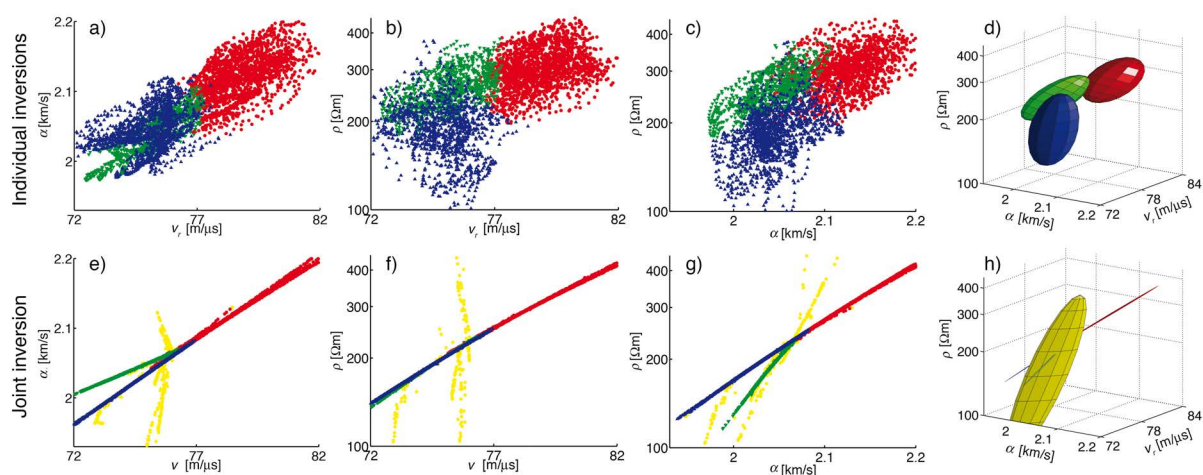


Figure 2.12. Scatter plots for the models obtained by (a-c) individual and (e-g) joint inversion together with visualizations of the automatically determined clusters used for zonation of the models obtained by (d) individual and (h) joint inversion. The scatter plots obtained from the individual inversion models are rather diffuse. They demonstrate a generally positive correlation between the geophysical parameters. In contrast, the scatter plots from the joint inversion models show well-defined linear correlations. (d) and (h) The different character of the scatter plots is also observed in the cluster visualizations. The large yellow cluster in (h) “collects” all of the poorly defined scatter points. These cells are reclassified by geostatistical interpolation (indicator kriging).

2.5.3 Classification and zonal inversion

Application of the classification algorithm to the scatter plots in Figure 2.12a-c and subsequent zonal inversion yields a high wavespeed and high resistivity zone in the center of the aquifer, but it cannot distinguish the regions at the top and bottom of this zone from each other (Figure 2.13a and d). Increasing the number of clusters does not improve this result.

To achieve the most meaningful classification of the scatter plots in Figure 2.12e-g, the results for different numbers of clusters were compared. We obtained the best result using four clusters, three of which are meaningful. The fourth is a “collector” cluster (yellow region in Figure 2.13b and e) in which most poorly resolved cells are placed. These poorly resolved cells are mostly found along the top or bottom of the inversion domain. Rather than leave gaps in these regions, we interpolate/extrapolate values from adjacent areas using the indicator kriging method. The resulting three zones in Figure 2.13c and f (referred to as model 1) are overall spatially aligned and this model is used in the subsequent interpretation.

The RMS misfits that result from the zonal inversion (see tables at the base of Figure 2.13) are very similar for all zoned models; the relatively low 1.4-1.5 misfit for the seismic and radar wavespeeds and 2.8 - 3.5 for the ERT resistivities is largely controlled by the common definition of the high wavespeed/resistivity zone in the center. Separating the top and the bottom layer does not significantly improve the misfit, even though the v_r and ρ values vary between these layers. The low RMS misfit for the ray-based methods indicates that a zoned wavespeed model is reasonable, whereas the higher RMS misfit for the ERT values indicates that smaller scale resistivity variations are necessary to fit the data adequately.

2.6 HYDROGEOPHYSICAL INTERPRETATION

2.6.1 Petrophysical analysis

The radar and resistivity values of model 1 (Figure 2.13c and f) for each zone (see table at the base of Figure 2.13f) are used as input to our petrophysical analysis along with the following parameters: (i) the resistivity of the pore water $\rho_w = 27 \text{ } \Omega\text{m}$ (established from measurements in a nearby borehole at the time of the survey), (ii) the relative permittivity of the matrix κ_s , which we cannot determine exactly but is unlikely to have strong variations within the gravel aquifer (see later), and (iii) the cementation factor m which we take to be 1.5-1.6 [Lesmes and Friedman, 2005].

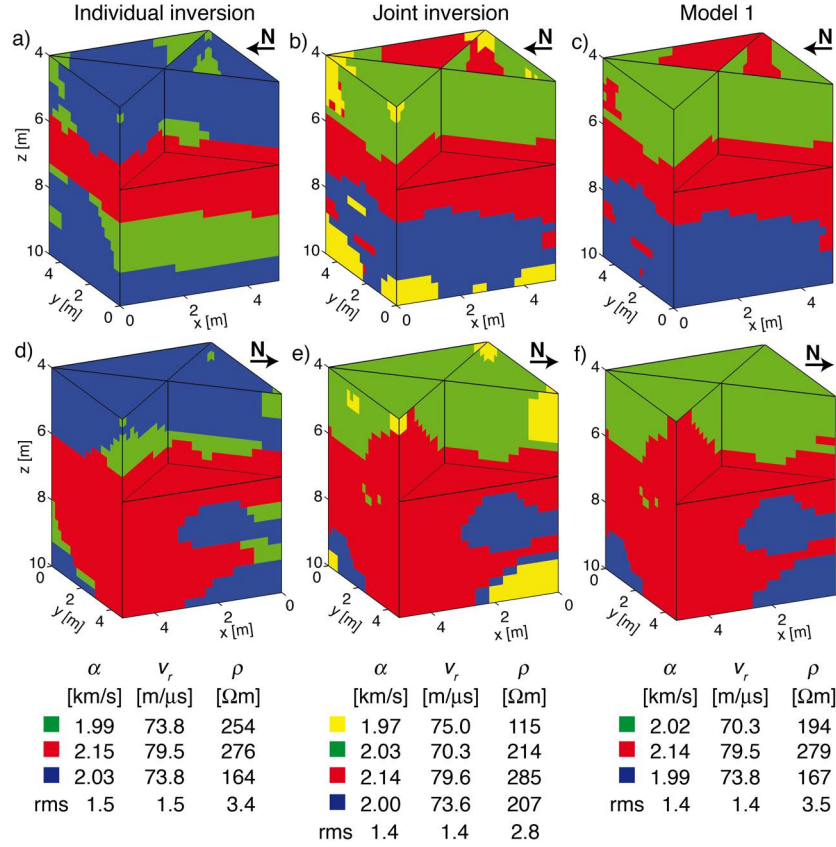


Figure 2.13. Zonal models based on the (a and d) individual and (b and e) joint inversions shown in Figures 2.10 and 2.11 viewed from two different directions. The final zonation based on the models obtained by joint inversion (model 1) in (c) and (f) is described in the text.

Seismic wavespeed is not explicitly included in the analysis. In unconsolidated environments, both seismic and radar wavespeeds are a function of porosity, but porosity estimates from seismic wavespeed are not as well constrained as those from radar wavespeed. Comparison of the seismic and radar wavespeeds with the Hashin-Shtrikman bounds [Hashin and Shtrikman, 1963] indicates a very well connected pore space [Linde and Doetsch, 2010] and thus motivates our choice of a relatively low cementation factor.

We use the petrophysical model of *Pride* [1994] to relate the relative permittivity

$$\kappa = \frac{c^2}{v_r^2} \quad (c = 300 \text{ m}/\mu\text{s}) \quad (2.4)$$

to the formation factor F and porosity ϕ , linked by

$$F = \phi^{-m}. \quad (2.5)$$

in the following way:

$$\kappa = \frac{1}{F} [\kappa_w + (F - 1)\kappa_s]. \quad (2.6)$$

Here $\kappa_w = 84$ is the relative permittivity of water at 10°C [Eisenberg and Kauzmann, 1969] and κ_s is the relative permittivity of the solid matrix. In the presence of fine-grain sediments (e.g., clays and silts), the electrical resistivity ρ can be related to F through a modified form of Archie's law [Linde *et al.*, 2006a]

$$\frac{1}{\rho} = \frac{1}{F} \left[\frac{1}{\rho_w} + (F-1)\sigma_s \right], \quad (2.7)$$

where σ_s is surface conductivity. Surface conductivity occurs as a result of the electrical triple layer that forms at the interface between grains that comprise the sediment matrix and water. It is most prominent in materials with large specific surface areas such as clays and silts [e.g., Revil *et al.*, 1998].

We solve Equation 2.6 for F (and ϕ using Equation 2.5) and then use Equation 2.7 to estimate σ_s . To estimate F and ϕ we have to assume a value for κ_s . We use $\kappa_s = 8.0$ to force surface conductivity $\sigma_s > 0$ in all three zones. The value of κ_s is not established at this site, although it is known to lie within a restricted range for the lithologies under consideration. It is also reasonable to assume that variations of κ_s within the gravel aquifer are likely to be quite small. Whatever value is used should not affect the relative variations in the deduced petrophysical parameters, but absolute values should be interpreted with caution. The range for ϕ in Table 2.2 corresponds to the likely variation in cementation factor m .

2.6.2 Interpretation

Two main findings result from this analysis (Table 2.2): (i) there is a distinct increase in surface conductivity σ_s with depth and (ii) porosity ϕ is significantly lower in the middle layer. The bottom layer was found to have a total average conductivity of 6 mS/m (167 Ω m), of which surface conductivity σ_s is predicted to contribute about one third (2.1 mS/m). The increase in σ_s can be attributed to a higher clay/silt fraction, demonstrating that it cannot be neglected in this sedimentary setting. Application of the conventional Archie's law [Archie, 1942] to the resistivity values for the bottom layer would overestimate ϕ by 25%.

A ~30% variation of ϕ between the middle and the top and bottom layers is quite well resolved. Small scale variations are expected to be even larger. In contrast, the differences between ϕ in the top and bottom layers are not very well defined. For example, the differences in radar wavespeed can be explained by variations in the cementation factor (see Table 2.2). This possibility is supported by the very small differences in seismic wavespeed between the

upper and lower zones, which imply similar porosities assuming that there are no major differences in lithology [e.g., *Carcione et al.*, 2007].

Although porosity is not well defined by our data and analysis, the more relevant parameters as far as fluid transport is concerned are the well-constrained formation factor F and surface conductivity σ_s [e.g., *Revil and Cathles*, 1999]. The hydrological implications of our results are being investigated with ongoing time-lapse ERT measurements.

Table 2.2. Result of the petrophysical analysis.

Layer	F	σ_s [mS/m]	ϕ [%]
Top (green)	7	0.2	26 - 29
Center (red)	12	0.6	19 - 21
Bottom (blue)	9	2.1	23 - 26

2.7 DISCUSSION

The tomographic models from the joint inversion and the corresponding zonal models are complementary representations of the situation at our field site. Models obtained from joint inversion display small-scale variability, but these variations are strongly affected by the regularization applied. As a consequence, they cannot be used directly to determine quantitative petrophysical values from theoretical models such as those described by Equations 2.6 and 2.7 [*Day-Lewis and Lane*, 2004]. By comparison, the zonal inversion based on structures determined from clustering the joint inversion results yields physical parameters (e.g., seismic wavespeed) for relatively large zones. Such effective parameters are suitable for petrophysical analysis at field scales, but because small-scale variability is neglected the results are only meaningful if large-scale zones dominate the physical property fields.

The data misfit of the zonal parameter estimates is a measure of confidence in the zonal representation. For our field example, this implies that there are only minor seismic and radar wavespeed variations within the zones, because the zonal models can fit the data relatively well with a normalized RMS misfit of 1.4. In contrast, additional small-scale variability or vertical trends are probably needed to improve the fit to the ERT data (RMS misfit is a comparatively poor 3.5 for the zonal inversion values). This high misfit can also partly be caused by small errors in the assumed location of the water table and the clay aquitard, because no electrodes were located outside the saturated gravel.

2.8 CONCLUSIONS

We have presented a methodology for hydrogeophysical aquifer characterization based on cross-gradients joint inversion of 3-D crosshole seismic, radar, and ERT data followed by classification of zones and an over-determined inversion for zonal parameters. A zonation approach based on Gaussian mixtures was used to identify zones in the inversion models. Our synthetic example demonstrates how joint inversion reduces the misclassification rate from 21.3% for the individual inversions to 3.7% for the three-method joint inversion. The joint inversion zonal models also provide much better estimates of the zonal parameters (0.3% error compared to 1.8% using the individual inversion tomograms).

Our strategy of jointly inverting three types of 3-D data was applied to an active gravel aquifer adjacent to the Thur River in northern Switzerland. Clustering of the joint inversion tomograms produced noticeably better results than clustering of the individual inversion tomograms, primarily because of the clearer scatter plots obtained from the joint inversion models; the Gaussian mixture cluster estimation technique capitalized on this decreased scattering. The joint inversion and zonation models are complementary. The smooth joint inversion tomograms include information about lateral variability and general trends (e.g., decreasing resistivity with depth). The zonal representation summarizes important geometrical information about the aquifer and it enables petrophysical analysis at the field scale. The validity of the zonation can be assessed by zonal inversion for each method.

At our field site, we found three different sub-units within the gravel aquifer. The relative variation in porosity was estimated to be ~30% and the percentage of fine materials was found to increase with depth. The geometries and properties of the aquifer subunits determined here will be the starting point for hydrogeophysical modeling that will include data from extensive ongoing time-lapse ERT experiments at the same field site.

3 STRUCTURAL TIME-LAPSE JOINT INVERSION

Published in *Geophysical Research Letters*:

Doetsch, J., Linde, N., and Binley, A.,
2010. Structural joint inversion of time-
lapse crosshole ERT and GPR traveltimes
data, *Geophysical Research Letters*, **37**,
L24404.

ABSTRACT

Time-lapse geophysical monitoring and inversion are valuable tools in hydrogeology for monitoring changes in the subsurface due to natural and forced (tracer) dynamics. However, the resulting models may suffer from insufficient resolution, which leads to underestimated variability and poor mass recovery. Structural joint inversion using cross-gradient constraints can provide higher-resolution models compared with individual inversions and we present the first application to time-lapse data. The results from a synthetic and field vadose zone water tracer injection experiment show that joint 3-D time-lapse inversion of crosshole electrical resistance tomography (ERT) and ground penetrating radar (GPR) traveltime data significantly improve the imaged characteristics of the point injected plume, such as lateral spreading and center of mass, as well as the overall consistency between models. The joint inversion method appears to work well for cases when one hydrological state variable (in this case moisture content) controls the time-lapse response of both geophysical methods.

3.1 INTRODUCTION

Time-lapse geophysical monitoring and inversion are valuable tools in a wide range of application areas, such as hydrogeology, seismology, volcanology, landslide studies, and reservoir management. By inverting for temporal changes in geophysical properties it is possible to focus on resolving changes in state variables, such as water content and pore water salinity. The quality and resolution of time-lapse inversion results may also improve compared with static inversions as modeling and observational errors are generally smaller [e.g., *LaBrecque and Yang*, 2001]. Time-lapse inversion results are, unfortunately, also resolution-limited, leading to models that might be physically implausible or the resolved scales might be larger than those of interest [e.g., *Day-Lewis et al.*, 2005]. Well known problems include the difficulty of recovering the injected mass of tracer or water from time-lapse inversion results [e.g., *Binley et al.*, 2002b] and significant smearing in the horizontal directions [*Singha and Gorelick*, 2005] that reduce the value of geophysical time-lapse models in quantitative flow and transport studies.

Structural joint inversions of geophysical data acquired under static field conditions provide geometrically similar models and improve model resolution compared with individual inversions [e.g., *Gallardo and Meju*, 2004; *Linde et al.*, 2008]. We focus here, for the first time, on the applicability of a structural joint inversion approach to time-lapse data. Structure is imposed by penalizing deviations from cases when the gradients - for different geophysical

properties - of the total model updates from background models point in the same or opposite directions. These background models are obtained by inversion of the data acquired prior to any perturbation. We investigate the merits of this cross-gradient-constrained joint inversion using a synthetic and field vadose zone water-injection experiment, both of which employ time-lapse crosshole electrical resistance tomography (ERT) data and first-arrival ground-penetrating radar (GPR) traveltimes. Under these conditions, the time-lapse changes in both data types are related solely to variations in moisture content.

3.2 METHODS

3.2.1 Time-lapse inversion strategy

The first step of our time-lapse inversion strategy is to obtain background (and initial) models of the logarithm of electrical resistivity ($\mathbf{m}_{e,0}$) and radar slowness ($\mathbf{m}_{r,0}$) by inverting data sets acquired prior to any perturbations. The data are inverted following an Occam's type inversion by penalizing differences from a homogeneous model as defined by an exponential covariance model [*Linde et al.*, 2006b]. We then use a difference inversion approach to invert the time-lapse data [e.g., *LaBrecque and Yang*, 2001] in which we, in a similar manner, penalize deviations from $\mathbf{m}_{e,0}$ and $\mathbf{m}_{r,0}$.

For the ERT inversions, we use an error model consisting of a systematic contribution $\boldsymbol{\epsilon}_{es}$ that is the same for all time-lapse steps, and a random observational error $\boldsymbol{\epsilon}_{e,p}$ ($p = 0, 1, 2, \dots, P$, where P is the number of time steps) that is different for each time-lapse data set [e.g., *LaBrecque and Yang*, 2001] but assumed to stem from the same zero-mean Gaussian distribution. The observed data at time 0 are thus

$$\mathbf{d}_{e,0}^{obs} = g(\mathbf{m}_{e,0}) + \boldsymbol{\epsilon}_{es} + \boldsymbol{\epsilon}_{e,0}, \quad (3.1)$$

with the forward response $g(\mathbf{m}_{e,0})$. The main contribution to the background residual

$$\mathbf{r}_{e,0} = \mathbf{d}_{e,0}^{obs} - g(\mathbf{m}_{e,0}) = \boldsymbol{\epsilon}_{es} + \boldsymbol{\epsilon}_{e,0} \quad (3.2)$$

is the systematic error $\boldsymbol{\epsilon}_{es}$, which is a combination of modeling errors and systematic measurement errors due to ground coupling problems or geometrical errors. It is largely removed from the time-lapse data by using the differences $\tilde{\mathbf{d}}_{e,p}^{obs}$ (for time step p), to invert for the model update $\boldsymbol{\delta}\mathbf{m}_{e,p}$, where

$$\tilde{\mathbf{d}}_{e,p}^{obs} = \mathbf{d}_{e,p}^{obs} - \mathbf{r}_{e,0} = g(\mathbf{m}_{e,0} + \boldsymbol{\delta}\mathbf{m}_{e,p}) + \boldsymbol{\epsilon}_{e,p} - \boldsymbol{\epsilon}_{e,0}. \quad (3.3)$$

This formulation improves ERT time-lapse inversion results, where typically $\boldsymbol{\epsilon}_{\text{es}} > \sqrt{\boldsymbol{\epsilon}_{\text{e},0}^2 + \boldsymbol{\epsilon}_{\text{e},p}^2}$ due to permanently installed electrodes and stable coupling conditions. In our case, we assume that $\boldsymbol{\epsilon}_{\text{es}}$ is 5 times larger than $\boldsymbol{\epsilon}_{\text{e},p}$.

For the first-arrival GPR data, we assume that the constant and systematic error contribution is smaller than the errors associated with picking, time-zero, and antennae positioning for each time-lapse data set. We thus solve for $\boldsymbol{\delta m}_{\text{r},p}$ using (at time step p)

$$\mathbf{d}_{\text{r},p}^{\text{obs}} = g(\mathbf{m}_{\text{r},0} + \boldsymbol{\delta m}_{\text{r},p}) + \boldsymbol{\epsilon}_{\text{r},p}. \quad (3.4)$$

Our inversions for $\boldsymbol{\delta m}_{\text{e},p}$ and $\boldsymbol{\delta m}_{\text{r},p}$ proceeds iteratively by decreasing the weight that penalize deviations from $\mathbf{m}_{\text{e},0}$ and $\mathbf{m}_{\text{r},0}$, as quantified by an exponential covariance function, until the residuals are as large as the assumed data errors [Linde *et al.* 2006]. Tests using models from the previous time step as background models gave inferior results, as artifacts appeared at previously occupied positions of the plume.

3.2.2 Joint inversion strategy

Coupling between the ERT and GPR time-lapse updates $\boldsymbol{\delta m}_{\text{e},p}$ and $\boldsymbol{\delta m}_{\text{r},p}$ is introduced in the inversion by cross-gradient constraints [Gallardo and Meju, 2004]. The cross-gradients function of the model updates at time-step p

$$\boldsymbol{\tau}_p(x, y, z) = \nabla \boldsymbol{\delta m}_{\text{e},p}(x, y, z) \times \nabla \boldsymbol{\delta m}_{\text{r},p}(x, y, z) \quad (3.5)$$

is discretized with a central-difference scheme and subsequently linearized. Deviations from zero of the discretized $\boldsymbol{\tau}_p$ are heavily penalized at all discretized locations x, y, z of the inversion domain with a constant weight for all inversion steps. The joint inversion proceeds as for the individual inversions, but with the additional cross-gradient constraints.

The assumption of structural similarity between $\boldsymbol{\delta m}_{\text{e},p}$ and $\boldsymbol{\delta m}_{\text{r},p}$, as quantified by Equation 3.5, is valid when only one state variable varies with time or when the methods employed are sensitive to the same physical property (e.g., electrical conductivity). The assumption holds for vadose zone tracers that have the same electrical conductivity as the pore water such that time-lapse ERT and GPR data only sense changes in moisture content. Simulations and joint inversions of field data acquired following saline tracer injection (not shown here) reveal that $\boldsymbol{\delta m}_{\text{e},p}$ and $\boldsymbol{\delta m}_{\text{r},p}$ are not structurally similar and that the resulting inversion models display artifacts.

3.3 RESULTS

3.3.1 Site characteristics

At Hatfield in the UK, a test site was developed to study flow and transport in unsaturated media (for details see the work of *Binley et al.* [2002b]). The dominant sub-lithology at the site is medium grained sandstone, but with fine and medium sandstone sub-horizontally laminated on a millimeter scale (occurring in 0.2-0.5 m thick units, spaced at 1-3 m vertical intervals). *Binley et al.* [2002b] document a water tracer test carried out at the Hatfield site; here we use geophysical data from this test to illustrate our approach in a field setting. The center of mass and the spread of geophysically-defined plumes using individually inverted time-lapse data were previously used to characterize the hydrodynamics at Hatfield based on individual inversions and allowed deriving field-scale properties such as effective hydraulic conductivity [*Binley et al.*, 2002b].

For the ERT measurements, 16 stainless steel electrodes were installed at 0.73 m intervals between a depth of 2 and 13 m in four boreholes in a trapezoid-like manner with side-lengths varying between 5 and 8 m. For the GPR measurements, two boreholes (along the x -axis) were drilled with 5 m spacing in-between one of the diagonals formed by the ERT boreholes.

Between 14:30 on 7 October and 13:40 on 10 October 1998, 2100 l of water tracer was injected at a uniform rate of approximately 30 l/h in a borehole slotted between 3 and 3.5 m depth located in-between the two GPR boreholes ($x=3$; $y=4$). To obtain a pure flow (no transport) experiment, the conductivity of the injected water was chosen to match the conductivity of the pore water. Multiple ERT and GPR data sets were acquired before and after tracer injection. We concentrate below on the time-lapse data set recorded directly after the end of injection (day 3) and two days later (day 5).

3.3.2 Synthetic example

A synthetic example mimicking the Hatfield water injection experiment was first used to evaluate our time-lapse joint inversion. We use a FEFLOW v6.0 Richards' equation solution assuming a uniform geological media. For this we discretized a region 8 m by 10 m (in plan) and 12 m deep into 73,202 6-node triangular-prism linear finite elements, with specific refinement around the tracer injection area. The lower boundary of the region defined a water table, and hence Dirichlet boundary conditions. The saturated hydraulic conductivity for all elements was set to 4.63×10^{-6} m/s, which is consistent with *Binley et al.* [2002b]. We used

the widely adopted *van Genuchten* [1980] representation of unsaturated hydraulic characteristics, with a residual saturation of 0.0025, exponent $n_{vG} = 1.964$ and $\alpha_{vG} = 4.1 \text{ m}^{-1}$. In order to develop more natural initial conditions we first setup a uniform saturation of 0.5 within the model and then ran a 20 day drainage period. The tracer was then imposed within the model and the tracer movement was simulated with a maximum time step of 0.05 days. Synthetic GPR and ERT data were simulated using interpolated moisture content θ at days 0, 3 and 5. The bulk electrical resistivity ρ was calculated as a function of saturation $S = \theta/\phi$ (where ϕ is porosity) using Archie's second law [Archie, 1942]

$$\rho = \rho_s S^{-n}, \quad (3.6)$$

where $\rho_s = 66 \text{ }\Omega\text{m}$ is the bulk resistivity at full saturation and $n = 1.13$ is Archie's saturation exponent determined from three samples of the main lithology at the Hatfield site [see *Binley et al.*, 2002a].

The relative permittivity κ was calculated using the complex refractive index model (CRIM) [Birchak *et al.*, 1974]

$$\sqrt{\kappa} = (1-\phi)\sqrt{\kappa_s} + \theta\sqrt{\kappa_w} + (\phi-\theta)\sqrt{\kappa_a} \quad (3.7)$$

where $\kappa_w = 81$ and $\kappa_a = 1$ are the relative permittivities of water and air, respectively. The porosity $\phi = 0.32$ and the relative permittivity of the sediment grains $\kappa_s = 5$ were obtained from lab measurements on retrieved cores [West *et al.*, 2003]. Radar slowness, s , was calculated from the permittivity using $s = \sqrt{\kappa}/c$, with c the speed of light in a vacuum.

Forward solvers were used to calculate electrical resistances and radar traveltimes for these models. The electrical responses and related sensitivities were computed using a finite-element solver implemented by *Rücker et al.* [2006], and the traveltimes and sensitivities were calculated in the high frequency limit using a finite-difference algorithm [Podvin and Lecomte, 1991]. The ERT measurement scheme included a variety of four-electrode configurations using electrodes in a varying number of boreholes and the data were filtered to only include configurations with a geometrical factor of less than 600. The multiple-offset gathers were calculated using 0.25 m intervals between antenna positions over the range 0-11 m below ground level for cases when the angle between the transmitter and receiver antennas were within $\pm 45^\circ$ from the horizontal. For each time-step, the resulting data sets of 833 resistances and 1181 multiple offset GPR traveltimes were contaminated by Gaussian noise according to the error models of Equations 3.1-4 with zero mean and standard deviations $std(\mathbf{e}_{e,s}) = 2.5\%$, $std(\mathbf{e}_{e,0}) = std(\mathbf{e}_{e,p}) = 0.5\%$ and $std(\mathbf{e}_{r,0}) = std(\mathbf{e}_{r,p}) = 0.5\% + 0.5 \text{ ns}$. The same

configurations and data error descriptions were also used to invert the field data described below.

The background data sets (i.e., before water injection) were inverted individually in 3-D (not shown) and the time-lapse data were inverted both individually and jointly in 3-D using a regular inversion grid with voxel side lengths of 0.35 m. Integral scales of the exponential covariance model used to regularize the inversion of the background data set was 2 m in the horizontal and 1 m in the vertical direction to respect the independently observed anisotropy at the field site. The integral scale chosen for the time-lapse inversion was 0.7 m in all directions, corresponding to the expected length scale at which the tracer plume might be resolved. Values in the range of 0.5-1.0 m provide similar results. After 10 iterations, all inversion models fit the data to the specified error level with the largest possible weight to the model regularization.

The water content was calculated from the resulting models using Equations 3.6 and 3.7 with the petrophysical parameters mentioned above. Vertical profiles of the inferred time-lapse change in moisture content, $\Delta\theta$, from the background model are shown in Figure 3.1. It is seen that the magnitude of $\Delta\theta$ is rather well estimated in the GPR inversion but markedly underestimated in the ERT inversion for both the individual and joint inversions, which can be explained by the more significant resolution limitations of ERT inversions [Day-Lewis *et al.*, 2005].

To quantify the changes we define a plume boundary, for each model, at 1/3 of the maximum $\Delta\theta$. These plumes were then used to calculate the mass, center of mass and the variances of the plumes, with the resulting statistics presented in Table 3.1. This plume definition is rather simplistic [c.f. Day-Lewis *et al.*, 2007], but the relative differences between the individual and joint inversions are similar for other cut-off values, and serves here only to investigate if the plume definition is improved by the joint inversion. Note that the 3-D shape of the plume is heavily dependent on the regularization used as the data sets are acquired between pairs of boreholes.

The individual GPR inversion model overestimates the mass (+46% (+58%) for day 3 (day 5)), whereas it is more reasonable for the joint inversions (+5% (+13%) for day 3 (day 5)). These results indicate that the ERT data helps to constrain the geometry of the GPR model that otherwise is only based on data acquired along one plane and extended in 3-D based on the regularization. The individual (-49% (-56%) for day 3 (day 5)) and joint ERT (-

61% (-51%) for day 3 (day 5)) models significantly underestimate the mass with no improvement for the joint inversions.

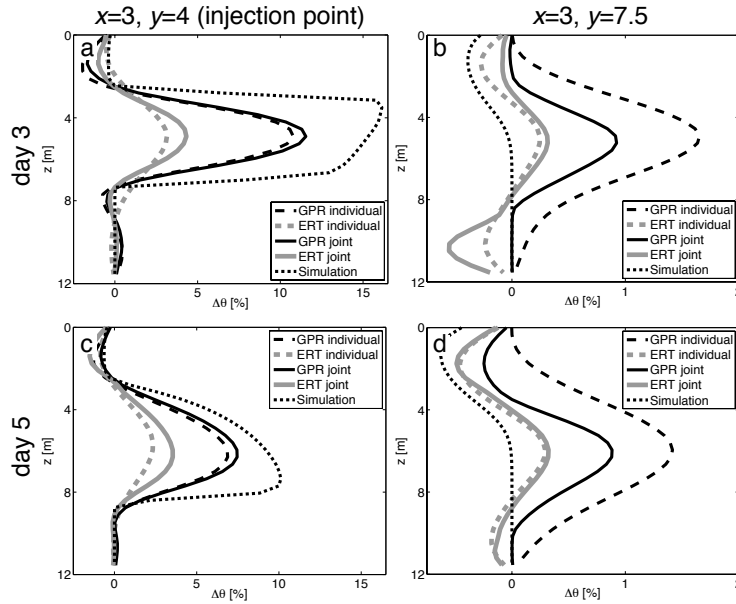


Figure 3.1. Vertical profiles of moisture content change ($\Delta\theta$) since the beginning of a synthetic water injection test as inferred from individual and joint inversion of time-lapse crosshole ERT and GPR traveltimes data. (a) Through the injection point at the end of injection (day 3), (b) 3.5 m away from the injection point and the GPR acquisition plane at the end of injection (day 3), (c-d) same as (a-b) but two days after the end of injection (day 5).

Table 3.1. Statistics of the geophysically-defined plumes for the synthetic example using cut-offs of 1/3 of the maximum moisture content change ($\Delta\theta$) for each geophysically-derived model. The ERT data and model weight in the joint inversions is 2.8 times that of the GPR to assure that both models converge to the same target data misfit.

Synthetic	Mass [m ³]	Center of Mass [m]			Variance [m ²]		
		x	y	z	σ_{xx}^2	σ_{yy}^2	σ_{zz}^2
True	2.12	3.00	4.00	5.05	0.37	0.37	1.00
day 3							
GPR individual	3.06	2.54	3.89	5.07	1.36	1.05	0.61
ERT individual	1.08	3.19	4.36	5.17	1.17	1.12	0.92
GPR joint	2.20	2.92	4.16	5.07	0.90	0.76	0.57
ERT joint	0.81	2.92	4.15	5.08	0.89	0.75	0.57
day 5							
True	2.08	3.00	4.00	6.01	0.55	0.55	1.43
GPR individual	3.32	2.85	3.98	6.14	1.82	1.32	1.10
ERT individual	0.93	3.05	4.34	6.04	1.36	1.34	0.98
GPR joint	2.39	3.13	4.20	6.14	1.14	0.92	1.04
ERT joint	1.02	3.10	4.20	6.12	1.06	0.83	0.99

The error in the center of mass from the individual GPR (0.47 m (0.20 m) for day 3 (day 5)) and ERT inversions (0.42 m (0.34 m) for day 3 (day 5)) are improved in the joint inversion (0.18 m and 0.17 m, respectively) for day 3, but less so for day 5 (0.20 m and 0.25 m, respectively). The horizontal variances of the estimated GPR and ERT plumes from the joint inversions are less overestimated (+100 % on average) than for the individual inversions (+190 % on average). This is due to resolution improvements of joint inversions of crosshole data that are the most important in the horizontal direction [Linde *et al.*, 2008].

3.3.3 Hatfield 1998 water injection

Our time-lapse inversion methodology was then applied to the Hatfield field data. Radar transmission data were acquired using Sensors and Software's Pulse EKKO radar system with 100 MHz antennas. ERT measurements were acquired using the DMT Resecs resistivity instrument. The background data sets were inverted individually in 3-D and the final models (not shown) are consistent with the known geology and fit the data to the specified error levels (see previous section). The time-lapse data were inverted both individually and jointly in 3-D for 12 iterations such that all inversion results fit the prescribed error level.

Figure 3.2 shows vertical profiles of the inferred $\Delta\theta$ using Equations 3.6 and 3.7 with the specified parameter values. These results are consistent with the synthetic example in that the joint inversion models are more focused. Scatter plots of the inversion results show that the scatter observed in the individual inversions (Figure 3.3a and c) is much reduced and that the $\Delta\theta$ magnitudes are increased in the joint inversions (Figure 3.3b and d). The plumes defined by the fractional thresholding procedure were then used to calculate the center of mass and the variances of the plumes (see Table 3.2). The individual GPR inversion model overestimates the injected mass of 2100 l (+39% (+57%) for day 3 (day 5)), whereas it is more reasonable for the joint inversions (+4% (+37%) for day 3 (day 5)). The individual (-50% (-53%) for day 3 (day 5)) and joint ERT (-56% (-54%) for day 3 (day 5)) models both underestimate the mass with no improvement for the joint inversions.

The differences in the center of mass between the individual GPR and ERT models (0.35 m (0.34 m) for day 3 (day 5)) are improved for the joint inversion at both time-steps (0.05 m (0.18 m) for day 3 (day 5)). The variance estimates of the GPR and ERT plumes are smaller in the horizontal direction for the joint compared to the individual inversions (24% on average) indicating that the joint inversion improves resolution.

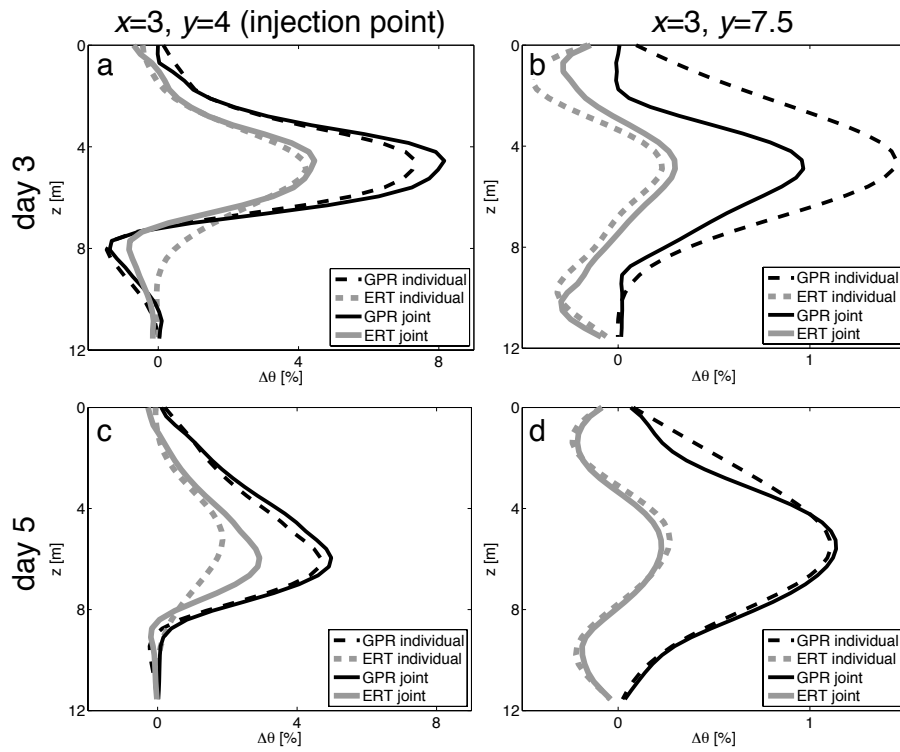


Figure 3.2. As in Figure 3.1, but with data from the Hatfield 1998 water injection test.

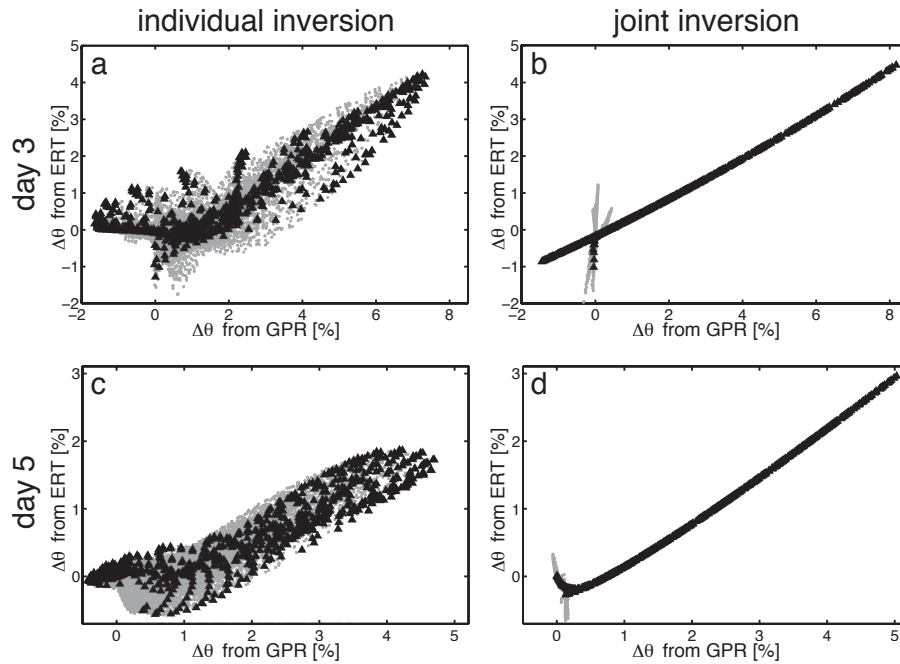


Figure 3.3. Scatter plots of moisture content change ($\Delta\theta$) inferred from (a) individual and (b) joint time-lapse inversions of the Hatfield data at day 3, (c-d) same as (a-b) but for day 5. The black triangles indicate model cells with GPR ray coverage.

Table 3.2. Statistics of the geophysically-defined plumes for the Hatfield water injection experiment. The ERT data and model weight is 1.8 times that of the GPR in the joint inversions to assure that both models converge to the same target data misfit.

Hatfield		Mass [m ³]	Center of Mass [m]			Variance [m ²]		
			<i>x</i>	<i>y</i>	<i>z</i>	σ_{xx}^2	σ_{yy}^2	σ_{zz}^2
day 3	GPR individual	2.92	2.87	4.05	4.77	1.78	1.21	0.85
	ERT individual	1.06	3.07	4.24	4.99	0.79	0.96	0.86
	GPR joint	2.18	3.13	4.21	4.84	1.02	0.92	0.81
	ERT joint	0.93	3.10	4.17	4.85	0.87	0.76	0.70
day 5	GPR individual	3.30	3.49	4.08	5.55	2.35	1.44	1.85
	ERT individual	0.85	3.28	4.34	5.47	1.42	1.29	1.19
	GPR joint	2.80	3.47	4.31	5.57	1.63	1.36	1.69
	ERT joint	0.92	3.34	4.23	5.66	1.11	0.84	1.19

3.4 CONCLUDING REMARKS

A synthetic experiment based on flow simulations together with field data from a water injection experiment in unsaturated sandstone show clearly that cross-gradients joint inversion of crosshole time-lapse ERT and GPR traveltimes data decrease horizontal smearing of plumes, that they increase the similarity between models, and the estimated center of mass of plumes compared to individual time-lapse inversions. The examples also illustrate that higher resolution 2-D traveltimes GPR data might benefit from lower resolution 3-D ERT data. We emphasize that the inversion methodology presented here is only valid when one state variable varies at each location of the model domain. For example, if the fluid salinity of the tracer was different to the native pore water salinity then the resistivity would be a function of moisture content and salinity, which would violate the assumptions of structural similarity underlying the cross-gradient constraints.

4 THE BOREHOLE-FLUID EFFECT IN ERT

Published in *Geophysics*:

Doetsch, J. A., Coscia, I., Greenhalgh, S.,
Linde, N., Green, A., and Günther, T.,
2010. The borehole-fluid effect in electrical
resistivity imaging, *Geophysics*, **75**, F107-
F114.

ABSTRACT

Fluid that fills boreholes in crosswell electrical-resistivity investigations provides the necessary electrical contact between the electrodes and the rock formation, but it is also the source of image artifacts in standard inversions that do not account for the effects of the boreholes. The image distortions can be severe for large resistivity contrasts between the rock formation and borehole fluid and for large borehole diameters. We have carried out 3-D finite-element modeling using an unstructured-grid approach to quantify the magnitude of borehole effects for different resistivity contrasts, borehole diameters, and electrode configurations. Relatively common resistivity contrasts of 100 : 1 and borehole diameters of 10 and 20 cm yielded, for a bipole length 5 m, apparent resistivity underestimates of approximately 12% and 32% when using AB-MN configurations and apparent resistivity overestimates approximately 24% and 95% when using AM-BN configurations. Effects are generally more severe at shorter bipole spacings. We report here the results obtained by either including or ignoring the boreholes in inversions of 3-D field data from a test site in Switzerland, where approximately 10,000 crosswell resistivity tomography measurements were made across six acquisition planes between four boreholes. Inversions of raw data that ignored the boreholes filled with low resistivity fluid paradoxically produced high resistivity artifacts around the boreholes. Including correction factors based on the modeling results for a 1-D model with and without the boreholes did not markedly improve the images. The only satisfactory approach was to use a 3-D inversion code that explicitly incorporated the boreholes in the actual inversion. This new approach yielded an electrical resistivity image that was devoid of artifacts around the boreholes and that correlated well with co-incident crosswell radar images.

4.1 INTRODUCTION

Crosswell and borehole-to-surface electrical resistance tomography (ERT) is a popular and powerful method of subsurface imaging in engineering and environmental investigations [LaBrecque *et al.*, 1996a; Slater *et al.*, 2000; Linde *et al.*, 2006a; Wilkinson *et al.*, 2010 and references contained therein]. The boreholes used for such ERT investigations are usually partially filled with water, either naturally if below the water table or artificially if measurements are made in the unsaturated zone. The water provides electrical contact between the suspended electrode string and the surrounding rock formation (i.e., the rock matrix with its associated pore-filling fluids). Other methods of installing the electrodes less

common but still provide adequate electrode coupling. For example, electrodes can be mounted on the outside of a PVC tube that is lowered down the well and held in firm contact with the borehole wall (mandatory in air-filled holes), or the borehole can be back-filled with mud or moist sand after the electrode string is deployed.

In most common near-surface geological settings, the rock has a higher electrical resistivity than its contained fluid [Keller and Frischknecht, 1966]. Regardless of the method of electrical contact used (fluid-filled or soil-filled holes), there is usually a substantial contrast between the resistivity of the rock formation ρ_r and that of the borehole fluid ρ_f . This contrast usually results in a narrow cylindrical conductive anomaly that influences the ERT measurements. The current from a borehole source will preferentially flow within the more conductive fluid rather than out into the rock. The $\rho_r : \rho_f$ contrast, and hence the associated borehole effect on ERT measurements, will be particularly large if the borehole is filled with saline fluid or clay and the host material is hard rock. In a later section of this paper we investigate an ERT field example involving a saturated gravel aquifer. Using Archie's law [Archie, 1942], and assuming a porosity of 0.25, a cementation factor of 1.5, and the same salinity water in the borehole as in the pore space of the rock, the expected resistivity contrast $\rho_r : \rho_f$ between the saturated gravel and water-filled borehole is about 8 : 1. Even such a modest contrast has a significant effect on the cross-hole apparent resistivities. It should be remarked that a resistive air-filled borehole also constitutes a 3-D anomalous structure that will affect the measurements (when electrodes are held in direct contact with the formation), but not as severely as in the conductive case.

The borehole fluid effect is well known in electric-well logging, in which the influence of not only the borehole fluid but also that of the mud cake and mud filtrate surrounding the borehole are taken into account [Darling, 2005]. Special focused well-logging resistivity tools incorporate additional guard electrodes to force the current to flow radially outwards into the formation, rather than axially within the conductive fluid.

In ERT investigations, the borehole effect is rarely considered. Data are generally inverted and interpreted without due account for the resistivity contrast between the rock formation and borehole fluid. Yet, a number of studies [Daily and Ramirez, 1995; Osiensky et al., 2004; Daily et al., 2005; Nimmer et al., 2008] have demonstrated that this approach can produce serious artifacts (i.e., fictitious features in the inverted resistivity images). One reason why this effect is often ignored in crosswell ERT is that to adequately incorporate the boreholes in both the forward modeling and inversion codes requires a 3-D representation of

the subsurface that allows the narrow boreholes and adjacent regions to be very densely meshed. This can only be achieved satisfactorily with an unstructured finite-element mesh, such as described by *Rücker et al.*, [2006], *Günther et al.* [2006], and *Blome et al.* [2009]. Most ERT forward modeling and inversion codes are based on structured (regular) grids or meshes that cannot adequately or efficiently represent boreholes, particularly when they deviate from the vertical or horizontal. With structured meshes, it is computationally prohibitive to use very fine grids, especially in 3-D. As a consequence, most ERT reconstructions are based on 2.5-D modeling that treats the boreholes (if at all) as infinite sheets (2-D structures) rather than as cylinders (3-D structures).

By means of a regular 3-D finite-difference modeling approach, *Osiensky et al.* [2004] compute the equipotential pattern surrounding a current source placed at the bottom of a square borehole located within a homogeneous rock formation. They present results for the borehole being either fully air-filled (i.e., more resistive than the host formation) or partially liquid-filled with fresh or saline water (i.e., more conductive than the host formation). The air-filled hole yields quasi-circular equipotential contours, whereas in the case of a conductive fluid the equipotentials are more elliptical and elongated in the direction of the borehole. The ellipticity increases with the resistivity contrast. Voltage levels in the rock formation differ substantially for the two cases (air-filled versus saline-fluid-filled) in the near-vicinity of the borehole, but the equipotentials appear quite similar in shape and magnitude at a distance of two to three times the borehole depth. *Osiensky et al.* [2004] suggest that failure to consider this “noise” in crosswell or borehole-to-surface measurements can lead to incorrect interpretations of the apparent resistivities.

Nimmer et al. [2008] used a structured finite-element method (FEM) approach to numerically compute the spatial variations of voltage ratio for a downhole current electrode in either an air-filled or a partially liquid-filled borehole. The ratio was taken relative to the situation of no borehole at all (i.e., current electrodes buried in a half-space). They show that the increased current density in the liquid-filled borehole results in lower current density in the formation and therefore anomalously reduced voltages (i.e., ratios of < 1). Conversely, the air-filled hole results in slightly higher voltages in the formation (i.e., increased current density) due to the resistive cylinder. They also present inversion results for synthetic tomography experiments involving roving bipoles of 3 m length in two 15-m-deep boreholes placed 10 m apart. Each 10×10 cm square borehole, which is represented by a regular FEM grid of $2 \times 2 \times 30$ cells, is occupied by 16 electrodes. *Nimmer et al.* [2008] consider $\rho_r : \rho_f$

values of 10 : 1 and 100 : 1. Inversion results based on the lower contrast differ little from those obtained for a medium without boreholes (i.e., current electrodes buried in a half-space), whereas the results based on the higher contrast contain significant artifacts. They repeated the experiments for 20×20 cm square boreholes (using four times as many cells to represent each borehole) and found the artifacts to intensify. The image discrepancy compared to the no-borehole case was a consequence of the inversion algorithm trying to compensate for increased current density in the liquid-filled borehole.

Nimmer et al. [2008] caution against ignoring the borehole-fluid effect whenever the distances involved are small, when the borehole diameters exceed 20 cm, or when the $\rho_r : \rho_f$ approaches 100 : 1. In such situations they recommend measuring the borehole fluid resistivity and incorporating it in the forward modeling as part of the inversion. However, they suggest that the borehole effects are far less severe in time-lapse tomography investigations, such that they can possibly be ignored if the ratios of voltage (or apparent resistivity) data acquired at different times are inverted, rather than the individual data sets themselves. In this way, the problem of creating biased time-lapse inversion results is effectively hidden.

In this contribution, we demonstrate that accurate forward modeling using a singularity removal technique for the borehole sources and an unstructured mesh for representing narrow boreholes are essential for reliable inversions of crosswell-ERT data. Our study differs from that of *Nimmer et al.* [2008] in that we (1) only consider borehole-related artifacts in the forward modeling of a homogeneous half-space and not other models, (2) consider a wider range of bipole electrode configurations, (3) invert an extensive field data set rather than a synthetic one, and (4) explore the possibility of eliminating the borehole-fluid effects from the apparent resistivity data by calculating and applying correction factors.

After describing the homogeneous model, assumed borehole geometry, and very brief details on the computer code, we present simulated apparent resistivities and related statistics for a range of $\rho_r : \rho_f$ ratios, borehole diameters, electrode configurations, and bipole separations. We then introduce our observed 3-D crosswell-ERT data [*Coscia et al.*, 2010] and show, for the very first time, the results of inverting data with the boreholes explicitly included. For comparison, we also show the results of inverting the data without accounting for the boreholes (i.e., the common practice in crosswell-ERT experiments). In an attempt to minimize the computational effort, we next examine whether correction factors based on

forward modeling studies enable corrected data to be inverted without the need to include the boreholes in the models.

4.2 MODELING THE BOREHOLE-FLUID EFFECT

To investigate the borehole-fluid effect, we used a 100- Ωm homogeneous half-space model penetrated by two 10-m-deep vertical boreholes separated by 5 m (Figure 4.1). This geometry matched that of the crosswell-ERT experiment at our field test site described later in the paper. Modeling was performed for borehole diameters of 5, 10, and 20 cm and various resistivities of the borehole fluid, such that the $\rho_r : \rho_f$ contrasts ranged from 1 : 1 to 600 : 1. Depending on the objectives of the simulation, electrodes were placed at regular intervals of 0.25 or 1 m along the length of each borehole. Two basic recording configurations were simulated (Figure 4.1). Either both current electrodes A and B were placed in one hole and both potential electrodes M and N were located in the other hole (i.e., the so-called AB-MN configurations) or the current electrodes were placed in separate holes, as were the potential electrodes (i.e., the so-called AM-BN configurations). The spacings between the active electrodes were varied from 1 to 9 m.

The modeling is carried out with the versatile 3-D FEM library DCFEMLIB [Rücker *et al.*, 2006], which uses an unstructured finite-element mesh. To achieve sufficient accuracy, a singularity removal technique [Lowry *et al.*, 1989] was used to accommodate the rapid decay of electric potential around each point source position and a high density of elements is automatically meshed around the boreholes (Figure 4.2). The singular potential can be calculated either analytically for homogeneous flat-topography models or numerically using a boundary-element method when surface topography is significant. The singular potential is based on the true resistivity at the point source position (i.e., the borehole-fluid resistivity). The non-singular potential is then computed numerically by the finite-element method. Details on the procedure are given by Rücker *et al.* [2006] and Blome *et al.* [2009]. Final results are presented as apparent resistivities.

We begin by examining apparent resistivity distributions for the three borehole diameters, each $\rho_r : \rho_f$ contrast considered, and all possible recording configurations of the AB-MN and AM-BN types (with electrode spacings incremented progressively by 1 m). If the borehole-fluid effect is negligible, then the apparent resistivities would equal the true 100 Ωm resistivity, such that differences from 100 Ωm are a measure of the borehole-fluid effect. Figure 4.3 shows, in a simplified frequency-polygon form, illustrative data corresponding to a

contrast $\rho_r : \rho_f$ equal to 10 : 1. The spread of apparent resistivities around the true rock-formation resistivity of 100 Ωm increases with increasing borehole diameter. Even for this narrow borehole-diameter, the variation in values is significant (of the order of 10%) at this modest resistivity contrast. The discrepancies grow to 40% for the large diameter case. Clearly, some recording geometries are more sensitive to the borehole-fluid effect than others, as indicated by the outliers on the frequency polygon plot. The variations become larger as the resistivity contrast increases (not shown). We found that the apparent resistivities can become negative for certain asymmetric AB-MN configurations. Negative apparent resistivities are neither uncommon nor unphysical and have been reported in previous studies [e.g., *Marescot et al.*, 2006; *Jung et al.*, 2009].

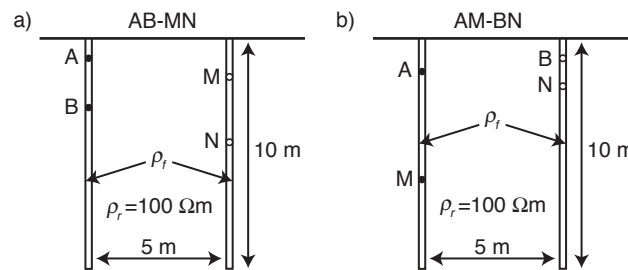


Figure 4.1. Model and crosswell recording geometries used in computing synthetic borehole responses. (a) AB-MN configuration: both current electrodes in one hole and both potential electrodes in the other. (b) AM-BN configuration: each hole contains one current electrode and one potential electrode.

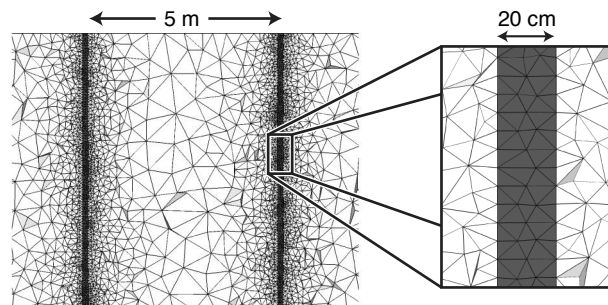


Figure 4.2. Typical unstructured mesh used to represent the subsurface within, around, and between boreholes in a crosswell-ERT experiment.

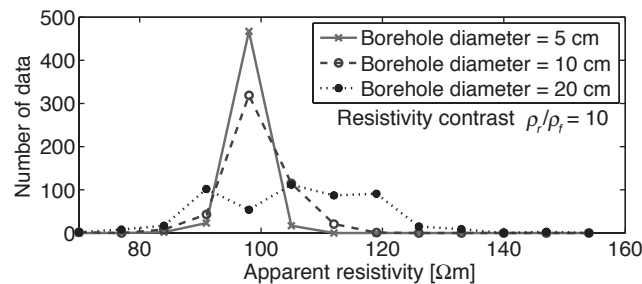


Figure 4.3. Frequency polygons of apparent resistivities obtained for all possible recording configurations (i.e., all combinations of A, B, M, and N electrode depths) and $\rho_r : \rho_f = 10 : 1$. The three curves correspond to borehole diameters 5, 10, and 20 cm.

Figure 4.4 shows apparent resistivities for electrodes at fixed depths of 1 m and 6 m in both boreholes and varying $\rho_r : \rho_f$ contrasts. The 5 m bipole length and 5 m hole separation equate to 25 times the largest borehole diameter that we tested. The borehole-fluid effect produces anomalously low apparent resistivities for the AB-MN configurations (Figure 4.4a), which means that the voltages are smaller than if the boreholes were not present. The effect is substantial (i.e., apparent resistivities too low by up to 80 %) for large resistivity contrasts and large borehole diameters. Even for $\rho_r : \rho_f$ contrasts of just 100, the effects are $\sim 12\%$ and $\sim 32\%$ for the 10 and 20 cm borehole diameters. The reason for the decrease in apparent resistivity over the no-borehole situation is that current density is increased in the source borehole and reduced elsewhere, including within the borehole containing the potential electrodes. Since the measured voltage is proportional to both the current density and the true resistivity in the immediate vicinity of the potential electrodes, having the potential electrodes in the low resistivity borehole fluid remote from the current source and sink results in anomalously low voltages and hence anomalously low apparent resistivities.

For the AM-BN configurations (Figure 4.4b), the apparent resistivities are anomalously high relative to the no-borehole situation. For a $\rho_r : \rho_f$ contrast of 100, the effects are $\sim 24\%$ and $\sim 95\%$ for the 10 and 20 cm borehole diameters, markedly higher deviations than for the AB-MN configurations. The reason for the increase in apparent resistivity is that each potential electrode shares the same hole as either the current source or the current sink where current density is increased because of the conductive fluid. The increase in current density overwhelms the effect of the low resistivity of the borehole fluid, such that it is sensed by the potential electrodes as anomalously high voltages and apparent resistivities.

Plots of apparent resistivity versus bipole size for a 10-cm borehole diameter and a resistivity contrast of 30 : 1 are displayed in Figure 4.5 for the AB-MN and AM-BN configurations; an electrode spacing of 0.25 m was used to generate these plots. The bipoles were centered at the midpoint of the holes and their common sizes were varied. This Figure reveals that the borehole-fluid effect increases with decreasing bipole size (AB, MN, AM, and BN). It is more pronounced for the AM-BN configurations, with apparent resistivities anomalous by as much as 36 % for a bipole spacing of 1 m. We also examined the influence of bipole-midpoint depth in each hole. There is essentially no difference (not shown) for symmetric configurations, as in normal scanning where each bipole is at the same depth, but there are effects associated with the bottom and top of each hole. For asymmetric configurations, in which the two bipoles do not share the same depth, the pattern is fairly

stable for AM-BN configurations but erratic for AB-MN configurations, with negative apparent resistivities appearing when the depth difference between the two bipoles exceeds half the borehole depth. This means that the AB-MN configurations can produce singularities in the geometric K factor, which is defined as

$$K = \frac{4\pi}{\frac{1}{AM} + \frac{1}{A'M} - \frac{1}{AN} - \frac{1}{A'N} - \frac{1}{BM} - \frac{1}{B'M} + \frac{1}{BN} + \frac{1}{B'N}}$$

and is thus a function of the distances between the potential electrodes M and N, and the true underground sources A and B as well as the above ground mirror image sources A' and B' [Günther, 2004, page 45]. Physically this means that the voltage differences are very small (i.e., potential electrodes lie close to the same equipotential surface) and can even change sign.

The information contained in Figures 4.3 - 4.5 together with the results of earlier synthetic studies by *Osiensky et al.* [2004] and *Nimmer et al.* [2008] demonstrate that apparent resistivities in crosswell-ERT experiments are significantly influenced by the borehole fluid. Unless the effects of the borehole fluids are accounted for, either by explicitly including the boreholes in the finite-element mesh or possibly by applying correction factors to the raw data, regularized tomographic inversions are likely to yield images contaminated with artifacts. Some of the artifacts will be obvious (e.g., anomalous features along the lengths of the boreholes), whereas others may not be easy to identify. In the following, we explore both approaches for handling the borehole-fluid effect, namely: (1) explicitly including the boreholes in the computational mesh, and (2) determining correction factors that can be applied to the raw data, so that the boreholes can be ignored in the inversion process.

4.3 MULTI-HOLE 3-D ERT DATA SET

As part of a multidisciplinary effort to map changing aquifer conditions associated with flood events in an adjacent river, we have recorded a large number of crosswell-ERT data sets at a test site in Switzerland. The geology at this location includes a 3-m-thick surface layer of alluvial sandy loam successively underlain by 1 m of unsaturated gravel, 6 m of water-saturated gravel, and lacustrine clay of considerable thickness. The electrical characteristics are listed in Table 4.1.

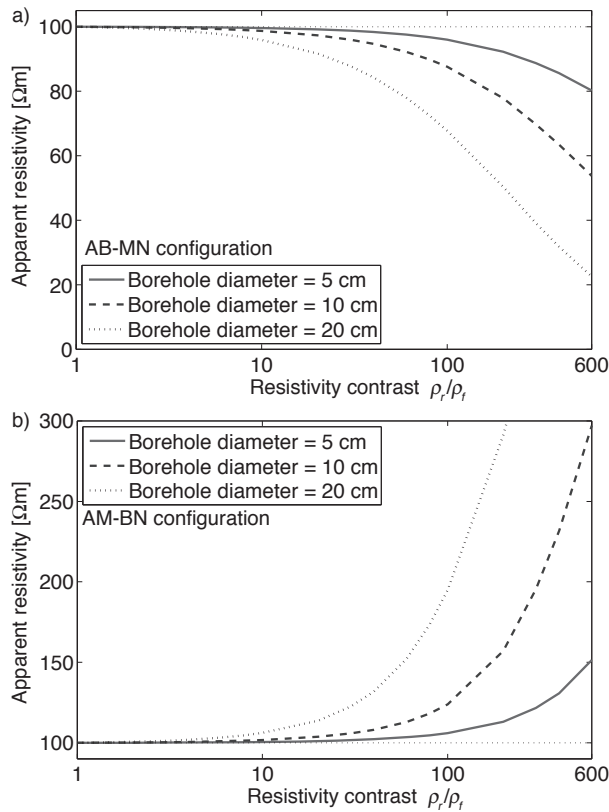


Figure 4.4. Apparent resistivity as a function of $\rho_r : \rho_f$ contrast (log scale) for electrode configurations (a) AB-MN and (b) AM-BN (see Figure 1). Depths to the upper and lower electrodes are kept constant at 1 and 6 m. The three curves shown in each diagram correspond to borehole diameters of 5, 10, and 20 cm.

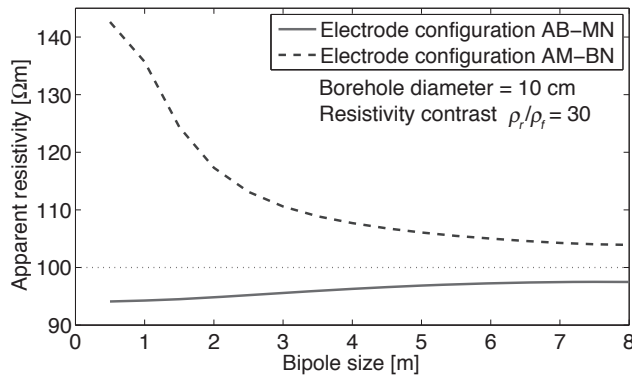


Figure 4.5. Apparent resistivity versus bipole length (the same in each borehole) for a 10 cm borehole diameter and $\rho_r : \rho_f = 30 : 1$. The bipoles are centered at a depth of 5 m in each hole. Results are given for the two recording configurations AB-MN and AM-BN.

Table 4.1. Layered (1D) model at the test site.

Unit	Thickness [m]	Resistivity [Ωm]
Loam	3	40
Unsaturated gravel	1	1000
Saturated gravel	6	250
Clay	>	20

During a period of stable hydrological conditions when no flood events occurred (and thus no temporal changes in electrical properties of the subsurface), we acquired one large 3-D crosswell-ERT data set using four vertical boreholes located at the corners of a 5 x 5 m square. The 11.4-cm-diameter boreholes penetrated the entire geological section down to the upper part of the clay-rich aquitard. Ten electrodes equally spaced at 0.7 m intervals were installed along the screened part of each borehole that passed through the gravel aquifer. At the time of the experiment, 9 of the electrodes were located within the water-saturated part of the aquifer. The primary purpose of this experiment was to define resistivity variations within the water-saturated part of the aquifer and to investigate the resolving capabilities of different electrode configurations. Complementary crosswell radar and seismic experiments were carried out between the same boreholes over the same depth range for hydrogeophysical characterization of the aquifer (see Chapter 2).

Electrodes within the saturated zone of the gravel aquifer were used to give 3-D coverage across the six possible acquisition planes provided by the 4 boreholes (see sketches at the top of Figure 4.6). Of the 10,224 electrode combinations we employed, 2,464 configurations were of the AB-MN type and 7,760 configurations were of the AM-BN type. The recording instrument allows the repeatability of each voltage reading to be determined from multiple measurements over each current cycle. Data having measurement deviations of more than 1% were eliminated, reducing the data set to 10,035 measurements. We also eliminated potentially noisy data acquired with electrode configurations distinguished by geometric K factors > 1000 ; in fact electrode configurations with high K factors usually have low signal levels, because the two potential electrodes are close to the same equipotential contour. The remaining 9,203 raw measurements formed the full dataset.

Although it is possible to invert data sets with >9000 values, it is relatively time-consuming. For this reason, we employed an optimized experimental-design procedure to reduce the number of values without significantly reducing the resolution capabilities of the data set. The sensitivities for each electrode configuration were first calculated using a 4-layered earth model (Table 4.1) derived from previously acquired surface- and crosswell-ERT data. The rows of the Jacobian matrix of sensitivities, each one corresponding to a particular configuration, were then compared and used in an optimized experimental-design procedure. Those configurations having the greatest degree of linear independence were added to the base set of 1,000 most sensitive combinations. Details about this optimization approach are described by *Stummer et al.* [2004] and *Coscia et al.* [2008]. In this way, we selected the

5,000 most independent measurements. Our inversions were based on this reduced data set of 5,000 measurements.

4.4 3-D INVERSION RESULTS WITH AND WITHOUT BOREHOLES

We first inverted the 3-D data set using the BERT code [Günther *et al.*, 2006], with an unstructured mesh that incorporated an adequate representation of the boreholes. Each borehole was treated as an independent inversion region with spatial regularization five times stronger than for other inversion regions, but there were no assumptions regarding the electrical resistivity of the borehole fluid (for a discussion on region constraints, see Günther and Rücker [2009]). Although the active electrodes were limited to the water-saturated part of the gravel aquifer, the resistivities of the overlying and underlying units as well as the resistivities of immediately adjacent regions outside the cuboid defined by the boreholes will influence the inversion results [Maurer and Friedel, 2006]. Accordingly, the inversion domain was defined to be a cuboid of 10×10 m horizontal extent and 13.0 m depth.

For reliable and consistent inversion results, it was necessary to decouple the smoothness constraints between the different layers, separating the unsaturated zone and the clay layer from the principal zone of interest. The boundaries at the top and bottom of the saturated zone were known to be sharp, such that smoothing across such boundaries can introduce spurious features. It was therefore important to preserve the abrupt nature of the known lithological and hydrological boundaries (based on the borehole geological logs) to allow subtle but important 3-D variations in resistivity within the gravel aquifer to be mapped. Inversions in which the sharp boundaries were not enforced yielded highly variable and unrealistic resistivities within the aquifer. By adopting this inversion approach, data misfit at the 3 - 4% error level was achieved after four iterations. The starting model for the inversions was a 1-D layered sequence (Table 4.1), based on the average resistivities determined from surface ERT and borehole logs.

Results of the inversion are depicted in 3-D perspective view in Figure 4.6a and b for the 4 outer observation planes. To take advantage of the full color spectrum to represent the relatively narrow but significant 100 - 270 Ωm range of resistivities in the water-saturated aquifer (the primary target of our investigations), the results for the overlying and underlying layers are not presented in Figure 4.6. The inverted values for the lumped loam-unsaturated zone are in excess of 500 Ωm and those for the clay are less than 50 Ωm . The former are consistent with results from companion surface ERT surveys, which yielded values of 60 Ωm

for the loam and approximately 1000 Ωm for the unsaturated gravel. Figure 4.6a and b reveal quasi-subhorizontal resistivity layering near three of the boreholes and a rather diffuse relatively high resistivity feature near the fourth borehole. The resistivity of the borehole fluid has an average value of 27 Ωm , only eight times lower than the average for the rock formation.

Figure 4.6c and d show results of the unstructured BERT inversion with layer decoupling of the gravel-clay and the saturated-unsaturated gravel interfaces, but completely ignoring the boreholes (i.e., by not including them in the mesh generation). Even though the data misfit is similar to runs that included the boreholes, this image is visually different to Figure 4.6a and b; the correlation coefficient between the log resistivities in the two models across the six borehole planes is 0.88. This coefficient might at first sight seem rather high but it should be appreciated that the actual resistivity variations in the aquifer are quite small, and the differences are further compressed when taking logarithms. The quasi-subhorizontal resistivity layering seen in Figure 4.6a and b is not evident in Figure 4.6c and d. Paradoxically, artificial high resistivity zones have been introduced at and around the borehole locations, where in fact the resistivities are low. This is a consequence of the majority of measured apparent resistivities being of the AM-BN type, which have anomalously high values because of the increased current density within the borehole fluid (Figure 4.4b). When the boreholes are not taken into account, the inversion algorithm cannot differentiate whether an increased voltage is due to an increase in current density or an increase in ground resistivity.

We have compared the two 3-D ERT models in Figure 4.6 with the coincident but independently derived 3-D radar and seismic velocity models in Chapter 2. There is excellent correspondence between the resistivity pattern depicted in Figure 4.6a and b and the radar and seismic velocity patterns. The quasi-subhorizontal layering near three of the boreholes and the diffuse feature near the fourth borehole are characteristics of all three 3-D tomograms. We can quantify the correlations. For example, since electrical resistivities likely decrease and radar permittivities likely increase with increased porosity within the saturated gravel, we expect these two parameters to be strongly anti-correlated in the region of interest (even though spatial variations of clay content will probably decrease this anti-correlation). Cross-correlations of the radar permittivity model with the resistivity models based on the ERT inversions with and without the boreholes yield correlation coefficients of -0.66 and -0.52, demonstrating that the ERT inversion with boreholes produces a model that corresponds more

closely to the radar permittivity model than that produced by the inversion that ignores them. These results indicate that the model that ignores the borehole is of limited value to make inferences about internal lithological variations within the gravel aquifer.

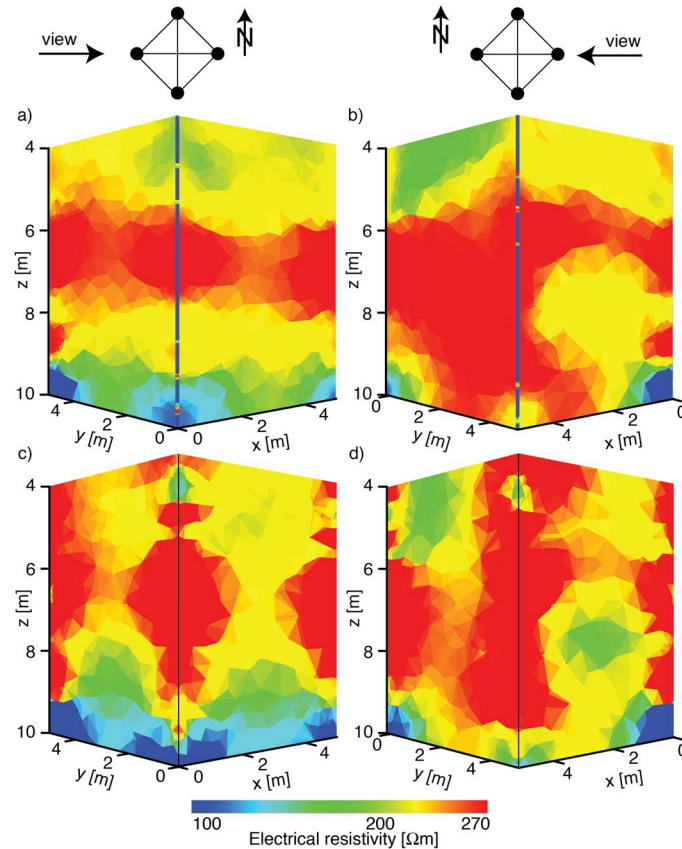


Figure 4.6. Crosswell-ERT data were acquired between 4 boreholes located at the corners of a 5 x 5 m square (a total of 6 planes; see sketches at the top) and inverted using the program BERT with an unstructured mesh. (a) and (b) Two perspective views of a model derived from a 3-D inversion that explicitly incorporates the boreholes (the outer 4 planes are shown). (c) and (d) Corresponding views for a 3-D inversion that did not incorporate the boreholes. Note the high resistivity artifacts along the boreholes in (c) and (d). Note that the color bar is clipped at each end so that any resistivities lower than 100 Ωm remains blue and any resistivity higher than 270 Ωm remains red. The actual recovered borehole resistivity is 27 Ωm .

4.5 THE INADEQUACY OF CORRECTION FACTORS

To avoid the extra computational effort and sophistication that results from including the boreholes in the finite-element meshes, we now investigate the possibility of calculating and applying borehole-fluid correction factors to the data prior to inversion. If this approach proves to be viable, standard schemes based on structured meshes that do not incorporate the boreholes could be used to invert the corrected crosswell-ERT data. We determine the first

suite of correction factors by applying the forward component of the BERT software to the 1-D layered model shown in Table 4.1 with the boreholes and then without the boreholes. The correction factors are the ratios of apparent resistivities from the two forward modeling runs. They are shown in frequency polygon form by the dashed line in Figure 4.7 for the various electrode configurations. The values range from 0.7 to 1.15.

These correction factors were applied to the observed apparent resistivity data and the corrected data were then inverted using the BERT code and an unstructured mesh that ignored the boreholes. The inverted model shown in Figure 4.8a and b is quite different to both the model obtained incorporating the boreholes (Figure 4.6a and b) and the one obtained without applying correction factors (Figure 4.6c and d). The correlation coefficient between this model and the model that explicitly incorporates the boreholes is 0.93. The artifacts along the boreholes in Figure 4.8a and b are not as pronounced as in Figure 4.6c and d, but they are sufficiently strong to obscure the pattern of resistivities between the boreholes. This result clearly shows that corrections based on a layered model are inadequate for this data set.

We repeated the calculation and application of correction factors, but this time we replaced the 1-D model (Table 4.1) with the final 3-D model of Figure 4.6a and b. The distribution of these correction factors is shown by the solid line in Figure 4.7. The shape of this histogram is notably different from that generated for the 1-D model. These 3-D-model-based correction factors were then applied to the field data and an inversion was performed ignoring the boreholes. The resultant model displayed in Figure 4.8c and d is very similar to that presented in Figure 4.6a and b, with a correlation coefficient of 0.98 between the two models.

Of course, in practice, the true model is not known in advance, so using correction factors based on the final 3-D model is not feasible. Since correction factors based on a 1-D starting model are demonstrably insufficient, the only satisfactory approach to account for the borehole-fluid effect is to represent the boreholes in an appropriate unstructured mesh and explicitly include them in the inversion process.

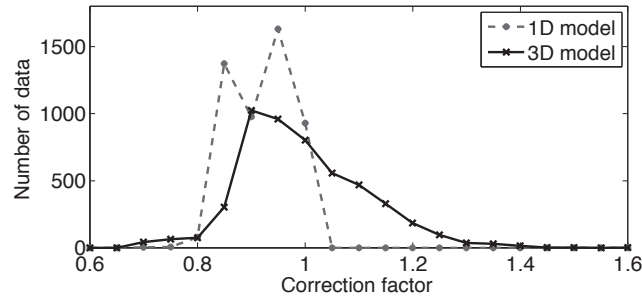


Figure 4.7. Frequency polygons of borehole-correction factors based on apparent-resistivity ratios computed for each electrode configuration with and without the boreholes. The two curves are for the layered (1-D) model of Table 4.1 and the actual 3-D inverted model in Figure 4.6c and d. The difference in the patterns is quite large.

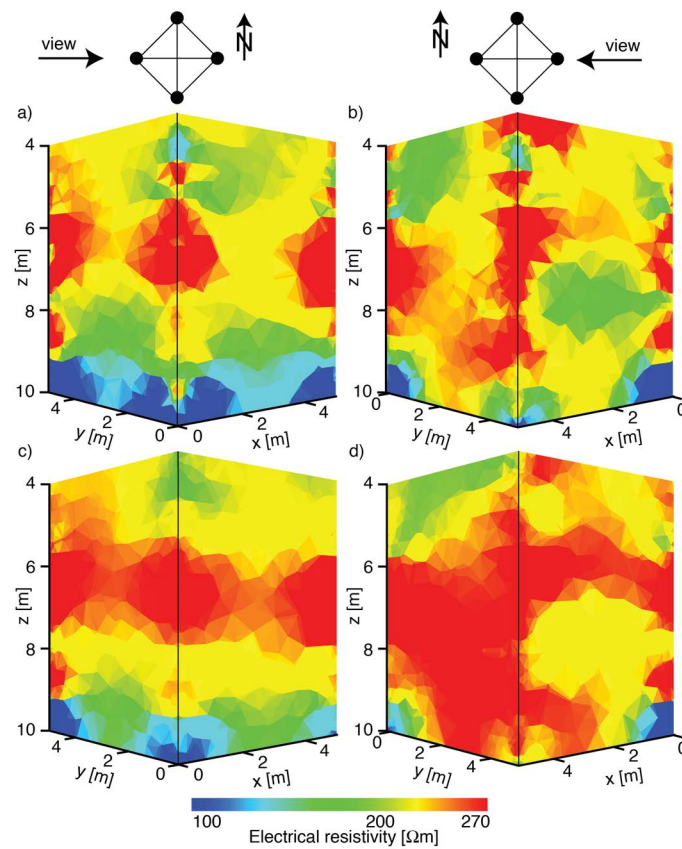


Figure 4.8. (a) and (b) 3-D inversion result using the program BERT with an unstructured mesh after first correcting the input data for the borehole effects according to the layered model of Table 4.1 and then ignoring the boreholes in the actual inversion. Note the high resistivity artifacts around the boreholes compared to Figure 4.6a and b. (c) and (d) As for (a) and (b), but first correcting the input data for the borehole effect according to the 3-D inversion result of Figure 4.6a and b. The result is quite similar to that of Figure 4.6a and b. Of course, one would not have the true model (i.e., Figure 4.6a and b) to make such corrections in practice, so the only purpose of doing it here is to emphasize the inadequacy of corrections based on the 1-D model (albeit with the approximately correct background resistivity). Note that the color bar is clipped at each end so that any resistivities lower than 100 Ωm remains blue and any resistivity higher than 270 Ωm remains red.

4.6 CONCLUSIONS

We have undertaken a systematic investigation of the influence of fluid-filled boreholes on the modeling and inversion of crosshole-ERT data. Our study is the first to include the boreholes and their fluid fill in the inversion process. This was achieved by representing the borehole by a dense network of elements in an unstructured mesh. The most important conclusions to emerge can be summarized as follows.

- The electrical resistivity structure of the ground, the resistivity contrast between the rock formation and borehole fluid, as well as survey design/geometrical factors (e.g., the borehole diameter, depth, hole spacing, electrode recording configuration) all play an important role in the borehole-fluid effect. This effect intensifies as the resistivity contrast $\rho_r : \rho_f$ and borehole diameter increase, and as the bipole spacing decreases. For AB-MN configurations, the apparent resistivities are underestimated whereas for AM-BN configurations they are overestimated.
- At our field study site, a very low resistivity contrast of 8 : 1 between the rock formation and the borehole fluid in the 11.4-cm-diameter boreholes produces artifacts that are much more significant than predicted by synthetic modeling; the effect appears to be severe even for the 5-cm-diameter boreholes used in complementary time-lapse ERT investigations at the site (results not presented here). Our results show that the effect is minor for forward modeling borehole diameters < 10 cm and a resistivity contrast of 10 : 1, but the effect greatly intensifies for inversions, such that significant artifacts can be produced in an inversion model; such error amplification effects are well known in seismic tomography.
- Correction factors based on simulations for a 1-D resistivity model with and without boreholes does not allow an inversion procedure that ignores the boreholes to recover the subsurface resistivity distribution.
- Trustworthy models of minor electrical resistivity variations based on ERT data acquired in fluid-filled boreholes can only be achieved by including the boreholes in the inversion. This is not really feasible with structured grids and necessitates an unstructured mesh approach. Time-lapse inversion utilizing ratios or differences of apparent resistivities or voltages is likely to be less influenced by the borehole effect and could be a partial remedy to the problem. However, this requires further investigation. In a strict theoretical sense, the sensitivity kernels

required in the inversion-parameter updates at each iteration to resolve subtle electrical resistivity variations should be based on an accurate model that incorporates the boreholes.

- Since the inclusion of particularly small boreholes increases the number of tetrahedral, this could increase the memory and run time of the inversion process considerably. In the case of a constant borehole fluid conductivity one could easily combine the inversion cells of each borehole to one unknown, which is possible with the code used.
- If unstructured-mesh numerical modeling and inversion capability is not available to practitioners, then our advice would be to use an alternative to fluid coupling of the electrodes in the boreholes. Examples would include electrodes mounted on the outside of a PVC pipe in an air-filled hole and held in firm contact with air-filled borehole walls.

5 CONSTRAINING 3-D ERT WITH GPR REFLECTION DATA

In press with *Journal of Applied Geophysics*:

Doetsch, J., Linde, N., Pessognelli, M., Green, A. G., and Günther, T., 2011. Constraining 3-D electrical resistance tomography with GPR reflection data for improved aquifer characterization, *Journal of Applied Geophysics*, in press.

ABSTRACT

Surface-based ground penetrating radar (GPR) and electrical resistance tomography (ERT) are common tools for aquifer characterization, because both methods provide data that are sensitive to hydrogeologically relevant quantities. To retrieve bulk subsurface properties at high resolution, we suggest incorporating structural information derived from GPR reflection data when inverting surface ERT data. This reduces resolution limitations, which might hinder quantitative interpretations. Surface-based GPR reflection and ERT data have been recorded on an exposed gravel bar within a restored section of a previously channelized river in northeastern Switzerland to characterize an underlying gravel aquifer. The GPR reflection data acquired over an area of 240×40 m map the aquifer's thickness and two internal sub-horizontal regions with different depositional patterns. The interface between these two regions and the boundary of the aquifer with the underlying clay are incorporated in an unstructured ERT mesh. Subsequent inversions are performed without applying smoothness constraints across these boundaries. Inversion models obtained by using these structural constraints contain subtle resistivity variations within the aquifer that are hardly visible in standard inversion models as a result of strong vertical smearing in the latter. In the upper aquifer region, with high GPR coherency and horizontal layering, the resistivity is moderately high ($>300 \Omega\text{m}$). We suggest that this region consists of sediments that were rearranged during more than a century of channelized flow. In the lower low coherency region, the GPR image reveals fluvial features (e.g., foresets) and generally more heterogeneous deposits. In this region, the resistivity is lower ($\sim 200 \Omega\text{m}$), which we attribute to increased amounts of fines in some of the well-sorted fluvial deposits. We also find elongated conductive anomalies that correspond to the location of river embankments that were removed in 2002.

5.1 INTRODUCTION

Near-surface geophysical techniques can be useful in a wide range of hydrogeological applications [Rubin and Hubbard, 2005; Hubbard and Linde, 2011]. Surface-based ground penetrating radar (GPR) and electrical resistance tomography (ERT) are perhaps the most common geophysical methods used, primarily because of the hydrogeological relevance of the respective physical properties and their relative ease of application along profiles ranging from 1 to 10,000 m and surface areas ranging from 1 to 10,000 m^2 . Electrical resistivity in saturated alluvial systems is mostly a function of pore-water salinity, porosity, tortuosity and

the specific surface area of the grains (i.e., the amount of fine materials) [Lesmes and Friedman, 2005]. Unfortunately, surface-based ERT suffers from resolution limitations [Ellis and Oldenburg, 1994] that enhance the inherent non-uniqueness of the resistivity inverse problem [Parker, 1984]. In contrast, GPR reflection data can, under favorable conditions (e.g., for soil and sediments with low clay content and only moderate pore-water salinity), be used to map the 3-D sedimentary structure of the subsurface in great detail down to about 10 m depth [Smith and Jol, 1992; Beres et al., 1995; Beres et al., 1999; Lunt et al., 2004]. Since GPR reflections are mainly sensitive to contrasts in water content, it is often difficult to relate GPR images to the bulk properties of a hydrogeological model. We propose here to incorporate structural information derived from surface GPR reflection data as constraints in the inversion of surface ERT data that provides such bulk properties.

The sedimentary structures of fluvial deposits have been extensively studied using GPR reflection imaging [e.g., Smith and Jol, 1992; Huggenberger, 1993; Beres et al., 1995; Beres et al., 1999]. For example, Lunt et al. [2004] used GPR measurements to develop a model for the evolution of gravelly braided bars. Surface-based ERT has also been widely used for aquifer characterization [e.g., Kosinski and Kelly, 1981; Mazac et al., 1987; Koch et al., 2009]. In a number of studies, surface-based GPR reflection and ERT methods have been combined to improve the characterization of alluvial aquifers [e.g., Sandberg et al., 2002; Bowling et al., 2005; Bowling et al., 2007; Bélanger et al., 2010].

Integration of different geophysical data or models for interpretation purposes can be achieved by the (1) joint interpretation of results from separately processed / inverted data, (2) joint inversion of different data sets and (3) constrained inversion of one data set using information from other geophysical data / models. Joint interpretation of different models is common practice [e.g., Sandberg et al., 2002; Bowling et al., 2005; Bélanger et al., 2010], but becomes ambiguous when the models disagree or their resolution properties differ significantly. These problems can be partly avoided by performing joint inversion, which is becoming increasingly used since the development of structural joint inversion [Haber and Oldenburg, 1997; Gallardo and Meju, 2003]. In crosshole configurations, joint inversion of GPR traveltimes and ERT has been used for aquifer characterization [e.g., Linde et al., 2006a] to provide higher resolution and geometrically similar models that can be used to estimate effective petrophysical parameters (see Chapter 2). Constrained inversion is particularly useful when one wants to combine geophysical data that are mainly sensitive to structure (e.g., seismic and GPR reflection data) with data that are primarily sensitive to bulk properties

(e.g., ERT data). As examples, *Favetto et al.* [2007], *Jegen et al.* [2009] and *Li et al.* [2003] improved the inversion results of gravity and magnetotelluric data by constraining the inversions using interfaces defined in seismic reflection models.

Here, we investigate the extent to which GPR-derived interfaces can improve ERT inversion and subsequent aquifer characterization. The constraints are implemented by conditioning an unstructured inversion mesh to these interfaces and by not imposing any smoothness constraints across these interfaces during the inversion. An unstructured mesh is essential to include surface topography [*Günther et al.*, 2006], arbitrary electrode positions and prior structural information.

We test our methodology (see Figure 5.1 for a flow chart) on data acquired on a gravel bar within a restored section of the Thur River channel in northeastern Switzerland (see inset in Figure 5.2). The primary goals of this study are to (1) map the geometry of the gravel aquifer on the scale of the gravel bar, (2) resolve the sedimentary structure of the aquifer, and (3) determine if any evidence of the old river embankment remains. Other researchers working at the site will use this information and it will serve as a basis for a saline tracer experiment to be monitored with ERT. After introducing our field site, we describe the GPR acquisition and processing, followed by ERT acquisition and inversion, and a joint interpretation of the resulting models.

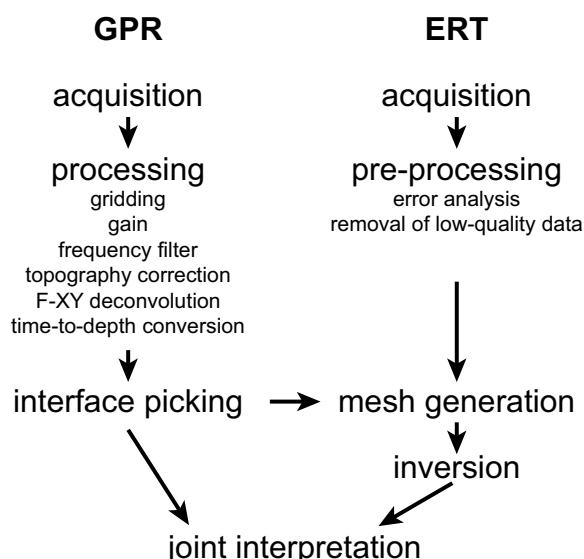


Figure 5.1. Work flow for the combined processing of 3-D GPR and ERT data. The GPR processing is fully independent, but the ERT mesh generation, regularization, and thus the subsequent inversion results are strongly influenced by the GPR-mapped interfaces.

5.2 THUR RIVER FIELD SITE

The Thur River is the largest Swiss river without natural or artificial reservoirs. It is a peri-alpine tributary of the Rhine River with a catchment area of $\sim 1750 \text{ km}^2$. Water level and discharge variations in the Thur River are similar to those of unregulated alpine rivers. Like many other rivers, the meandering Thur River was channelized towards the end of the 19th century for flood protection and to gain arable land. In an attempt to combine flood protection with ecological objectives, a more natural environment was restored along a 2.5 km long reach of the Thur, starting in 2002. The effects of this restoration effort are currently being investigated within the RECORD project [for details see *RECORD*, 2011; *Schneider et al.*, 2011].

While the channelized river was practically flowing along a straight course prior to restoration (Figure 5.2a), the river bed morphology changed substantially once the northern embankment and overbanks were removed. By 2005, a gravel bar had developed on the northern shore of the river (Figure 5.2b) with a surface exposure that strongly depends on the varying river discharge. Under low flow conditions ($20 \text{ m}^3/\text{s}$), a low-lying region with clean gravel is exposed at the surface, whereas under intermediate flow conditions ($100 \text{ m}^3/\text{s}$), this region is flooded and the gravel bar consists mainly of grass-colonized gravel. Under high-flow conditions ($200 \text{ m}^3/\text{s}$), the entire gravel bar is flooded. The frequent flooding of large parts of the gravel bar and the resulting movement of sediments precludes permanent installations, such as monitored boreholes, and thereby increases the importance of geophysics for site characterization. The GPR and ERT data were acquired at low flow conditions. The aquifer below consists of highly permeable fluvial gravel deposits with a varying fraction of fine material.

Ten boreholes instrumented with loggers (temperature, electrical conductivity and pressure) were located on the upper regions of the gravel bar to investigate river-groundwater interactions at the site [*Vogt et al.*, 2010b; *Vogt et al.*; *Schneider et al.*, 2011]. The GPR and ERT data presented here were acquired on the gravel bar to delineate the subsurface aquifer structure for future hydrogeological studies. The surveys were designed to cover as much of the gravel bar as possible; the GPR survey area was limited to the areas of open and grass-colonized gravel, whereas the ERT measurements also covered the *Salix*-populated northern part of the gravel bar (Figure 5.2). The coordinate system used in this paper has its origin at Swiss grid coordinates 272036 / 700218 and is rotated 17° counterclockwise to align the x -axis with the river flow direction.

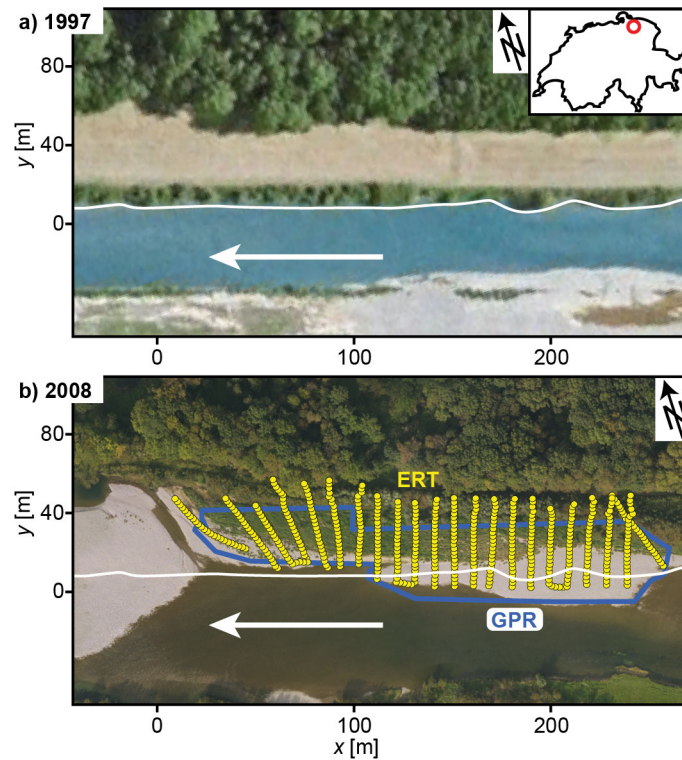


Figure 5.2. Aerial photographs of the Thur River (northeastern Switzerland) (a) before and (b) after restoration. Since the river restoration in 2002, the river bed morphology has been rapidly changing. For reference, the location of the 1997 embankment (shoreline) is highlighted in both photos (white line) and the river flow direction is indicated by a white arrow. Overlain on the 2008 image are the ERT electrode positions and the extent of the 3-D GPR surveys.

5.3 GPR DATA ACQUISITION, PROCESSING AND INTERPRETATION

5.3.1 Data acquisition

The GPR data were acquired in March 2008 (western part at $x < 100$ m in Figure 5.2b) and January 2009 (eastern part at $x > 100$ m). A 100 MHz PulsEkko Pro system was used to collect traces semi-continuously with an internal stacking of 8 and a trace length of 320 ns (trace interval of ~ 5 cm). The measurements were time stamped using a static GPS receiver. An additional mobile GPS receiver attached to the antenna sledge was used to record accurate midpoint positions using differential processing [Streich *et al.*, 2006]. Densely spaced lines (line spacing of 0.5 m) acquired parallel to the river were used to cover the gravel bar. Because the resulting data set had limited crossline resolution, eight complementary 2-D lines were recorded perpendicular to the river. These lines were important to avoid spatial aliasing on the crosslines extracted from the 3-D data.

In addition to the common-offset measurements, 12 common-midpoint (CMP) measurements were made at 9 different positions to determine velocities and velocity variations within the survey area. A representative CMP is presented in Figure 5.3.

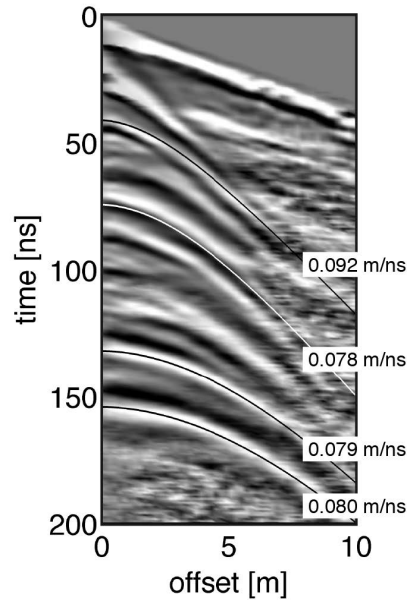


Figure 5.3. Representative common-midpoint (CMP) gather for GPR velocity determination from a high-lying point on the gravel bar.

5.3.2 Processing

Pre-processing of all traces included dewow filtering, alignment of zero times and coordinate assignment based on the differential GPS data. The coordinate assignment was achieved by matching the GPS times of each trace with the time stamps of the GPS attached to the acquisition sledge. The total number of acquired traces for the 3-D surveys was 111,291 (2008) and 245,130 (2009). These traces were summed within regular 0.2 m (in-line) by 0.5 m (crossline) bins. To obtain the best gridding result for the uneven trace spacing, we adapted the natural neighbor gridding algorithm of *Sambridge et al.* [1995]. The two gridded data volumes had a spatial extent of 80×25 m (2008) and 160×36 m (2009) and together covered the full gravel bar over a length of 240 m (Figure 5.2b).

Further data processing included application of a gain function, frequency filtering, topography correction and F-XY deconvolution. The gain function was based on a smoothed inverse of the Hilbert transform of the data with a maximum gain set to 500. The frequency bandpass filter around a center frequency of 80 MHz was cosine tapered with corner frequencies of 15-45-115-145 MHz. In the next step, the data were corrected for topography

using the elevation data obtained from the differential GPS measurements. We used a velocity of 0.09 m/ns for the topography correction (based on the CMP results for the unsaturated gravel; see Figure 5.3). Topography correction and F-XY deconvolution were carried out using commercial software, whereas in-house MATLAB[®] routines were used for the other processing steps. The F-XY deconvolution suppressed laterally incoherent signal and improved the images of coherent features. Migration was not necessary, because the steepest dips observed in the data were $<20^\circ$. Migration tests confirmed this assertion and showed that migration decreased the signal quality in some areas due to the different in-line and crossline trace spacings.

For interpretation, the vertical axis was converted from time to depth using a two-layer velocity model that represented the unsaturated and saturated gravel. The velocity estimates, based on the analysis of the 12 CMP measurements, were $v_u = 0.09 \text{ m/ns} \pm 10\%$ for the unsaturated gravel and $v_w = 0.075 \text{ m/ns} \pm 10\%$ for the saturated gravel.

5.3.3 GPR interpretation

Figure 5.4 shows a chair plot of the western part of the GPR data volume together with a photograph of fluvial deposits at a gravel pit 10 km from the survey area. The data quality is generally very high within the gravel aquifer, such that coherent reflections can be traced to 5 - 6 m depth. At this level, reflections originate from the boundary between the gravel aquifer and underlying lacustrine clay aquitard (marked in Figure 5.4b).

The GPR image (Figure 5.4b) provides many details about the fluvial deposits. These images are comparable with those obtained across nearby gravel deposits [e.g., *Huggenberger, 1993; Beres et al., 1995; Beres et al., 1999*]. Regions with well-sorted gravels, such as the foresets FO in Figure 5.4b (see also FO' in Figure 5.4a), can be distinguished from sub-horizontal features (GS and GS') that were deposited in a different flow regime. Based on Figure 5.4a, it seems likely that these different depositional units have different hydrogeological properties [*Beres et al., 1995; Beres et al., 1999*]. The foresets (FO and FO') consist of a sequence of open framework gravel and units with a bimodal grain size distribution. The clean gravel zones are expected to have a very high hydraulic conductivity, such that the controlling factor for determining the hydraulic conductivity in this region is the connectivity of these small gravel sub-units. In contrast, the gravel sheets (GS and GS') have a much larger extent, a wider grain size distribution and are poorly sorted. It is expected that the

hydraulic conductivity distribution in the gravel sheets is less heterogeneous than in the foresets [e.g., *Heinz et al.*, 2003].

The same depositional units can be identified in the full GPR volume displayed in Figure 5.5a and b. Three different units are separated by two interfaces that appear as continuous reflections in the GPR image. The lower interface is the gravel-clay boundary, whereas the upper interface separates the different depositional structures (FO and GS in Figure 5.4b) of the gravel aquifer. The two main interfaces were semi-automatically picked throughout the GPR volume (Figure 5.5b) using commercial interpretation software. Simultaneous display of in-line and crossline sections with associated picks allowed consistent 3-D picking. These interfaces were extrapolated short distances outside the GPR survey area for the ERT mesh generation (see Figure 5.2b).

Differences between the two regions of the aquifer are highlighted in the coherency plot of Figure 5.5c. The coherency of the GPR data was calculated using a moving cell [*McClymont et al.*, 2008] with a side-length of 2.5 m in the horizontal and 0.5 m in the vertical direction, with a maximum assumed dip of 20°. The coherency is highest in the upper part of the aquifer with the predominantly horizontal layering and is much reduced in the lower part. This strong horizontal layering is restricted to the region underlying the river channel prior to restoration (Figure 5.2a). Below the region of this pre-restoration channel, the top 3 m of the aquifer are strongly layered (Figure 5.6a), which is not observed outside this region (Figure 5.6b and c). Figure 5.6a also shows a channel-like feature (SC) that corresponds to the location of a side channel mapped in 1811 (Amt für Geoinformatik des Kantons Thurgau, personal communication).

5.4 ERT DATA ACQUISITION AND INVERSION

5.4.1 Acquisition and pre-processing

ERT data covering the entire gravel bar were acquired over a period of two days in March 2009. To survey the full gravel bar, we employed a 3-D roll-along scheme with a total of 22 quasi-parallel lines perpendicular to the river (Figure 5.2b). A total of 528 electrode positions were used, with an electrode spacing of 2 m along the lines and a line separation of ~8 m. Three-dimensional measurements were made on patches covered by electrodes from 6 of the parallel lines. This setup was then moved by 4 lines to have an overlap of 2 lines between the patches (5 of these patches covered the gravel bar). Within each of the patches, dipole-dipole,

equatorial dipole, Wenner and gradient data sets (for details of these configurations, see [Zonge *et al.*, 2005]) were collected both along and across the quasi-parallel lines. The quality of the 35,514 raw measurements was evaluated on the basis of the stacking errors (4-6 stacks) and by comparing the repeated measurements associated with overlapping patches. The data set was reduced by combining the repeated measurements, deleting poor-quality data and removing data with geometrical factors >1000 to yield a final data set of 16,349 values. Most of the eliminated data were not included in the design of the measurement sequence, but were added to optimize the recording on the 10-channel SyscalPro instrument. We included these measurements in the initial processing, but had to remove most of them due to their unfavorable electrode geometry. An overall error level of 3% (estimated from the repeated measurements) was added to the standard deviations estimated from the stacking process; these error estimates were used in the inversions.

The horizontal and vertical positions of the electrodes were measured with a differential GPS system and surface topography was estimated using linear interpolation between the electrode positions.

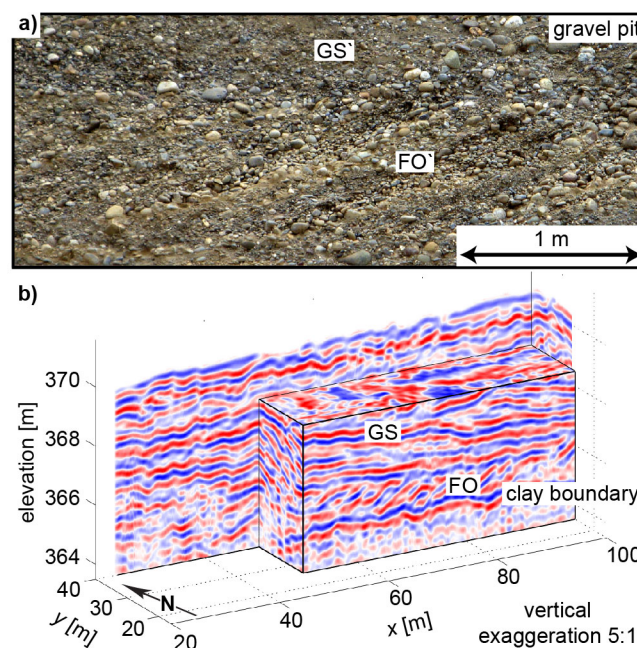


Figure 5.4. (a) Photo of fluvial deposits at a gravel pit (located 10 km away from the survey area) and (b) chair plot of the GPR results for the western (downstream) end of the gravel bar. Foresets (FO in (b) and FO' in (a)) and the subhorizontal layering (GS in (b) and GS' in (a)) illustrate the different sedimentation types of the fluvial system. The strong reflection at 5 - 6 m depth marks the interface between the gravel aquifer and the underlying clay aquitard.

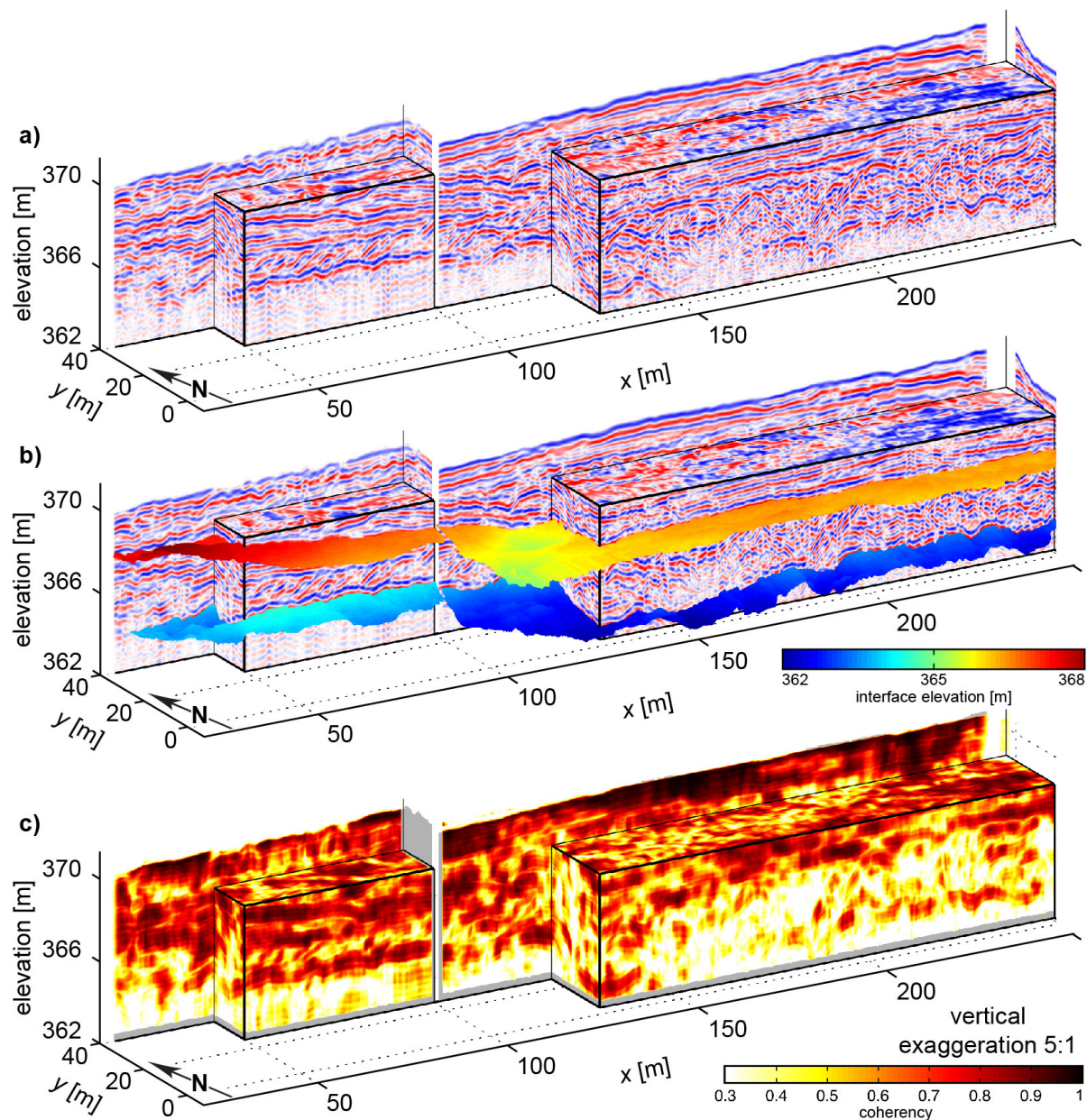


Figure 5.5. GPR results for the entire gravel bar. (a) Chair plot of the fully processed and depth converted data. (b) As in (a), but including the picked interfaces within the GPR volume. (c) Coherency of the GPR signal based on a coherency analysis. The signal coherency is much decreased in the lower part of the gravel aquifer at $x > 150$ m.

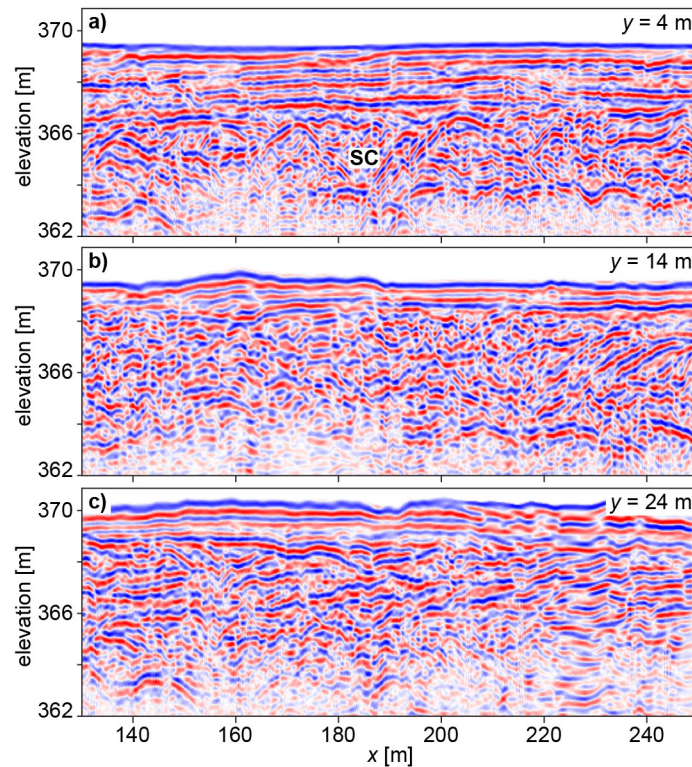


Figure 5.6. Vertical cuts through the GPR volume, parallel to the x -axis at a) $y = 4$ m (corresponding to one of the cuts in Figure 5), (b) 14 m and (c) 24 m. One can observe a clear difference in the depositional pattern in the top 3 m of the aquifer between (a) the pre-restoration river channel and (b) and (c) the outside regions that never experienced channelized river flow. SC marks a channel-like feature, which corresponds to the location of a side channel mapped in 1811.

5.4.2 Mesh generation

The mesh or grid that represents the models plays a critical role in 3-D ERT inversion [Günther *et al.*, 2006]. We use an unstructured tetrahedral mesh that allows us to include arbitrary electrode positions, surface topography and such additional structural information as the water table and GPR-defined interfaces.

The gridding was performed in two steps: (1) mesh the 2-D surfaces and (2) create a 3-D tetrahedral mesh based on the 2-D meshes. In the first step, the 2-D surfaces were represented by a mesh of triangles that included the electrode positions as points. The water table was assumed to be constant at the measured elevation of 371.2 m (the hydraulic gradient is very low due to the high permeability of the aquifer [Vogt *et al.*, 2010b]) and the interfaces within and at the base of the gravel aquifer were interpolated from the horizons shown in Figure 5.5b.

In the second step, the 2-D grids were used as a starting point for the 3-D tetrahedral mesh generation [Rücker *et al.*, 2006]. Three different meshes were created (see Figure 5.7a, c

and e) to evaluate the effects of the GPR-defined structural constraints on the ERT results. The first mesh (Figure 5.7a) only included the surface topography, whereas the second mesh (Figure 5.7c) also included the water table and the gravel-clay boundary, and the third mesh (Figure 5.7e) included all of these interfaces together with the GPR-defined interface within the gravel aquifer. Regions above and below intra-gravel and gravel clay interfaces were treated as separate regions during the inversion (i.e., no smoothing constraints were applied across the interfaces). By comparison, the water table was included in the meshing, but the unsaturated zone was not decoupled from the layer below during the inversion. Each of the three inversion meshes had approximately 100,000 cells and a $270 \times 80 \times 25$ m extent.

For the forward calculations, the inversion mesh was refined by splitting each tetrahedron into eight. The modeling domain was extended 30 m in all directions to reduce boundary effects. The singularity removal technique of Lowry et al. [1989] was used to achieve high accuracy by accounting for the rapid decay of electric potential around each current-source position [Rücker et al., 2006]. Since there is no analytical solution for the primary potentials in the presence of topography, the potential field (for a homogeneous earth) was calculated using a refined mesh around the electrodes before the inversion. For the forward calculations, Neumann (no current flow) boundary conditions were used at the surface and mixed-type boundary conditions were used along the other sides of the mesh [Rücker et al., 2006].

5.4.3 ERT inversion

For each of the three meshes described above, the ERT data were inverted using the electrical resistance tomography program BERT of Günther et al. [2006]. The starting models had a homogeneous resistivity of $200 \Omega\text{m}$ in the aquifer and $40 \Omega\text{m}$ in the clay (for the meshes in Figure 5.7c and e). Tests using uniform resistivities of $20 \Omega\text{m}$, $200 \Omega\text{m}$ and $500 \Omega\text{m}$ throughout the models showed that the features in the aquifer were well-resolved and that the resistivity of the clay layer varies only moderately between $35 \Omega\text{m}$ and $55 \Omega\text{m}$, depending on the starting model. An anisotropy factor of 0.5 was assumed for the smoothness constraints within the aquifer to honor the layered structure imaged by the GPR (for the formulation of these constraints, see Coscia et al., [2011a]). The data were first inverted using the three-region mesh (Figure 5.7e) and the inversion algorithm was allowed to slightly adapt the error model by robust data reweighting [Claerbout and Muir, 1973] from a median of 3.0% to 3.5%. The final error estimates from this inversion were then assigned to each data point and the data were inverted to this error level for all three meshes.

For each of the three meshes, the data were inverted using seven different regularization weights ranging from $\lambda=20$ to $\lambda=300$. For the interpretation, we chose the model with the strongest regularization that explained the data to the specified error model. Inversions using the two- and three-layer meshes (Figure 5.7c and e) reached the data misfit criterion (normalized RMS = 1) in 6 and 5 iterations using a regularization weight of $\lambda=70$ and $\lambda=100$ [Günther *et al.*, 2006], respectively. The lowest data misfit for the standard inversion without any interface decoupling was obtained using $\lambda=50$, but the final normalized RMS after 9 iterations was 1.3 times the assumed data error, with no improvement after additional iterations. The three resulting models are shown in Figures 5.7b, d, f and 5.8 (in this latter figure, the ERT models are shown in the same view and with the same vertical exaggeration (5:1) as the GPR images in Figure 5.5).

Although the inversion parameters are comparable and the three models with roughly the same number of cells fit the data to approximately the same error level, the inversion results (especially at depth) are very different. These results illustrate the inherent limitations of ERT data to determine uniquely subsurface structure with depth [e.g., Parker, 1984]. Standard ERT that only includes surface topography as a structural constraint yields a vertically and horizontally smooth model (Figure 5.7b). Such smoothness is an inherent feature of Occam-type inversions that may hinder interpretations of the models [Ellis and Oldenburg, 1994]. It is possible to identify the low-resistivity clay, as well as the high-resistivity aquifer in Figure 5.7b, but it is difficult to discern a clear boundary between the two layers and interpret features within the aquifer. In the model obtained using the mesh that includes the water table and the gravel-clay boundary (Figure 5.7d), it is possible to differentiate clearly between the gravel aquifer and the clay, thereby creating an image that better matches our prior knowledge. Two effects contribute to the differences between the models in Figure 5.7b and d. First, by including the gravel-clay boundary in the meshing, there are no cells that are partly located in the gravel and partly in the clay, thus allowing the inversion algorithm to define a much sharper boundary. This effect is enhanced by the relatively coarse model discretization of the aquifer, which is a consequence of computational limitations when inverting large-scale 3-D ERT data sets. Second, disconnecting the regularization above and below this interface allows the discrete jump in resistivity from $\sim 200 \Omega\text{m}$ (gravel) to $\sim 30 \Omega\text{m}$ (clay). This is implemented by neglecting cells across the defined interfaces in the roughness operator that penalizes changes between neighboring cells [Günther and Rücker, 2006]. Varying the interface depth within the uncertainty range of $\pm 10\%$ slightly changed the

resistivity model in the vicinity of the interfaces, but did not change the features discussed in the interpretation.

Including the interface within the gravel layer (Figures 5.7e, f and 5.8c) makes it possible to resolve better the resistivity variations within the aquifer that are only hinted at in Figures 5.7d and 5.8b. The model clearly shows that the aquifer at the position marked with A in Figure 5.8c is divided into two zones of distinctly different resistivity. Whereas Figure 5.8b shows resistivities of $\sim 300 \Omega\text{m}$ in this region, Figure 5.8c indicates resistivities of $\sim 400 \Omega\text{m}$ above and $\sim 200 \Omega\text{m}$ below the interface, although both models fit the data to the same error level.

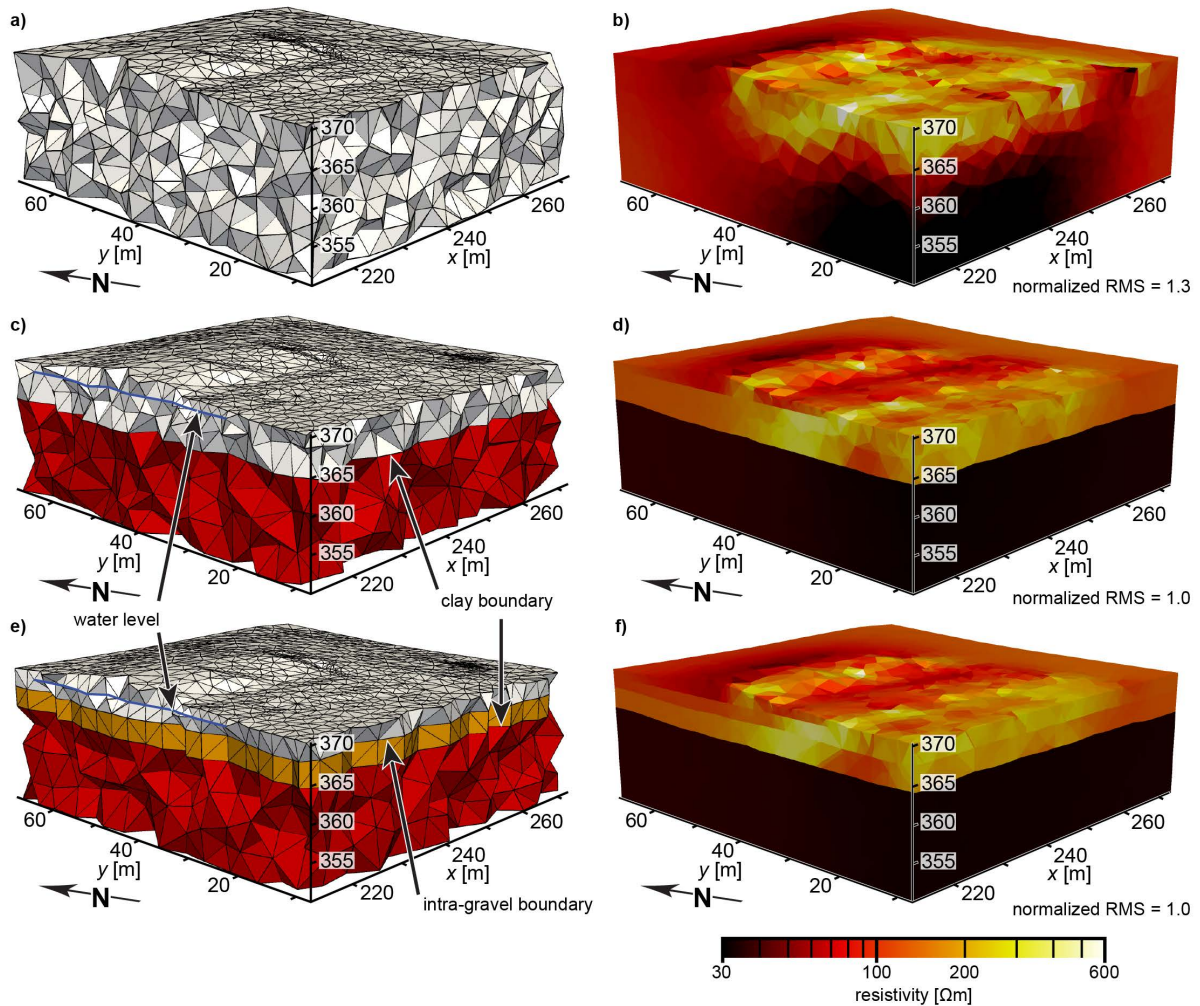


Figure 5.7. Part of the ERT inversion (parameter) mesh for the cases with (a) no interfaces (standard inversion), (c) including the gravel - clay boundary and (e) additionally including the interface within the gravel. Note, that (c) and (e) also incorporate the water table, but without layer decoupling (see text). All three meshes have approximately the same number of cells. (b), (d) and (f) Inversion models for the parts of the three meshes shown in (a), (c) and (e), respectively. More details are visible in (d) and (f), due to reduced vertical smearing over known interfaces.

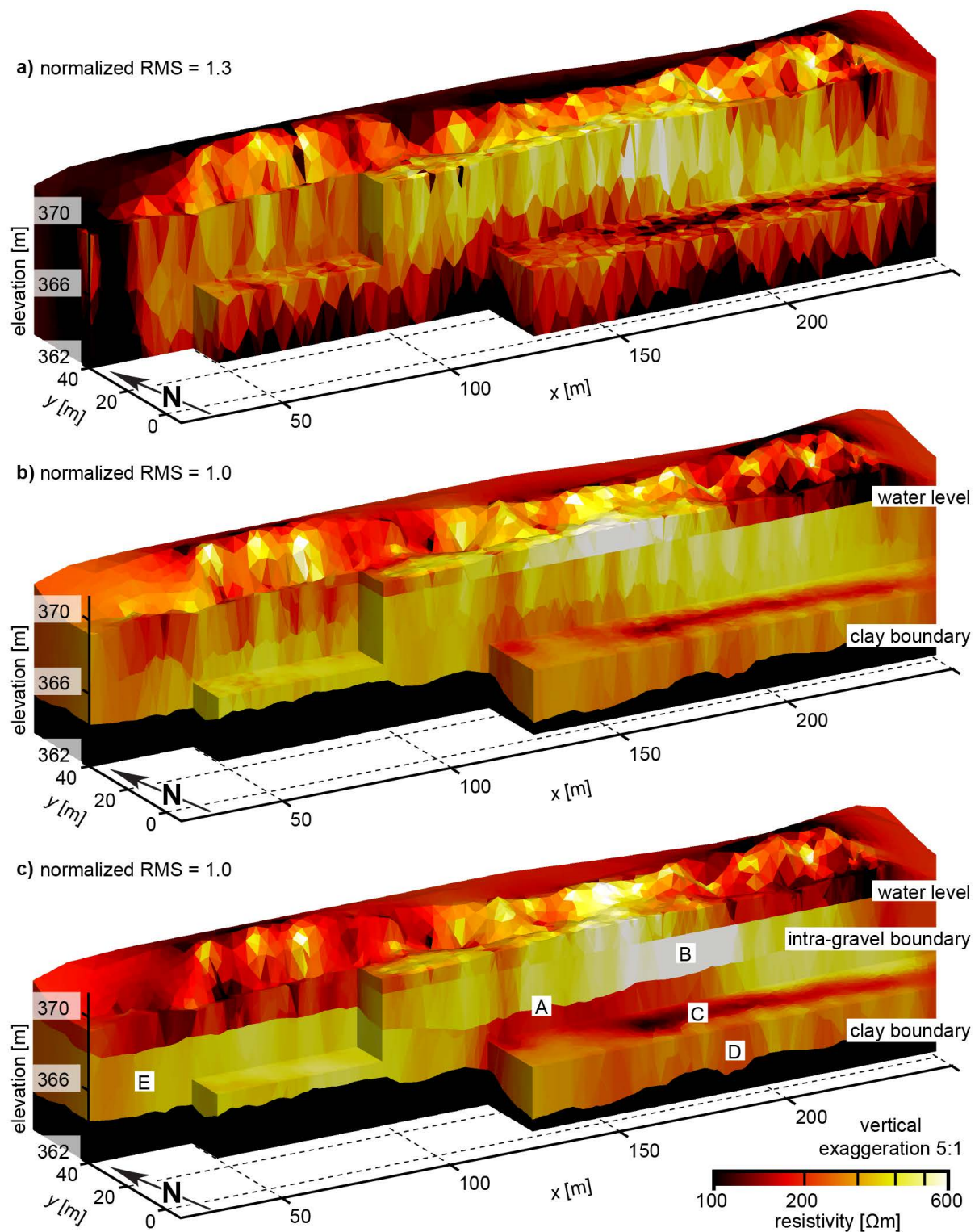


Figure 5.8. ERT models obtained using the inversion meshes shown in (a) Figure 5.7a, (b) Figure 5.7c and (c) Figure 5.7e. The view is the same as in Figure 5.5. Note that the colour scale is saturated at $100 \Omega\text{m}$ to focus on the resistivity variations within the aquifer. The deepest layer in (b) and (c) has a resistivity of $\rho \sim 30 \Omega\text{m}$. For a discussion of A-E, see text.

5.5 INTERPRETATION AND DISCUSSION

We know from the piezometer installations that the gravel aquifer is underlain by a thick clay aquitard at 5 - 6 m depth [Vogt *et al.*, 2010b]. Our GPR data have allowed us to map this interface throughout the surveyed part of the aquifer (Figure 5.5b). However, depth errors occur as a consequence of the constant GPR velocity model assumed for the aquifer. Velocities within the aquifer vary by about $\pm 10\%$ according to the CMP analyses and crosshole GPR measurements at a neighboring site (Chapter 2), which leads to corresponding relative depth errors in the same range. The aquifer is thickest in the middle of the gravel bar, becoming thinner in the western ($x < 100$ m) part. The interface within the gravel is relatively flat in the eastern ($x > 150$ m) part, deepening towards the middle and approaching the surface at the western end.

The ERT model obtained by incorporating all interfaces in the inversion (Figure 5.8c) allows us to interpret resistivity variations within the aquifer, which is hardly possible otherwise (Figure 5.8a and b). Resistivities in the unsaturated zone are largely controlled by the soil cover. We interpret high resistivities ($\rho > 500 \Omega\text{m}$) as indicative of unsaturated relatively clean gravels and low resistivities (as low as $60 \Omega\text{m}$) as sandy loam. The relatively high resistivity of $\rho > 400 \Omega\text{m}$ in the upper part of the aquifer at B in Figure 5.8c indicates clean gravel with a relatively low porosity of $\sim 20\%$ (Chapter 2). We suspect that this region of the aquifer comprises sediments deposited after channelization of the river. This hypothesis is supported by the GPR data, which maps strong horizontal layering in this region and a lateral change towards more heterogeneous depositional patterns from the old river embankment (Figure 5.2a) towards the north (Figure 5.6). Low resistivities coincide with the old river embankments (C in Figure 5.8c). The source of these low resistivities is unclear, but they may be due to an increased deposition of fines during the period of channelized flow, which may mean that the restored site still has an unnatural flow barrier with implications for hyporheic processes.

The resistivities and GPR coherencies vary in the lower part of the aquifer (Figure 5.8c). Low resistivities ($\sim 200 \Omega\text{m}$) indicating higher porosities and higher clay content are found at the eastern ($x > 150$ m) end (D in Figure 5.8c), whereas intermediate resistivities ($\sim 300 \Omega\text{m}$) are seen at the western end (E in Figure 5.8c). Although these features can be seen in Figure 5.8b, they are imaged more clearly in Figure 5.8c. The low resistivities coincide with low GPR coherency, whereas intermediate and high resistivities coincide with high GPR coherency (compare Figures 5.5c and 5.8c). We interpret regions of high resistivity and high

coherency as clean gravel with strong horizontal layering and low resistivity and low coherency within the aquifer in terms of more heterogeneous deposits consisting of sequences of fine and coarse sediments. The low resistivities are mainly caused by the fine materials found in some of the lower sub-units [Heinz *et al.*, 2003]. We suggest that this region consists of sediments that were deposited before the channelization of the river.

The two regions of the gravel aquifer with differing reflection patterns and resistivity are likely to have different hydrogeological properties. The upper part is expected to be less heterogeneous and to have intermediate hydraulic conductivities compared to the end members of the more heterogeneous units in the deeper part [Heinz *et al.*, 2003]. Even though a quantitative hydrogeological interpretation is not feasible at this stage, our models are useful for developing a conceptual hydrogeological model. We plan to investigate groundwater flow patterns at the site by performing a saline tracer test to be monitored with 3-D ERT.

One important challenge in hydrogeophysics is to create quantitative hydrogeological models at high resolution on scales that are larger than the 5-10 m borehole separation typically employed in quantitative hydrogeophysical studies [Hubbard and Linde, 2011]. We find that the estimated range of resistivities in the aquifer is very similar to those obtained using crosshole ERT within a suite of boreholes located 15 km upstream adjacent to an unrestored section of the river [Chapters 2 and 4; Coscia *et al.*, 2011a]. Since the depositional environments are very similar at the two sites, it is possible that any field-scale relationship between resistivity and porosity/hydraulic conductivity established at the unrestored upstream site could be applicable at the restored site, but for a model volume that is 10-100 times larger.

It appears that the combination of joint inversions of smaller scale crosshole data (Chapter 2) with constrained inversions of larger scale surface-based data is a promising approach for improving the information content extracted from surface-based geophysical data at intermediate scales. The combination of at least two complementary geophysical data types is important. Consider the lower conductive part of the aquifer in the eastern area. The GPR image supplies details on the heterogeneous sedimentary units, whereas the ERT model provides upscaled effective bulk properties.

5.6 CONCLUSIONS

We have acquired surface-based 3-D GPR reflection and ERT data to characterize an alluvial aquifer underlying a gravel bar at a restored river section. The GPR data imaged undulations in the thickness of the aquifer and delineated two layers in the aquifer with different reflection patterns. Whereas the upper part of the gravel aquifer appeared to be only weakly heterogeneous and displays subhorizontal layering, the deeper part is moderately heterogeneous and displays complex fluvial features. By including GPR reflection interfaces corresponding to the base and internal layers of the aquifer in the ERT mesh and by disconnecting the regularization across these interfaces, we were able to improve markedly the resulting ERT models. The standard and constrained inversion results illustrated to what extent ERT data constrain features, particularly at depth, and how important it is to (wherever possible) perform constrained inversions to obtain quantitative information on resistivity structure and properties. Models that incorporated the GPR interfaces revealed resistivity variations within the aquifer that were not resolved in the unconstrained model.

The final GPR-constrained ERT model has moderate resistivities in the upper part of the aquifer indicating rather low porosities and negligible clay content. In the same region, the GPR coherency is very high. In the lower part of the aquifer, the electrical resistivity is significantly lower with values decreasing in the x -direction. The GPR coherency shows a remarkably similar pattern.

The lower part of the aquifer is expected to have a highly variable hydraulic conductivity. The magnitude of the upscaled conductivity in this zone is likely to be dependent on the connectivity of the more permeable deposits. With respect to river restoration, we suggest that the upper part of the aquifer consists of gravel sheets that were probably rearranged by the river as a result of channelization at the end of the 19th century. Furthermore, we find that a low-resistivity feature, probably indicating enhanced clay-content, coincides with the location of the former river embankment. Regardless of origin, it appears that 100 years of a channelized flow regime has had a strong and persistent influence on the aquifer structure.

6 IMAGING SALT TRACER TRANSPORT BY MEANS OF 3-D ERT MONITORING

Submitted to *Water Resources Research*:

Doetsch, J., Linde, N., Vogt, T., Binley, B.,
and Green, A. G., 2011. Imaging salt tracer
transport in a restored riparian groundwater
system by means of 3-D ERT monitoring.

ABSTRACT

A prerequisite for any groundwater transport modeling is knowledge of the subsurface flow pathways within the system under investigation. Studying riparian groundwater dynamics is challenging due to temporal and spatial heterogeneity. We monitor the transport of a salt tracer plume under natural gradient conditions within a riparian groundwater system adjacent to the Thur River in northeastern Switzerland using 3-D surface electrical resistance tomography (ERT). Our ERT time-lapse images define the plume's shape, flow direction, and velocity. These images allow the movement of the plume to be followed for 35 m, at which point it leaves the survey area. Although the hydraulic head is only 1.43 ‰, the ERT time-lapse images demonstrate that the plume's center of mass and its front propagate with velocities of 2×10^{-4} m/s and $>5 \times 10^{-4}$ m/s, respectively. These velocities are compatible with monitoring data in observation boreholes 5 m from the injection borehole. Sensors in observation boreholes further downstream did not detect the plume. Comparison of the ERT time-lapse images with a groundwater transport model and time-lapse inversions of associated synthetic ERT data indicate that the movement of the plume can be described for the first 6 h after salt tracer injection by a uniform flow model with a hydraulic conductivity of 4×10^{-2} m/s. At later times, heterogeneity of the gravel aquifer has a strong influence on the plume's direction and velocity.

6.1 INTRODUCTION

Reliable information on subsurface flow pathways is essential for the development of groundwater transport models. For reactive transport, it is also necessary to have knowledge of solute residence times for determining exchanges, losses, and gains along flow pathways. The utility of traditional hydrological techniques (e.g., borehole sampling) for characterizing pathways is generally limited, because of uncertainties in the measured hydraulic gradients and complex subsurface heterogeneity. Although solute tracer tests offer means to establish pathways through multi-borehole sampling, the significant number of sampling boreholes needed to outline tracer plumes under natural flow conditions make such approaches excessively invasive and expensive and the risk of tracer bypassing still exists [e.g., *Boggs and Adams*, 1992]. Geophysical monitoring of tracers may be a useful complement to conventional tracer tests, offering larger scale integrated measurements of solute mass in a minimally invasive manner. The results from such measurements may help target more direct conventional sampling.

Studying riparian groundwater dynamics is challenging due to temporal and spatial variations of flux exchanges between rivers and groundwater over a wide range of scales [Woessner, 2000]. Temporal variations are caused by changing hydrological conditions like rising or decreasing river level [Keery *et al.*, 2007; Vogt *et al.*, 2010a], whereas spatial variations result from riverbed morphology and curvature and laterally varying hydraulic conductivities [e.g., Storey *et al.*, 2003; Cardenas *et al.*, 2004]. The hydraulic conductivity of fluvial sediments may range over several orders of magnitude, with the highest conductivity zones dominating the flow patterns. For example, highly conductive open framework gravels in alpine to pre-alpine aquifers provide preferred flow paths for water, solutes, and aquatic biota [Huggenberger *et al.*, 1998]. The impact of solute transport after river water infiltration on biogeochemical processes in the hyporheic and riparian zones are well recognized [Bencala, 1984; Stanford and Ward, 1988]. This implies that having trustworthy information on the groundwater flow path also allows groundwater sampling for investigating biogeochemical processes in the hyporheic and riparian zones to be optimally located.

For the 1 – 100 m investigation scale of most recent studies of river - groundwater interactions, reliable field methods for estimating groundwater flow paths and velocities are limited to artificial tracer tests monitored in observation boreholes. Although natural fluctuations of physical variables like the temperature and electrical conductivity of water [e.g., Hoehn and Cirpka, 2006; Cirpka *et al.*, 2007; Constantz, 2008; Vogt *et al.*, 2010b] provide the possibility of quantifying river - groundwater interactions via their travel times, the flow directions and velocities are usually not well determined. Appropriately designed geophysical experiments may improve estimates of these properties [e.g., Ward *et al.*, 2010].

Common geophysical techniques for monitoring solute transport in groundwater systems are borehole and crosshole ground-penetrating radar (GPR) [e.g., Binley *et al.*, 2001; Day-Lewis *et al.*, 2003; Dorn *et al.*, 2011] and surface and crosshole electrical resistance tomography (ERT) [e.g., Slater *et al.*, 2000; Binley *et al.*, 2002b; Kemna *et al.*, 2002; Michot *et al.*, 2003; Singha and Gorelick, 2005; Cassiani *et al.*, 2006; Miller *et al.*, 2008; Ward *et al.*, 2010; Wilkinson *et al.*, 2010; Coscia *et al.*, 2011a]. Surface ERT monitoring has the advantage of being largely automated and non-intrusive, because electrodes only penetrate ~20 cm below the surface and thus have insignificant influence on groundwater flow. Although boreholes for crosshole surveys and hydrological measurements generally do not influence groundwater flow, vertical flow through open or screened boreholes could have an important effect in highly heterogeneous or stratified media [e.g., Butler *et al.*, 2009].

Geophysical monitoring of salt tracer tests has been successfully performed in the laboratory [Slater *et al.*, 2000] and in the field using 2-D and 3-D crosshole techniques [Singha and Gorelick, 2005; Wilkinson *et al.*, 2010]. Studies in which a salt tracer has been monitored from the surface have so far been restricted to measurements along single or several 2-D lines [Cassiani *et al.*, 2006; Monego *et al.*, 2010; Ward *et al.*, 2010; Cardenas and Markowski, 2011]. To map the positions and full extents of tracer plumes, measurements over time and inversion in 3-D are necessary.

Here, we investigate groundwater flow direction and velocity and hydraulic conductivity using 3-D surface ERT for tracking a salt tracer. The general goal is to provide an improved understanding of groundwater transport in river corridors, and the specific target is a dynamic riparian groundwater system that includes a gravel aquifer adjacent to a restored river bed. Previous conventional tracer tests at our study site had been unsuccessful, largely because of very low tracer recovery rates in the observation boreholes. Our experiment involves injecting a salt tracer into the gravel aquifer and then monitoring the evolution of the tracer plume using surface ERT and continuous measurements of hydraulic head and water electrical resistivity in a number of observation boreholes. We invert the ERT time-lapse data by solving for changes in subsurface resistivity relative to baseline conditions. The time evolution of the tracer plume resolved by the time-lapse resistivity tomograms is compared to predictions based on a simple groundwater transport model. This model is defined by parameters determined from previous hydrological investigations at the study site, the pressure gradient obtained from hydraulic head measurements, and a single hydraulic conductivity value calibrated using the propagation velocity of the tracer plume resolved by the time-lapse resistivity tomograms. Synthetic ERT data based on the groundwater transport model are then inverted in the same fashion as the field data. Finally, we compare the time-lapse inversion results of the field and synthetic ERT data to assess the resolution capabilities of the surface ERT time-lapse method as a 3-D monitoring tool and evaluate the effects of heterogeneity on transport in the subsurface.

6.2 OUTLINE OF THE METHODOLOGY

Our approach to aquifer characterization through salt tracer monitoring with ERT is summarized in Figure 6.1. The core of the approach is outlined in the central column. It includes survey design, data acquisition, and time-lapse inversion of the ERT data. The right column illustrates how groundwater transport modeling is used to evaluate the ERT inversion

results, whereas the left column emphasizes the use of independent constraints to parameterize the ERT inversion mesh (Chapter 5).

A prerequisite for this approach to work was a basic understanding of the geological, hydrogeological, and geophysical characteristics of our study site. Prior geophysical surveys provided key site-relevant information before planning the labor-intensive monitoring. In particular, the static ERT data set discussed in Chapter 5 was vital for designing the ERT monitoring layout, because it helped to predict the error sources, data quality, and resolution, which strongly depended on the ERT sensitivities and thus the subsurface resistivity distribution. The results of previous geological and hydrological studies by *Vogt et al.* [2010b; 2010a] and [*Schneider et al.*, 2011] helped to define an appropriate groundwater transport model.

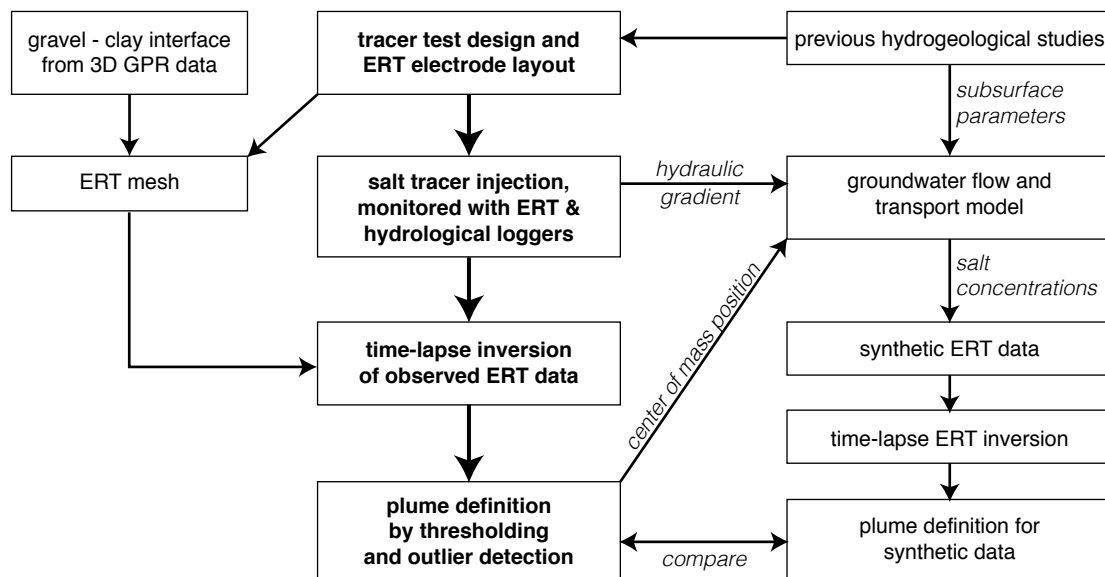


Figure 6.1. Workflow for ERT monitoring a salt tracer injection test and analyzing the recorded data. Results data analysis are compared to results of a synthetic study based on groundwater simulations and petrophysical transformations.

6.2.1 ERT time-lapse inversion

An adequate mesh and suitable regularization are crucial for both static and time-lapse ERT inversions [e.g., *Günther et al.*, 2006]. Unstructured (e.g., tetrahedral) finite-element meshes offer the possibility to incorporate surface topography and known subsurface structures; Chapter 5 shows that including GPR-defined interfaces as constraints in the ERT mesh generation is necessary to produce realistic resistivity models at our study site.

We express a data set \mathbf{d}_i recorded at time step i as:

$$\mathbf{d}_i = g(\mathbf{m}_i) + \boldsymbol{\varepsilon}_s + \boldsymbol{\varepsilon}_n + \boldsymbol{\varepsilon}_{ri}, \quad (6.1)$$

where g is the forward operator that calculates the response of the model \mathbf{m}_i with errors being distributed as static $\boldsymbol{\varepsilon}_s$, numerical $\boldsymbol{\varepsilon}_n$, and random $\boldsymbol{\varepsilon}_{ri}$ contributions. We assume $\boldsymbol{\varepsilon}_s$ to be the same for all time-lapse data. Numerical errors $\boldsymbol{\varepsilon}_n$ caused by imperfections in the forward operator are similar for all resistivity models as long as the models do not change significantly during the time-lapse inversion process. Random observational errors $\boldsymbol{\varepsilon}_{ri}$ vary between time-lapse data sets. Using the same electrodes installed for the entire duration of an experiment, it is usually reasonable to assume that $|\boldsymbol{\varepsilon}_s + \boldsymbol{\varepsilon}_n|_2 \gg |\boldsymbol{\varepsilon}_{ri}|_2$. Removing the effects of $\boldsymbol{\varepsilon}_s$ and $\boldsymbol{\varepsilon}_n$ from the input data is therefore desirable when inverting for resistivity changes.

Daily et al. [1992] introduced a ratio inversion, in which the ratios of the data \mathbf{d}_i and \mathbf{d}_0 acquired during and just prior to a time-lapse experiment are inverted:

$$\tilde{\mathbf{d}}_i = \frac{\mathbf{d}_i}{\mathbf{d}_0} g(\mathbf{m}_{bg}), \quad (6.2)$$

where \mathbf{m}_{bg} is a baseline model. We use \mathbf{d}_0 to invert for the baseline model. In the time-lapse inversion, we solve for updates to this model using the logarithms of $\tilde{\mathbf{d}}_i$. This approach practically removes the effects of $\boldsymbol{\varepsilon}_s$ and $\boldsymbol{\varepsilon}_n$ and ensures reliable sensitivity patterns.

6.2.2 ERT resolution assessment

Standard formulations of ERT resolution [e.g., *Oldenburg and Li, 1999; Friedel, 2003*] are inappropriate for assessing the resolution of subsurface resistivity changes from the time-lapse inversions alone. We introduce an approach (right column in Figure 6.1), in which resolution is assessed using a groundwater transport model that is partly based on the time-lapse images. The groundwater transport model is used to create synthetic ERT data by assuming a plausible petrophysical relationship between salinity and bulk resistivity and by contaminating the simulated data with random noise. These synthetic data are then inverted using the same procedures and parameters as employed to invert the field data. Comparisons between the two inversion results highlight qualitative differences between the ERT-inferred transport processes and the simplified groundwater transport model. Furthermore, by employing a homogeneous groundwater transport model, the similarities in the two inversion results help identify apparent homogeneous transport behavior, whereas the differences help identify the influence of heterogeneity.

6.3 THUR RIVER STUDY SITE

The Thur River is the largest Swiss river without natural or artificial reservoirs. It is a perialpine tributary of the River Rhine with a catchment area of $\sim 1750 \text{ km}^2$. Water level and discharge variations in the Thur are similar to those of unregulated alpine rivers with low, medium, and maximum peak discharges of roughly 3, 35, and $1000 \text{ m}^3/\text{s}$, respectively [BAFU, 2010]). Like many other rivers, the meandering Thur was channelized towards the end of the 19th century for flood protection and to gain arable land. In an attempt to combine flood protection with ecological objectives, a more natural environment was restored along a 2.5 km long reach of the Thur starting in 2000. The effects of this restoration effort are currently being investigated through a large multidisciplinary research initiative [Schneider *et al.*, 2011].

The riverbed morphology is constantly changing, especially in response to high discharge events at the restored field site (Figure 6.2). Most research is concentrated on a gravelbar on the northern side of the river and in an adjacent woodland, within which numerous observation boreholes have been instrumented. Sensors and loggers $\sim 5 \text{ m}$ below the groundwater table in the seven boreholes of Figure 6.2 provide quasi-continuous estimates of groundwater level, temperature, pressure, and resistivity [Schneider *et al.*, 2011]. Sensors and loggers are also installed $\sim 2 \text{ m}$ below the groundwater table in one of the boreholes (R073) and at a river station. The site is equipped with a meteorological station. Changes in river morphology are continuously monitored by cameras mounted on two towers [Pasquale *et al.*, 2011].

Information from the boreholes and surface and crosshole geophysical surveys reveals a three-layered geological-hydrological sequence at the study site. An upper variably thick layer of largely unsaturated topsoil and gravel overlies a 5 - 6 m thick gravel aquifer that is bounded below by a clay-rich aquitard.

The river is well connected to the groundwater system, such that river level fluctuations produce rapid changes to the groundwater table; the main groundwater recharge at the study site originates from continuous river water infiltration. Seepage velocities in the river bed vary between 1.5 and $4.0 \times 10^{-5} \text{ m/s}$ [Vogt *et al.*, 2010a] and groundwater flow velocities in the riparian zone are estimated to be about 10^{-4} m/s [Vogt *et al.*, 2010b]. According to slug tests in fully screened boreholes, the hydraulic conductivity of the aquifer has a geometric mean of $3.1 \times 10^{-3} \text{ m/s}$ [Schneider *et al.*, 2011]. The geology around the borehole used in this

study for tracer injection has a hydraulic conductivity of $5.8 \pm 2.9 \times 10^{-3}$ m/s, with the highest values in the middle and the lowest values at the bottom of the aquifer.

Extensive surface 3-D ERT and 3-D GPR measurements have been made on the gravelbar (Chapter 5). They extended from the region of the tracer injection borehole to ~ 240 m downstream. Figure 6.3a displays a vertical slice through the 3-D GPR volume that clearly delineates the base of the aquifer at 5 - 6 m depth. This gravel - clay boundary, which was mapped beneath the entire GPR survey area, was included in the mesh generation for the ERT inversions.

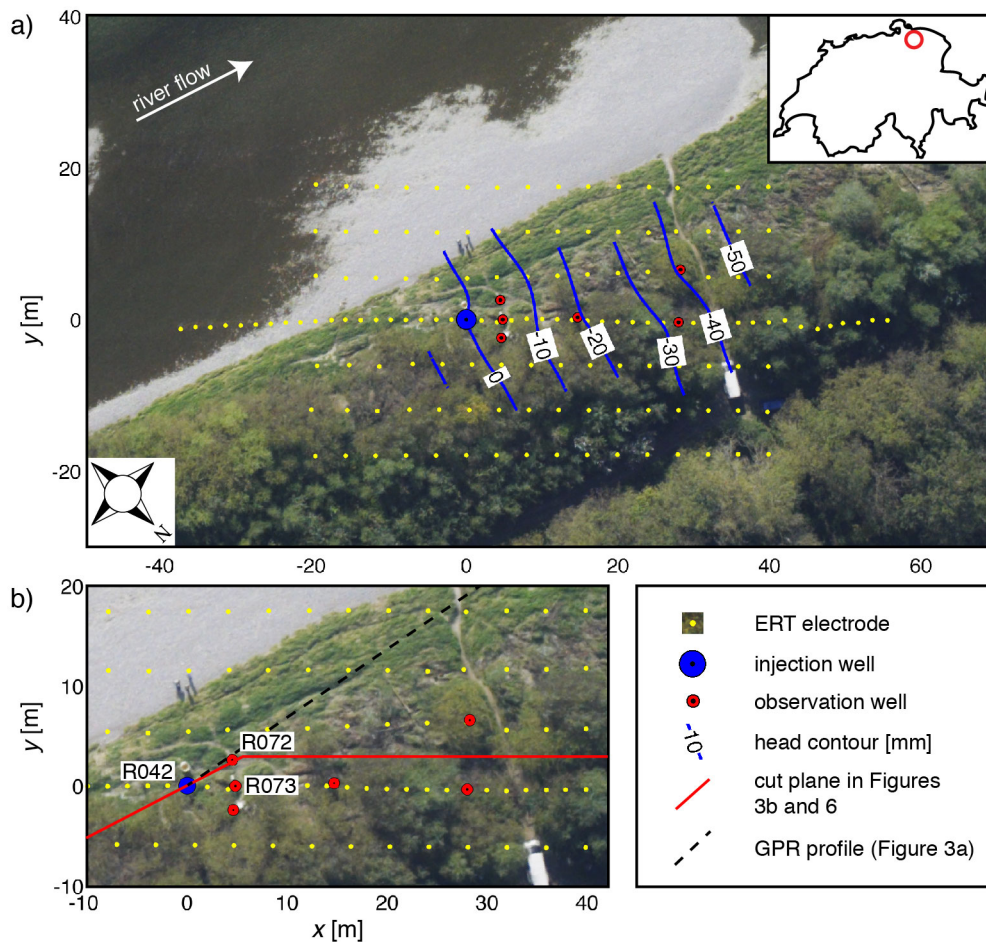


Figure 6.2. (a) Aerial Photograph of the Thur River bank (northeastern Switzerland, see inset) showing the injection (blue circle) and observation boreholes (red circles), ERT electrodes (yellow dots) and hydraulic head variation (in mm) with respect to the injection borehole. The head contours are interpolated from measurements in the seven boreholes. (b) Zoomed area of part of (a) showing the ERT model planes in Figures 6.3b and 6.6 (solid red lines) and GPR profile (dashed black line) in Figure 3a. The aerial photograph was taken at the time of the tracer test.

6.4 SALT TRACER EXPERIMENT

6.4.1 Tracer injection

The boreholes for the injection and observations were chosen to be close to the river where previous studies had been conducted and future biogeochemical and hydrogeological studies are planned [e.g., *Samaritani et al.*, 2011]. Since the main purpose of the tracer test was to determine undisturbed groundwater flow direction and velocity, there was no pumping in the observation boreholes. The injection borehole R042 (see Figure 6.2b) was located ~5 m from the main river channel and ~15 m from the flowing river at the time of the tracer test. For all relevant figures in this contribution, the coordinate system has its origin at borehole R042 (SwissGrid coordinates 700467.86 / 271981.94) and its x -axis approximately parallel to the groundwater flow direction (rotated -45° from North).

Measurements made in the seven boreholes (Figure 6.2) just before tracer injection were used to estimate the hydraulic head field. The interpolated hydraulic head distribution with respect to borehole R042 is presented in Figure 6.2a. The hydraulic head gradient inferred from these measurements is 1.43 ‰ with a direction subparallel to the river. The Thur River, which usually has strongly varying discharge and water levels, was very stable during the ERT monitoring experiment (11 – 13 October 2010). Figure 6.4a demonstrates that water level fluctuations during the entire monitoring experiment were minor. For the 16 h period that was the focus of our interpretation (gray shaded area in Figure 6.4a), the variation in river water level was a mere ± 2 cm. Figure 6.4b demonstrates that the electrical resistivity of the river water was also relatively stable during this period. These minor changes in river water level and resistivity are not expected to have significantly influenced the groundwater flow and geophysical measurements during the time-lapse experiment.

A total of 500 l of saline water containing 18 kg of dissolved salt (36 g/l concentration with electrical conductivity of ~60 mS/cm or resistivity of ~0.17 Ω m) was injected into borehole R042 for 20 min starting at 15:33 on 11 October 2010. While being injected, the tracer was thoroughly mixed over the entire fully penetrating screen.

To relate water resistivities measured in boreholes to salt concentration as the tracer plume progressed, a linear calibration relationship was determined in a laboratory using tracer-free water samples from the boreholes and the same salt and sensors as used in the field experiment.

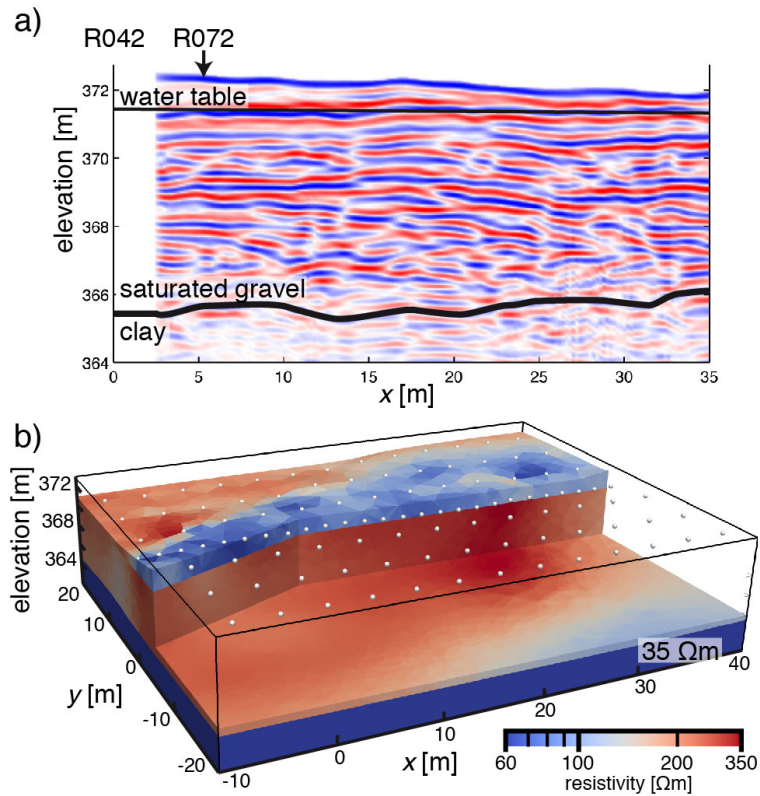


Figure 6.3. (a) GPR profile extending from the injection borehole in the direction of the initial tracer movement. The profile is extracted from the data in Chapter 5. (b) Resistivity model obtained from ERT inversion of data acquired prior to tracer injection. Dots at the surface are electrode positions. Resistivities in the unsaturated upper zone vary from 60 – 300 Ωm (blue to red in the model) are mostly a function of water and clay content of the soil. The saturated gravel aquifer with resistivities of 200 – 350 Ωm (uniformly red) is underlain by a clay aquitard with resistivity of ~ 35 Ωm (dark blue).

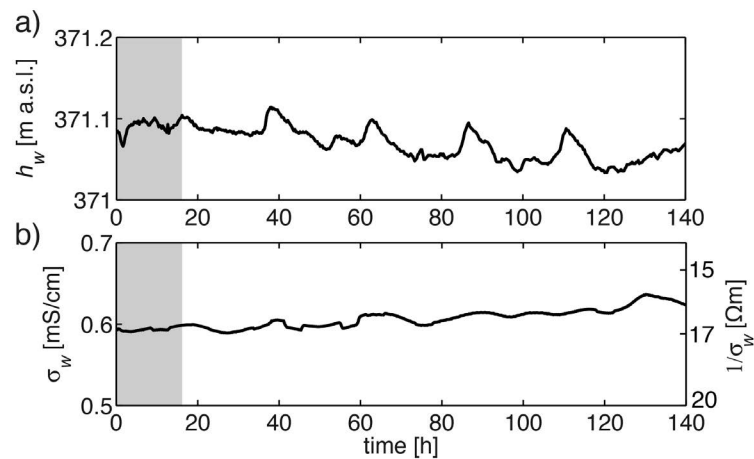


Figure 6.4. (a) River stage (water level) h_w and (b) electrical conductivity of the river water σ_w during the tracer test. Variations of h_w and σ_w are minor during the experiment, especially during the first 16 h that are used for the interpretation (gray shaded area).

6.4.2 ERT layout and monitoring

A total of 144 ERT electrodes were deployed (Figure 6.2) for the full duration of the monitoring experiment. This layout was designed to image the plume close to the injection borehole and track plume movement for ~ 30 m. It included 16×7 electrodes installed on a 4×6 m grid. Electrode spacing was decreased to 2 m along the extended central line of the grid (Figure 6.2a). The axis of the electrode grid was oriented parallel to the anticipated groundwater flow direction. A switching box individually addressed the electrodes, which were connected to a 10-channel resistivity instrument via multicore cables. Measurements were made using >3000 four-electrode configurations that included dipole-dipole, equatorial dipole-dipole, Wenner, and gradient configurations [Zonge *et al.*, 2005]. Good 3-D coverage was ensured by measuring all configurations along the two perpendicular directions of the electrode grid.

ERT monitoring was initiated 20 h before tracer injection to determine the influence of natural variations on the data. These measurements showed that the acquisition repeatability was very high and natural variations within the 20 h period were $<1\%$ for more than 90% of the ERT configurations. Monitoring was stopped during the injection and resumed once the tracer had been injected. The data set acquired just before tracer injection was used as the baseline data \mathbf{d}_0 for the time-lapse inversions. The acquisition time for each complete suite of >3000 measurements was ~ 45 min. We collected one suite of data per hour for the first 7 h hours and one suite approximately every 2.25 h thereafter. A total of 26 suites of data were recorded during roughly 50 h of post-injection recording. To quantify measurement errors, two complete reciprocal data sets were also collected, one directly before tracer injection and one at the end of the ERT monitoring period.

6.4.3 Preprocessing the ERT data

An apparent resistivity time series of 27 values (baseline plus post-injection data) was constructed for each of the electrode configurations. After rejecting data with high geometrical factors (>5000) and data affected by poor electrode coupling and excessive levels of noise, a total of 2461 ERT time series was available for further analysis. The static error ε_s associated with each configuration was determined from the two reciprocal data sets. A baseline error of 3% was then added to the reciprocal errors. These error estimates were used for the initial baseline ERT inversion using robust data reweighting [Claerbout and Muir, 1973], which adapts the estimated errors for data that do not agree well with the model

predictions. The resulting error estimates used for the baseline ERT inversion had a median value of 3.8%.

To interpolate data to identical times for each electrode configuration, a spline algorithm was applied to each smoothly varying time series. This process effectively compensated for subsurface resistivity changes during the ~45 minute acquisition periods. For most ERT monitoring experiments, the 1 - 2 h required to record each suite of data is short compared to the movement of the tracer (some days), thus justifying the common assumption that significant changes do not occur during data acquisition [e.g., *Binley et al.*, 2002b; *Kemna et al.*, 2002; *Cassiani et al.*, 2006; *Wilkinson et al.*, 2010; Chapter 3]. For experiments in fast dynamic environments, such as ours, the timing of each measurement has to be taken into account [*Day-Lewis et al.*, 2003].

6.5 ERT INVERSION

6.5.1 ERT meshes and inversion of baseline data

A tetrahedral mesh was used for the inversion of the ERT data. It included surface topography, the groundwater table, and the GPR-defined gravel - clay boundary at the base of the aquifer. No smoothing was imposed across these interfaces during the inversion. As described in Chapter 5, I found that including these interfaces, especially the gravel - clay boundary, was crucial for obtaining meaningful resistivity models of the subsurface at this site. The ERT inversion model consisted of 197,117 cells with a maximum 0.8 m³ cell volume. This mesh was extended and refined for the forward calculations, such that the forward mesh comprised 1,805,464 cells. Singularity removal [*Lowry et al.*, 1989; *Blome et al.*, 2009] was used for the forward calculations.

The baseline data set was inverted using the finite-element modeling and inversion code BERT based on the GIMLi library [*Günther et al.*, 2006; www.resistivity.net]. The starting model had a homogeneous resistivity of 200 Ωm above the gravel - clay boundary and 20 Ωm below; tests with homogeneous starting models gave very similar results. A horizontal anisotropy factor of two was assumed for the smoothness constraints to honor the layered structures imaged by the GPR survey. The inversion converged to the estimated error level after 3 iterations using a smoothing strength of $\lambda = 50$ (see *Günther et al.* [2006] and *Günther and Rücker* [2006] for details on the regularization used in BERT). In the final model (Figure 6.3b), the 60 – 300 Ωm resistivities of the unsaturated zone appear to be a function of water

and clay content. The resistivity of the saturated gravel aquifer is 200 – 350 Ωm and that of the clay aquitard is $\sim 35 \Omega\text{m}$.

6.5.2 ERT time-lapse inversion

For the time-lapse inversions of the ratios of the 26 post-injection apparent resistivity time series $\tilde{\mathbf{d}}_i$, (Equation 6.2), the model determined from inverting the pre-injection time series \mathbf{d}_0 was used as the starting and baseline models. The roughness regularization operator was chosen to be isotropic with a strength of $\lambda = 50$, and the time varying errors were taken to be $|\boldsymbol{\epsilon}_{ri}|_2 = |\boldsymbol{\epsilon}_s + \boldsymbol{\epsilon}_n|_2/14$. Other error levels were tested, but 1/14 of the non-time-related errors provided the best compromise between a well resolved plume and limited inversion artifacts.

We define the salt tracer plume in the resultant time-lapse models by a 3% decrease of resistivity with respect to the baseline model. The 3-D representation of the plume in Figure 6.5 clearly shows its appearance around the borehole ($x = y = 0$) 1 h after salt injection began and its subsequent evolution 6, 16, and 44 h later. For the first 6 h, the plume spreads broadly in a general 25° direction relative to the x -axis (compare Figure 6.5a and b). From a detailed study of intermediate time steps, we find that its center of mass moves with a velocity of 2×10^{-4} m/s and its front moves more than twice as fast at 5×10^{-4} m/s. After ~ 6 h, the main mass of the plume slows down while its front continues moving at a relatively high rate. A preferential flow path along which the plume rapidly propagates is clearly seen at ~ 16 h in Figure 6.5c. In contrast to movements during the first 6 h, the plume moves parallel to the x -axis at these later times. Shortly after 16 h, the front of the plume has moved ~ 35 m and then leaves the area covered by the electrode array. The $> 5 \times 10^{-4}$ m/s maximum velocity of the tracer is faster than anticipated from previous hydrological studies [Schneider *et al.*, 2011]. At times > 20 h, the region of preferential flow slowly shrinks and the remains of the plume within the electrode array are found moving very slowly near the base of the aquifer at > 40 h (Figure 6.5d).

The 2-D slices of relative resistivity change in Figure 6.6 indicate significant density effects associated with the salt tracer. The plume's center moves downwards with time, especially between 1 and 6 h after tracer injection (compare Figure 6.6a and b), but its front propagates with approximately equal resistivity over the entire depth of the aquifer (Figure 6.6c and d).

To calculate the effective mass recovery, the salt concentration in each cell representing the plume is estimated using the laboratory-based calibrated relationship between water

resistivity and salt concentration. The amount of salt in each cell is then calculated from its salt concentration and volume assuming a porosity of 25% and a formation factor of 10 (see Chapter 2 for a justification of these parameters). The resulting effective mass recovery varies from 10 - 25% depending on the time step. Clearly, the resistivity effects of much of the salt tracer have not been detected by the ERT inversions.

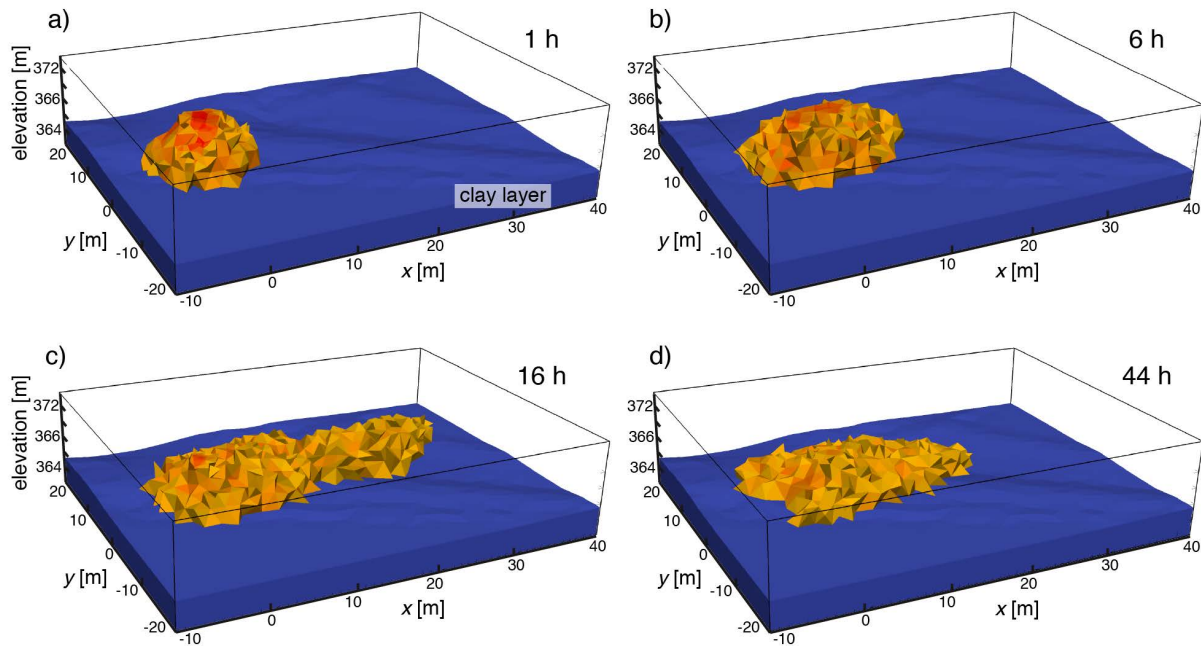


Figure 6.5 Tracer plume defined by a 3% decrease in resistivity threshold (a) 1 h, (b) 6 h, (c) 16 h and (d) 44 h after the start of the tracer injection. Baseline model of Figure 3b is used as a starting and reference model for the inversion.

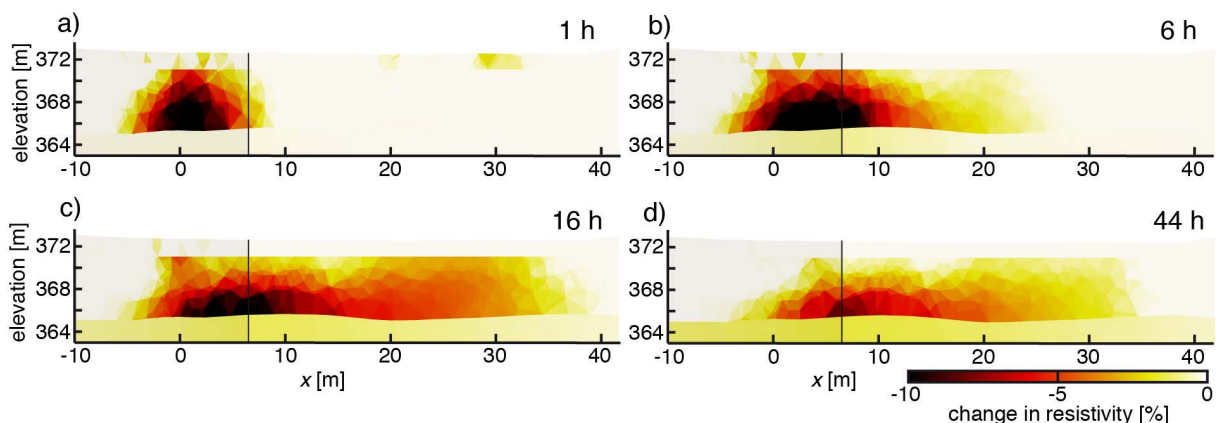


Figure 6.6 2-D slices of relative changes in resistivity (a) 1 h, (b) 6 h, (c) 16 h and (d) 44 h after start of the tracer injection. The change in resistivity is calculated with respect to the baseline model in Figure 3b. Position of the slice is shown in Figure 6.2b (red lines) and Figure 6.3b (face of the cut away). Vertical black line marks the position of borehole R072.

6.6 GROUNDWATER TRANSPORT MODELING

Our strategy for qualitatively assessing the resolution capabilities of the surface ERT time-lapse approach and for estimating the effects of subsurface hydrological heterogeneity is outlined in the right column of Figure 6.1. We begin by creating a groundwater transport model, the homogeneous hydraulic conductivity of which is calibrated using the ERT time-lapse images. The salt concentrations predicted by the groundwater transport model are converted to resistivities that are used to create synthetic ERT time-lapse data. These synthetic data are then inverted in the same way as the field data. Because of inherent resolution limitations in ERT, it is more meaningful to compare ERT time-lapse inversions of the field and simulated data than directly comparing the ERT time-lapse inversions of the field data with the groundwater transport model.

6.6.1 Groundwater transport model

For the groundwater transport model, we used SEAWAT, which couples the MODFLOW and MT3DMS codes to simulate variable-density saturated groundwater flow in three dimensions [Langevin *et al.*, 2008; Langevin, 2009]. We created a rectangular 3-D model of $171 \times 79 \times 33$ cells that extended $70 \times 50 \times 6.6$ m. Grid discretization in the vertical direction was uniformly 0.2 m and that in the horizontal direction was 0.1 m around the injection borehole and 0.2 m elsewhere. The upper two model layers could be either saturated or unsaturated during the simulation, whereas all other layers were fully saturated.

Based on the results of previous hydrogeological investigations at the study site, the initial horizontal hydraulic conductivity was set to 3.1×10^{-3} m/s, [Schneider *et al.*, 2011] and the anisotropy of hydraulic conductivity was taken to be 0.16 [Diem *et al.*, 2010]. Effective porosity was again set to 25%. Dispersivities were chosen to be 0.3, 0.03, and 0.003 m [c.f., Singha and Gorelick, 2005] in the longitudinal, transverse, and vertical directions, respectively. Fixed head boundary conditions were applied at the upstream and downstream ends of the model to sustain the hydraulic head gradient of 1.43 ‰ estimated from the head measurements before the tracer experiment, whereas no flow boundaries were imposed on the other sides.

The model was first run to steady state before simulating the salt injection and observation phases of the experiment. The flow equations were solved using a preconditioned conjugate-gradient solver with head and flow convergence criteria of 10^{-7} m and 10^{-7} m³/s, respectively. For the advective transport simulation, the ULTIMATE conservative difference

scheme [Leonard, 1991] and a generalized conjugate gradient solver with a 10^{-6} convergence criterion for relative concentrations were used. Automatic time stepping was employed for the combined flow and transport simulation. During the manual model calibration, hydraulic conductivity was adapted until the salt plume's center of mass in the hydrological simulations matched that of the ERT time-lapse results. The resulting calibrated horizontal hydraulic conductivity was 4×10^{-2} m/s, significantly higher than the initial 3.1×10^{-3} m/s value. Salt concentrations at the times of the ERT measurements were important outputs of the groundwater transport modeling.

6.6.2 Synthetic ERT data based on the groundwater transport modeling results

To create synthetic ERT data from the groundwater transport modeling results, the background electrical resistivity of the groundwater was set to the 20 Ω m value measured just prior to the experiment and the output salt concentrations were converted to water resistivities using the laboratory-derived relationship. For the aquifer region of the model, the water resistivities were converted to bulk resistivities using Archie's Law with a formation factor of 10 (Chapter 2). The bulk resistivities within the unsaturated zone and clay layer were adopted from the baseline model (Figure 6.3b). The bulk resistivity of the aquifer changed as the plume propagated, while the bulk resistivities of the unsaturated zone and clay layer did not vary.

Apparent resistivities are calculated for the time-varying resistivity models using the forward component of the BERT code [Günther *et al.*, 2006]. Field and simulated apparent resistivity time-series for four representative ERT measurement configurations are displayed in Figure 6.7. In general, the trends and general shapes of the observed time-series are captured well by the simulated data, especially considering that the groundwater transport model used to simulate the ERT data is not designed to mimic the ERT time-lapse results in detail (a single hydraulic conductivity is clearly insufficient for that). Although one might expect the apparent resistivities to decrease uniformly as the conductive salt tracer is injected, some apparent resistivities increase in response to the tracer, some decrease, and some change sign at different times after the injection. These variations are explained by the highly variable sensitivity pattern of the different electrode configurations and the inhomogeneous changes in resistivity caused by the tracer injection.

6.6.3 ERT inversion of synthetic data

After contaminating the simulated ERT data with Gaussian noise according to the error model described for the observed data (i.e., a time-invariant error level $|\boldsymbol{\epsilon}_s + \boldsymbol{\epsilon}_n|_2$ with a median of 3.8% and a time-varying error level of $|\boldsymbol{\epsilon}_r|_2 = |\boldsymbol{\epsilon}_s + \boldsymbol{\epsilon}_n|_2/14$), the resultant baseline and ERT time-lapse data were inverted in exactly the same manner and with exactly the same parameters as the observed data. Defining a plume by the same 3% threshold in apparent resistivity and calculating the salt mass within this plume allowed us to resolve 14-15 kg of the injected 18 kg.

6.7 RESULTS

6.7.1 Comparison of ERT inversion results and the groundwater transport modeling

The horizontal extent (black lines) and center of mass (blue dots) of the tracer plume in the (a) ERT time-lapse inversion results of the field data, (b) groundwater transport model, and (c) ERT time-lapse inversion results of the simulated data are presented in Figure 6.8. From the time-lapse inversion of the field data (Figure 6.8a), the plume is seen to disperse and propagate advectively from the injection borehole over a wide azimuth until about 6 h, after which it narrows and appears to flow along a relatively well-defined path. In the groundwater transport model (Figure 6.8b), the plume is elongated along a uniform flow direction. Because of general resolution limitations in ERT inversions [*Friedel, 2003*], it is difficult to compare ERT and groundwater transport modeling results (e.g., Figure 6.8a and b). Instead, it is more meaningful to compare the ERT time-lapse inversions of the field and simulated data (e.g., Figure 6.8a and c), because they are affected by the same resolution limitations. The shapes of the plumes in Figure 6.8a and c are similar for the first 6 h, but diverge at later times as the plume in Figure 6.8a starts to propagate along the well-defined path. Note how a portion of the tracer stays in the vicinity of the injection borehole for all times displayed in Figure 6.8a, whereas all of the tracer defined by the 3% resistivity threshold has moved away from the injection borehole by ~ 9 h in Figure 6.8c.

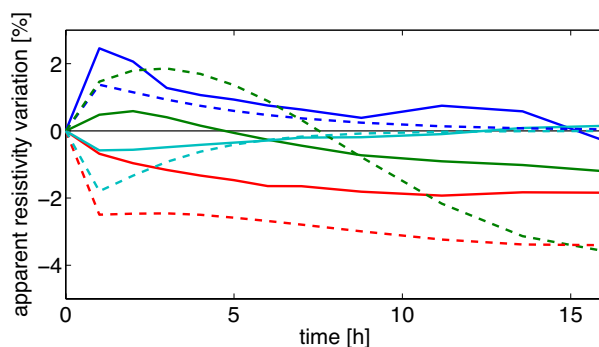


Figure 6.7. Sample apparent resistivity time-series for four selected ERT configurations. The solid line of each color is the measured time-series and the dashed line is the corresponding simulated time-series based on groundwater modeling.

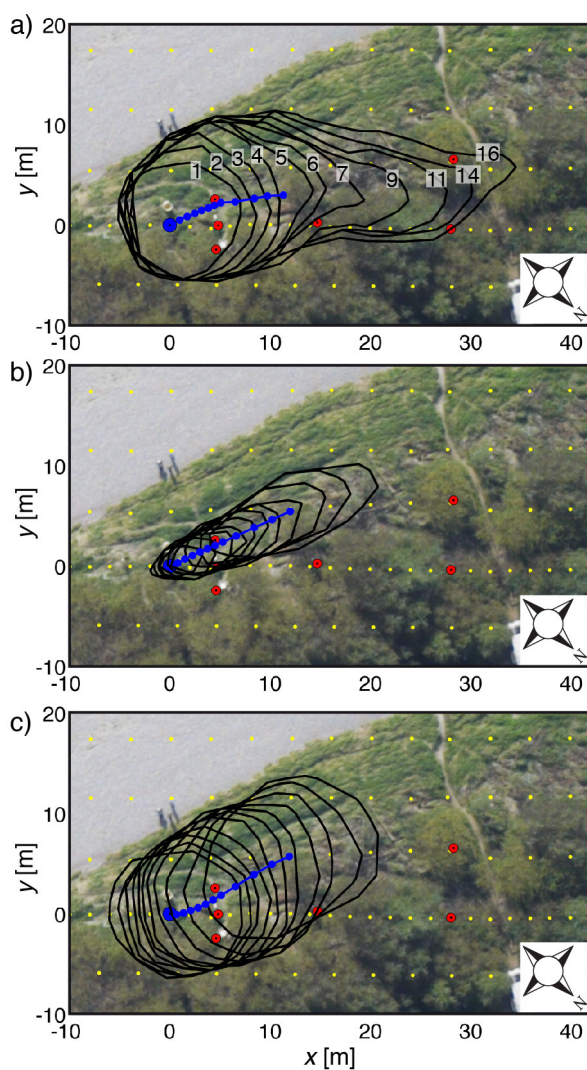


Figure 6.8. Plume outline from (a) ERT inversion of the field data, (b) groundwater modeling results and (c) ERT inversion of the synthetic data based on the groundwater simulation and petrophysical transformations. Black lines correspond to the plume defined by a 3% decrease in resistivity threshold for times 1, 2, 3, 4, 5, 6, 7, 9, 11, 14 and 16 h after the beginning of the tracer injection. Blue dots mark the center of mass.

6.7.2 Tracer breakthrough

Only two of the seven resistivity sensors installed in observations boreholes downgradient of the injection borehole detected groundwater resistivity changes that could be attributed to tracer arrival. The resistivity time-series recorded by these two closely spaced sensors, which were placed ~ 5 m below the groundwater table in boreholes located ~ 5 m from the injection borehole (Figure 6.2b), were converted to salt concentrations using the laboratory-determined calibration relationship. The resulting tracer breakthrough curves in Figure 6.9 demonstrate that the sensor in borehole R072 registered the first arrival of the tracer only 50 min after salt injection began. The peak concentration of 4.8 g/l (i.e., 13% of the injected concentration) was observed at 14.4 h. The breakthrough curve had a long tail with a significant amount of salt present after 120 h (5 days). The resistivity sensor installed in borehole R073, only 2 m from R072, recorded the effects of the plume much later and with much smaller concentrations, with the first arrival being detected at ~ 20 h and a peak concentration of 0.8 g/l at ~ 88 h. A second resistivity sensor installed ~ 2 below the groundwater table in borehole R073 did not detect any tracer.

Quantitative analyses of the breakthrough curves in Figure 6.9 are difficult, because the ends of the tails were not recorded. Moreover, the relatively sharp gradient changes in the R072 breakthrough curve are characteristic of salt solution entering the borehole via different flow paths. By fitting 2-D analytical solutions to the breakthrough curves, we obtain flow velocities in the $0.2 - 4 \times 10^{-4}$ m/s range for the three kinks of the R072 breakthrough curve and 0.15×10^{-4} m/s for that of the R073 curve.

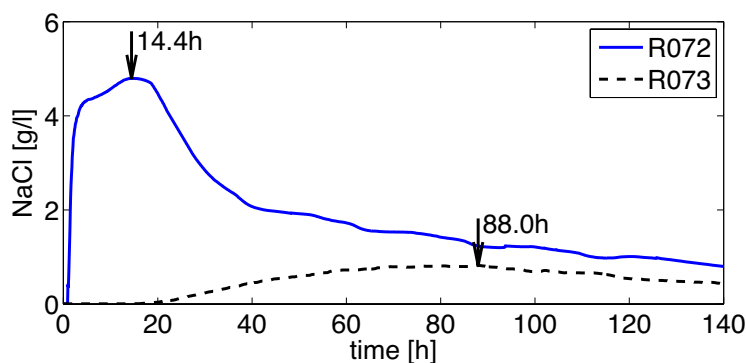


Figure 6.9. Salt tracer breakthrough curves measured ~ 5 m below the groundwater table in boreholes R072 and R073. The two boreholes are both located ~ 5 m from the injection borehole R042 (see Figure 6.2).

6.8 DISCUSSION

The ERT time-lapse images track the salt tracer plume for ~35 m in the dynamic riparian groundwater system adjacent to the Thur River. In a qualitative sense, the arrival times and volumes of tracer measured in the observation boreholes are consistent with the ERT time-lapse images. At borehole R072, which practically coincides with the path of the plume's center of mass (compare Figures 6.2b and 6.8a), the plume with high tracer concentrations arrives soon after injection begins. At borehole R073, which is ~2 m to the side of the plume's center of mass, the plume arrives much later and with much lower tracer concentrations. Since the groundwater system is likely influenced by pumping in the injection borehole for the first hour, we speculate that the very fast breakthrough in R072 is due to an anomalously high hydraulic gradient. Unfortunately, the mixing process in the injection borehole precluded us from measuring the change of water level there, so we cannot test this possibility. The $0.15 - 4 \times 10^{-4}$ m/s range of flow velocities estimated from the breakthrough curves are comparable to the ERT time-lapse estimates of 2×10^{-4} m/s and $>5 \times 10^{-4}$ m/s for the plume's center of mass and front.

In addition to being able to follow the salt tracer plume for ~35 m, two hydrogeological findings are of special interest. One is the change in the direction of plume propagation and the other is the large amount of tracer that appears to remain close to the injection point throughout the 50 h monitoring period.

A change in plume propagation direction could be caused by a change in river level, resulting in an asynchronous change in hydraulic head and thus hydraulic gradient within the aquifer. This seems unlikely, since Figure 6.4a demonstrates that river level fluctuations were minor (with ± 2 cm) during the experiment. For the same period, hydraulic head variations in the boreholes were similar to the river level fluctuations. As a consequence, we interpret the change in flow direction in terms of subsurface heterogeneity. This heterogeneity would have caused strong local variations in the hydraulic gradient. The high flow velocities and thus the dominance of advection over diffusion would have also contributed to the effects of heterogeneity. For times >6 h, the plume front appears to have moved through a high hydraulic conductivity zone. From the ERT time-slices, it is difficult to determine the width or depth of this zone, but from Figure 6.6c it seems that the preferential flow path was located in the lower part of the aquifer.

The long residence time of the tracer close to the injection borehole is best seen in Figures 6.5d and 6.6d. At times > 40 h, the injection point is at the edge of the plume defined by the

3% change in resistivity. We conclude that the corresponding fraction of tracer is moving, but much slower than the tracer front. This observation agrees well with the long tail of the breakthrough curve measured in R072 (Figure 6.9).

The different mass recoveries in the field (10-25%) and synthetic (~80%) ERT time-lapse images are caused by a combination of uncertainties in assumptions about the field and synthetic data and by effects not included in the groundwater transport model. First, whereas we know the true error level of the synthetic data, it is difficult to estimate the time-lapse error ϵ_{ri} for the field data (see Section 2.2). Second, our petrophysical model that assumes a linear and uniform relationship between bulk resistivity and salt concentration (i.e., Archie's Law) may not be strictly applicable at the study site (e.g., surface conductivity might be significant or the formation factor may be different than 10). Third and foremost, the measured ERT values are more sensitive to large features with small resistivity contrasts (relative to the background values) than small features with large resistivity contrasts. For the salt tracer test, this implies that a smooth well-distributed low-concentration plume would be reconstructed more accurately than a spatially focused high-concentration one. Simulations based on the groundwater transport model produce the former type of plume, for which the mass can be recovered rather well, whereas the real tracer distribution is likely to be more heterogeneous at scales smaller than the resolution of the ERT time-lapse images.

Heterogeneity in gravel deposits are known to be the source of significant hydraulic conductivity variations [see *Beres et al.*, 1995; *Huggenberger et al.*, 1998; *Beres et al.*, 1999 and references therein]. The different GPR-defined zones (Chapter 5) at the Thur River study site are thus likely to be characterized by quite different hydraulic conductivity ranges. Combining information from these GPR-defined zones with direct-push hydraulic profiling results [*Dogan et al.*, 2011] to parameterize groundwater transport models that are consistent with the ERT and breakthrough data would be a valuable extension of the present work.

6.9 CONCLUSIONS

Natural flow of a saline tracer within a dynamic riparian groundwater system close to a restored losing river has been monitored using a 3-D surface ERT time-lapse approach. A large volume (500 l) of saline solution (36 g/l salinity) was injected into a 6-m-thick gravel aquifer that had a natural hydraulic head gradient of 1.43 ‰. Besides the shape of the salt tracer plume, its propagation direction and velocity were estimated. The propagation direction was roughly parallel to the flow of the river for the first 6 h, after which it changed direction

away from the river flow by 25° . The plume's front moved at a high velocity of $>5 \times 10^{-4}$ m/s. After 16 h (~ 35 m), it left the ERT-monitored region. The plume's center of mass traveled with a lower velocity of 2×10^{-4} m/s and was slightly influenced by its higher density relative to the natural groundwater. The tail of the plume tracer moved at much slower rates. In addition to demonstrating strong differences in groundwater flow velocity, our ERT time-lapse images suggested the existence of preferential flow paths.

The utility of the 3-D surface ERT time-lapse approach was highlighted by our failure to follow the plume for more than 5 m using standard borehole-based hydrological observations. Only two of seven hydrological loggers located within ~ 30 m of the injection borehole registered a tracer signal. Moreover, breakthrough curves at these two boreholes were difficult to interpret, because one had a very fast (tracer breakthrough ~ 50 min after the beginning of tracer injection) and strong response and the other, which was only ~ 2 m from the first, had a slow (breakthrough after 20 h) and weak response. We conclude that solute transport controlled by complex subsurface structures typical of fluvial sedimentary environments cannot be resolved by borehole observations alone. Nevertheless, the $0.15 - 4 \times 10^{-4}$ m/s flow velocities estimated from the breakthrough curves generally agreed with the velocities determined from the ERT time-lapse images.

A groundwater transport model was used to assess qualitatively the resolving capabilities of the ERT time-lapse images and determine if a uniform flow model could explain the ERT inversion results. We found that the behavior of the plume could be explained by a uniform hydraulic conductivity of 4×10^{-2} m/s for the first 6 hours. At later times, this model with uniform flow characteristics provided an incomplete description of the dynamics occurring in this riparian groundwater system.

We recommend 3-D surface ERT for monitoring tracer experiments in dynamic groundwater systems, because it i) allows continuous 3-D imaging of the tracer plume over time, ii) needs relatively little prior information about flow direction and velocity, and iii) is minimally invasive and comparatively inexpensive (e.g., no permanent installations are necessary).

7 CONCLUSIONS & OUTLOOK

In this chapter, I summarize the principal conclusions of chapters 2 – 6. Starting from these conclusions, I discuss some possible future developments for structural joint inversion and potential approaches for further developing fully-coupled hydrogeophysical inversion.

7.1 SUMMARY OF CONCLUSIONS

The main focus of this thesis is geophysical data integration for improved imaging of aquifer structure and processes. In Chapters 2 and 3, I show that joint inversion of static and time-lapse crosshole data improves the inversion results and facilitates further analysis, such as classification of zones or spatial moment analysis of a tracer plume. Chapters 4 and 5 are concerned with incorporating structural information in ERT inversions and demonstrating how such constrained inversions can help in retrieving more reliable models for cases in which joint inversions are not possible. I illustrate in Chapter 6 the benefits of combining time-lapse ERT inversions with simulations of subsurface flow and transport for hydrogeological interpretations.

Methodologies for combining 3-D seismic, radar and ERT data in a cross-gradient joint inversion followed by classification of zones and an overdetermined inversion for zonal parameters are presented in Chapter 2. A zonation approach based on Gaussian mixtures is used to identify zones in the inversion models. A synthetic example demonstrates how joint inversion reduces the misclassification rate from 21.3% for the individual inversions to 3.7 % for the three-method joint inversion. The joint-inversion zonal models also provide much better estimates of the zonal parameter values, with a 0.3% error compared to a 1.8% error based on the individual inversion tomograms. Applying the joint inversion and classification methodology to data recorded at the Widen field site near the Thur River yields significantly better results than individual inversions and generally improved classification of the resultant models. I found three subunits within the gravel aquifer, with a relative porosity variation of ~30% and an increase of fine material with depth. The geometries and properties of the aquifer subunits determined in Chapter 2 and Appendix B will be incorporated in a flow and transport model currently being developed for this field site.

An extension of the cross-gradient joint inversion method to time-lapse data is presented in Chapter 3. A synthetic experiment based on flow simulations together with field data from a water injection experiment in unsaturated sandstone clearly show that cross-gradient joint inversions of crosshole time-lapse ERT and GPR traveltimes (1) decrease horizontal smearing of imaged plumes, (2) increase the similarity between models and (3) improve the estimated center of mass of plumes compared to individual time-lapse inversions. The examples also illustrate that higher resolution 2-D traveltimes GPR data might benefit from lower resolution 3-D ERT data.

Inversions of crosshole ERT data in Chapter 4 demonstrate the importance of including all significant aspects of the physical system in the modeling and inversion processes. I find that it is impossible to obtain reasonable crosshole ERT inversion results without considering the water-filled boreholes, in which the electrodes are suspended. The borehole-fluid effect is strongly dependent on the resistivity contrast between the rock formation and the borehole fluid, the survey design and geometrical aspects, such as borehole diameter, hole spacing and electrode configuration. I am able to retrieve trustworthy resistivity models by including the boreholes in the modeling and inversion mesh and disconnecting the regularization for the boreholes from that of the rock formation.

The surface ERT inversions in Chapter 5 benefit from structural information provided by surface-based GPR reflection surveys. The GPR data image undulations in the thickness of the aquifer and delineate two regions in the aquifer distinguished by different reflectivity patterns. By including GPR reflection interfaces corresponding to the basal and internal layers of the aquifer in the ERT mesh and by disconnecting the regularization across these interfaces, I am able to improve markedly the resulting ERT models. The standard and constrained inversion results illustrate to what extent ERT data resolve features, particularly at depth, and how important it is to (wherever possible) perform constrained inversions to obtain quantitative information on resistivity structure and properties. Models that incorporate the GPR interfaces reveal subtle resistivity variations within the aquifer that are not resolved in the unconstrained model.

In Chapter 6, I discuss the monitoring of a salt tracer injection in the gravel aquifer investigated in Chapter 5. I imaged the development of the saline tracer plume for 50 h and tracked the front of the plume for 35 m, at which point it left the electrode array after only 16 h. Comparison with groundwater flow and transport simulations show that for the first 6 h, the imaged plume can be explained by a homogeneous groundwater model with a hydraulic conductivity of 0.04 m/s. At later times, the transport of the plume is controlled by a preferential flow path, demonstrating that heterogeneity has a large influence on flow and transport in this dynamic alluvial aquifer.

7.2 OUTLOOK

7.2.1 Structural joint inversion

Structural joint inversion [*Haber and Oldenburg, 1997*] and its implementation by penalizing cross-gradients between models [*Gallardo and Meju, 2003*] is now a well-established method that has been further developed and employed by several researchers (see references in *Gallardo and Meju [2011]*). In my opinion, the examples from the scientific community have shown the value of cross-gradient joint inversion and it is now time to use this method in a wider field of applications. Future applications and developments could include:

- Implement cross-gradient joint inversion on the scale of the expected resolution instead of considering neighboring model cells only. This would be important when using unstructured (e.g., finite-element) meshes and combining methods with different cell sizes and grid types.
- Extend cross-gradient joint inversion to other geophysical techniques and scales. As long as the basic assumption of structural similarity between model parameters is valid, the methodology could be applied to scales relevant for mineral or oil exploration and methods like seismic full-waveform inversion and controlled-source electromagnetics.
- Directly include hydrogeological measurements in cross-gradient joint inversion. As an example, one could jointly invert crosshole GPR, ERT and hydraulic tomography data, the latter of which is directly sensitive to hydraulic conductivity. This could help to improve the resolution of the hydraulic tomography models and derive petrophysical relationships between hydrogeologically important properties and the properties sensed by geophysical techniques.

7.2.2 Integrating geophysical and hydrogeological data

The next logical step for data integration in hydrogeophysics is to couple directly the flow and transport models with the geophysical inversion schemes. Although still computationally challenging, such fully-coupled hydrogeophysical inversion is feasible as advanced modeling algorithms and computational power become available. In my opinion, a key factor for the success of hydrogeophysical inversion is the parameterization of the inverse problem. Inverting for many geophysical and hydrogeological parameters simultaneously could result

in a very non-unique and unstable inversion process, especially for non-linear systems. It is therefore crucial to constrain as many subsurface parameters as possible before starting a coupled inversion. The estimated parameters in the coupled inversion should be as few as possible, but they must be able to explain the physical phenomena.

Fully-coupled hydrogeophysical inversion should first be attempted on relatively simple albeit realistic systems, in which the dynamic geophysical signal of the monitored change is strong compared to ambient noise and other error sources. Possible candidates would be:

- Explore flow in the unsaturated zone by monitoring a water injection. *Kowalsky et al.* [2005] already jointly inverted crosshole GPR and hydrological data for such an experiment; incorporating crosshole ERT (as in the experiment of *Binley et al.* [2002b]) could be a valuable addition.
- Examine flow and transport in the unsaturated zone by monitoring a salt tracer injection [eg., *Winship et al.*, 2006]. Including crosshole GPR and ERT data in a coupled hydrogeophysical inversion could help to disentangle the flow and transport components, because GPR traveltimes are sensitive to water content and ERT senses a combined effect of water content and salinity. Structural time-lapse inversion would fail in this case, because the assumption of structural similarity between the GPR velocity and the resistivity perturbation is violated.
- Investigate groundwater flow and transport by monitoring a salt tracer injection. Experiments similar to that described in Chapter 6 could be a good test case for a coupled inversion in which surface ERT is used to constrain a groundwater model. *Pollock and Cirpka* [2010] have developed a fully coupled inversion approach for salt tracer tests in a 2-D sandbox and it might be possible to extend their approach to 3-D for field applications.

Once there have been some successful demonstrations of fully-coupled hydrogeophysical inversion, one could consider more complicated systems and larger scales. Applications could include monitoring of carbon sequestration, gas- and oil-extraction, as well as nuclear waste storage.

APPENDIX A: HYDROGEOPHYSICAL STUDIES AT THE THUR RIVER

Published in *First Break*:

Linde, N., Coscia, I., Doetsch, J. A., Greenhalgh, S. A., Vogt, T., Schneider, P., and Green, A. G., 2010. Hydrogeophysical studies in unrestored and restored river corridors of the Thur River, Switzerland, *First Break*, **28**, 69-75.

ABSTRACT

Dynamic hydrological systems are challenging targets for geophysical investigations, but they have the advantage that natural stimuli (e.g., fluctuations in river and groundwater height, salinity and temperature) may be used to infer system responses (e.g., infiltration rates and flow patterns). Three dimensional (3-D) high resolution crosshole and surface based ground penetrating radar (GPR) and electrical resistance tomography (ERT) studies have been carried out at unrestored and restored sections of the Thur River in Switzerland to improve our understanding of how lithological heterogeneities affect river - groundwater interactions. Hydrological and apparent resistivity time series acquired between 18 boreholes located close to the river at the unrestored section are found to be very sensitive to infiltration processes. Information that can be retrieved from geophysics at the two sites are different primarily because (1) a surficial 3 m thick low resistivity loam layer at the unrestored site precludes the application of surface based GPR and ERT methods and (2) because the frequently flooded gravel bars at the restored section make long term monitoring very challenging. Since it is extremely difficult and costly to retrieve undisturbed cores in coarse gravel deposits, we argue that geophysics should form an integral part in investigations of the internal structures and porosity variations of gravel bars in restored river corridors. We recommend that geophysical surveys and geophysical monitoring be included in larger scale river restoration projects both before and after restoration to determine how river restorations affect aquifer morphology and infiltration patterns.

A.1 INTRODUCTION

Most major European rivers were channelized over the past two centuries, primarily to facilitate transport of goods and people, gain arable land and decrease the risk of flooding. Unfortunately, these measures have had adverse effects on ecological diversity, the self-cleaning capacity of river systems, fish stocks and recreation possibilities. Channelization may even be an ineffective approach to flood protection at some locations, since it creates very fast response times that may lead to catastrophic events in the case of levee failure. Alternative engineering measures, such as re-creating floodplain wetlands, might moderate flow variability while cleaning pollutants [Palmer *et al.*, 2005].

Many rivers worldwide are being restored to enhance water quality, improve in-stream habitat, facilitate fish passage, increase bank stabilization, reconnect floodplains, modify flows, improve aesthetics or recreation possibilities, and reconfigure river channels

[Bernhardt *et al.*, 2005]. In the USA alone, river restoration is a billion dollar industry with huge growth during the past decade [Bernhardt *et al.*, 2005]. A similar situation exists in Europe where river restoration offers one strategy for obtaining good ecological states of the freshwater bodies as required by the EU Water Framework Directive [EC, 2000].

It is often tricky when designing a river restoration programme to strike a balance between the objectives stated above while accounting for existing infrastructure (e.g., houses, roads and water extraction wells) and the associated remediation costs. Past restoration programs have been poorly monitored. For example, only 10% of river restoration projects in the USA have included some form of assessment or monitoring, implying that opportunities to learn from past successes and failures have been lost [Bernhardt *et al.*, 2005]. As a consequence, the performance of different river restoration designs remains largely speculative and there is little agreement on what constitutes successful river restoration [Palmer *et al.*, 2005].

We present here some preliminary results from ongoing geophysical characterization and monitoring at both an unrestored channelized section (Widen) and a restored section (Neunforn) of the Thur River in Switzerland (see Figure A1), in which subsurface fluid flow takes place in a 6 - 7 m thick highly permeable gravel aquifer. This work is performed within the framework of the RECORD project [RECORD, 2011], a multidisciplinary research program aimed at developing a mechanistic understanding of ecological - hydrological - geochemical processes in river corridors. The Thur River is the largest Swiss river without natural or artificial reservoirs. It exhibits discharge and river stage fluctuations similar to unregulated alpine rivers.

We have been determining the background structural, lithological and hydrological framework at the two sites and monitoring changes to these properties. A dense array of boreholes with permanent geophysical and hydrological monitoring equipment has been installed at the first study site across rarely flooded overbank deposits in an unrestored channelized section of the river. The dynamic nature of the restored river section and associated sediment transport at the second study site makes it very challenging to install permanent monitoring stations in the river or on the surrounding gravel bars [Schneider *et al.*, 2011]. Consequently, geophysical work at this second site has been largely limited to periods of low flow stable hydrological conditions.

Our framework studies have included detailed crosshole geophysical characterization at the unrestored channelized site through 3-D individual and joint inversions of electrical

resistances and seismic and radar traveltimes (Chapter 2), whereas our larger scale surface-based framework investigations at the restored site have involved 3-D GPR and ERT surveys (Chapter 5). A 3-D framework is needed, because 3-D geological heterogeneity controls river groundwater interactions (e.g., distribution of seepage, groundwater table configurations and the connections between the river and the aquifer [Fleckenstein *et al.*, 2006]), which in turn is important for modeling biochemical reactions in catchments [Wriedt and Rode, 2006].

For surveillance of the unrestored section, we monitor the response of multi-borehole ERT data to natural forcing that is mainly caused by variations in river height and electrical resistivity of the river water and a relatively minor contribution due to temperature fluctuations. We intend to obtain information about preferential infiltration patterns from the monitoring data. Time series of groundwater electrical resistivity in these settings can be used to calculate traveltime distributions at both unrestored and restored sites [Cirpka *et al.*, 2007; Vogt *et al.*, 2010b], but the application of these concepts remains to be tested for ERT data that have large support volumes (e.g., at our study sites). Geophysical surveillance on the gravel bar consists of self-potential (SP) monitoring under natural flow conditions and ERT monitoring following saline tracer injections.

Preliminary results from a small subset of these investigations are presented here to demonstrate that it is possible using a combination of geophysical and borehole techniques to (1) obtain 3-D models of the gravel aquifer structure and properties and (2) monitor groundwater flow and infiltration processes through the effects of natural forcing.

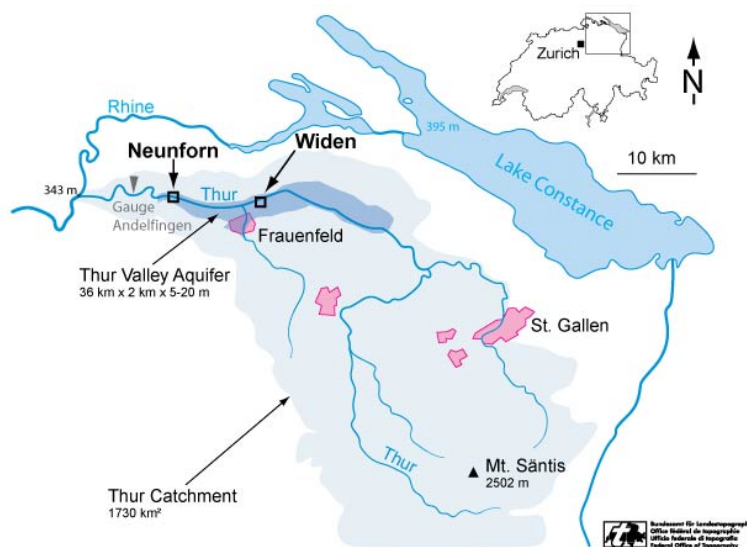


Figure A1. Location of the Thur catchment, Thur valley aquifer and unrestored channelized (Widen) and restored (Neunforn) test sites in NE Switzerland.

A.2 SITE DESCRIPTIONS AND INSTRUMENTATION

The lower Thur River was originally a braided river that was channelized in the 1890s. It was converted into a double channel (trapezoidal cross sections) with a 45 m wide low water channel (flow capacity 230 m³/s) that had stabilized banks and overbanks on both sides (total flow capacity 1100 m³/s) bounded by levees with a 160 m spacing between the levee crowns. The vertical distance between the river bed and levee crown averaged 6 m.

One research facility was established at an unrestored section of the river (Widen, see Figure A1) that was known to display significant temporal fluctuations in the groundwater electrical resistivity [Cirpka *et al.*, 2007] and that allowed equipment to be permanently installed. Following initial investigations based on several parallel 2-D surface ERT profiles, the dense borehole array was installed on an agricultural site close to the river. The 10 × 15 m array comprises eighteen 12 m deep monitoring boreholes spaced 3.5 m apart that completely penetrate the 7 m thick gravel unit (Figure A2). The underlying thick lacustrine clay layer can be considered to be impervious to flow. The borehole array pattern is sketched in Figure A2a and photographs of the installation process are displayed in Figure A3. Our borehole layout has the advantage that in addition to full 3-D studies, it is also possible to perform dedicated high-resolution geophysical and hydrological 2-D studies in four different directions (i.e., parallel and perpendicular to (1) the river and (2) the expected flow direction).

Each borehole has been instrumented with ten 0.7 m spaced electrodes that span the thickness of the aquifer. A multichannel geoelectrical system programmed to cycle through various 4 point electrode configurations of the 180 electrodes in a rolling sequence allows ~15 000 measurements to be made every ~7 hours. In addition to the electrodes, 6 of the boreholes are equipped with sensors at different depths that provide time series (every 15 minutes) of groundwater table height and groundwater resistivity and temperature.

In 2002, a 2.5 km long section of the Thur River near Neunforn (see Figure A1) was restored by completely removing the northern overbank, so that a nearby forest (Figure A4) became part of the active floodplain again. This widening increased sediment deposition and re-established dynamic fluvio-morphological processes with frequently forming and alternating gravel bars that provide habitats for fauna and flora. This river section was chosen as the research site representing a restored river [Schneider *et al.*, 2011]. Figure A4 displays the gravel bar that is of primary interest together with some photos taken during GPR data acquisition campaigns.

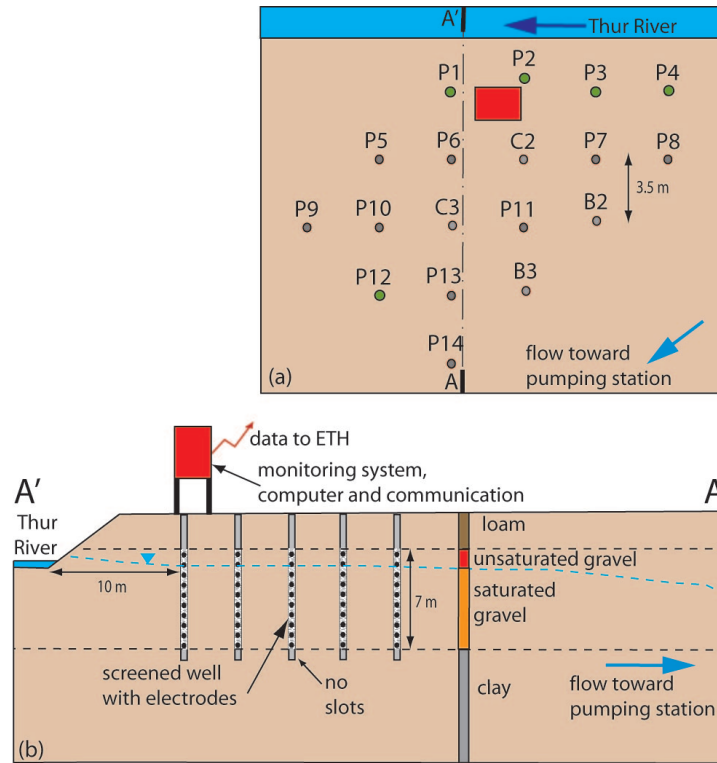


Figure A2. Crosshole ERT monitoring system at the unrestored channelized (Widen) site with the flood protected housing of the ERT system. (a) Plan view and (b) profile view. The resistivity image shown in Figure A5 was extracted from the full 3-D inversion model along the line of boreholes P1 - P4 shown in (a).

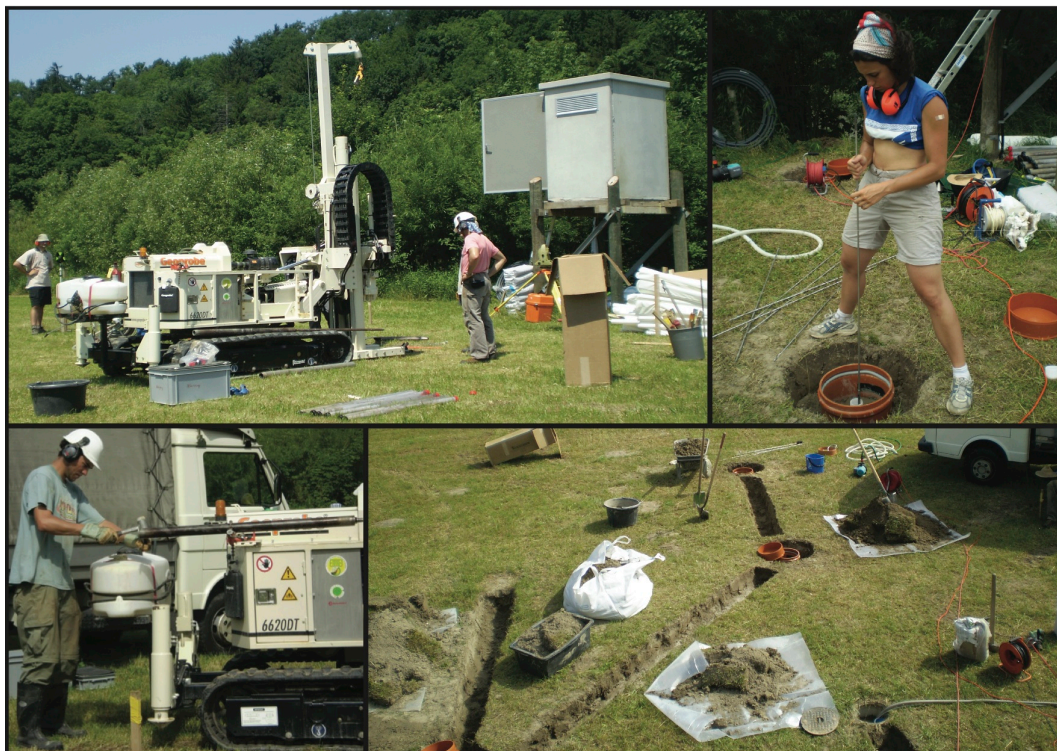


Figure A3. Borehole and ERT monitoring installation at the unrestored channelized (Widen) site. Location of the site is shown in Figure A1.

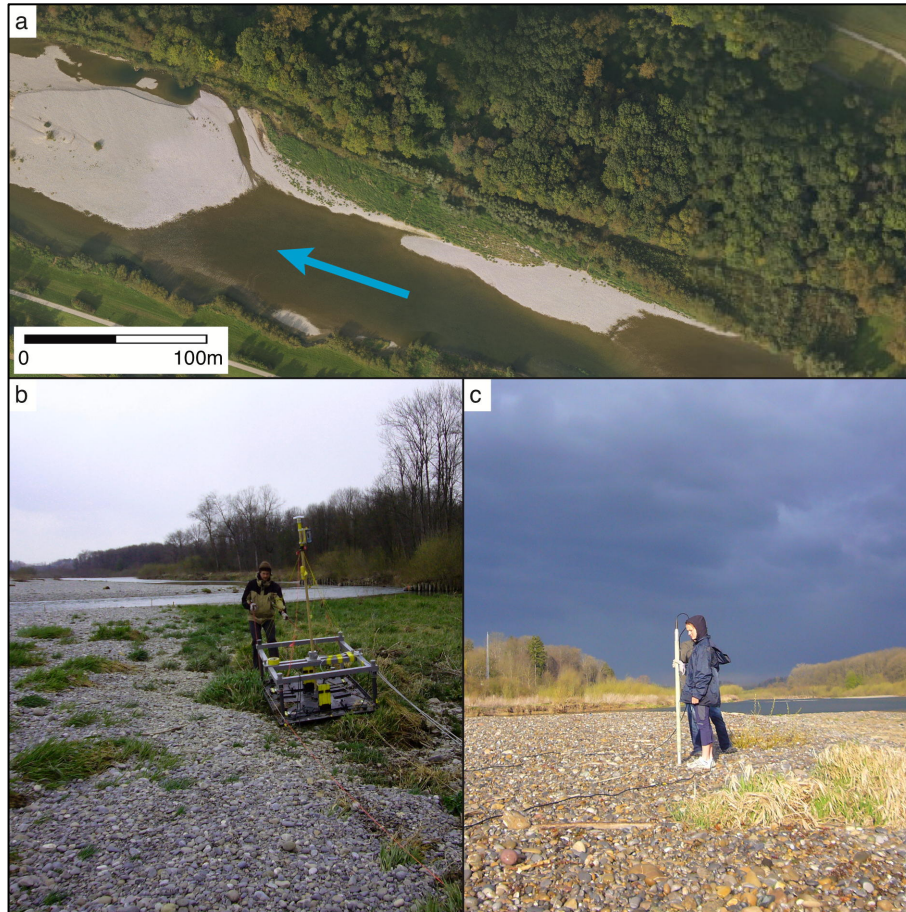


Figure A4. (a) Aerial photograph of the gravel bar (North of arrow) where most of the research on the restored part of the river section is focussed. Blue arrow identifies the water flow direction. (b) Acquisition of surface based GPR and (c) calibration for crosshole GPR data on the gravel bar. Location of the site is shown in Figure A1.

A.3 INVESTIGATIONS AT THE UNRESTORED CHANNELIZED SITE

At the unrestored channelized river site, joint inversion of 3-D crosshole electrical resistances and seismic and radar traveltimes have revealed that the typically 6 m thick saturated part of the gravel unit is composed of a middle lower porosity layer (relatively high resistivity and high seismic and radar wavespeeds) embedded in higher porosity formations [Chapter 2, *Linde and Doetsch*, 2010]. The conductive borehole fluid was found to create significant artifacts. Chapter 4 shows that including the boreholes and their fluids explicitly in the inversion process using an unstructured finite element mesh [*Günther et al.*, 2006] largely removes these artifacts. Neutron - neutron and gamma - gamma logs provided information about total porosity and natural gamma logs that are related to the clay content were acquired in all boreholes.

Initial 3-D ERT inversions were performed on data acquired during low flow stable conditions. The inversions accounted for topography and the boreholes (including their lateral deviations) and the regularization was disconnected across the known groundwater table level and gravel - clay boundary. It was important to disconnect the smoothness constraints at these interfaces, since failure to do so generated false structures. For example, the low resistivity of the clay "created" artificial low resistive anomalies that spread into the more resistive gravel.

Figure A5 shows a resistivity section extracted from a 3-D ERT model along the line of boreholes closest to the river (for location see Figure A2a). The lower (blue) layer corresponds to the clayey aquitard. The saturated part of the aquifer displays an upper central zone two to three times more resistive than the overlying and underlying parts (i.e. the red - orange zone bounded above and below by the yellow regions; Chapter 4). We also observe a less resistive block (green) with resistivities of $\sim 100 \Omega\text{m}$ that corresponds to a lens of clayey silt and sand sediments seen in neutron - neutron well logs and encountered in drill core from neighboring boreholes.

The neutron - neutron data were converted to approximate porosity estimates using the approach of *Barrash and Clemo* [2002], in which the highest number of counts in all 18 boreholes corresponds to a porosity of 50% and the lowest to 12%. The deduced porosities over the saturated section (Figure A5) match values obtained for the three-layer aquifer (26%, 19%, 23%) by means of traveltime (Chapter 2) and full waveform [*Klotzsche et al.*, 2010] inversion of crosshole GPR data. Both the GPR and neutron - neutron determined porosity estimates correlate closely with the aquifer's electrical variability defined by our ERT model.

The temporal variations in apparent resistivities at this site are mainly affected by groundwater table variations and changing pore water resistivity and less so by temperature. Figure A6 displays time series of apparent resistivity and groundwater resistivity measured in the boreholes during a period of strong variation in river stage following heavy precipitation in the catchment [*Coscia et al.*, 2010]. Clearly, there is a strong correlation between these parameters. Our initial results suggest that apparent resistivities based on certain electrode configurations are highly sensitive to variations in groundwater resistivity (e.g., Figure A6), whereas others are dominated by the effects of groundwater table height. We are currently investigating how to correct the apparent resistivity data for the effects of groundwater table fluctuations and temperature before inverting the corrected apparent resistivity time series to image the flow patterns of the infiltrating river water.

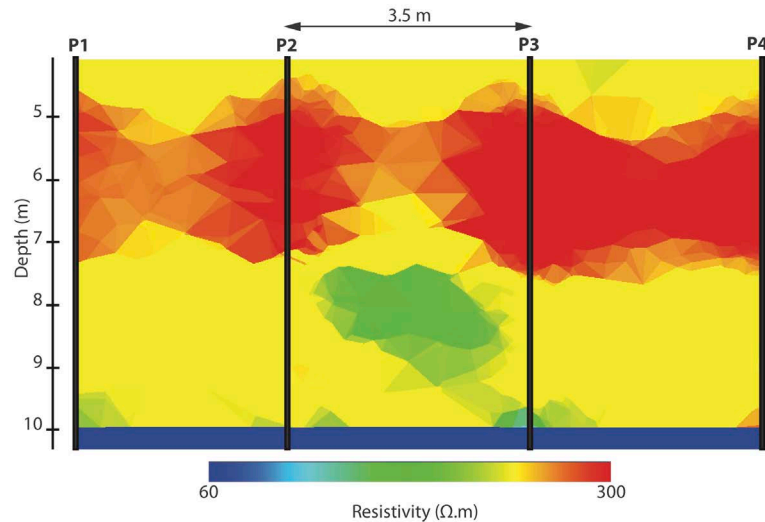


Figure A5. Vertical section extracted from the 3-D ERT inversion model (logarithmic scale) along the boreholes located closest to the river (P1 - P4 in Figure A2). The high resistivity (low porosity) zone in the upper middle part of the section can be traced throughout the resistivity volume. Location of the site is shown in Figure A1.

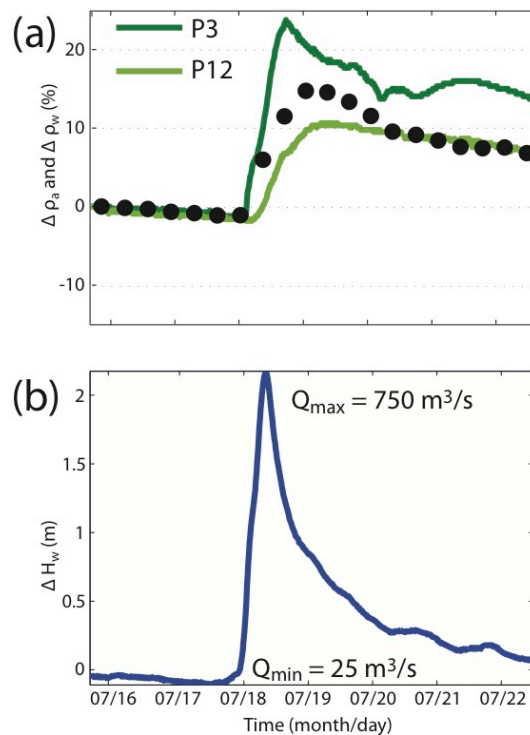


Figure A6. For the unrestored channelized (Widen) site, comparison between time series acquired in July 2009 of (a) percent variation of apparent resistivity ($\Delta\rho_a$ - black dots), percent variation of groundwater electrical resistivity ($\Delta\rho_w$ - two green curves) and (b) variation of the groundwater table height (ΔH_w - blue curve). Our studies demonstrate that for this particular electrode configuration the variations in apparent resistivity are mostly caused by changes in the electrical properties of the infiltrating river water. For other electrode configurations, the apparent resistivity variations are dominated by changes in groundwater table height. Location of the site is shown in Figure A1 and the geometry of the boreholes is presented in Figure A2.

A.4 INVESTIGATIONS AT THE RESTORED SITE

The main experiments conducted on the gravel bar (for location see Figure A4a) involved 3-D surface GPR and ERT surveys covering a total area of approximately 240×40 m (Chapter 5). We used a commercial GPR system with 100 MHz antennae mounted on a sledge together with a GPS tracking unit (Figure A4) to acquire data continuously along lines spaced 0.5 m apart. Figure A7 displays a chair type plot of a sub-section of the processed 3-D GPR data on one of the gravel bars. The processing included time zero shifts, gridding and applications of gain functions, frequency filters, topography corrections and F-XY deconvolution. The time-to-depth conversion was achieved using a constant velocity based on averaged common midpoint profiles. The lowermost prominent reflection in Figure A7 originates from the interface between the gravel aquifer and underlying clay layer. Other laterally continuous structures that can be traced throughout the gravel bar are probably reflections from interfaces between gravel sheets. Smaller scale dipping features represent foreset bedding [Beres *et al.*, 1999].

Our surface ERT data were acquired using 522 electrode positions along 22 lines, with each suite of 3-D measurements taking advantage of 6 lines. The total ERT data set includes > 100 000 measurements made over two days. We are currently exploring how to use the GPR sections to guide the 3-D inversion of the ERT data (Chapter 5). An initial 3-D ERT inversion constrained by the boundaries defined by the 3-D GPR image indicates a 100 - 400 Ωm range of resistivities for the gravels and ~ 40 Ωm for the underlying clay at the restored site. We also plan to investigate (1) how the different depositional features displayed in Figure A7 affect groundwater flow and transport and (2) how this information can be used to build hydrogeological models.

The groundwater level, electrical resistivity and temperature display both small (daily) and large scale fluctuations due to precipitation or snowmelt [Vogt *et al.*, 2010b]. These fluctuations make it challenging to monitor saline tracer experiments with time lapse ERT, since it is difficult to assess to what degree observed changes are due to the tracer mass vis-à-vis natural river fluctuations. One could consider time lapse ERT monitoring using natural fluctuations in a similar manner to the investigations at the unrestored channelized section. In all cases, it appears necessary to acquire ERT time-lapse data prior to tracer injection to better differentiate between induced and natural variability.

We have also explored the use of self-potential (SP) monitoring data in these settings. The SP data are of high quality, displaying a strong correspondence with the hydrological data.

Unfortunately, interpretation of the SP data is complicated because they are sensitive to several variables (e.g., variations in the groundwater table height, flow in the vadoze zone, the hydrological flow regime and the pore water electrical resistivity). A dedicated modeling analysis should help us assess the influence of these possible effects on the data. For a quantitative hydrogeological understanding in this type of dynamic environment, we suggest that it is necessary to develop 3-D groundwater flow and transport models in which the geophysical data, images and models are used for calibration purposes.

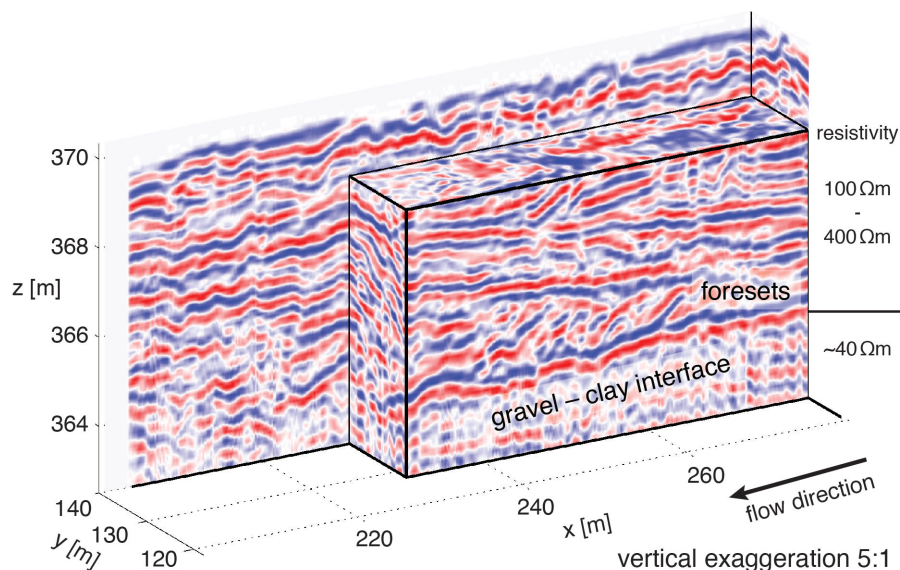


Figure A7. Chair plot of processed GPR data acquired across the western part of the gravel bar within the restored site. Resistivities shown on the right side of the model represent average values for the gravel- and clay-rich layers derived from an inversion of 3-D surface ERT data constrained by the boundaries defined by the GPR data. Location of the site is shown in Figure A1.

A.5 DISCUSSION

Comparisons between the results obtained at the unrestored and restored sections of the Thur River are difficult because the geophysical methods employed at the two sites are different. Surface based GPR and ERT methods are of only limited value along the unrestored section as a result of the low resistivity surface loam layer. At this site, we rely on crosshole geophysical investigations and long term autonomous ERT monitoring. Our geophysical models (electrical resistivity and radar and seismic wavespeeds) demonstrate that the gravel aquifer is made up of three layers. The middle layer having a lower porosity and a lower content of fines, which is in qualitative agreement with the higher permeabilities found by *Diem et al.* [2010]. The amplitudes of the apparent resistivity time series agree with those of the pore water resistivities. We intend to investigate how such time series can be used to

investigate infiltration processes and the permeability structure of the site. Because of the different resolution characteristics, it is going to be challenging to compare the results of the lower resolution static and time lapse geophysical experiments with those of the borehole logging and hydrological testing [Day-Lewis *et al.*, 2005].

The situation at the restored river section is quite different from that at the unrestored section, since surface-based geophysical measurements can be performed in close proximity to the gravel aquifer of interest. Geophysical characterization can be achieved non-invasively at high spatial resolution over much larger volumes than is possible with crosshole data alone. In particular, the surface GPR data provide detailed images of the sedimentary structure that can hardly be obtained from the crosshole data. Since frequent flooding precludes permanent installations along the restored section, time-lapse studies are more challenging in this environment.

A.6 CONCLUSIONS

Geophysical methods provide detailed 3-D information on the lithological sub-units of the gravel aquifers at both the unrestored and restored sections of the Thur River. A combination of crosshole GPR and ERT techniques at the unrestored section makes it possible to obtain high resolution images and models of the gravel aquifer underlying a low resistivity 3 m thick surface loam layer. At the restored section, where there is only very limited conductive overburden or none at all, surface-based measurements can be made literally on the groundwater table. At this location, surface-based 3-D GPR and ERT techniques provide very high-resolution images and models throughout the full thickness of the gravel aquifer. These images and models will now be correlated with results from detailed biogeochemical, water chemistry and ecological sampling to improve our understanding of how variations in geophysical properties might facilitate the interpretation of such results. We expect that time lapse monitoring of natural variations in the apparent resistivity data can be used to better understand river - groundwater interactions and to determine preferential flow paths. We have also performed targeted saline tracer experiments (not shown here) to image specific flow paths and to understand the origin of SP signals. A future goal is to develop hydrogeological models that are consistent with the diverse geophysical and hydrological data at the two sites.

APPENDIX B: 3-D ERT FOR MONITORING OF INFILTRATING RIVER WATER

Published in *Geophysics*:

Coscia, I., Greenhalgh, S. A., Linde, N., Doetsch, J., Marescot, J., Günther, T., Vogt, T., and Green, A. G., 2011. 3D crosshole ERT for aquifer characterization and monitoring of infiltrating river water, *Geophysics*, **76**, G49-G59.

ABSTRACT

We are investigating the hydrogeological properties and hydrological responses of a productive aquifer in northeastern Switzerland. For this purpose we use 3-D crosshole electrical resistance tomography (ERT) to define the main lithological structures within the aquifer (through static inversion) and to monitor the water infiltration from an adjacent river. During precipitation events and subsequent river flooding, the river water resistivity increases. As a consequence, the electrical characteristics of the infiltrating water can be used as a natural tracer to delineate preferential flow paths and flow velocities. In this paper we focus primarily on the experiment installation, data collection strategy, the structural characterization of the site and give a brief overview of the ERT monitoring results. The monitoring system comprises 18 boreholes each equipped with 10 electrodes straddling the entire thickness of the gravel aquifer. A multichannel resistivity system programmed to cycle through various four-point electrode configurations of the 180 electrodes in a rolling sequence allows the measurement of approximately 15,500 apparent resistivity values every seven hours on a continuous basis. The 3-D static ERT inversion of data acquired under stable hydrological conditions provides a base model for future time-lapse inversion studies and the means to investigate the resolving capability of our acquisition scheme. In particular, it enables us to define the main lithological structures within the aquifer. The final ERT static model delineates a relatively high-resistivity low-porosity intermediate-depth layer throughout the investigated aquifer volume, consistent with results from well logging, and seismic and radar tomography models. The next step will be to define and implement an appropriate time-lapse ERT inversion scheme using the river water as a natural tracer. The main challenge will be to separate the superposed time-varying effects of water table height, temperature, and salinity variations associated with the infiltrating water.

B.1 INTRODUCTION

Electrical resistance tomography (ERT) is a popular subsurface imaging technique in hydrogeological, environmental, and civil engineering investigations [e.g., *Daily et al.*, 2005; *Kruse et al.*, 2006; *Robinson et al.*, 2008; *Sjödahl et al.*, 2009]. Crosshole implementations of the technique offer improved resolution and depth penetration over surface surveying [e.g., *Daily and Owen*, 1991; *Bing and Greenhalgh*, 2000; *Chambers et al.*, 2007]. Time-lapse studies, in which repeat measurements are made at different time intervals to track changes in the subsurface properties, have been performed for salt tracer experiments [*Slater et al.*, 2000;

Kemna et al., 2002; *Singha and Gorelick*; *Cassiani et al.*, 2006; *Wilkinson et al.*, 2010] and for the monitoring of steam injection [*Ramirez et al.*, 1993], environmental remediation [*Daily and Ramirez*, 1995; *LaBrecque et al.*, 1996a], biostimulation [*Lane et al.*, 2006], watershed characterization [*Miller et al.*, 2008] and various other processes [*Binley et al.*, 2002b; *Deiana et al.*, 2007; *Nimmer et al.*, 2007].

In this paper, we describe results of a novel 3-D crosshole resistivity monitoring experiment designed to investigate the hydrological properties and infiltration patterns of a producing gravel aquifer in direct connection with an adjacent river in northeastern Switzerland. Rainwater generally contains significantly lower concentrations of total dissolved solids (i.e., ions) than river water. As a consequence, strong precipitation in the catchment can cause the electrical resistivity of river water to increase. At our experimental site, high discharge events cause strong fluctuations of the river water electrical properties (increase in electrical resistivity). Therefore the river water which continuously infiltrates the aquifer can be used as a natural tracer to delineate the more hydraulically conductive sections of the aquifer and, as shown by *Cirpka et al.* [2007], to determine travel-time distributions.

Our research is part of a much larger project (RECORD - REstored CORridor Dynamics) aimed at assessing and modeling coupled hydrological, ecological, and biochemical effects of river restoration [*RECORD*, 2011]. In the project there are two study sites, one along a restored section (Neunforn) and one along an unrestored section (Widen) of the Thur River in Switzerland (Figure B1). Here, we restrict our attention to an initial hydrogeophysical study at the unrestored site. The eventual 4-D ERT model should provide new constraints for understanding interactions between the river and the connected aquifer. As summarized in the following paragraphs, our study differs from most earlier investigations in four ways: (1) the full 3-D inversion of an extensive crosshole data set acquired using electrodes deployed in a large number of boreholes, (2) an inversion strategy that accounts for surface and sediment layer topography, borehole inclinations, and the electrical properties of the borehole fluids, (3) the use of river water as a natural tracer to investigate an adjacent aquifer, and (4) continuously recorded data over a long time period at a sufficiently high sample rate to capture the transient process.

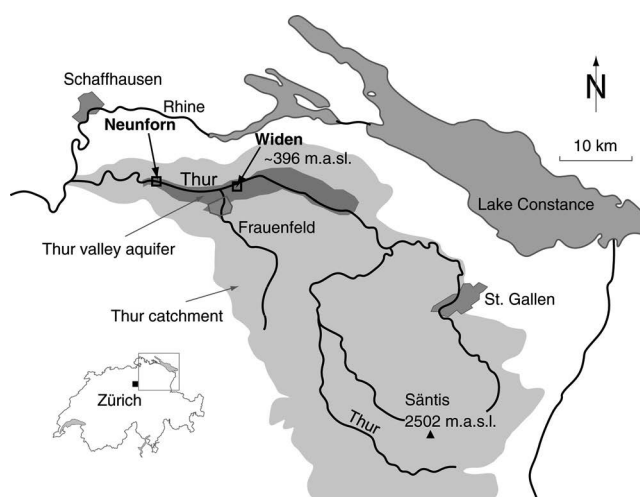


Figure B1. Location of the Thur catchment, Thur valley aquifer, and Nuenforn and Widen test sites in northeastern Switzerland. Modified from a figure prepared by Swisstopo (Swiss Federal Office of Topography).

ERT has previously been used for studying the interactions between rivers and their surroundings and for improving the modeling of fluvial systems. For example, *Crook et al.* [2008] used the technique to obtain information about the continuity and structure of stream-bed sediments. They employed information provided by a static resistivity model obtained from an ERT inversion of surface 2-D geoelectrical data. *Nyquist et al.* [2008] identified a zone of groundwater seepage into a river by combining the structural information about the site with that provided by the comparison of 2-D ERT images along the riverbed at low and high river stage conditions. Recently, *Ward et al.* [2010] investigated to what extent surface 2-D time-lapse ERT images, when combined with stream tracer experiments, can provide information about temporal and spatial dynamics in the hyporheic zone. Crosshole ERT, which is the basis of our work, usually yields more definitive information than surface ERT, especially if conducted in a time-lapse fashion. Previous such studies [e.g., *Singha and Gorelick*, 2005; *Slater and Binley*, 2006; *Kuras et al.*, 2009; *Müller et al.*, 2010; *Wilkinson et al.*, 2010], even if based on 3-D inversions, have generally involved sequential 2-D measurements only (i.e., between just one pair of boreholes at a time). Furthermore, the inversions have seldom been performed on data from more than four boreholes, because of the inability of standard inversion software to handle large 3-D data sets. In our study, we test a new acquisition and inversion strategy for carrying out a fully 3-D crosshole ERT experiment using electrodes located in 18 boreholes. We utilize a finite-element modeling (FEM) and inversion code based on unstructured meshes that allows us to incorporate typical

complexities associated with surface topography, sharp boundaries, and the boreholes themselves.

Most previous time-lapse ERT studies have been aimed at improving our understanding of subsurface solute transport by using time-varying electrical responses related to known injections of saline tracers into aquifers or known injections of water into the vadose zone [e.g., Slater *et al.*, 2000; Singha and Gorelick, 2005; Slater and Binley, 2006; Müller *et al.*, 2010; Wilkinson *et al.*, 2010]. Only a few studies have taken advantage of pre-existing electrical contrasts between the properties of subsurface fluids, such as those related to movements of contaminant plumes [Slater and Sandberg, 2000; Nimmer *et al.*, 2007] or those related to salt water - fresh water contacts within coastal aquifers [e.g., Slater and Sandberg, 2000; Acworth and Dasey, 2003; de Franco *et al.*, 2009; Maurer *et al.*, 2009; Ogilvy *et al.*, 2009]. In other investigations [e.g., Hauck, 2002; Jayawickreme *et al.*, 2008; Yeh *et al.*, 2008] natural occurring contrasts have been exploited. But as far as we know, no previous researchers have used the electrical properties of river water as a natural tracer to investigate aquifer response.

Time-lapse ERT usually involves frequently repeated measurements over a short period [e.g., Wilkinson *et al.*, 2010] or sparse measurements at infrequent intervals over a long period to determine seasonal variations in some property [e.g., French and Binley, 2004; Hayley *et al.*, 2009; Krautblatter *et al.*, 2010]. The present study is one of only a few examples (see also de Franco *et al.* [2009] and Ogilvy *et al.* [2009]) of a long-term ERT monitoring study (approximately one year of data have been collected in our case) with short-period data sampling (one data set of approximately 15,500 data points is acquired every 7 hours on a continual basis). This permits the investigation of aquifer infiltration and solute transport following river flooding events. It also enables us to investigate seasonal variations in electrical resistivity (e.g., same water height but different water resistivity due to snow melt, de-icing chemicals, or water temperature changes).

We begin by introducing the 18-borehole 180-electrode 3-D monitoring system and the geology of the site. Next, we describe the different electrode combinations and procedures used for remote data acquisition and then show the electrical signature of a typical flood event from the summer of 2009, which produces time-series of clear apparent resistivity anomalies. Finally, we present the results of a static 3-D ERT inversion for subsurface structure, incorporating various complexities such as surface and layer topography, decoupling of regularization across sharp layer boundaries, the borehole fluid effect, and borehole

deviations. Such 3-D images will be used as initial and reference models for future time-lapse inversion investigations.

B.2 WIDEN FIELD EXPERIMENT

B.2.1 Site description

The Widen study site (Figure B1) is located in northeastern Switzerland along the Thur River (a tributary of the Rhine River), which has a total length of approximately 127 km and a catchment area of approximately 1750 km². Due to the pre-alpine character of the upper Thur catchment that includes Mount Säntis (2502 m above sea level) and because of the absence of any natural or man-made reservoirs, the Thur River exhibits fluctuations in discharge and water table height similar to unregulated alpine rivers. Base flow has its maximum during snowmelt in spring, but flow peaks can occur at any time of the year in response to rainfall in the upper catchment (low discharge: 3 m³/s; mean discharge: 20–50 m³/s; peak discharge: up to 1000 m³/s [BAFU, 2010]).

Our study site is located within the central Thur floodplain (altitude approximately 400 m above sea level, 2 km wide, and 30 km long), where the Thur River flows from east to west along the northern edge of a valley (Figure B1) that formed during the Pleistocene period by glaciers cutting into the underlying Tertiary bedrock. After the glaciers retreated, a lake was left behind and subsequently filled with fine silt and clay sediments were deposited in a lake. These sediments now constitute the aquitard at this location. The productive aquifer above the clay comprises a 6.5- to 7-m-thick layer of gravel and sand that is overlain by approximately 3 m of alluvial loam (see Figure B2b). During the 1890s, this area of the Thur River was channelized. The main channel is approximately 40 to 45 m wide. There is no overbank on the northern side because of a prominent hillslope that acts as a natural barrier at high discharge, whereas on the southern side there is a levee approximately 130 m from the river. Behind this levee, a side channel has been constructed to capture discharge from tributaries and drain the nearby agricultural land. There is a pumping well approximately 80 m from the levee that produces approximately 9000 m³/d of drinking water for the 30,000 inhabitants of a nearby town (Frauenfeld in Figure B1).

At our local study site, the Thur River infiltrates year-round into the aquifer [Cirpka *et al.*, 2007], with a shallow local flow component at the top related to the infiltration of river water and a regional flow component in the lower sections following the main direction of the

valley. The overall direction of groundwater flow, influenced also by pumping well activity, is from northeast to southwest with fairly high velocities ranging between 1 and 50 m/day. The hydraulic conductivity of the aquifer is estimated from pumping and slug tests [Diem *et al.*, 2010] to range between 10^{-3} m/s and 10^{-2} m/s. Depending on the water table position, the aquifer displays unconfined and confined behavior.

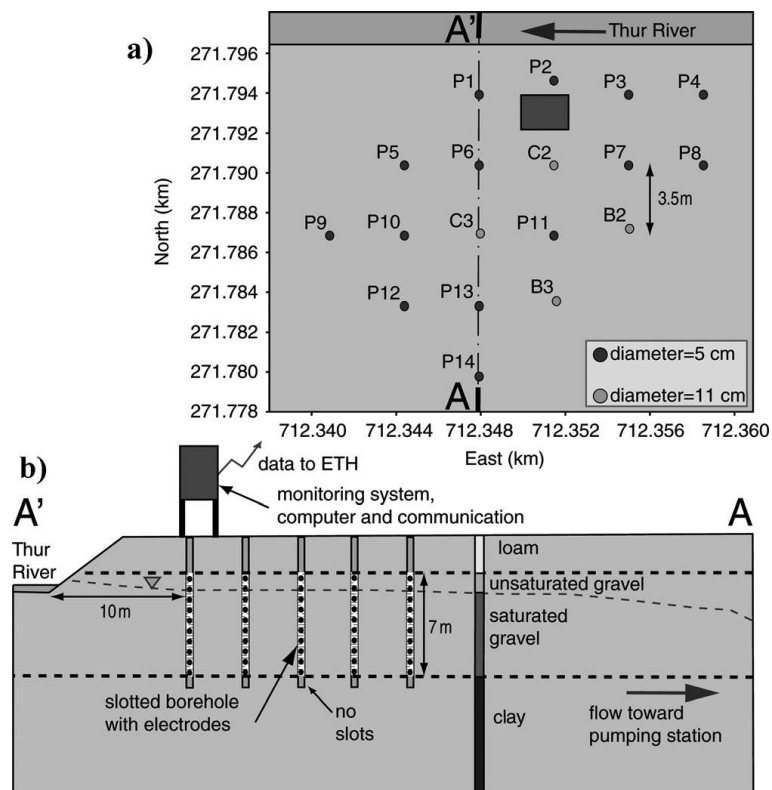


Figure B2. (a) Plan view of part of the Widen site showing borehole positions in Swiss grid coordinates with respect to the river and flood-proof hut (square). (b) Vertical section A' - A through the test site showing electrode installations, stratigraphy, groundwater table, and flow direction. Location of the section is shown in (a).

B.2.2 Experimental setup and field instrumentation

The main direction of groundwater flow, the hydrogeological parameters described in the previous section and surface ERT surveys to delineate the major vertical and horizontal resistivity variations at the site, guided the design of the electrical monitoring experiment. Eighteen boreholes at a nominal spacing of 3.5 m (Figure B2a) were installed with depths varying from 10 - 12 m. Four of them (B2, B3, C2, C3) are located at the corners of a square with 5 m side lengths and have 11 cm diameters to enable crosshole seismic and radar measurements to be made (Chapter 2) and to obtain samples in the coarse grain sedimentary

formation [Diem *et al.*, 2010]. The remaining 14 boreholes with 5 cm diameters were drilled using a direct-push machine. The entire borehole installation covers a surface area of 10 m × 15 m, which together with the 6.5 - 7 m thickness of the aquifer defines an investigation volume of approximately 1000 m³. All 18 boreholes are lined with PVC or HPDE casing that is slotted along the aquifer section. (see Figure B2b). Each borehole contains 10 stainless steel cylindrical electrodes, spaced 0.7 m apart. The electrodes are each equipped with rubber disk packers fixed above and below (Figure B3c) to reduce as much as possible the vertical flow of water and partially focus the electric current flow outwards into the formation. The electrodes are connected via waterproof cables to the recording system (Figure B3d). The lowest 9 electrodes are usually below the water table, providing good electrical connection to the sedimentary formation through the borehole water and slotted casing. The top electrode can only be used when it makes electrical contact during periods of high water level.

A flood-proof hut at the site houses the recording system (Figures 2b and 3a and e) and provides access to mains power and a wireless link for data transmission to ETH Zurich. The resistivity instrument provides 10 channel recording capability and is interfaced to a switching unit that allows up to 192 electrodes to be connected and automatically selected according to a pre-determined sequence. Software is used to control the recording unit from a field computer also housed in the elevated flood-proof hut. It is possible to pre-program the sequence of measurements at user-defined timing intervals and to store the recorded voltage data (and other information, such as current strength, electrode geometry) directly on the PC hard disc. Wireless connection to the field computer enables the measurements to be controlled in real time and the data downloaded from the PC disc to a computer back at ETH Zürich for back up, quality control, and processing purposes.

Geophysical well logs (natural gamma, gamma-gamma, and neutron-neutron) run in each borehole define the gravel - clay interface in a more precise way than just using the disturbed cores retrieved during the borehole drilling campaign. The logs are useful in evaluating the static inversion model results. To reduce systematic errors associated with incorrect positions of the electrodes, the trajectories of each borehole were determined by a three-axis magnetometer and three-axis accelerometer downhole system. In addition to the electrodes, 14 multisensor devices and integrated data loggers are installed in 6 of the boreholes at different depths. These multisensors measure temperature, electrical conductivity, and hydraulic head of the groundwater every 15 minutes. This information will be vital for meaningful interpretations of the time-lapse ERT data.

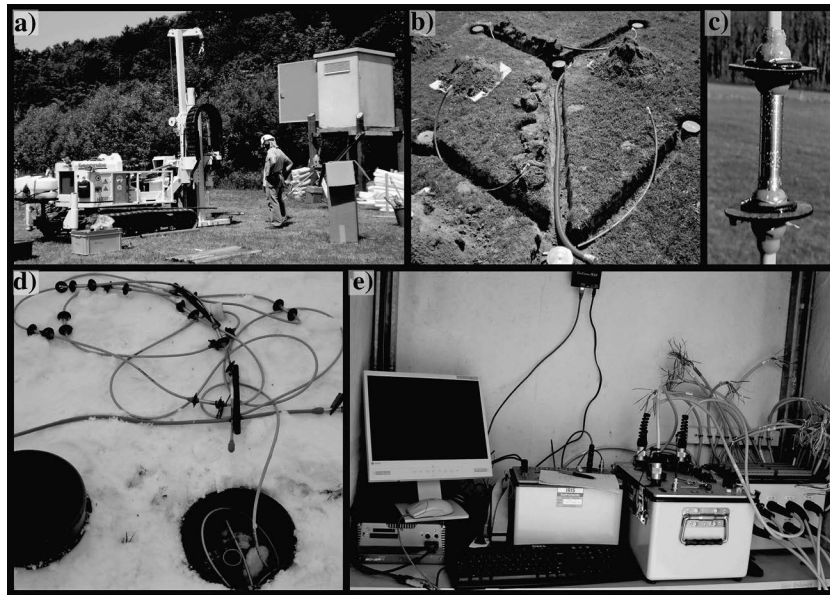


Figure B3. a) Direct-push drilling rig and, on the right, flood-proof hut. (b) Underground pipes connecting the geoelectric cables in the 18 boreholes with the measuring system inside the flood-proof hut. (c) Electrode with “packers”. (d) Geoelectric cable equipped for a 5 cm borehole. (e) Field computer and components of the geoelectric acquisition system with a modem for wireless connection (top) inside the flood-proof hut.

B.2.3 ERT data collection scheme

To have a fast and fully 3-D data-capture sequence, we designed, after some preliminary synthetic studies and taking into account the borehole fluid effect (Chapter 4), a circulating four-point measurement scheme with the current and potential bipoles split between multiple boreholes. The data collection sequence operates as follows (Figure B4). One current electrode (A) occupies only one of 2 allowed positions in the 2 central boreholes C1 and C2 (i.e., the third electrode position in borehole C2 or the sixth electrode position in borehole C3 - see Figure B2 for the borehole locations), and the other current electrode (B) is always in the same borehole as one potential electrode (M). This second current electrode can be at any one of 3 different depths (counting from the top: the second, fifth, and eighth electrodes), whereas the potential electrode in the same hole moves through 3 other depths (counting from the top: the third, sixth, and ninth electrodes). Finally, the remaining potential electrode (N) scans all the positions in the boreholes immediately surrounding the one where the bipole BM is located (Figure B4b). This data collection scheme is repeated until all boreholes have been occupied once by the bipole BM and the remaining mobile potential electrode N has created all possible electrode combinations as described above (see Figure B4c).

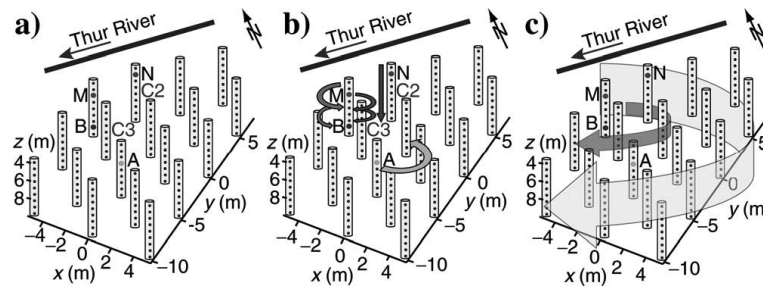


Figure B4. Illustration of how the configurations of the current electrodes A and B and potential electrodes M and N used in the geoelectric data acquisition system are circulated. (a) The 4 electrodes are always located in 3 different boreholes with A in only 2 possible positions in the two central boreholes. B and M always share a borehole and N is always in one of the boreholes immediately adjacent to them. (b) Movement of the electrodes is repeated for each borehole occupied by the current - potential (B - M) bipole. (c) Scheme repeated throughout the electrode array until the roving bipole has occupied all boreholes not occupied by the fixed current electrode.

This scheme is optimized to take advantage of the 10 independent channels of the recording system. A complete circulating sequence of approximately 15,500 data values (different electrode configurations across all 18 boreholes) is collected in 7 hours. The process is then repeated so that the aquifer is being continually monitored.

B.2.4 The river water as a natural electrical tracer

The hydrological regime of the Thur River is characterized by rapid undamped fluctuations of water level along its entire course after precipitation in the upper catchment. Associated with these fluctuations are significant changes to the electrical resistivity of the river water. As it infiltrates the aquifer, it acts as a resistivity anomaly that can be used as a natural tracer in time-lapse ERT imaging.

Figure B5 provides an example of the monitoring capability of the ERT system to track the magnitude and changing nature of this propagating resistivity anomaly. The presented data are for a flood event in the summer of 2009. When the river discharge increases, the river water resistivity increases. This can be readily observed by comparing the curve that represents the average water table height variation in the aquifer (Figure B5c) with the two curves that represent changes in water resistivity in the boreholes measured by the point loggers (Figure B5a). We show results from two loggers, one in borehole P3 close to the river and the other in borehole P12 some distance from the river (for locations see Figure B2a). Note the time delay between the peaks on the dotted and dashed curves (Figure B5a), clearly showing the transient nature of the infiltrating anomaly. It hits the borehole closest to the river

half a day earlier than that 15 m further away, and the signal magnitude is damped with increasing distance from the river. Figure B5a also shows the apparent resistivity time series (black circles) measured using the electrode configuration depicted in Figure B5b. This is a typical example of the ERT data trend during and following all flood events. The effect of the higher resistivity of the infiltrating water is readily apparent from the 15% anomaly over a period of several days

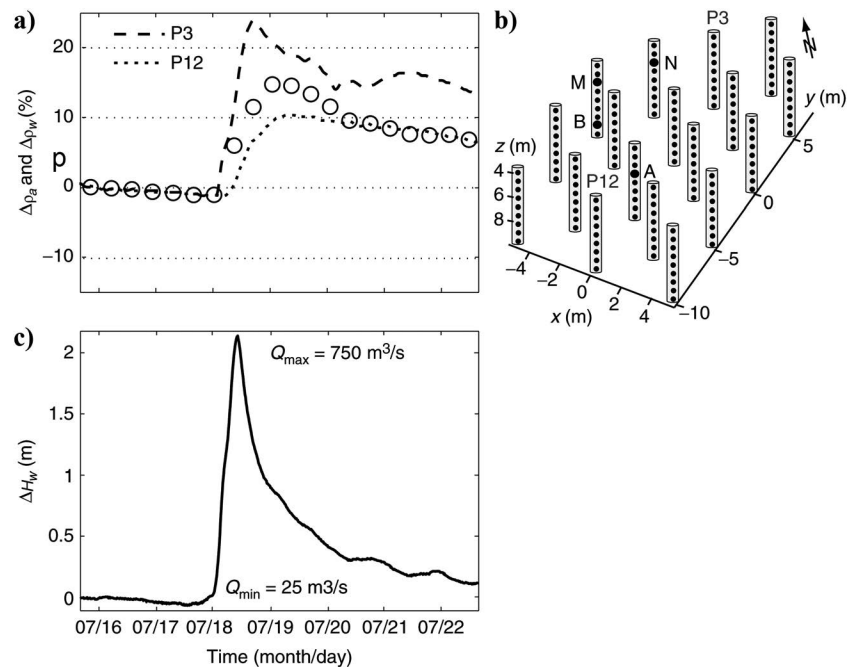


Figure B5. (a) Comparison between time series of relative apparent resistivity variations (black circles) during a strong hydrological event, and relative electrical-resistivity variations of the water at two locations (dotted and dashed curves - P3 and P12 near and far from the river, respectively). (b) ERT configuration used to record the apparent resistivity data shown in (a). (c) Mean variations of the water table position within the electrode array together with minimum and maximum discharges during the event.

B.3 FULL 3-D CROSSHOLE STATIC INVERSION

B.3.1 Static inversion approach and features

Our 3-D static inversions were performed using the open-source code BERT that is based on an unstructured finite-element framework [Günther *et al.*, 2006; Rücker *et al.*, 2006; www.resistivity.net]. It enabled all important aspects of the study site to be modeled in detail, including the surface topography, boreholes, and main geological boundaries (Figure B6).

The boreholes were explicitly modeled, taking into account their inclinations and declinations to correctly position all electrodes and reduce geometrical errors, which

otherwise could be significant (Figure B6b). Chapter 4 shows that the conductive borehole fluid has a strong effect on crosshole electric measurements for most standard AM-BN and AB-MN electrode configurations. They also demonstrated that this effect can be removed by explicitly including the boreholes in the modeling and inversion. This is especially important if the boreholes are closely spaced, the borehole diameters are large, and the resistivity contrasts between the fluid and host rock are high.

The overall stratigraphy at the site is well established. The approximate layer thicknesses are known from the boreholes and geophysical well logs, and the average layer resistivities are estimated from surface resistivity surveys. Under low river water conditions, the unsaturated part of the aquifer is approximately 1 m thick. It presents a significant resistivity contrast with the underlying saturated part of the aquifer that strongly influences the voltage measurements. As a consequence, the actual height of the water table should be determined from the borehole data loggers and fixed in the inversion, without imposing smoothness constraints (regularization) across what is known to be a sharp boundary (i.e., the very thin capillary fringe of gravel). From synthetic tests, we ascertain that the presence of the unsaturated gravel makes the sensitivities of the crosshole ERT measurements to the surface loam layer almost negligible. Therefore, the surface loam is not included in the initial model, allowing us to reduce slightly the number of inversion parameters. In analogy with the saturated - unsaturated interface, the clay - gravel interface is a boundary across which there is an order of magnitude resistivity contrast, such that it is desirable not to impose smoothness constraints across it.

The unsaturated and saturated zones of the aquifer, the gravel and clay layers, and the boreholes themselves constitute different regions in the inversion domain shown in Figure B6. This allows us to assign different initial values and different inversion parameters to each zone and to disconnect the regularization between the zones (see Table B1). A layered 1-D model of unsaturated gravel ($\rho_{m0} = 700 \Omega\text{m}$) underlain sequentially by saturated gravel ($\rho_{m0} = 250 \Omega\text{m}$) and clay ($\rho_{m0} = 25 \Omega\text{m}$) constitutes a reasonable starting model for the inversions (Figures B2 and B6b).

The inversion domain (Figure B6b), in which the above-mentioned initial model is defined, is embedded within a much larger forward modeling domain (Figure B6a). The former is kept small to reduce the size of the inversion problem; it extends horizontally approximately 2 meters outward from the most external boreholes and vertically to include the unsaturated gravels and approximately 2 meters of the clayey aquitard (Figure B2b). The

latter needs to be large to avoid boundary effects and, for the same purpose, has internal boundaries controlled by mixed boundary conditions [Günther *et al.*, 2006]. At each iteration of the inversion routine, the resistivity values defined in the inversion domain are laterally extrapolated into the forward modeling domain.

The approximately 205,500 tetrahedra of the mesh for the inversion domain were generated using the meshing code Tetgen (<http://tetgen.berlios.de>). This code allowed different mesh properties to be defined in each region of the domain. To delineate the structures precisely, we imposed a maximum volume of 0.05 m^3 on all tetrahedra within the saturated aquifer (Figure B6b). The forward mesh created by the code BERT refined the inversion mesh [Rücker *et al.*, 2006] to have approximately 1,800,000 elements corresponding to approximately 300,000 nodes. Some of the cells (9%) were very small (less than 5 cm side length) in order to represent the boreholes around which abrupt resistivity changes occurred. Accordingly, singularity removal [Blome *et al.*, 2009] was not required. This was recognized after running several modeling and inversion tests, which demonstrated that the very fine mesh allowed the high potential gradients around the borehole sources to be accurately modeled.

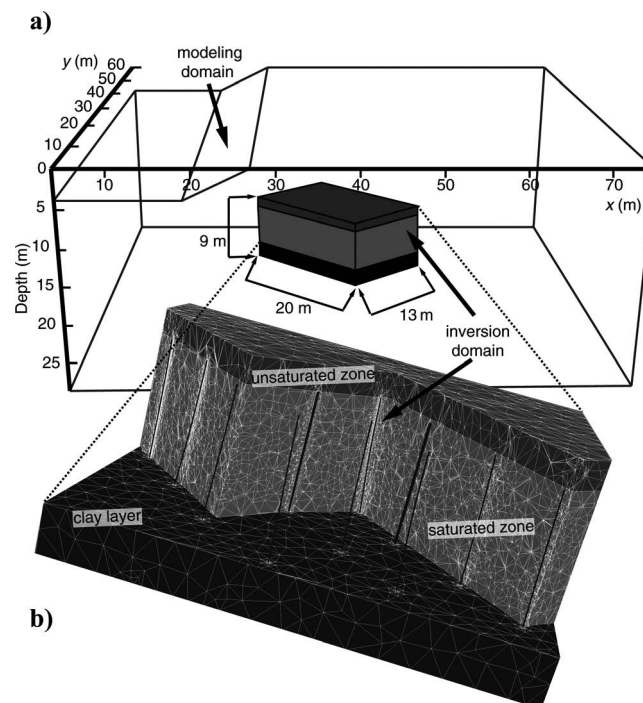


Figure B6. (a) Modeling domain with topography and the embedded inversion domain for the different regions (see Table B1), which shows the geometry of the input model for the inversion. (b) Unstructured parameter mesh, tilted boreholes and input topography of the saturated - unsaturated gravel and gravel - clay interfaces of the inversion domain.

We inverted for a logarithmic model function of the resistivity described as [Günther, 2004]:

$$m = \log(\rho - \rho_{lower}) - \log(\rho_{upper} - \rho), \quad (B1)$$

where ρ_{lower} and ρ_{upper} are lower and upper bounds defined for each region (see Table B1).

Within the aquifer, we employed anisotropic smoothing that penalized variations in the horizontal directions more than in the vertical direction to enhance the expected sub-horizontal layering in this region [see also Linde *et al.*, 2006a]. This was achieved by calculating a weighting factor W for the roughness matrix based on the vertical component of the normal vector n_z on each boundary between each tetrahedron of the mesh. The formulation for each tetrahedron boundary i is given by:

$$W_i = 1 + (w_z - 1) \cdot n_z, \quad (B2)$$

where w_z is a user-defined factor that can vary in each region of the model. This along with all other parameters used in each region of the inversion model are listed in Table B1.

The data set selected for determining a static 3-D resistivity model of the site was collected on 15 November 2009, during a period of stable hydrological conditions. The water level in the river was low and the groundwater table was approximately 4.2 m below the surface. Consequently, approximately 1 m of the aquifer was unsaturated. The approximately 22 Ωm electrical resistivity and approximately 8°C temperature of the water was similar on all the borehole sensors.

First we only considered configurations having electrode geometrical factors $K \leq +/- 1000$, as a protection against probable low signal-to-noise data. Then, from the raw apparent resistivity data, we excluded all data values having standard deviations $> 1\%$ based on repeat measurements or voltages < 1 mV. After that, we eliminated all data based on electrode configurations in which one or more of the electrodes were above the water table (i.e. those that had very high contact resistances). We also discarded all the negative apparent resistivities because of the limitation of the inversion code in handling negative values. Furthermore, we rejected any apparent resistivities greater than 500 Ωm or smaller than 30 Ωm . These upper and lower limits were set after first observing the frequency distribution (histogram) of apparent resistivities and considering the likely range of resistivities for saturated sandy gravel. Finally, approximately 12,000 data points (approximately 77% of the original data set) were used in an initial inversion aimed at defining the remaining outliers in the data set not removed in the previous data selection sequence (see later).

Finally, we apply an error model for weighting the data and the elements of the Jacobian matrix (sensitivities) during the inversion. The error (or uncertainty) for each voltage measurement is considered to consist of two parts [see *LaBrecque et al.*, 1996b]: a fixed absolute value of 0.1 mV (set by the instrument precision) and a relative error of 2% of the measured value (although we did experiment with other values in the range 1 - 4%). This yields an uncertainty of $\delta U = (0.1 + 0.02U)$ mV, where U is the recorded voltage in mV. When considering resistance or apparent resistivity as the input data, one should ideally take into account sources of errors related to the current strength and electrode positions, but these are judged to be much smaller than the voltage uncertainties. Moreover, the inversion code that we employ uses the logarithms of apparent resistivities $\log(\rho_a)$, rather than voltages or apparent resistivities themselves, therefore the estimated errors in these quantities used in data weighting matrix should be computed from the calculus of small changes (i.e., $\delta(\log(\rho_a)) = \delta U / U = (0.1 + 0.02U) / U$). Although time consuming, we recalculate the Jacobian matrix (slightly less than 20 GB) after each iteration of the inversion and apply a robust reweighting of the data according to their misfit. For this reason, the initial median data error (2.02%) was, at the end of the inversion, slightly increased to 2.04%.

For all regions we apply a regularization parameter λ equal to 100 with an upscaled smoothness factor for the borehole region of the model (see Table B1). Tests were conducted with other λ values in the range 5 - 200. Conventional wisdom is to opt for the largest value consistent with being able to fit the data within a specified tolerance (say 2%). Smaller values of λ can introduce more detail in the model, some of which might be spurious, whereas overly large values yield excessively smooth models. We found that using values larger than 100 removed a small conductive feature that was independently known from the borehole logging [for further details about the error model and the choice of the regularization see also *Günther*, 2004].

After an initial inversion, we plotted the frequency distribution of data misfits and excluded those measurements lying outside a threshold given by 5 times the standard deviation of the distribution. The final data set, corresponding to almost 11,000 data points, was inverted using the same parameters as for the initial inversion. The inversion run time on a 2.66 GHz quad-core computer with 32 Gb of RAM was approximately 15 hours and it converged to the specified tolerance level ($\chi^2 = 1$) in 6 iterations.

Table B1. Inversion parameters used for each region of the model shown in Figure B7.

Region	Initial model resistivity ρ [Ωm]	Regularization type	Scaling factor n for the regularization parameter	Bounding values $\rho_{\text{lower}} - \rho_{\text{upper}}$ [Ωm]
Unsaturated gravel aquifer	700	Anisotropic smoothing ($w_z = 0.3$)	1	50 - 2000
Saturated gravel aquifer	250	Anisotropic smoothing ($w_z = 0.1$)	1	50 - 500
Aquitard (clay layer)	25	Anisotropic smoothing ($w_z = 0.3$)	1	5 - 45
Boreholes	22	Isotropic smoothing ($w_z = 1$)	10	10 - 50

B.3.2 Results

Figure B7 shows two vertical slices through the final 3-D model volume corresponding to the saturated part of the aquifer, one close and mainly parallel to the river (Figure B7a) and the other mainly along the principal diagonal (Figure B7b). The top and bottom layers (not shown) of the entire model correspond to the unsaturated gravel and the clay aquitard, respectively.

A central zone within the saturated gravel that is roughly 50 % more resistive (up to 320 Ωm) than the upper and lower parts (120 - 220 Ωm) is clearly delineated in the tomogram. It has an average thickness of approximately 2 m and lies in the 5 - 5.5 to 7 - 7.5 m depth range. It appears to be horizontal and continuous throughout the investigated volume. Earlier inversions, which were run without horizontal smoothing, show slightly inferior continuity of the resistive layer but still recover the layer.

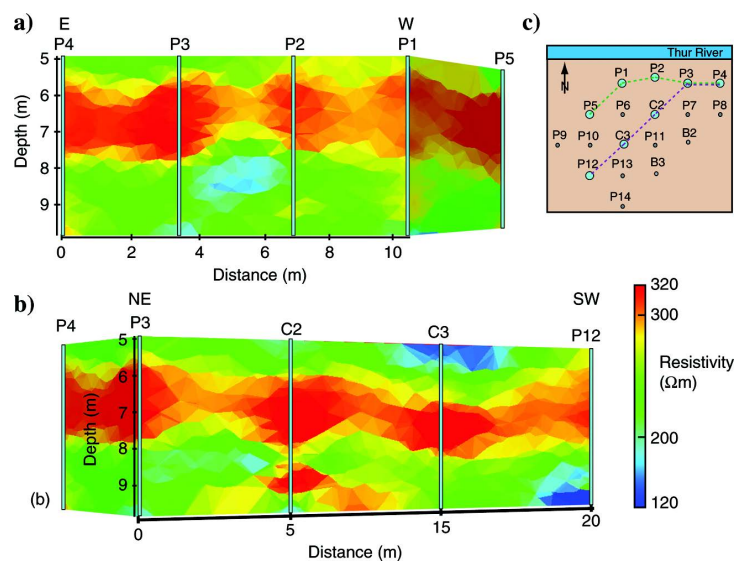


Figure B7. Resistivity cross sections extracted from the final inverted 3-D model viewed from the river looking to the (a) south (green dashed line) and (b) southeast (violet dashed line). (c) The locations of boreholes corresponding to the 2 slices in (a) and (b) are light blue.

In the plane containing the line of boreholes that lie close to the river (Figure B7a), the tomogram contains a more conductive zone (in blue) of approximately 1 m thickness. This zone is characterized by resistivities of approximately 130 Ωm . It corresponds to a lens of fine sediments observed in the drill core of nearby boreholes (P2 and P3). The resistive zone above this conductor appears less continuous, but this is probably caused by the resolution pattern in this area, which is strongly influenced by the presence of the conductive zone; being relatively conductive, the current is drawn into the zone, thereby decreasing current density and hence sensitivity elsewhere.

Further from the river, a decrease in the resistivity of the lower part of the aquifer is observed (Figure B7b). This could represent a higher percentage of fine material in proximity to the underlying clay.

B.4 DISCUSSION

B.4.1 Inversion aspects

The distances between the boreholes are rather small (3.5 m), such that any borehole deviations need to be considered. Given the maximum tilt of some boreholes (3°), electrode mispositioning can be as much as 0.5 m if the boreholes are incorrectly assumed to be vertical. The tomograms would be adversely affected by such an error. We undertook some tests on a subset of data from 8 of the boreholes and found that the central more resistive layer within the aquifer becomes noticeably less continuous when the boreholes are taken to be uniformly vertical instead of slightly tilted.

Chapter 4 investigates the borehole fluid effect, whereby the resistivity contrast between the borehole fluid and host rock can introduce false structure in the medium after inversion if the boreholes are not explicitly modeled. We have established from a series of inversion tests that for the particular unconventional electrode configurations that we employed (see Section B.2.3) the borehole effect is minor. Very similar images (not shown) were obtained by ignoring the boreholes in the inversion process. This was partly a consequence of the relatively low resistivity contrast between the borehole fluid and the formation (8:1) and the fact that for most of the data collected with our unconventional configurations, the electrodes were placed in small diameter holes (5 cm); there would be significant artifacts in the images if classical electrode configurations (especially those having either the current electrodes or the potential electrodes in the same borehole) were to be employed, as in the study of Chapter

4. Inversions without including the boreholes require substantially fewer cells, thus reducing the memory requirements and the under-determined nature of the problem.

Another important technical consideration is decoupling the regularization across the layers and preserving the sharp boundaries where they are known to exist (e.g., at the water table and at the clay - gravel interface). This entails setting the weight of the individual model cells to zero in the presence of a known boundary, resulting in sharp gradients at this position. Failure to do so produces significant smearing and artifacts in the images. For example, since the clay is 10 times less resistive than the wet gravel, without layer decoupling the inversion produces an interface much shallower than that defined by the drill core and well-log data. This is illustrated in Figure B8, which shows inversion results along the section presented in Figure B7a adjacent to the river. The two plots correspond to inversions with (Figure B8a) and without (Figure B8b) decoupling the regularization between the layers. Notice the distortion of the clay interface and the disappearance of the low resistivity lens when no decoupling is applied. We performed several tests to confirm the importance of incorporating the correct positions of the known resistivity discontinuities. Surface topography should also, as a general rule, be incorporated in the inversion process, but from various synthetic tests we were able to establish that the zone of interest (saturated aquifer) is far enough away (i.e., at sufficient depth) that the measurements are only weakly sensitive to the sloping river bank topography.

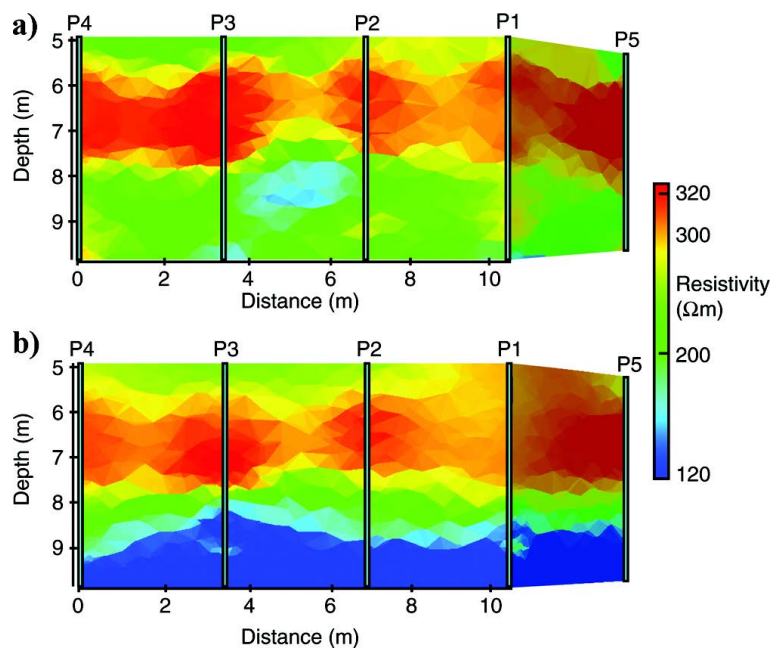


Figure B8. Cross sections extracted from inversion models in which the regularization between the layers is (a) decoupled (same as Figure B7a) and (b) not decoupled.

We have also compared our inversion model with that obtained at the site (Chapter 2) by jointly inverting seismic, radar, and ERT data sets acquired in the 11-cm-diameter boreholes (see Figure B2a for locations). The resistivity structures observed in the two studies were very similar.

B.4.2 Comparison between the inversion model and other data

Neutron-neutron, gamma-gamma, and natural-gamma well logs are available for all 18 boreholes. To compare the electrical variability of the aquifer with the well-log information, we compute average vertical resistivity profiles for each borehole. For this purpose, the average resistivity is calculated for a 40-cm-diameter 20-cm-high cylindrical volume centered about the borehole and about each point. Assuming that the highest number of counts of the neutron-neutron logs represents 50 % porosity and the lowest represents 12% porosity, corresponding to values estimated at the geologically similar Boise hydrogeophysical research site [Barrash and Clemo, 2002], the raw logs can be converted to approximate porosity estimates. The natural gamma log (not calibrated) gives information about the clay content [Revil *et al.*, 1998]. Figure B9 shows a comparison of the average vertical profile through the resistivity tomogram of borehole P3 with the relevant neutron-neutron (converted to porosity) and the natural gamma logs. The correlation coefficients between the average resistivity profile and well logs are -0.88 and -0.94, respectively. The central high resistivity zone of the aquifer has a relatively low porosity and low clay content (see also Chapter 2), whereas the lower resistivity region at the base of the aquifer is characterized by relatively high porosities and high clay content, consistent with the lens of fine sediments located in this depth range (see Figure B7a and Section B.3.2).

Electrical conductivity logs were also recorded at the site using a direct-push machine [Schulmeister *et al.*, 2003]. This system incorporated a Wenner array with an electrode spacing of 10 cm. The measurements were progressively made as the tool was hammered into the ground. Such resistivity logs were acquired at a total of 10 different locations between the boreholes. The instrument measured the average resistivity of the earth to a radius of approximately 10 cm (one third the current electrode spacing) centered about the borehole, whereas the vertical resolution was estimated to be approximately 10 cm. Measurements were taken at 2-3 cm depth intervals. Before each data set was acquired, the system was tested and calibrated. Figure B10 shows a representative vertical resistivity profile extracted from the inversion model at the same location where an electrical conductivity log was recorded. To be

comparable with the lower resolution ERT profile, the log data were averaged over 40-cm-depth intervals using a running average smoother. The trends of the two data sets are similar with a correlation coefficient of 0.73.

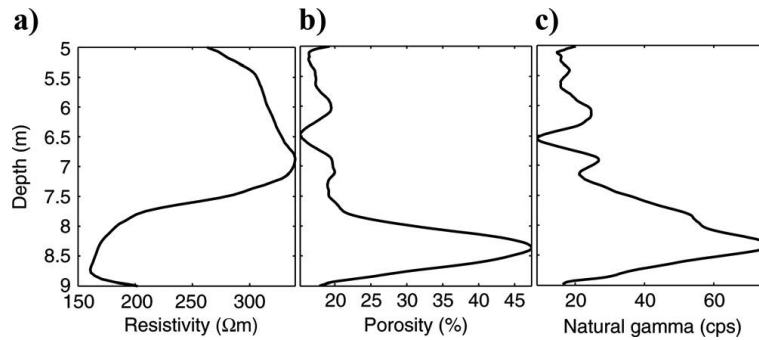


Figure B9. For borehole P3, comparison between vertical profiles of (a) resistivity extracted from the final inverted 3-D model around the borehole, (b) the neutron-neutron log converted to porosity, and (c) the natural gamma log.

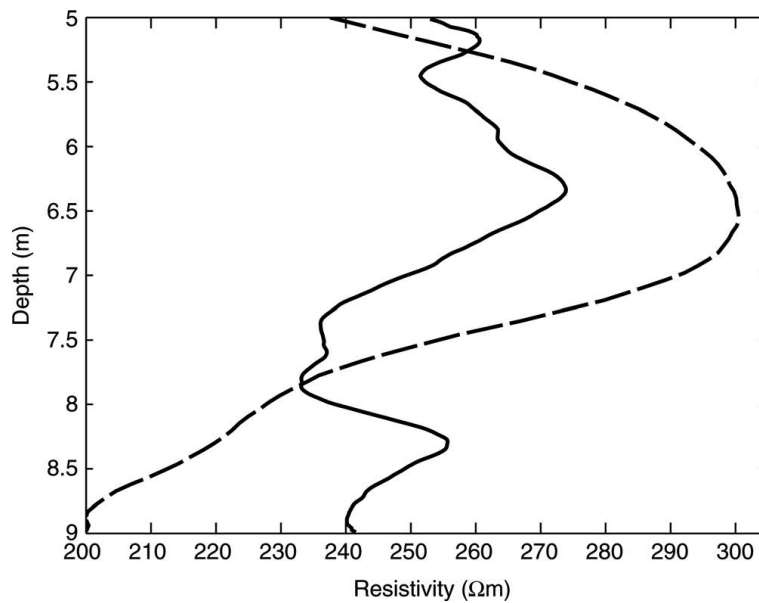


Figure B10. Example of a vertical resistivity profile extracted from the final ERT inversion model (dashed line) and a coincident resistivity log obtained with a Direct Push probe system (full line).

B.5 CONCLUSIONS

We have installed a resistivity monitoring system to study the hydrogeological properties of a gravel aquifer using flood events of an adjacent river as a natural electrical tracer. Eighteen boreholes equipped with total of 180 electrodes allow continuous collection of crosshole ERT measurements that can be used in both a static and dynamic sense to characterize the lithological sub-units and hydraulic properties of the aquifer. We utilize an unconventional fully 3-D data acquisition sequence that enables the collection of approximately 15,500 voltages (apparent resistivities) every 7 hours, of which roughly 11,000 are retained for the final inversions.

Approximately one year of ERT time series have now been acquired. They show the natural fluctuations of the water electrical properties of the adjacent infiltrating river. We have presented one example of a flood event, which produces a 15 % apparent resistivity anomaly, clearly showing how the geoelectrical data contain valuable information about the river infiltration process.

We have investigated problems related to inverting a very large static crosshole ERT data set. Disconnecting the regularization across the known sharp layer boundaries (water table and gravel - clay interface) and correct positioning of the electrodes were necessary to obtain meaningful results. Including the boreholes in the inversion (i.e., the borehole-fluid effect) would have avoided generating artifacts when using more classical electrode configurations. For the unconventional circulating 3-D electrode acquisition scheme employed in this study, we determined that the borehole-fluid effect was not significant. Accordingly, this scheme is a viable option when computing limitations are an issue or when unstructured FEM codes are unavailable.

The 3-D inversion of the chosen static ERT data set yielded a roughly 3-layer gravel aquifer model with superimposed minor variations. The central zone of the model, corresponding to roughly one third of the aquifer thickness, is 50 % more resistive than the upper and lower regions. The inverted model correlates with the geophysical well log data at the site. In particular, we observe strong correlations between the resistivity and neutron-neutron (representing porosity) and natural gamma (representing clay content) logs. From these comparisons, we interpret the relatively high-resistive central zone as being of lower porosity and the relatively low-resistive lower part of the aquifer as containing a larger proportion of fine sediments. These results are consistent with those previously obtained from

jointly inverted crosshole seismic, radar and ERT data acquired over a sub-volume of the experimental site.

This research forms the basis for future time-lapse ERT inversion that will be used to track preferential flow paths in the aquifer delineated by the infiltrating river water with different electrical properties and flow rates. A key challenge for the 4D imaging will be to separate the temporal effects of water table height, resistivity (salinity), and temperature variations. In fact, these three state variables, which are simultaneously sensed by the ERT data, can even have opposing effects on the data and make difficult the interpretation of the time-lapse results. To this end, we plan to investigate in detail the observed correlation between the input time series of the water height, resistivity and temperature in the river and the output ERT time series, and then filter the data in order to isolate the signal of interest related to the infiltrating less saline river water.

APPENDIX C: FULL-WAVEFORM INVERSION OF GPR DATA FROM THE THUR RIVER AQUIFER

Published in *Near Surface Geophysics*:
Klotzsche, A., van der Kruk, J., Meles,
G. A., Doetsch, J., Maurer, H., and Linde,
N., 2010, Full-waveform inversion of cross-
hole ground-penetrating radar data to
characterize a gravel aquifer close to the
Thur River, Switzerland: *Near Surface
Geophysics*, **8**, 635-649.

ABSTRACT

Crosshole radar tomography is a useful tool for mapping shallow subsurface electrical properties viz. dielectric permittivity and electrical conductivity. Common practice is to invert crosshole radar data with ray-based tomographic algorithms using first arrival traveltimes and first cycle amplitudes. However, the resolution of conventional standard ray-based inversion schemes for crosshole ground penetrating radar (GPR) is limited because only a fraction of the information contained in the radar data is used. The resolution can be improved significantly by using a full-waveform inversion that considers the entire waveform, or significant parts thereof. A recently developed 2-D time-domain vectorial full-waveform crosshole radar inversion code has been modified in the present study by allowing optimized acquisition setups that reduce the acquisition time and computational costs significantly. This is achieved by minimizing the number of transmitter points and maximizing the number of receiver positions. The improved algorithm was employed to invert crosshole GPR data acquired within a gravel aquifer (4 - 10 m depth) in the Thur valley, Switzerland. The simulated traces of the final model obtained by the full-waveform inversion fit the observed traces very well in the lower part of the section and reasonably well in the upper part of the section. Compared to the ray-based inversion, the results from the full-waveform inversion show significantly higher resolution images. At either side, 2.5 m distance away from the crosshole plane, borehole logs were acquired. There is a good correspondence between the conductivity tomograms and the Natural Gamma logs at the boundary of the gravel layer and the underlying lacustrine clay deposits. Using existing petrophysical models, the inversion results and Neutron-Neutron logs are converted to porosity. Without any additional calibration, the values obtained for the converted Neutron-Neutron logs and permittivity results are very close and similar vertical variations can be observed. The full-waveform inversion provides in both cases additional information about the subsurface. Due to the presence of the water table, and associated refracted/reflected waves, the upper traces are not well fitted and the upper 2 m in the permittivity and conductivity tomograms are not reliably reconstructed because the unsaturated zone is not incorporated into the inversion domain.

C.1 INTRODUCTION

Crosshole radar tomography is a useful tool for mapping shallow subsurface electrical properties, such as dielectric permittivity (ϵ) and electrical conductivity (σ), in connection with assorted geological, hydrological and engineering investigations. These parameters are

closely linked with important hydrogeological parameters like salinity, water content, porosity and pore structure, clay content, and lithological variations [Archie, 1942; Topp *et al.*, 1980; al Hagrey and Müller, 2000; Barrash and Clemo, 2002; Garambois *et al.*, 2002; Linde *et al.*, 2006a; Turesson, 2006]. Crosshole radar surveying entails the generation of high-frequency electromagnetic pulses from a dipole-type antenna which is sequentially positioned at a number of locations along a borehole. The resulting transmitted and scattered waves are detected (and subsequently recorded) by means of a dipole antenna which is progressively moved to a number of discrete locations in a second borehole. The center frequency of most borehole antennas for GPR lies in the range 20-250 MHz (dominant wavelengths of 5-0.4 m) for common geologic materials.

A number of studies have estimated hydrogeological parameters by inverting crosshole ground penetrating radar (GPR) data using ray-based inversion schemes, similar to that described by Holliger *et al.* [2001]. For example, Tronicke *et al.* [2002] examined the integration of surface GPR and crosshole radar tomography on braided stream deposits while Binley *et al.* [2002b; 2002a] and Winship *et al.* [2006] used crosshole GPR to monitor moisture content changes arising from tracer experiments. Linde *et al.* [2006a] were able to improve hydrogeological characterization by using a joint inversion of crosshole electrical resistance and (GPR) traveltime data. Looms *et al.* [2008] monitored unsaturated flow and transport by using cross-borehole GPR and electrical resistance tomography (ERT). These traditional tomographic inversions of crosshole GPR data use separate inversions of traveltimes and maximum first cycle amplitudes based on ray theory and provide velocity and attenuation images of the subsurface that can be transformed into electromagnetic permittivity and electrical conductivity. Radar tomography based on ray theory provides only limited resolution and can account for just a small fraction of the information in the traces, such that small targets (smaller than the dominant wavelength) cannot be satisfactorily detected and imaged. By contrast, full-waveform inversion not only takes into account the arrival-times and first cycle amplitudes, but considers the entire waveforms (or at least the first few cycles) which include secondary events like forward scattered and refracted waves. Therefore, full-waveform inversions provide higher resolution images and can thus yield more detailed information for a wide range of applications.

Waveform-based inversion schemes were first developed in seismic exploration subject to the acoustic (P-wave only) approximation [Tarantola, 1984a; b; 1986] and later modified for elastic (P + S) wave propagation [Mora, 1987]. Following these early developments, several

inversion methods were developed and applied to seismic data for surface and/or borehole measurements. The methods have been adapted to the acoustic-, elastic-, viscoelastic-, and anisotropic-wave equations in both the time and frequency domain, using finite-difference and finite-element approaches to solve the forward problem i.e. to generate the synthetic seismograms [e.g., *Bing and Greenhalgh*, 1998a; b; *Pratt*, 1999; *Pratt and Shipp*, 1999; *Zhou and Greenhalgh*, 2003; *Watanabe et al.*, 2004]. Full-waveform seismic inversion is extensively discussed in the November 2008 issue of the journal *Geophysical Prospecting* and contains numerous other references. Comparable efforts for the full-waveform inversion of GPR data have been limited to just a few papers [*Ernst*, 2007; *Ernst et al.*, 2007b; *Ernst et al.*, 2007a; *Kuroda et al.*, 2007; *Meles et al.*, 2010]. *Ernst et al.* [2007a] developed a full-waveform scalar inversion scheme for electromagnetic waves for crosshole GPR data based on the 2-D finite difference time domain solution of Maxwell's Equations using generalized perfectly matched layers (GPML) to reduce artifacts from reflections at the boundaries and edges of the model space. This scheme was tested on synthetic and observed crosshole data [*Ernst et al.*, 2007b]. It was shown that this algorithm provides higher resolution permittivity and conductivity images of the subsurface than conventional ray-based techniques. Similar to *Ernst et al.* [2007b], *Kuroda et al.* [2007] applied a full-waveform inversion algorithm to synthetic crosshole radar data. *Meles et al.* [2010] improved the method of *Ernst et al.* [2007b; 2007a] by including the vector properties of the electric field, which enabled extension of the algorithm to incorporate surface-to-borehole measurements, in addition to crosshole measurements. Furthermore, the permittivity and conductivity parameters were simultaneously updated, which proved to be superior to the sequential (cascaded) update approach of *Ernst et al.* [2007a].

In this work we apply the approach described in *Meles et al.* [2010] to invert a crosshole GPR data set acquired within a gravel aquifer in northern Switzerland (Chapter 2). First, we give an overview of the full-waveform inversion algorithm. Then, we discuss the borehole setup and measurements, followed by our data analysis procedures. Finally, the reliability of the inversion results is investigated by comparisons with borehole logging data.

C.2 FULL-WAVEFORM INVERSION METHODOLOGY

The workflow of the full-waveform inversion scheme which uses a simultaneous updating of permittivity and conductivity is shown in Figure C1. First, we describe the pre-processing

followed by the source wavelet estimation. Then we discuss the inversion algorithm and implementation details.

C.2.1 Pre-Processing

Initially, the data are band-pass filtered to remove noise outside the source spectrum (Figure C1, step A). A good initial model is required for the full-waveform inversion algorithm to converge to the global minimum. Otherwise it may get trapped in a local minimum. The starting model is typically obtained by standard ray-based inversion techniques. First-arrival traveltimes and first-cycle amplitude are used for the ray-based inversion to obtain velocity and attenuation tomograms of the subsurface which are then transformed into permittivity and conductivity distributions (Figure C1, step B).

To apply the 2-D-full-waveform inversion algorithm to real data it is necessary to account for the 3-D radiation characteristics of electromagnetic wave propagation. Similar to *Ernst et al.* [2007b] we apply a 3-D to 2-D transformation technique developed by *Bleistein* [1986] to compensate for differences in geometrical spreading and pulse shape (frequency scaling and phase shifting; Figure C1, step C).

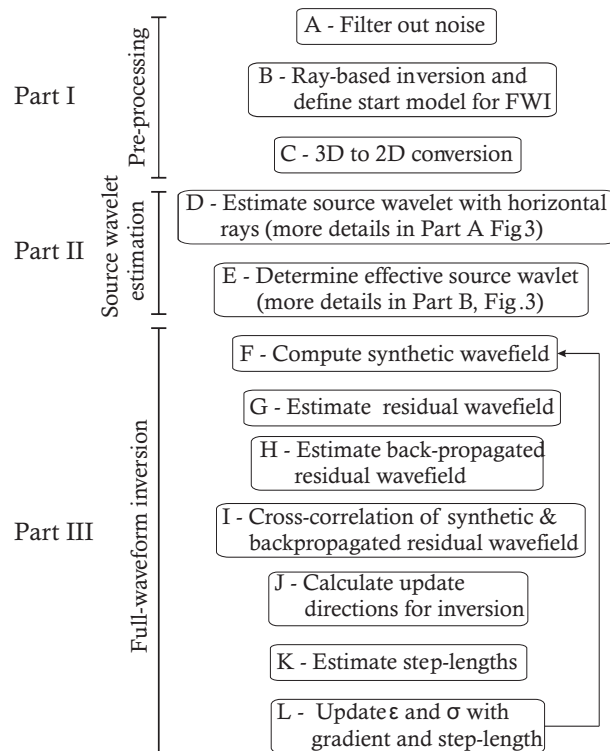


Figure C1. Full-waveform inversion workflow showing the three main parts: pre-processing, source wavelet estimation and full-waveform inversion. The arrow indicates that these steps should be repeated until the misfit between the observed and synthetic data between iterative steps is below 1%.

C.2.2 Source wavelet estimation

The source wavelet estimation (Figure C1, steps D and E) is a critical step in the inversion. Only through obtaining an effective source wavelet is it possible to match the measured waveforms, including any small nuances, which may be present. This wavelet not only reflects the current density pattern of the finite length GPR antenna but also its radiation pattern in a water-filled borehole. The steps in the source wavelet recovery are illustrated in detail in Figure C2 [extended from *Ernst et al.*, 2007b], where the Fourier transformed quantities are indicated by $\hat{\cdot}$. First, an initial source wavelet is estimated (Figure C2, Part A), where only the shape of the wavelet is determined without considering any amplitude information. All traces from a vertical zero offset profile (ZOP), containing only horizontally traveling waves, are normalized and aligned to estimate an average pulse (Figure C2, step 1). By cross-correlating the ZOP traces, data containing erroneous wave shapes due to e.g., interfering reflections are identified and excluded. We know from Maxwell's equations that the electric field is proportional to the time derivative (multiplication with $i\omega$ in the frequency domain) of the current density source wavelet. To obtain the shape of the initial source wavelet we divide the average Fourier transformed pulse (electric field) by $i\omega$ in the frequency domain (Figure C2, step 2).

In Part B (Figure C2) we calculate a corrected wavelet with detailed amplitude and phase characteristics. The forward modeling is done using the Cartesian coordinate, 2-D finite-difference time-domain (FDTD) code of *Ernst et al.* [2007a]. The synthetic radargrams \mathbf{E}^{syn} , for each transmitter-receiver position, are calculated using the model of permittivities and conductivities obtained from the ray-based inversion (indicated by “ray”) and the initial source wavelet (Figure C2, step 3 and 4). The radar data can be viewed as the convolution of the source wavelet with the impulse response (Green's function) in the time-domain or as the multiplication of the source spectrum with the Fourier-transformed Green's function. Therefore, an effective source wavelet can be obtained by deconvolving the radar data $\hat{\mathbf{E}}^{\text{obs}}$ with an appropriate Green's function $\hat{\mathbf{G}}$ calculated using the traveltimes inversion results as input. This is best done using a least-squares approach in the frequency domain [*Ernst et al.*, 2007b; *Streich and van der Kruk*, 2007b]. The transfer function $\hat{\mathbf{G}}$ is calculated by spectral division of $\hat{\mathbf{E}}^{\text{syn}}$ in the frequency domain with the initial wavelet spectrum $\hat{\mathbf{S}}_{k=0}$ for each separate trace (Figure C2, step 5). Next, we estimate $\hat{\mathbf{S}}_{k=1}$ by dividing the actual observed data $\hat{\mathbf{E}}^{\text{obs}}$ with the transfer function $\hat{\mathbf{G}}$, using all traces in a least squares sense (Figure C2, step 6). Quantities η_{D} and η_{I} are prewhitening factors which are applied to stabilize the solution and

avoid dividing by zero (should there be any notches in the spectrum of \mathbf{G}). The time-domain source wavelet $S_{k+1}(t)$ is obtained by an inverse Fourier transformation (Figure C2, step 7). Steps 3-7 can be repeated until the source wavelet has converged (Loop 1), where k indicates the iteration number. In Part C (Figure C2) a source wavelet refinement can be applied during the full-waveform inversion to improve the wavelet when necessary (Loop 2).

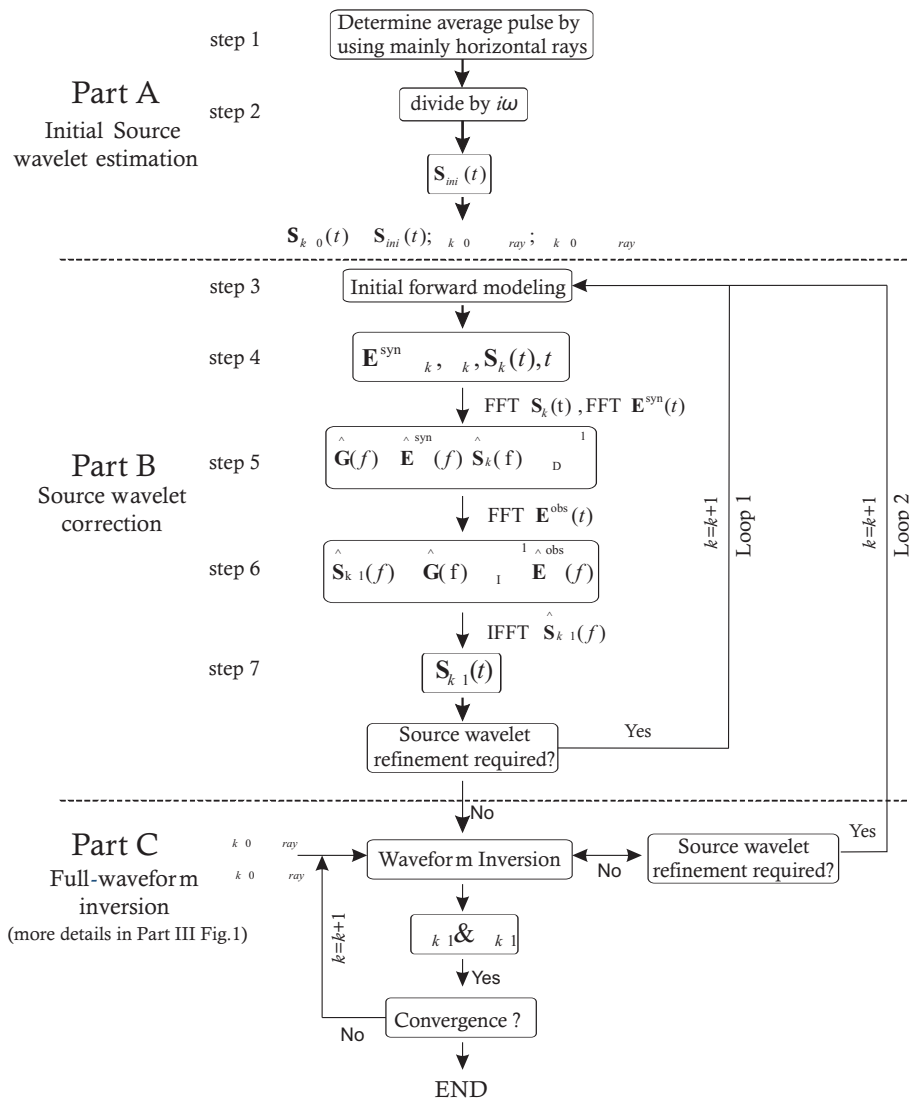


Figure C2. Source wavelet estimation flow consisting of three parts: Part A - initial source wavelet estimation using averaged horizontal rays (steps 1-2), Part B - the source wavelet correction (steps 3-7) with the deconvolution method using all available data (extended from *Ernst et al. [2007b]*) and Part C - source wavelet refinement during the full-waveform inversion. This source wavelet estimation is always carried out before starting the full-waveform inversion (loop 1), and can also be performed after several iterations of the full-waveform inversion (loop 2).

C.2.3 Inversion algorithm

The full-waveform inversion is based on Tarantola's approach [1984a; b; 1986] and uses a gradient-type method (Figure C1, Part III). The cost function (or misfit function) $C=0.5 \|\mathbf{E}^{\text{syn}}-\mathbf{E}^{\text{obs}}\|^2$, which is the difference between the simulated (\mathbf{E}^{syn}) and observed (\mathbf{E}^{obs}) traces, is minimized for all transmitter-receiver combinations within a selected time window. This is achieved by computing the gradient of C , which indicates the update direction of the permittivity and conductivity models. Furthermore, individual step lengths need to be determined that indicate the magnitude of the model updates.

To calculate the gradient ∇C , the forward propagated wavefield \mathbf{E}^{syn} is computed using the estimated source wavelet and the model from the previous inversion iteration (the ray-based inversion model is used for the first iteration). The wavefields are stored in memory for each transmitter and each time step (Figure C1, step F). Then, the residual wavefield is calculated by subtracting the synthetic wavefield from the observed wavefield (Figure C1, step G) and for each transmitter, this residual wavefield is backpropagated from all receivers to the corresponding transmitters (Figure C1, step H). Finally, the gradient at each point \mathbf{x} is obtained by a zero-lag cross-correlation of the stored values of \mathbf{E}^{syn} with the backpropagated residual wavefield, and by summing over all transmitters and times (Figure C1, step I and J). Constructive interference occurs at positions in space where the true and modeled medium properties deviate, and the gradient indicates how to change the model parameter values to reduce the misfit function.

After estimating the permittivity and conductivity gradients (Figure C1, step J), the step-lengths are calculated (Figure C1, step K). According to *Meles et al.* [2010] individual step-lengths are necessary to simultaneously update the permittivity and conductivity models. Finally, the permittivity ϵ and conductivity σ at the current iteration are updated with the obtained gradient directions and step lengths (Figure C1, step L). For terminating the inversion loop, we use a stopping criterion of 1% change of the root mean square (RMS) error between the observed and synthetic data between subsequent iterations [*Ernst et al.*, 2007b].

C.2.4 Implementation details

The computational costs of the full-waveform inversion are determined mainly by the FDTD calculations. The full-waveform algorithm requires solving the forward problem four times during each iteration. With the first solution the residual wavefield is calculated, the second solution is required to compute the model update directions (gradients) and two FDTD

calculations are needed for determining the step-lengths. The calculations for each transmitter position are independent from each other. Therefore, the algorithm can be parallelized easily (for each transmitter one slave CPU is required, and one master CPU coordinates the computations). The overhead for the distribution of the computations is about 10% using the MPI system [Ernst *et al.*, 2007b; Ernst *et al.*, 2007a].

During the calculation of the gradient, the forward modeled field \mathbf{E}^{syn} remains in the computer memory. The required memory M is estimated by

$$M(\text{bytes}) = \frac{n_{xf} \cdot n_{zf} \cdot \text{timesamples} \cdot 2 \cdot 8}{\text{invfwd}^2} \cdot N_{TRN}, \quad (\text{C1})$$

where n_{xf} and n_{zf} are the numbers of the horizontal and vertical forward modeling cells, the value 2 indicates the two components (\mathbf{E}_x and \mathbf{E}_z) of the electric field, the 8 indicates the double-precision number representation in bytes of the electric field values and N_{TRN} is the number of transmitters. Due to memory constraints, each inversion cell consists of $\text{invfwd}=3$ forward modeling cells in the x and z directions, which is indicated by the square of the factor invfwd . For the data set presented in the next section, this requires approx. 2.4 Gbytes. The computation time is

$$T_{\text{comp}} = 4 \cdot 1.1 \cdot T_{\text{forward}} \cdot N_{\text{iter}}, \quad (\text{C2})$$

where T_{forward} is the time for a single FDTD calculation and N_{iter} is the number of iterations (Meles *et al.* 2010). For the calculations, two different computer clusters are used; the JUMP (Research Center Jülich) and the HPC cluster (RWTH Aachen). The computing times on the JUMP and HPC cluster are 0.2 min per iteration (for 51 iterations 12.4 min) and 0.6 min (for 51 iterations 32 min), respectively.

C.3 CASE STUDY: THUR RIVER HYDROGEOPHYSICAL TEST SITE

In this section, we explore the potential and limitations of the ray-based and full-waveform inversion schemes using an experimental data set. First, we describe the field site and the survey geometry. Then, we show the ray-based inversion results, estimate the source wavelet and describe the full-waveform inversion. Finally, we compare the results obtained with geophysical well logs acquired in neighboring boreholes.

C.3.1 Test site

The crosshole GPR data set was acquired in the Thur valley close to Frauenfeld, Switzerland. The Thur valley was initially formed by glaciers during the Pleistocene, which

cut into the older underlying Tertiary bedrock. Today, the valley is filled with lacustrine sediments and the central part of the Thur River is 40 to 45 m wide. On the south side of the Thur River, an overbank was formed with an approximate width of 130 m [Cirpka *et al.*, 2007]. The aquifer comprises a 7 m thick glaciofluvial gravel deposit, which is embedded between a thick sequence of low permeable clays (lacustrine sediments) below and alluvial loam above, which has a thickness of 3 m (Figure C3). Within the framework of the RECORD project [RECORD, 2011] four 11.4 cm diameter monitoring wells were installed in 2007 close to the Thur River, where measurements of crosshole GPR, ERT and seismic data have been performed (Chapter 2 and 4, and Appendix B). We consider here only the crosshole GPR data acquired along the south-west plane of the six planes interpreted in Chapter 2.

C.3.2 Measurement setup

A limited number of transmitter positions were used during the data acquisition to minimize acquisition time. To ensure that enough information is captured to reliably invert the data, a much larger number of receiver positions were occupied. The disadvantage of this approach is that ray coverage close to the transmitter borehole is relatively low (see Figure C4a). This is overcome by using a semi-reciprocal transmitter-receiver setup shown in Figure C4b, in which transmitter and receiver boreholes are interchanged. The combination of both data sets results in adequate ray-coverage over the entire domain (Figure C4c). In addition, this setup also reduces the computational costs, as discussed above.

For the GPR measurements, a RAMAC Ground Vision system of Malå Geoscience with 250 MHz antennas was employed. The vertical spacing between the transmitters and receivers are 0.5 m and 0.1 m, respectively. For the purpose of characterizing the aquifer between 4 and 10 m depth, 12 transmitter and 59 receiver positions were chosen in the south and west borehole, respectively (SW setup) and for the semi-reciprocal setup 12 transmitter and 57 receiver positions were chosen in the west and south borehole, respectively (WS-setup, see also Figure C4). In Figure C5a, these setups are shown with the transmitters and receivers indicated by white circles and blue crosses in the boreholes, respectively. Due to the measurement setup, the receiver records rays up to an angle of approximately 50° and all measurements were performed below the water table, which is located at approximately 4 m depth. The zone above the water table is neither included in the measurements nor in the inversion volume, so any recorded signals which have refracted/reflected from this horizon are not accommodated in the forward modeling and inversion.

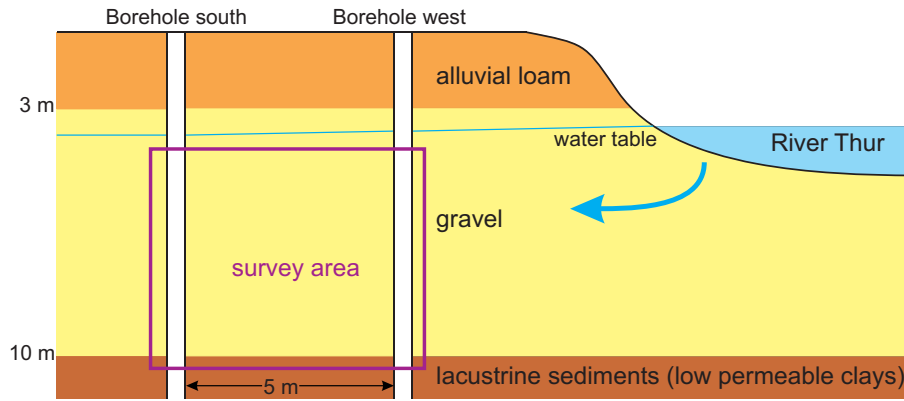


Figure C3. Simplified geological representation of the experimental area, showing a three-layer structure: alluvial loam, gravel, lacustrine (clay) sediments (from top to bottom); with boreholes close to the Thur River. The water table is approximately at 4 m depth.

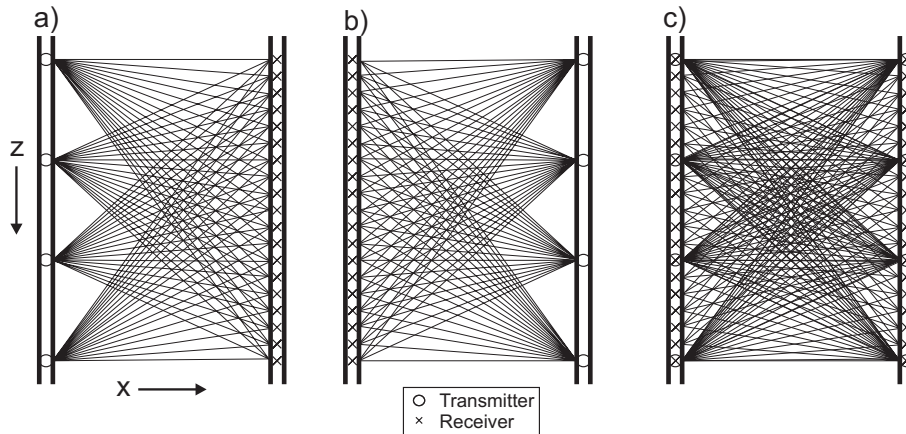


Figure C4. Schematic of the measurement setup employed that requires significantly less transmitter than receiver positions, but has low ray-coverage in the transmitter borehole. Semi-reciprocal measurements, in which transmitter and receiver boreholes are interchanged, are indicated in (a) and (b). The combination of these measurements, shown in (c), improves the ray-coverage compared to the individual setups.

C.3.3 Estimation of the initial model with ray-based inversion scheme

The first step in the processing sequence consists of picking the first-arrival traveltimes and the first cycle amplitudes of the measured data. The ray-based inversion is performed by minimizing the misfit between the picked traveltimes and the first cycle amplitudes of the measured and calculated data for a given fixed model regularization that includes both damping and smoothness constraints [Holliger *et al.*, 2001; Maurer and Musil, 2004]. The obtained velocity and attenuation tomograms are transformed into permittivity and conductivity images (Figure C5a and b). For convenience, we use the relative permittivity $\epsilon_r = \epsilon / \epsilon_0$ (or dielectric constant), where ϵ_0 is the free space permittivity. Both permittivity and

conductivity images reveal roughly three zones. A zone of higher permittivity and higher electrical conductivity is found in the top 4 m to 5.5 m, followed by lower permittivity and lower conductivity values between 5.5 m to 8 m. The bottom part exhibits intermediate values for both parameters. Neglecting the critically refracted waves results in a low ray density in the uppermost part of the tomographic plane. In addition, the high permittivities (low velocities) cause most of the rays to avoid the upper part (Figure C5c). Therefore, small-scale features found within this zone should be viewed with caution and not be over-interpreted.

C.3.4 Source wavelet estimation

Before the source wavelet estimation can be performed, it is necessary to apply a 3-D to 2-D conversion to transform the 3-D field data to make them comparable with the 2-D modeling data i.e. synthetic traces [Ernst *et al.*, 2007b]. These transformed data are then used in all the following processing steps, as well as the full-waveform inversion.

Initial source wavelet estimation

Following the scheme outlined in Figure C2 Part A, the traces of the upper and lower neighboring receivers of the ZOP data are at first averaged. Then the similarity of these waveforms obtained for each transmitter is investigated using a cross-correlation procedure for the horizontally traveling waves. Waveforms having relative cross-correlation values below 0.8, which indicate significant differences, are discarded. Waveforms of SW-transmitters 1, 2 and 12 and WS-transmitters 13, 14, 23 and 24 were excluded.

In the next step, all traces are aligned to the largest pulse minimum, which results in a better alignment than using the largest maximum of the pulses [as used by Ernst, 2007], and integrated (see also Figure C2). A bandpass filter is applied in the frequency domain to remove frequencies below 40 MHz and above 150 MHz. The tapered and normalized initial wavelet is plotted in blue in Figure C6. Note that only the shape is estimated and the amplitude scale is not considered.

The initial source wavelet is employed for modeling the radargrams using the ϵ and σ distributions obtained from the ray-based inversion. In Figure C7, the experimental data for the SW-setup are compared with the synthetic data. The amplitudes for each trace are normalized to the maximum to enable a better comparison of the data. Negative and positive amplitudes are indicated by the blue and red color in the image, respectively. The images show a similar trend for both data sets. However a timeshift of about 3 ns is apparent, especially in Figures C8a, b and c, where the observed and synthetic data are compared in

more detail and normalized wiggle plots are shown for the selected transmitter positions 2, 7 and 11, respectively, of the SW-setup with their respective receivers. The red and blue traces show the observed and synthetic traces, respectively. Only traces containing waves that mainly travelled horizontal paths show a good fit with the synthetic data (green ellipses). High-angle data contain significant time shifts and transmitters close to the water table have a significant misfit, which is probably due to reflections being present in the top 20 traces from transmitters 2 and 7. Similar results were obtained for the WS-setup.

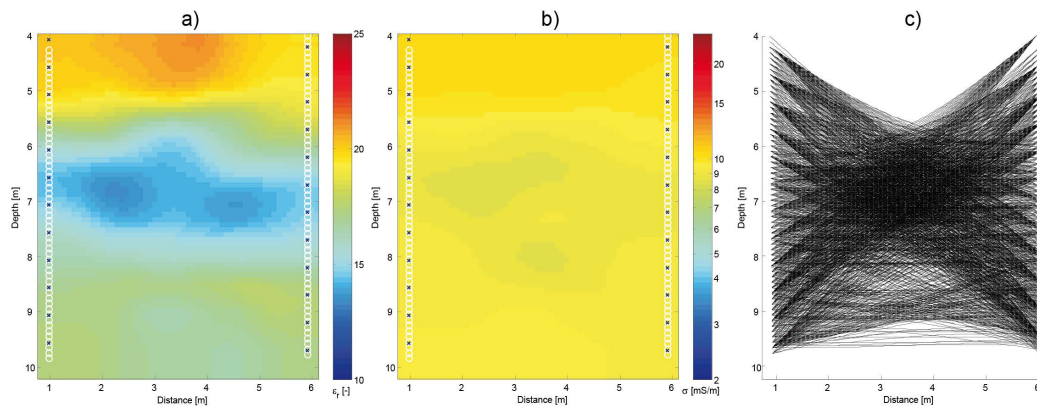


Figure C5. Ray-based inversion results that are used as the initial model for the full-waveform inversion. (a) The distribution of permittivity and (b) conductivity; transmitter and receiver positions are indicated with crosses and circles, respectively. (c) The ray-coverage based on the traveltimes inversion.

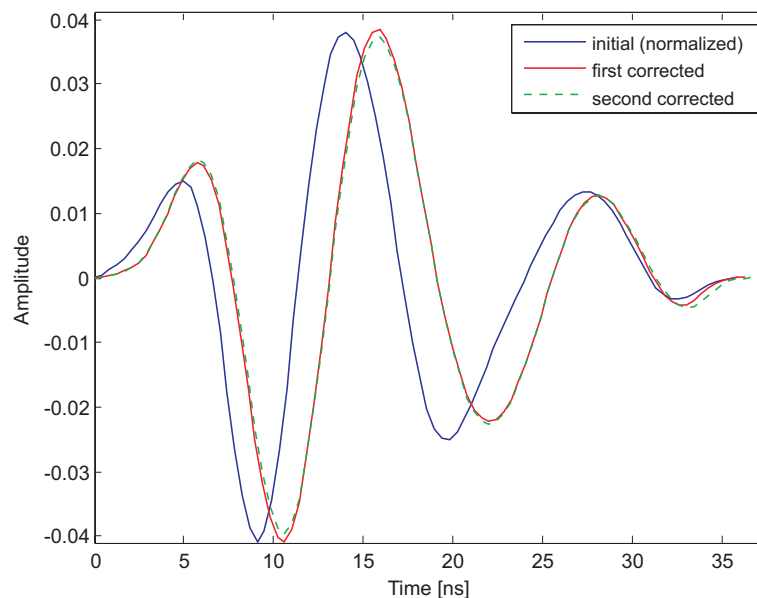


Figure C6. Wavelets for different processing steps: the initial wavelet which is normalized to the maximum amplitude of the first corrected wavelet (blue), first corrected wavelet (red), and the second corrected wavelet (green).

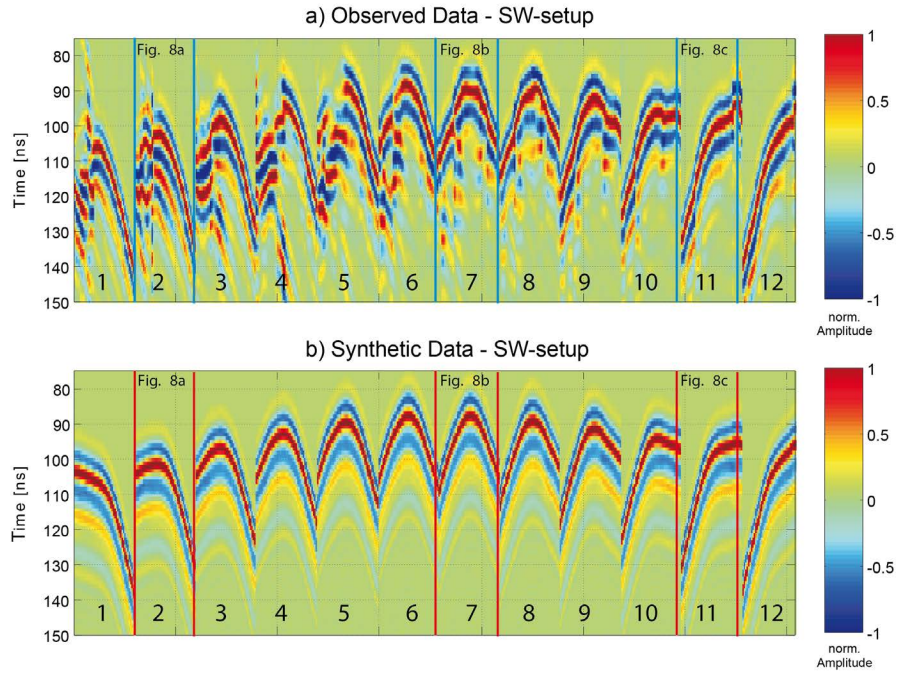


Figure C7. Comparison after one forward modeling run of the observed (a) and synthetic (b) data for the SW-setup (amplitudes normalized to their maximum). The numbers indicate the transmitter positions. Wiggle trace plots for observed and synthetic data for transmitters 2, 7 and 11 are shown in Figure C8a, b and c, respectively.

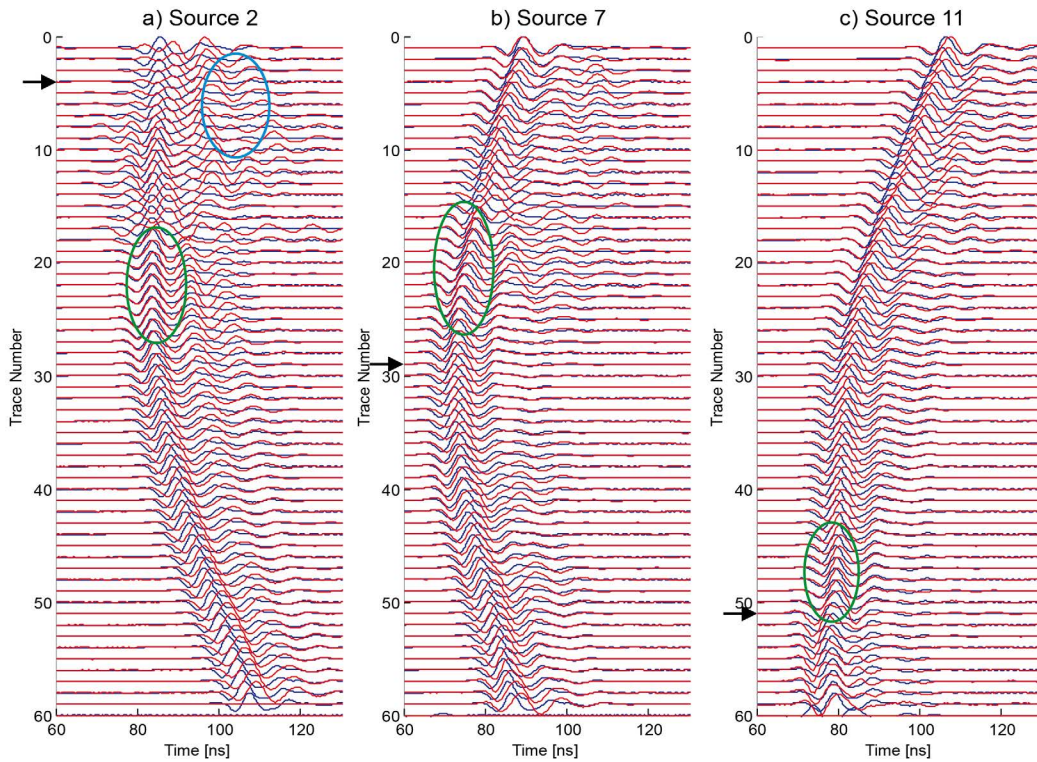


Figure C8. Comparison of normalized observed (red) and synthetic (blue) traces after the first forward modeling run for the transmitter gathers at positions (a) 2, (b) 7 and (c) 11. The green ellipses indicate the areas of best fit between the traces. The arrows at trace number (a) 4, (b) 29 and (c) 51 indicate the locations of transmitters 2, 7 and 11, respectively.

Source wavelet correction and refinement

In the next step, the source wavelet is corrected according to Figure C2, Part B. In contrast to the initial source wavelet estimation, where only horizontal rays are considered, we now use all traces to estimate the corrected wavelet. The amplitude and phase spectra of the wavelets are shown in Figures C9a and b, respectively. The blue, red and dashed black lines show the initial wavelet, the wavelet after the deconvolution and the final corrected wavelet, respectively. The frequency band (corner frequencies) of the bandpass filter applied during pre-processing is shown by the vertical dotted green lines. Within the bandpass there is a good match of the amplitude spectrum (Figure C9a), whereas the phase spectrum still shows a significant shift. The resulting wavelet, marked as the red curve in Figure C6, shows a compensation of the earlier observed timeshift between the observed and synthetic data in Figures C7 and C8. This shift probably arises because the first estimation of the wavelet is based only on a limited number of averaged direct waves, and no exact time zero is known and only the general form is obtained. Note that the amplitude of the corrected wavelet is now also determined, whereas the initial wavelet (blue line in Figure C6) is normalized to the maximum of the first corrected wavelet to allow a comparison of the shape with the corrected wavelet (corrected wavelet amplitude is about 1/25 of the initial wavelet amplitude).

To investigate and refine the shift and the amplitude, one more correction of the source wavelet is applied. The same steps and parameters are used in the second correction cycle (green wavelet in Figure C6). The wavelet did not change much and was found to be stable, suggesting that the shape and the amplitude are properly obtained. Figure C10 shows a comparison of the observed and synthetic data for the same transmitter positions as in Figure C8. The events show similar trends and no normalization is applied. It is obvious that the data fit improves and that both data sets are more comparable. The observed and synthetic traces have now the same first-arrival times, and the amplitudes for the traces correspond well when the transmitter and receiver positions are aligned sub-horizontally (see green ellipses). The time shift of 3 ns, which was observed after the first forward modeling, is absent. However, with increasing angle from the transmitter, the fit to the observed amplitudes becomes progressively worse.

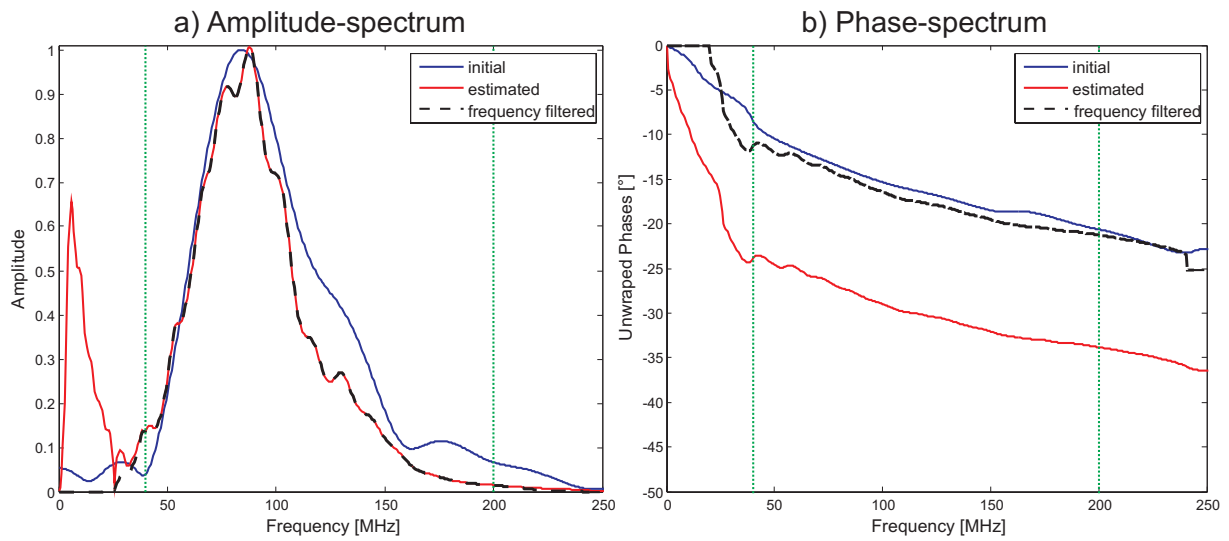


Figure C9. (a) Amplitude and (b) phase spectra of the initial source wavelet (blue), the estimated wavelet (red) and the frequency filtered wavelet (dashed black). A bandpass frequency filter is applied, having corner frequencies indicated by the green dotted lines.

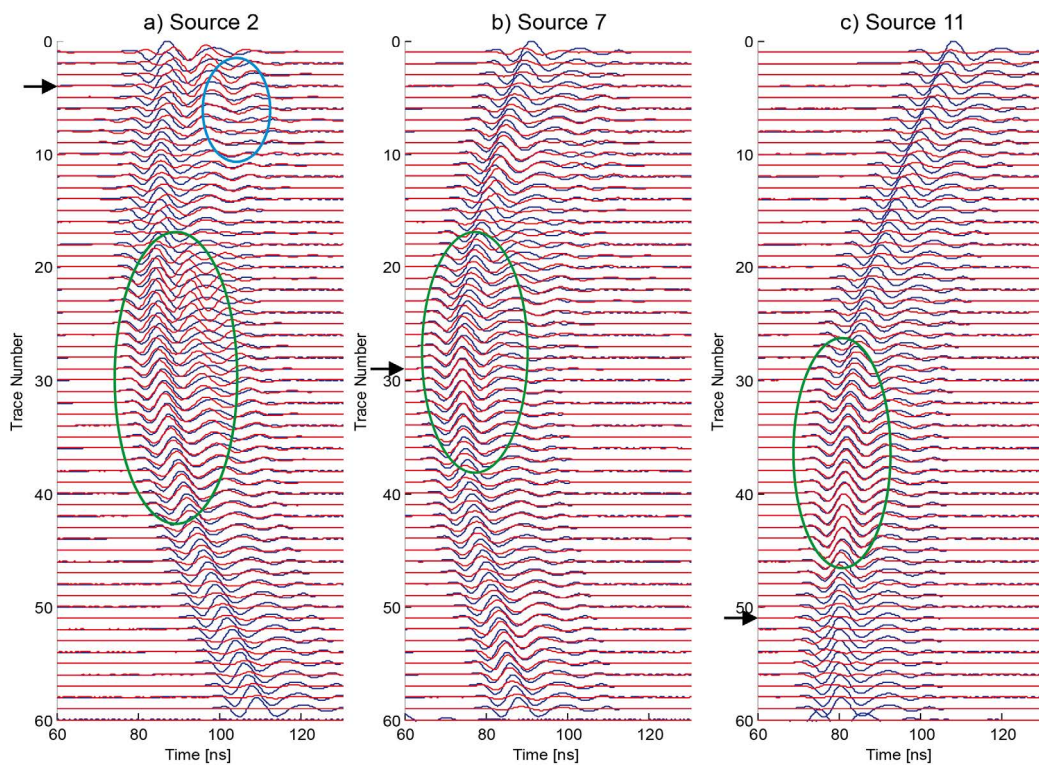


Figure C10. Comparison of non-normalized observed (red) and synthetic (blue) traces after the second forward modeling run for the measurements of the transmitter positions (a) 2, (b) 7 and (c) 11. The green ellipses indicate where the best fit between the traces.

C.3.5 Full-waveform permittivity and conductivity inversions

The Full-waveform inversion (Figure C1 Part III) begins by computing a synthetic wavefield using the ray-based results, shown for the permittivity in Figure C11a (iteration 0). Figures C11b, c and d show the permittivity tomograms obtained for iterations 10, 20 and 35, respectively. In the upper 2 meters the image changes between iteration 0 and 20, and regions with a higher permittivity become visible. Also, over the depth range 5.5 m to 10 m more structures and layering become evident. After iteration 20, the tomograms remain relatively constant until the final solution (iteration 35) in Figure C11d. The final permittivity image shows much more details than the ray-based inversion result. The aquifer area between depths of 4 m and 5.5 m contains thin layers having very high contrasts. Instead of the more or less homogenous middle layer obtained from the traveltimes inversion, the area between 6 m and 7.5 m depth contains two areas of relatively low permittivity. Below this area four intermediate and two lower permittivity zones are resolved.

Figure C12a shows the initial conductivity model (logarithmic scale) obtained from the ray-based inversion (iteration 0) using the first cycle amplitudes. The conductivity tomograms for iterations 10, 20 and 35 are shown in Figure C12b, c and d, respectively. In contrast to the permittivity tomograms, where small-scale features become visible in the earlier iterations, the conductivity tomograms remain relatively smooth during the first 20 iterations whereas finer details only occur for the later iterations. The reason is that the permittivity inversion model must first converge to ensure matching the phases between the synthetic and real data. Otherwise, the waveforms are not time-aligned and the amplitudes cannot be effectively optimized. A kinematic shift of more than one quarter of a pulse period precludes a satisfactory dynamic inversion. The final conductivity tomogram shows much more detail than the ray-based model (iteration 0). A very pronounced higher conductivity zone is imaged at a depth below 9.5 m (black dashed line in Figure C12d), which was not obtained with the ray-based inversion results (Figure C12a).

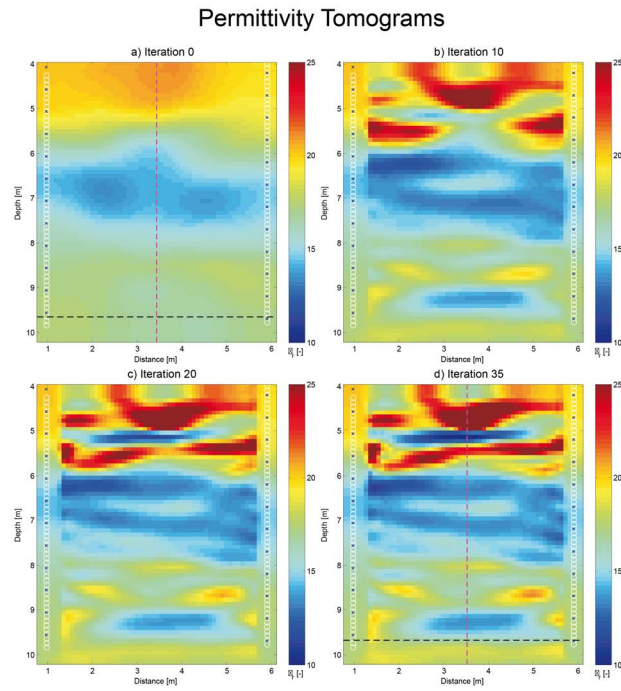


Figure C11. Relative permittivity tomograms for different iteration steps from (a) initial model of the full-waveform inversion obtained from the ray-based inversion, (b), (c) and (d) show the models obtained at iterations 10, 20 and 35, respectively. The dashed black line refers to Figure C15a, where a comparison of Neutron-Neutron logging data is presented. The violet dashed line indicates the position of the logging boreholes (2.5 m away).

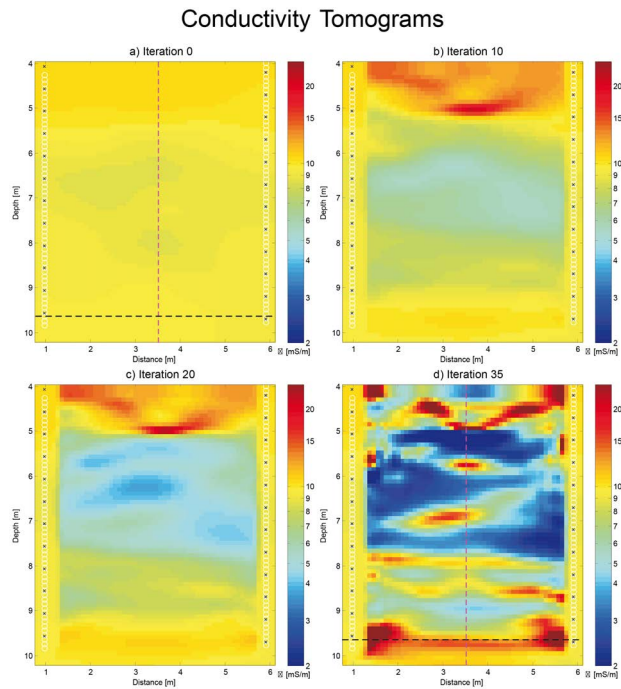


Figure C12. Conductivity tomograms for different iteration steps from (a) initial model of the full-waveform inversion obtained from the ray-based inversion, (b), (c) and (d) show the models obtained at iterations 10, 20 and 35, respectively. The dashed black line refers to Figure C15b, where a comparison Natural Gamma logging data is presented. This line indicates the resolved underlying lacustrine sediments. The violet dashed line indicates the position of the logging boreholes (2.5 m away).

C.3.6 RMS convergence

The RMS misfit between observed and predicted traces is shown in Figure C13. The vertical axis is normalized such that the RMS of the initial model (obtained with the ray based inversion) is equal to 1.0. The convergence criterion of less than 1% change in the misfit between iterations is achieved after 35 iterations.

C.3.7 Comparison between observed and modeled traces

Figure C14 compares the observed traces (red) for transmitter positions 2, 7 and 11 at iteration 35 with the modeled traces (blue). A very good fit between the synthetic and measured traces is apparent. The agreement for transmitter 2 (Figure C14a) is less convincing, which is probably due to transmitter 2 being located in the upper region close to the water table (see arrow in Figure C14a), where the additional refractions and reflections (not included in the modeled data) are strongly present. Note that transmitter 2 was excluded from the source wavelet estimation. Due to the presence of the water table, the obtained model is probably unreliable for the depth range between 4m and 6 m. Instead of discarding the traces containing refracted waves which have travelled through the unsaturated gravel, as is done in the ray-based inversion (see Figure C5c), we included all traces in the full-waveform inversion. The algorithm tried to fit these events without taking into account the presence of the unsaturated zone. The presence of the water-table is indicated by the prominent reflections shown in the blue ellipse in Figure C14 for transmitter 2 in the upper 5 traces. This probably produces anomalous structures (low and high permittivity and conductivity values) in the upper 2 m. To improve these results, data above the water table should be measured and included in the inversion. The full-waveform inversion should be able to fit these critically refracted waves and reflected waves when a proper starting model is used, which includes this zone

For transmitters 7 and 11 (Figure C14b and c), the simulated amplitudes and phases fit the measured data remarkably well. Therefore, we expect that the tomogram details below 6 m depth represent reality rather well. By comparing Figures C8, C10 and C14 it is obvious that the fit between the observed and synthetic data becomes significantly better after wavelet estimation and especially after the full-waveform inversion. The green ellipses indicate the areas with the best fit. All these results indicate that the simultaneous full-waveform inversion of both permittivity and conductivity performs well!

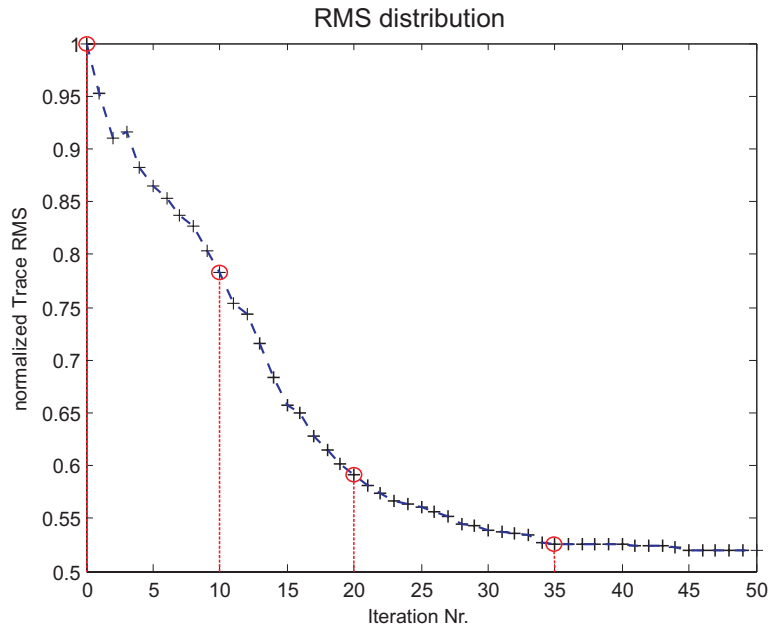


Figure C13. RMS values as a function of iteration number for the ray-based inversion starting model. The RMS is normalized to the ray-based inversion result and after 35 iterations the RMS misfit changes less than 1%. The red circles along the graph indicate the iteration number for which the permittivity and conductivity results are shown in Figures C11 and C12.

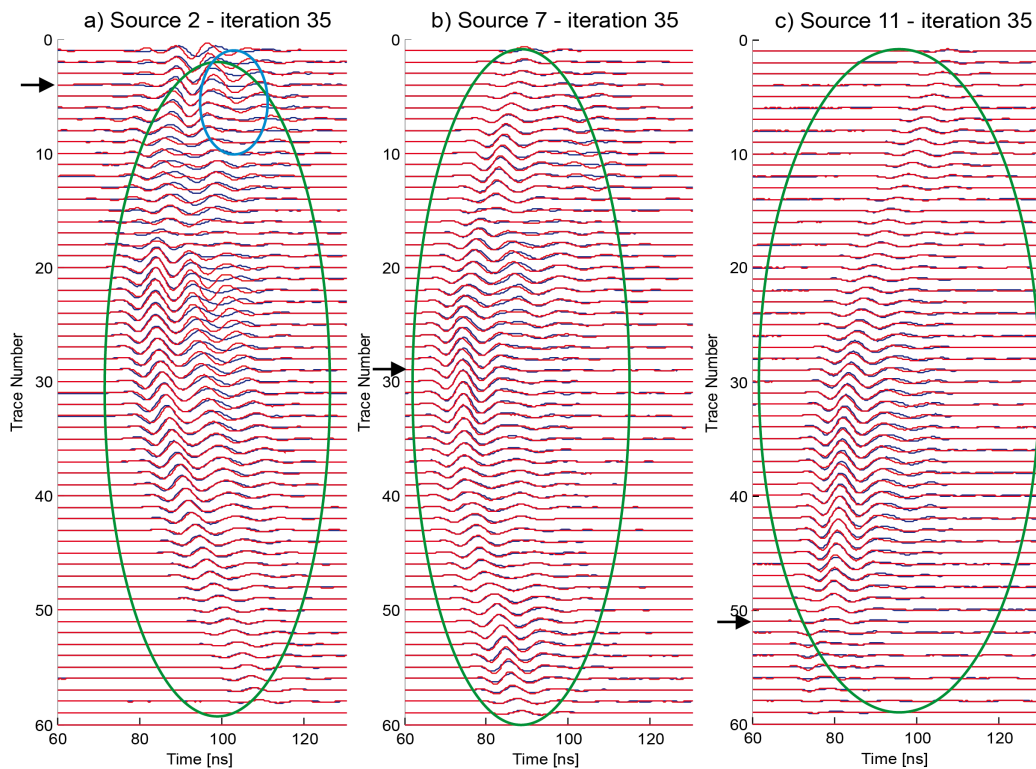


Figure C14. Un-normalized traces after 35 iterations for the measurements of transmitters (a) 2, (b) 7 and (c) 11. A general good agreement of the observed traces (red) and the simulated traces (blue) is visible. The green ellipses indicating where the fit is best between the traces, whereas the blue ellipse shows the reflections from the water table (see text for further discussion).

C.3.8 Interpretation and comparison with borehole logging data

The permittivity is influenced mainly by the pore structure and the porosity of the gravel, which contains particle sizes between 0.2 mm and 60 mm [Füchtenbauer, 1988; Diem *et al.*, 2010] and also a small fraction of fines. Permittivity values for saturated gravel are reported to lie between 20 to 30 [Daniels *et al.*, 2005]. The conductivity is determined by porosity and pore structure, salinity, and surface conductivity at the grain/solution interface. Moreover, if clay is present in the gravel, conductivities will increase with an increasing amount of clay. Clay particles contribute the exchange of cations to the electrolyte, which increases the conductivity of the formation [Waxman and Smits, 1968; Worthington, 1993].

To assess the reliability of the full-waveform results we analyzed geophysical borehole logs acquired at two wells located at either side, 2.5 m distance away from the crosshole plane. The plane between these north-east (P11) and south-west (P13) boreholes cross our tomographic plane at the center (indicated by the violet dashed line in Figure C11d and C12d). Neutron-Neutron data indicate water content (and thus porosity), whereas Natural Gamma data indicate the presence of clay. Neutron-Neutron logs are transformed into porosity using the approach and parameters of Barrash and Clemo [2002] for both boreholes P11 and P13 and plotted in Figure C15a in blue and cyan, respectively. The obtained permittivities for the traveltimes ($I=0$) and full-waveform inversion ($I=35$) at the center of the planes (see dashed violet lines in Figure C11a and d) are converted to porosity using the petrophysical model of Linde *et al.* [2006a] with the parameters of Chapter 2 and plotted in Figure C15a in red and green, respectively.

Without any additional calibration, the values obtained for the converted Neutron-Neutron logs and permittivity results are very close and similar vertical variations can be observed. Especially from 6.8 m to 7.3 m and from 8.5 m to 9.3 m the porosity values for P13 fit very well the inversion results and from 7.8 m to 8.3 m the values for P11 fit well the inversion results. Note that both borehole logs indicate a lateral variation and the curves shown in Figure C15 represent porosity values 2.5 m away from each other. In future, the borehole logs should be taken at the center of the tomographic plane to enable a direct comparison.

In Figure C15b, the obtained conductivities for the traveltimes ($I=0$) and full-waveform inversion ($I=35$) at the center of the planes (see dashed violet lines in Figure C12a and d) are plotted in Figure C15b in red and green, respectively. The dashed black line in Figure C15b indicate the high conductivity zone in the tomographic plane at the base of the aquifer below

9.6 m depth (see also black dashed line in Figure C12d), which indicates the boundary of the lacustrine sediment. These results fit very well with the Natural Gamma logs of P11 and P13 (blue and cyan lines in Figure C15b) that clearly indicate the presence of a high clay content layer below 9.6 m. The Neutron-Neutron results also indicate a strong discontinuity at the same depth level. Note that these lacustrine sediments could not be resolved with the ray-based inversion. As expected, a poor match is found between the borehole logs and the tomograms within the uppermost 2 m.

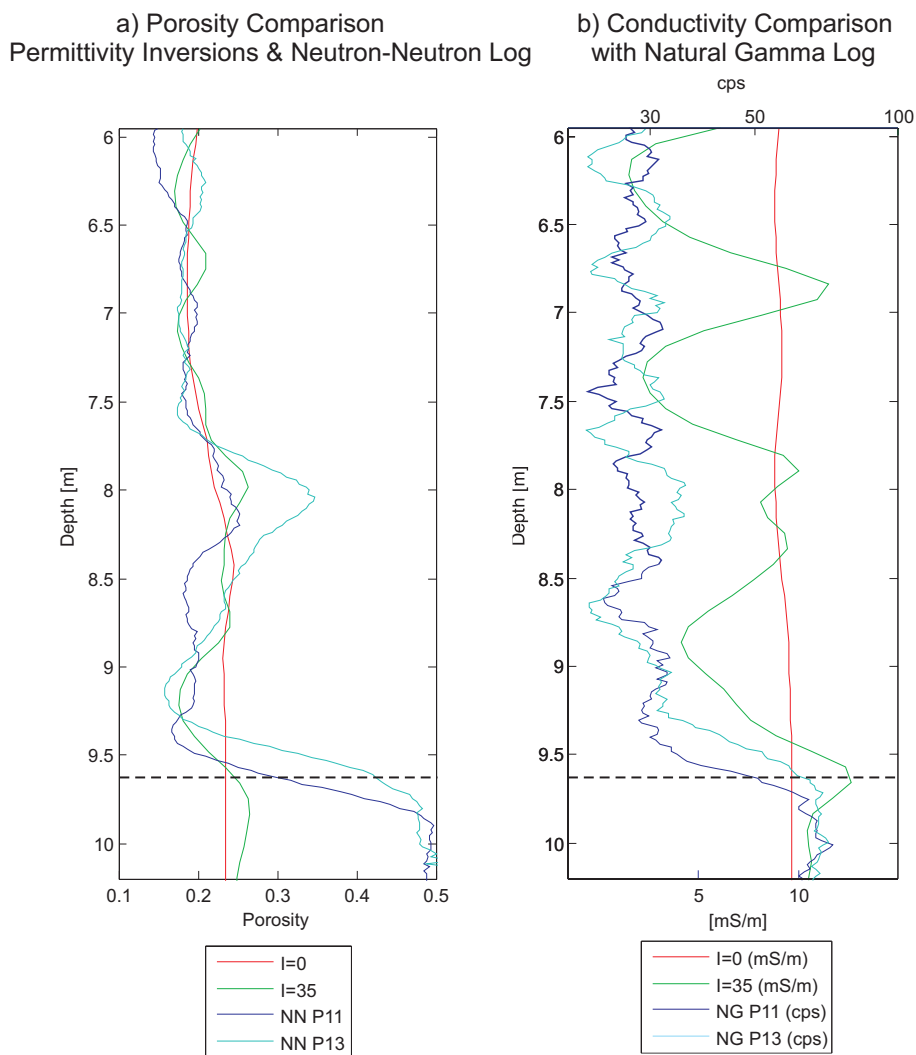


Figure C15. (a) Comparison of the Neutron porosities of the boreholes P11 and P13 with the porosities obtained from the permittivities observed at the same level for the ray-based inversion result ($I=0$) and the final solution of the full-waveform inversion ($I=35$) over the depth interval 6 m to 10.2 m. (b) Comparison of the Natural Gamma counts for both boreholes with the conductivity observed at the same level for the ray-based inversion ($I=0$) and the final solution of the full-waveform inversion ($I=35$) over the depth interval 6 m to 10.2 m. All graphs are plotted logarithmically. Note that the lacustrine sediments (clays) are indicated by the black dashed line (compare with the dashed line in Figure C12d).

C.4 CONCLUSIONS AND OUTLOOK

A recently developed full-waveform inversion algorithm for crosshole GPR data [Meles *et al.*, 2010] was optimized by introducing an improved acquisition setup. Using a limited number of transmitter positions and many more receiver positions, the acquisition time and the computational cost (memory and CPU time) could be reduced compared to a conventional setup that uses an equal number of transmitter and receiver positions. To improve the low ray-coverage close to the transmitter borehole, a semi-reciprocal setup was employed which entailed populating the original receiver borehole with new transmitter positions (and conversely populating the original transmitter borehole with a dense array of receiver positions). This approach has been evaluated by analyzing crosshole GPR data acquired within an aquifer composed of gravelly river deposits and resulted in a good data fit between the measured traces and the synthetic traces. As expected, the permittivity and conductivity tomograms obtained are much more detailed than conventional ray-based inversion results.

The obtained results are compared with Neutron-Neutron and Natural Gamma logging data measured at either side, 2.5 m distance away from the crosshole plane. The inverted permittivity values and the measured Neutron-Neutron logs are converted to porosities using conversions described in literature and show very similar absolute values and vertical variations with high resolution. At some depth ranges a good correspondence is observed for one of the logs whereas at other depths this is observed for the other log. This is explained by the presence of lateral variation observed in the two Neutron-Neutron borehole logs measured at either side, 2.5 m distance away from the crosshole plane, such that a direct comparison is not possible. Note that the ray-based permittivity tomogram only provided low resolution porosity information. The full-waveform conductivity tomogram indicates an increased conductivity below 9.6 m at all lateral positions, which corresponds to the lacustrine sediments. Comparison of the conductivity tomogram with the Natural Gamma logs confirms that the thick clay layer at the base of the aquifer is present at a depth of approximately 9.6 m. The Neutron-Neutron logs also indicated a strong discontinuity below this depth. Note that this layer was not clearly identified in the ray-based conductivity tomogram.

Comparison with ERT models obtained in Chapter 4 indicates that the electrical conductivities at a center frequency of 100 MHz obtained by full-waveform inversion are approximately 50% higher than those obtained by the ERT inversion (DC or low frequency values). This apparent discrepancy may be explained by the frequency-dependency of

electrical conductivity [*Knight and Nur, 1987*]. This needs to be investigated further in future work.

Thin horizontal layers were imaged for the upper part (4 m to 5.5m) of the aquifer having strongly alternating permittivities and conductivities, but no agreement with the borehole logs was found. On the basis of the poor match of the observed and predicted traces in the upper part of the aquifer (Figure C14a), we expect the full-waveform models to be unreliable in this region. A likely explanation for this is the presence of the groundwater table, which represents a very strong discontinuity in electrical subsurface parameters. This leads to non-linear effects that can cause the inversion to get trapped in local minima. A possible solution would be to incorporate the water table as a priori information in the initial model, to increase the model space and to use transmitters in the unsaturated zone. Another factor that might also influence the results in the upper part of the aquifer is the 3-D to 2-D conversion, which is only valid for far-field conditions. Here, the minimum distance between transmitter and receiver is seven wavelengths and recent publications [*Streich and van der Kruk, 2007a*] indicate that the far-field assumption may be thus not valid. The use of a 2½ D forward modeling program [e.g., *Bing and Greenhalgh, 1998a*] might solve this problem.

Our analyses showed that estimation of the source wavelet is critical. A possible improvement could be the estimation of an effective source wavelet for different areas, where the medium parameters and the corresponding dielectric coupling are different [*Tronicke and Holliger, 2004*]. Instead of assuming a point source, it would also be possible to implement finite antennas in the modeling [*Streich and van der Kruk, 2007b*], to consider the real dimensions of the antennas. Until now, only a source wavelet correction is applied before the full-waveform inversion, but the source wavelet could be updated after a few iterations and possibly the results can be further improved.

In summary, we optimized the acquisition setup and incorporated this in the full-waveform inversion of crosshole GPR measurements such that the acquisition time and computational costs are significantly reduced. The permittivity and conductivity images of the gravel aquifer show a much higher resolution compared to the ray-based inversion (see Figures C11 and C12). For the first time, high conductivity lacustrine sediments underlying a gravel aquifer were imaged using full-waveform inversion of crosshole GPR data, in correspondence with Natural Gamma logs. In addition, high resolution porosity values were obtained having similar vertical changes as the Neutron-Neutron logs. Since the logs and the inversion plane were not co-located, direct comparison was not possible, but the obtained

results show that this approach has high potential to characterize and image gravel aquifers for hydrological purposes.

APPENDIX D: INSTRUMENTATION OF A RESTORED RIVER CORRIDOR

Published in *HESS*:

Schneider, P., Vogt, T., Schirmer, M.,
Doetsch, J., Linde, N., Pasquale, N.,
Perona, P., and Cirpka, O. A., 2011.
Towards improved instrumentation for
assessing river-groundwater interactions in
a restored river corridor, *Hydrological
Earth Systems Science*, **15**, 2531-2549.

ABSTRACT

River restoration projects have been launched over the last two decades to improve the ecological status and water quality of regulated rivers. As most restored rivers are not monitored at all, it is difficult to predict consequences of restoration projects or analyze why restorations fail or are successful. It is thus necessary to implement efficient field assessment strategies, for example by employing sensor networks that continuously measure physical parameters at high spatial and temporal resolution. This paper focuses on the design and implementation of an instrumentation strategy for monitoring changes in bank filtration, hydrological connectivity, groundwater travel time and quality due to river restoration. We specifically designed and instrumented a network of monitoring wells at the Thur River (NE Switzerland), which is partly restored and mainly channelized since more than 100 years. Our results show that bank filtration – especially in a restored section with alternating riverbed morphology – is variable in time and space. Consequently, our monitoring network sensing physical and sampling chemical water quality parameters was adapted in response to that variability. Although not available at our test site, we consider long-term measurements – ideally initialized before and continued after restoration – as a fundamental step, towards predicting consequences of river restoration for groundwater quality. As a result, process-based models could be adapted and evaluated using these types of high-resolution data sets.

D.1 INTRODUCTION

In Switzerland, 40% of drinking water is pumped from alluvial aquifers, which represents only 5% of the country's land surface [SVGW, 2004]. Mainly for sustaining high pumping rates, many larger drinking water wells are located close to rivers. Open water bodies may be polluted by pathogens or dissolved contaminants, which are introduced into running waters by the effluent of sewage treatment plants, stormwater overflow, and agricultural drainage, among others. The passage through the riverbed, the hyporheic zone, and the alluvial aquifer – summarized as bank filtration – acts as filter and reactor for contaminants, nutrients, and pathogens [Merkli, 1975; Schwarzenbach and Westall, 1981; Schwarzenbach et al., 1983; Bourg and Bertin, 1993; Bosma et al., 1996; Schwarzenbach et al., 2006]. The actual biogeochemical interactions sustaining the quality of the pumped bank filtrate depend on numerous factors including aquifer mineralogy and structure, oxygen and nitrate concentrations in the surface water, types of organic matter in the surface and groundwater environments, and land use in the local catchment area [Hiscock and Grischek, 2002]. In

ivers with continuous infiltration, the biologically most active zone is typically only a few centimeters thick [von Gunten *et al.*, 1994]. Microbial turnover processes are controlled by water temperature, redox potential, dissolved oxygen and available dissolved organic carbon [Jacobs *et al.*, 1988; von Gunten and Zobrist, 1993]. River water differs fundamentally from groundwater in respect to these parameters. Consequently mixing between comparably old groundwater, and fresh river-water infiltrate, together with travel times along flowpaths play a central role for the protection of wells affected by bank filtration [Tufenkji *et al.*, 2002; Eckert *et al.*, 2008; Shankar *et al.*, 2009].

Orghidan [1959] was the first to study the interstitial space below the riverbed as a habitat for aquatic organisms. The hyporheic zone is defined as the transition zone linking river water and groundwater. It is located in the uppermost sediment layers of the riverbed, which – under pristine conditions of alpine rivers – is typically highly permeable for water, organisms, and solutes. Physical, geochemical, or biological evidence of the mixing of the two systems is used to characterize the hyporheic zone [Triska *et al.*, 1989; Woessner, 2000]. This mixing is strongly influenced by heterogeneity of sediments and head gradients [Stauffer and Dracos, 1986; Stanford and Ward, 1993]. From an aquatic-ecology perspective, the hyporheic zone acts as (i) habitat and (ii) modulator for fluctuations in the river, such as those of water temperature, nutrients, and contaminants [Bourg and Bertin, 1993; Triska *et al.*, 1993a; b; Brunke and Gonser, 1997]. Our process knowledge about the hyporheic zone remains limited despite its crucial role in reproduction of aquatic organisms, exchange of water and solutes, as well as transformation of nutrients and contaminants.

Precise knowledge of water levels and their fluctuations are fundamental for interpreting river-groundwater interactions or for applying and calibrating groundwater models. Attempts to simulate local effects of river-aquifer exchange in river-scale models are usually hampered by the lack of field data on riverbed conductivities and hydraulic gradients within the riverbed, which are seldom available at the appropriate scale and temporal resolution. Regional groundwater monitoring networks usually do not have sufficient spatial density in the vicinity of the river to reliably calibrate local riverbed conductivities. Therefore, local conditions at the interface between the river and the aquifer may not be adequately represented in a model [Fleckenstein *et al.*, 2006].

Exchange fluxes between rivers and groundwater are highly variable in time and space [Brunke and Gonser, 1997; Wroblicky *et al.*, 1998]. Temporal fluctuations can be attributed to changing hydrological conditions [Wroblicky *et al.*, 1998; Vogt *et al.*, 2010a] as well as

clogging and declogging of the riverbed [Schälchli, 1992; Battin and Sengschmitt, 1999]. The heterogeneity of streambed sediments and associated hydraulic conductivity [Huggenberger et al., 1998; Fleckenstein et al., 2006; Kalbus et al., 2009], river morphology and stream curvature [Harvey and Bencala, 1993; Cardenas et al., 2004; Gooseff et al., 2005], and spatially varying hydraulic gradients [Storey et al., 2003] may cause spatial variations. All the above mentioned factors controlling river-groundwater interactions may be affected by river restoration measures.

The central goal of the EU water framework directive [EC, 2000] is to achieve a “good ecological status” of all water bodies. This requires intensive vertical hyporheic exchange, lateral connection with floodplains and alluvial forests and longitudinal connectivity for aquatic fauna of running water systems [Stanford and Ward, 1988; Ward, 1989; Stanford and Ward, 1993]. Consequently, Swiss law requires river restoration in all flood-protection measures [GschG, 1991; GSchV, 1998]. Typical components of river restoration include the widening of the river course, the removal of bank stabilization, and the reestablishment of a more natural sediment regime. In contrast to ecological benefits, enhanced hydrological connectivity and fast infiltration may cause problems, such as breakthrough of contaminants in drinking water wells located close to rivers. This made Swiss legislators prohibit river restoration measures within protection zones of drinking water wells [BUWAL, 2004; SVGW, 2007]. This legislation reflects the concern that river restoration might impair groundwater quality. It also shows that interactions of groundwater and river water at restored sites, and their effects on water supply, are not yet fully understood.

Each restoration project is potentially an opportunity to learn more about aquatic systems and how they are modified following restoration [Kondolf, 1998; Regli et al., 2003]. Adequate process knowledge is fundamental to understand the impact of river restoration on groundwater systems. Such a mechanistic system understanding can only be derived by site-specific monitoring, optimally performed prior and post restoration. Restoration should ideally be based on process understanding instead of mimicry of form (morphology). This has consequences on evaluating restoration success as current practice is restricted to mainly monitoring the morphodynamics of the restored river section and perhaps performing a few surveys on the abundance of indicator organisms [Woolsey et al., 2007]. This type of programs needs to be extended to include measures of system functioning with respect to hyporheic exchange, biogeochemistry and water quality. Such post-restoration performance evaluation is needed to avoid repeating mistakes, to develop an understanding of how rivers

respond to restoration actions and to allow for improved river restoration schemes in the future.

A variety of techniques have been developed to estimate water exchange rates between rivers and aquifers [Kalbus *et al.*, 2006], but a comprehensive analysis of rivergroundwater exchange and its effects on water quality requires more than estimates of water fluxes in the riverbed at individual locations and single points in time. Continuous monitoring of variables related to river-groundwater exchange is needed to understand dynamic behavior. These monitoring data are best analyzed by numerical models, which require geometric and structural information about the river and the aquifer. This paper deals with preliminary surveys, as well as instrumentation and monitoring strategies adapted for better hydrological understanding of restored river corridors. In particular, we focus on the following components:

- Surveys targeting topography and bathymetry, which record morphological changes used to create a hydraulic model of the river.
- Surveys targeting the subsurface structure, which are mainly performed by geophysical techniques; this structural information about the subsurface is necessary to characterize heterogeneity of aquifer deposits and to create reliable groundwater flow and transport models.
- Surveys targeting water levels, which consist of continuous level gauging both in the river and in monitoring wells, but also automated visual monitoring of the river with subsequent image analysis.
- Surveys targeting solute transport and water quality by continuous sensing of physical parameters (temperature and electrical conductivity) in the river and in the groundwater with subsequent time-series analysis, and by regular sampling campaigns for chemical parameters.

Instrumentation within the riverbed is desired but challenging, as equipment and monitoring networks would be prone to flooding, erosion, sedimentation and other physical stresses, leading to sensor failure and complete loss of data sets. We present an approach to tackle this problem by tailoring a monitoring-well network outside of the riverbed with focus on infiltration, groundwater travel times, hydrologic connectivity and related changes in water quality. We demonstrate the applicability of this process driven approach and show how targeted monitoring enables us to understand in- and exfiltration in space and time at a restored section of the Thur River in Switzerland, which forms our case-study.

The Thur River is currently under intensive investigation with respect to hyporheic exchange processes within the project “Assessment and Modeling of Coupled Ecological and Hydrological Dynamics in the Restored Corridor of a River – Restored Corridor Dynamics (RECORD)” [RECORD, 2011]. While the RECORD project also has an ecological component, this paper focuses on physical processes and water quality only. The purpose of the current contribution is to give an overview of the various methods applied at River Thur. Details of individual techniques have already been published by *Diem et al.* [2010], Chapters 2 and 4 - 6, *Schäppi et al.* [2010], and *Vogt et al.* [2009; 2010b; 2010a]. The special issue, in which this paper appears, contains additional descriptions about individual aspects [Edmaier et al., 2011; Hoehn and Scholtis, 2011; Linde et al., 2011; Pasquale et al., 2011; Samaritani et al., 2011]. In this paper, we put these individual contributions into a common context.

D.2 THUR CATCHMENT AND TEST SITE SELECTION

The Thur Valley aquifer is one of the largest groundwater systems in Switzerland with a length of 36 km, a width of 2 km and a depth of up to 20 m and it is mainly fed by the Thur River. As the aquifer is widely used for drinking water abstraction, changes in travel times from river to nearby pumping stations caused by river restoration are a critical issue, especially since this aquifer, like others in alpine environments, exhibits high hydraulic conductivities.

The Thur catchment is located in north-eastern Switzerland, draining the front ranges of the Swiss Limestone Alps (Alpstein) south of Lake Constance into the River Rhine (Figure D1). It is a primarily rural catchment, with agricultural activity mainly in the low-lands, and a few towns and villages (Table D1). Water quality in the Thur catchment is adversely influenced by intensive agriculture and sewage water inflows (Table D1) mainly in the lower part of the catchment. The geology is formed by mainly limestone dominated alpine headwaters with high annual rainfall [Mt. Säntis 2500 mm/yr, *Seiz and Foppa, 2007*], whereas the lowlands are dominated by Molasse Sandstones and pleistocene unconsolidated sediments. The Thur Valley and its aquifer are dominated by glacio-fluvial sandy gravels overlaying lacustrine clays (Table D2). The gravel deposition occurred within a few thousand years at the end of the last ice age during the retreat of the last Rhine glacier. In some parts of the valley, natural alluvial fines of up to 2 m thickness act as a confining layer. In the lower Thur Valley, the river cuts into sandy gravel sediments. Towards the western end of the valley, the gravel sediments form a single layered, 5 - 7 m thick aquifer with an average

hydraulic conductivity of 5×10^{-3} m/s derived by pumping tests (variance: $\sigma_{\log K}^2 = 0.4$, [Baumann *et al.*, 2009]). The lacustrine silty clay below the gravel can be considered impervious.

Regional groundwater flow is dominated by infiltration of the Thur River at the eastern (upstream) end of the valley (~ 0.26 m³/s), groundwater recharge over the entire area of the valley (~ 0.49 m³/s), groundwater extraction by pumping wells (~ 0.36 m³/s), and exfiltration into side channels at the western (downstream) end of the valley. This behavior is strongly modified in the vicinity of the river by river-water infiltration (~ 3.0 m³/s), short passages through the aquifer and exfiltration into the side channels in the western part of the valley. The water balance of a regional groundwater model (Table D2) revealed that about 86% of the total water collected by the side channels (~ 3.1 m³/s) is fresh river-water infiltrate [Baumann *et al.*, 2009].

Originally, the lower Thur River was a braided gravel-bed river characterized by a shifting mosaic of channels, ponds, bars and islands occupying most of the valley floor. Like most major rivers in central Europe, the lower Thur River was channelized by the end of the 19th century to gain arable land and avoiding frequent flooding. Thus, the Thur River was converted into a double trapezoidal channel with stabilized banks and bounded by levees (for a detailed description see [Pasquale *et al.*, 2011]). In 2002, a 2 km long section of the Thur River near Neunforn/Altikon was restored by completely removing the northern overbank, so that the nearby alluvial forest became part of the active floodplain again. This large widening increased sediment deposition, reestablished dynamic fluvio-morphological processes with frequently forming and alternating gravel bars, and created physical habitats for pioneer fauna and flora. This river section is the focus of this study.

Figures D1 and D2 provide an overview of the selected test site. While the upstream (eastern) reach of the site has remained channelized, the downstream (western) reach has significantly been modified by restoration, giving us the opportunity to compare bank filtration under pre- and post-restoration conditions at a single site. In the downstream reach, where the northern overbanks have been removed, the width of the active river channel has been extended to more than 100 m (Figure D3). A municipal abstraction well – referred to as the pumping station in the following – is located in the upstream reach of the test site (see transect A in Figure D2). The northern levee ends near the pumping station (Figure D2). Parallel to it runs a side channel draining the northern floodplain. This channel joins the river within the test-site perimeter and exhibits similar water level fluctuations as the river, which

implies only moderate hydraulic gradients in between. Consequently, the principle direction of groundwater flow along the northern bank of the Thur River is expected to be almost parallel to the river.

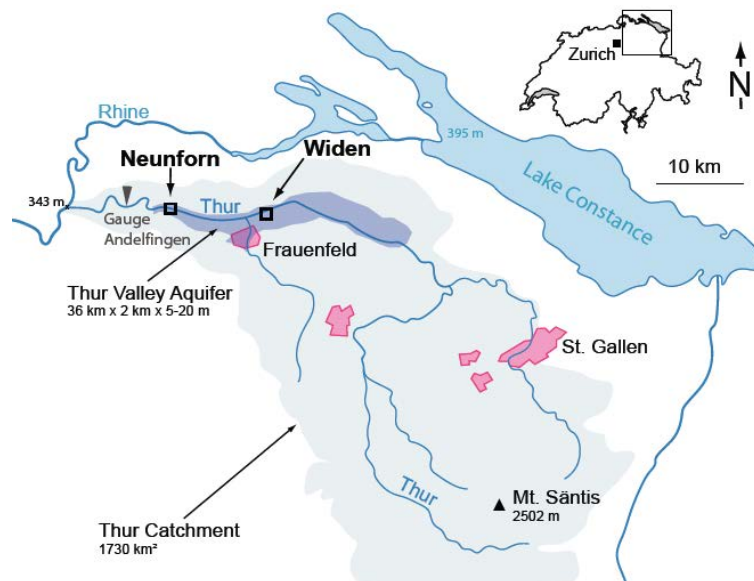
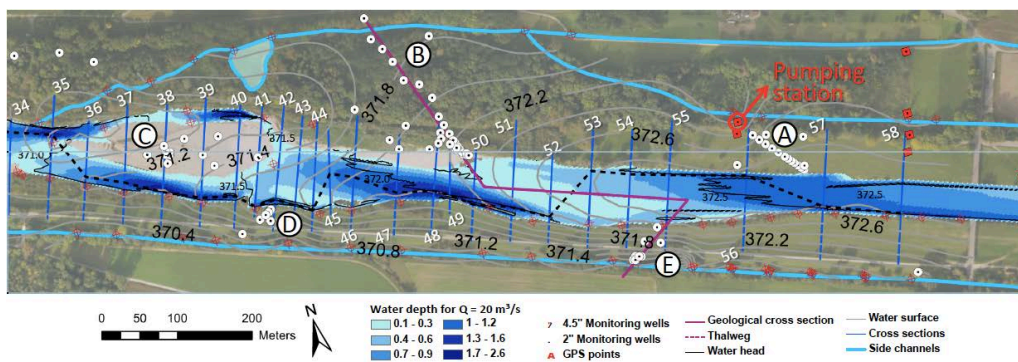
Widening of the river bed in the course of restoration has caused sedimentation of bedload at the site. *Schälchli* [2008] estimated the gravel deposition in the 2km long restored sector at the site to be approximately 8000 m³ per year (Figures D1, D2 and D3). This estimate highlights that significant changes in morphology is expected in the next years. A particular goal of this study is to assess the effects of these morphological changes on mixing ratios of groundwater and river water together with related traveltimes as well as nutrient and pollutant turnover.

Table D1. Key descriptors of the Thur River [BAFU, 2010].

Catchment Area	1730 km ²
Catchment Gauge	1696 km ²
Level of Gauge	356 m asl
Average Altitude	770 m asl
Maximum Altitude	2502 m asl
Glaciers	0.0%
Flow Regime	nivo-pluvial (snowmelt dominated)
Annual Rainfall (Thur catchment)	1413 mm (1961-1990)
Annual Rainfall (Thur Valley)	883 mm (1961-1990)
Mean Runoff (MQ)	47.0 m ³ /s 0.098 mm/h (1904-2008)
Max. Runoff (HHQ)	1130 m ³ /s 2.35 mm/h (1999)
Min. Runoff (NNQ)	2.24 m ³ /s 0.005 mm/h (1947)
99.7% exceedance (MNQ, Q ₃₆₅)	3.83 m ³ /s 0.008 mm/h
95% exceedance (Q ₃₄₇)	9.32 m ³ /s 0.019 mm/h
90% exceedance (Q ₃₂₉)	12.0 m ³ /s 0.025 mm/h
50% exceedance (Q ₁₈₂)	33.0 m ³ /s 0.069 mm/h
10% exceedance (Q ₃₆)	95.7 m ³ /s 0.199 mm/h
5% exceedance (Q ₁₈)	130 m ³ /s 0.271 mm/h
0.3% exceedance (Q ₁)	382 m ³ /s 0.795 mm/h
MHQ	585 m ³ /s 1.22 mm/h
HQ ₁₀	818 m ³ /s 1.70 mm/h
HHQ/MQ ratio	24:1
MNQ/MQ ratio	12:1
MNQ/MQ ratio	1:12
River Order (Strahler, 1952)	7
River Length	127 km
River Slope (upper, middle, lower part)	10-20‰, 3-4‰, 1.6-2‰
Northern Side Channel Slope	1-1.5‰
Southern Side Channel Slope	1-1.5‰
Landuse Agriculture	61% (85% grassland, 15% intensive agriculture)
Landuse Forest	30%
Landuse Residential	9% (66% settlements, 33% streets)
Livestock Unit Density	118 LU/km ²
Population Density: Inhabitants	223 In/km ²
Sewage Inhabitant Equivalents	221 InE/km ²
Sewage Contribution at low Flows	up to 30%

Table D2. Key descriptors of the Thur Valley aquifer [Baumann *et al.*, 2009].

Length	36 km
Width	2-3 km
Depth	5-20 m
Altitude	380 m asl
Hydraulic Conductivity of the Riverbed	$10^{-3} - 10^{-4}$ m/s
Annual Rainfall	900 mm
Potential ETP	600 mm
Local Recharge	$0.49 \text{ m}^3/\text{s}$
Lateral Inflows	$0.1 \text{ m}^3/\text{s}$
Exfiltration	$3.1 \text{ m}^3/\text{s}$
Infiltration	$3.0 \text{ m}^3/\text{s}$
Abstraction (via pumping wells)	$0.36 \text{ m}^3/\text{s}$

**Figure D1.** Location of the Thur catchment, the Thur valley aquifer and the test sites at Neunforn (partly restored) and Widen (channelized) in NE Switzerland.**Figure D2.** Test site Neunforn, partly restored (left) and partly channelized (right) with monitoring-well transects A, B, C, D, E (Table D3). Thalweg (dashed black line), surface water levels (solid black line) and water depths (blue color coded) for River Thur under low-flow conditions ($20 \text{ m}^3/\text{s}$). Contour lines of groundwater heads (yellow solid lines) are based on interpolated surface-water levels in the river (measured at flows of approximately $30 \text{ m}^3/\text{s}$) and the side channels with a differential GPS (red crosses). Bathymetric surveys are conducted annually in September by measuring predefined cross-sections (gray lines with white numbering).

D.3 PRELIMINARY INVESTIGATIONS

All existing data about the site were taken into account to design a continuously operating monitoring network. Existing reports (identification of well protection zone), maps (hydrogeology, paleochannels, digital terrain models or orthophotos) and data series (hydrological yearbooks of river and groundwater gauges, case studies) formed the initial basis for estimating hydraulic heads, groundwater flow direction, and hydraulic conductivities. In the Thur Valley, cantonal authorities have collected time series of hydraulic head, water temperature and electrical conductivity in the Thur River and at a small number of adjacent monitoring wells over the last ten years.

While Section D.4 mainly describes the design of the network of instrumented monitoring wells, we discuss in this section surveys performed prior to the installation of these monitoring wells that went beyond standard surveys performed by the cantonal authorities. Some of these surveys were repeated to document dynamic changes.

D.3.1 Geodetic surveys, bathymetry, and hydraulic-head measurements

River restoration significantly modifies river and floodplain morphologies and their dynamic behavior. Installing monitoring wells in the riverbed or close to the river thus requires knowledge of erosion and sedimentation dynamics. For instance, in the restored section of our test site, erosion and deposition processes are quite active because of frequent floods. This results in successive alterations of the fluvial morphology and the local riverbed topography, which in turn create dynamic boundary conditions for surface and groundwater flow. Consequently, monitoring and modeling of the topography of the riverbed and the floodplain area are fundamental. To achieve this, we developed a comprehensive approach to monitor the morphodynamic evolution of restored river corridors based on airborne laser scan surveys with synchronous bathymetric surveying [*Pasquale et al.*, 2011].

Figure D2 illustrates how the results of a differential-GPS survey can be used to estimate the hydraulic-head distribution within the aquifer. We measured the water level of the river, the side channels and the existing monitoring wells and interpolated these head values by ordinary kriging with a linear variogram, resulting in the yellow contour lines of Figure D2. The implicit assumptions made by this interpolation are that groundwater flow is strictly horizontal (Dupuit assumption) and that the hydraulic contact between river and groundwater is perfect. Both assumptions must be investigated, but the resulting maps of groundwater levels give a first indication of hydraulic gradients (Table D3) and groundwater flow

directions. Based on these data we could identify losing stream conditions, areas with high hydraulic gradients and locations of potentially significant exfiltration into the side channels.

The water table in the river is generally higher than in the side channels. The northern side channel is flowing back into the river downstream of the central gravel bar shown in Figure D2, whereas the confluence of the southern side channel is located 1.5 km further downstream. This explains the higher gradients towards the southern channel and the dominance of the southern side channel in draining the entire river corridor [Baumann *et al.*, 2009]. Similarly, the groundwater level and the direction of hyporheic flows through gravel bars could be initially estimated with simple measurements of the surface-water level.

Table D3. Comparison of the five monitoring-well transects at the test site Neunform.

Parameter Transect Name	A Pumping station	B Forest	C Central Bar	D Levee Downstream	E Levee Upstream
Number of Wells	18	29	12	7	9
Transect Length	135 m	190 m	80 m	70 m	60 m, 85 m
Head Difference	0.5 m	0.25 m	0.5 m	1.0 m	1.5 m
Hydraulic Gradient	3.7‰	1.3‰	6.3‰	14.3‰	25‰, 17.6‰
Slug-Tests	X	X	-	-	-
Focus Exfiltration	-	-	-	-	X
Focus Infiltration	X	X	-	X	X
Forced Tracer Tests	X	X	-	-	-
Unforced Tracer Tests	-	X	-	-	X
Geophysical Survey	X	XX	X	-	-
Sampling	X	XX (focus)	-	X	-
Sensing	X	XX	X	X	X
Multi Level Sensing	-	XX	-	X	XX
Online Sensing	-	XX	X	X	-
Lost Sensors	-	-	X	-	-

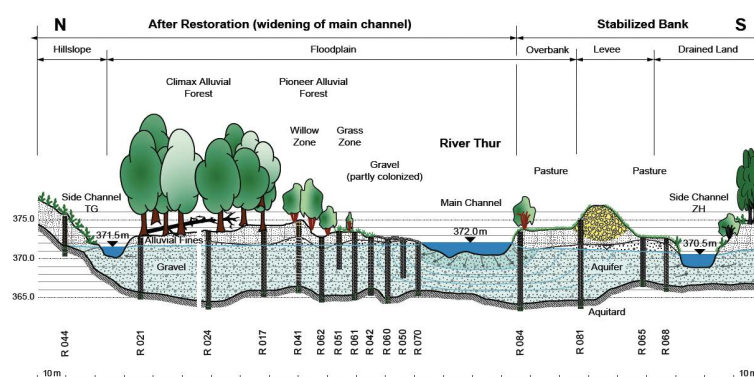


Figure D3. Geological cross-section representing restored (left; transect B in Figure D2) and channelized (right; transect E in Figure D2) transects at the test site Neunform. The restored parts comprises gravel bars developed naturally after restoration in 2002 - including the gravel zone, sparsely colonized with pioneer plants, and the grass zone characterized by thick layers of young alluvial overbank sediments densely colonized with mainly reed grass (*Phalaris arundinacea*) - the willow zone where older alluvial sediments were stabilized during restoration by planting young *Salix viminalis*, and the alluvial forest dominated by ash and maple growing on older alluvial sediments.

D.3.2 Geophysical surveys

Surface-based electrical resistance tomography (ERT) [Günther *et al.*, 2006] was used to obtain 2-D electrical resistivity profiles crossing the river. In saturated porous media, electrical resistivity is primarily related to porosity, pore structure, salinity, and clay content [Lesmes and Friedman, 2005]. Electrical resistivity models can thus be used to image the loam-gravel-clay sequences along the unrestored and restored river sections, as well as lateral variations in porosity within the gravel aquifer. In order to obtain reliable resistivity images it is important to incorporate the river water as a known conductive feature (we measured the electrical resistivity of the water when performing the measurements) and to accurately (within a few cm) determine the electrode positions.

Figure D4 displays an electrical resistivity model obtained for a profile that crosses the river upstream of the restored river section (close to transect A in Figure D2). We used 89 electrodes with an electrode spacing of 2 m and a total of 5743 measurements (a combination of Wenner and dipole-dipole arrays). The resulting model has a data misfit just over 3%. The gravel aquifer is readily identified as an approximately 6 m thick horizontal layer of moderate resistivities ($>100 \Omega \text{ m}$). The underlying less resistive layer corresponds to lacustrine clay and the upper 2 - 3 m on each side of the river corresponds to alluvial fines. The model does not indicate any conductive clogging layer at the river-gravel interface. Within the gravel aquifer it is possible to image regions of higher resistivities and thus lower porosities. ERT profiles that cross the river can only be acquired under low-flow conditions and three operators can acquire 2 - 3 such ERT profiles in a day.

Surface-based ground-penetrating radar (GPR) data provide more detailed information about the internal structure of the gravel aquifer [Beres *et al.*, 1999; Lunt *et al.*, 2004]. This technique transmits a high-frequency electromagnetic pulse into the ground and the reflected energy is recorded. Reflections occur at locations in which dielectric properties change, which mainly correspond to variations in water content. We have acquired extensive three-dimensional (3-D) GPR and ERT surveys at a gravel bar within the restored section of the Thur River (downstream of transect B in Figure D2).

Figure D5a displays a GPR reflection profile extracted along the beginning of transect B (Figure D2). From the GPR data we can identify the gravel-clay boundary as a rather strong reflection followed by much weaker signals (GPR signals are strongly attenuated in clay formations). The reflectivity patterns display a rather complex sub-horizontal layering within the gravel deposits. The fully processed 3-D GPR volume allowed us to map internal

interfaces within the gravel throughout the gravel bar and made it possible to identify different sedimentological features, such as an ancient paleochannel (Chapter 5).

Figure D5b displays an ERT model along transect B (Figure D2) using 23 electrodes and a 2 m spacing with a total of 408 measurements. The data misfit was just over 3%. The electrical resistivity model displays a top layer of alluvial fines, increasing in thickness with distance to the river (this soil layer and abundant vegetation make it impossible to obtain GPR images along the entire transect). To construct the ERT image, we used information about the depth of the gravel-clay interface from Figure D5a to better image the sharp transition between the underlying clay and the gravel aquifer.

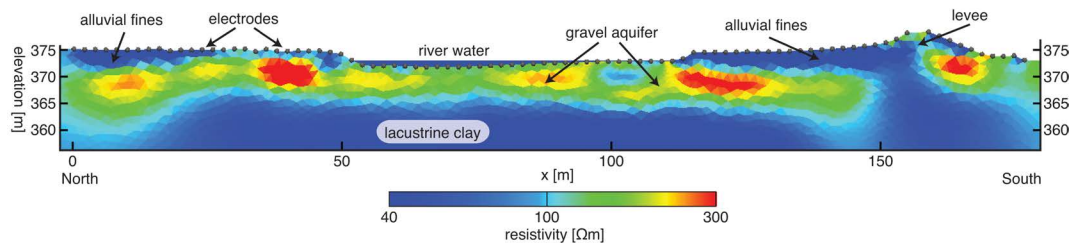


Figure D4. Electrical resistivity model crossing the Thur River at right angles in the vicinity of the pumping-station transect (transect A in Figure D2). The moderately resistive gravel deposits (green and red) can be distinguished from the overlying more conductive loamy topsoil (blue) and the underlying lacustrine clays (blue). Low porosity regions within the gravel deposits (red) can also be identified.

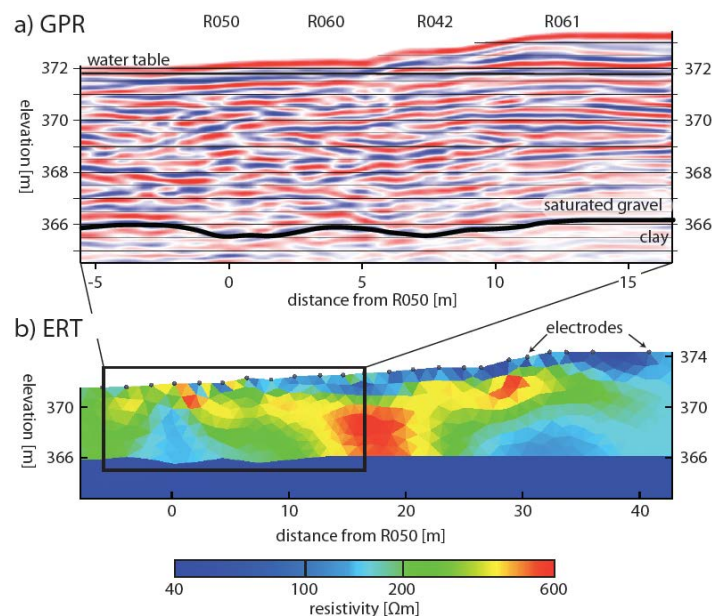


Figure D5. (a) GPR reflection profile and (b) ERT model obtained in the beginning of the forest transect (transect B in Figure D2). GPR reflections provide high-resolution information about porosity variations, whereas ERT provides information about average porosities and clay content at a lower resolution.

D.3.3 Streambed conductivity

Hydraulic conductivity of streambed and alluvial sediments ranges over several orders of magnitude. Therefore, the exchange between rivers and groundwater depends largely on the spatial arrangement of hydrofacies [Miall, 1995; Woessner, 2000; Fleckenstein *et al.*, 2006]. In order to investigate the hydraulic conductivity of the riverbed we have performed slug tests using temporary shallow piezometers. The experiments were conducted in the restored riverbed of our test site near Neunforn (Figures D1, D2 and D3). As it is difficult to permanently install and protect monitoring-wells in the main river channel (e.g., near the thalweg), we also performed slug tests at a reference test site about 15 km upstream near Widen, which is still channelized (Figure D1). Our results show that the uppermost 50 cm of the riverbed have a higher hydraulic conductivity than the deeper sediments (we measured at two test sites a total of 33 locations at depths of 50, 100, 150 and 200 cm). As hydraulic conductivities at the two sites do not differ significantly, we computed the statistics of the merged data set, obtaining a lognormal distribution with a geometric mean of 2×10^{-4} m/s and a log10 variance of 1.6. The mean value is considerably smaller than those expected for a gravel aquifer (see results presented in the following) suggesting that the hydraulic contact between the gravel aquifer and the river may be imperfect, at least at the locations where the slug tests were performed. Together with slug tests, hydraulic heads in the temporary piezometers and the river water were measured, facilitating the estimation of infiltration rates, which were in the range of $4 - 8 \times 10^{-5}$ m/s.

D.3.4 Hydrochemical surveys

We measured Radon-222 and other environmental tracers (SF6, CFCs, Tritium/Helium, O-18/Deuterium) in six pre-existing cantonal monitoring wells on the northern side of the Thur River (near the pumping station, transect A in Figure D2) to estimate groundwater residence times and mixing ratios [Kipfer *et al.*, 2002]. The travel times at our test site are in the range of several days, making Radon-222 the most suitable dissolved-gas tracer for dating. North of the river, fresh infiltrate was only observed between the Thur River and the side channel. At our test site, no monitoring wells existed between the river and the southern side channel prior to the RECORD project, but the large head difference between the Thur River and the southern side channel made us believe that the groundwater in between is dominated by fresh river infiltrate. In general, the groundwater of the investigation area can be described as calcium-hydrogencarbonate water.

Groundwater chemistry not only exhibits spatial trends but also temporal variations. Daily, event-based, and seasonal hydrochemical variations must therefore be incorporated into the sampling strategy. We studied the daily fluctuations of ion concentrations in the river and in a monitoring well located close to the river (distance ~15 m) using an automatic water sampler (6700, Teledyne ISCO Inc., USA) and subsequent chemical analysis in the laboratory. Hardness and hydrogencarbonate display strong diurnal oscillations in the river (Figure D6). These fluctuations are dampened in the adjacent monitoring wells. The other cation and anion concentrations vary only slightly and do not show periodic oscillations in the wells [Vogt *et al.*, 2010b].

D.3.5 Temperature surveys

In recent years, temperature has become popular as a natural tracer for the quantification of exchange fluxes between surface-water bodies and aquifers [Silliman and Booth, 1993; Constantz *et al.*, 2003; Hatch *et al.*, 2006; Schmidt *et al.*, 2006; Keery *et al.*, 2007; Schmidt *et al.*, 2007]. Distributed temperature sensing (DTS) is a rather new measurement techniques enabling comprehensive investigations of temperature distributions along an optical fiber based on Raman scattering [e.g., Selker *et al.*, 2006]. The method allows temperature measurements along a several kilometer long fiber with a spatial resolution of 1 m and a temperature resolution < 0.1 K at a time resolution of 15 min. By wrapping the fiber around a pole, the spatial resolution can be significantly increased (Figure D7a). Vogt *et al.* [2010a] obtained high-resolution temperature profiles within the riverbed of the Thur River by installing such a wrapped pole (vertical resolution: 5 mm). They analyzed the resulting temperature time-series by nonstationary spectral methods, observing temporal variability of infiltration in response to water-level changes (Figure D7b) and a vertical variation of seepage rates (Figure D7c), which they attributed to lateral flow. Infiltration velocities are ranging from 2 to 5×10^{-5} m/s when applying a 1-D solution, in which velocities of 4 to 5×10^{-5} m/s is found in the upper sediment layers (depths up to 0.6 m) and around 2×10^{-5} m/s is found in the deeper layers (depths greater than 0.6 m) respectively (Figure D7c).

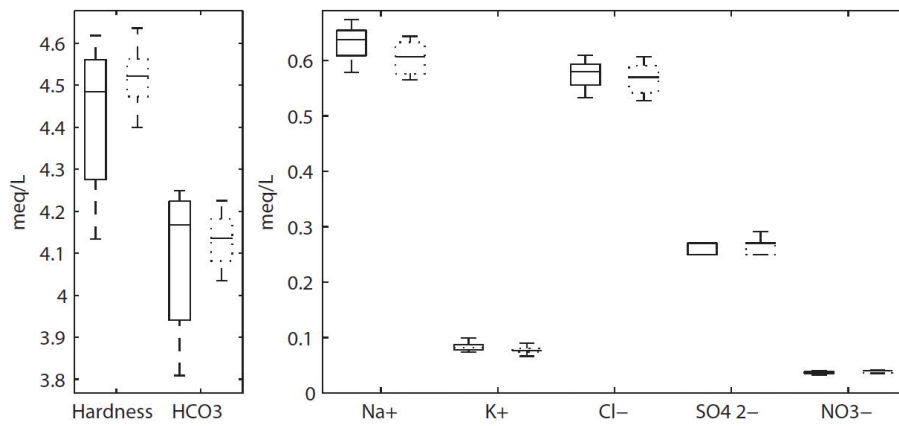


Figure D6. Box plots comparing daily variation in hydrochemistry in river (solid) and near-river groundwater (dotted) in a monitoring-well R042 in the forest transect (transect B in Figure D2) sampled every two hours over a period of two successive summer days.

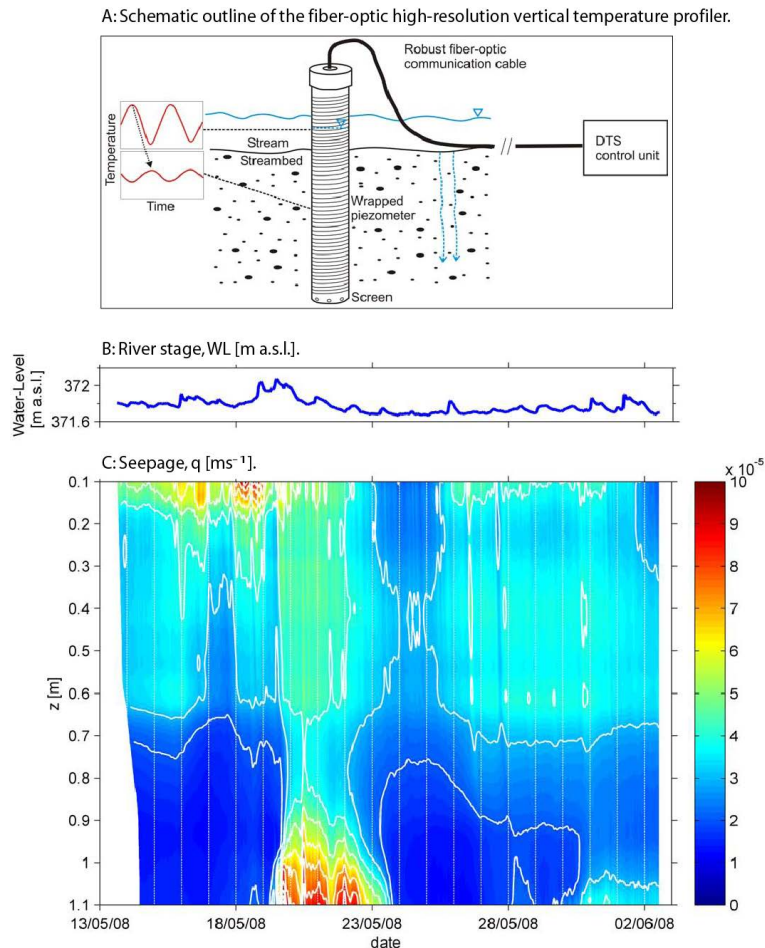


Figure D7. Estimated apparent seepage fluxes compared to the river stage. (A) Distributed temperature sensing (DTS) for vertical profiles. (B) River stage of gauging station. (C) Calculated vertical seepage fluxes. Contourlines: isolines 1×10^{-5} m/s. Figure modified after *Vogt et al. [2010a]*.

D.4 DESIGN OF CONTINUOUS MONITORING AND INSTRUMENTATION

Based on the results of the preliminary investigations discussed above, we designed a network of observation wells, organized in several transects and clusters, in order to monitor groundwater in the direct vicinity of Thur River. We aim to understand how key mechanisms of biogeochemical cycling of infiltrated river water are affected by the distance to the river, travel time within the subsurface, and characteristics of the river bank. This requires (1) installing monitoring-well transects oriented in the (assumed) direction of groundwater flow at locations with different river-bank characteristics, (2) the recording of quantities that allow the estimation of travel times, and (3) sampling strategies for water-quality parameters. Aspects pertaining to monitoring and instrumentation strategies of river morphodynamics and vegetation interactions at the site are described elsewhere [Pasquale *et al.*, 2011]. Also, detailed surveys using DTS in the river bed are reported elsewhere [Vogt *et al.*, 2010a]. In the following we will discuss (1) the design of the monitoring-well network and details of the installation, (2) hydraulic and geophysical tests performed in the monitoring-well transects, (3) the instrumentation of selected monitoring wells with continuously operating sensors, and (4) sampling strategies.

D.4.1 Design of monitoring-well network

A key objective of the groundwater monitoring is to study the transformation of river water into young groundwater. The river water is rich in oxygen and degradable organic carbon and it contains pollutants, while the young groundwater is depleted in oxygen and degradable organic carbon, may contain metabolites of the pollutants and is slightly more mineralized than the river water. At specific monitoring and sampling points, we want to (1) estimate travel times, (2) determine transformation rates from concentration differences and time information, and (3) aid developing a quantitative understanding of biogeochemical zonation and associated turnover of pollutants. The results concerning biogeochemistry and pollutant turnover will be presented elsewhere. Nonetheless, the monitoring-well network was designed with the goal of quantifying the turnover of solutes in mind.

Ideally, monitoring wells should be oriented along flow lines, thus allowing sampling of a wide range of groundwater ages, starting with very young (travel times of a few hours) hyporheic water. Hyporheic flow is seldom at steady state, so flow lines vary. Furthermore, riverbed sediments are reorganized during floods, leading to changed flowpaths in the subsurface. Even if these effects could be excluded, subsurface heterogeneity makes it

difficult to predict flowpaths and travel-time distributions using regional groundwater level data alone. Water sampled in a particular monitoring well will therefore most likely bypass subsequent wells. Finally, very young hyporheic groundwater is difficult to access, since permanent installation of monitoring wells within the riverbed is impossible. Rather than focusing on a single transect of monitoring wells, we designed a network of several transects and clusters at different locations within our test site. Figure D2 shows all monitoring wells installed at the site by January 2010.

All monitoring wells were installed with a dual-tube soil sampling system using a direct-push machine (Geoprobe® 6620DT). The two-inch monitoring wells are made of HDPE or PVC pipes with 53 mm inner and about 60 mm outer diameter. They are mostly fully screened (1 mm slot width) over the thickness of the gravel aquifer. Casing was installed over the thickness of the alluvial fines. One meter of casing was also added at the lower end extending into the underlying lacustrine clay. After extracting the outer direct-push tube of 83 mm diameter, filter gravel was added into the open space between the well tube and the open borehole up to a depth of approximately 1 m below ground. Bentonite was added to the top to prevent preferential infiltration along the well tube. Monitoring wells on overbanks terminate just below the ground surface within a concrete-cased PVC pipe of 300 mm diameter, capped at ground surface. The other monitoring wells end about 1 m above ground with standard well caps.

In a first step, we installed survey monitoring wells – forming hydrologic triangles or squares encompassing the full intended transect – to determine prevailing hydraulic gradients. We subsequently installed profiles of monitoring wells forming observation transects, following the hydraulic gradient determined by the initial monitoring wells. The spacing between the monitoring wells within the observation transect depends on the planned investigation methods and assumed travel times. For example, cross-borehole geophysical surveys require a maximum spacing in the range of the aquifer thickness, which is 4 - 7 m at our site. Practical issues such as bank stability and accessibility of the direct-push machine were also considered. Besides a few individual monitoring wells, needed to determine the regional ground-water flow field and background values of hydrogeochemistry, the monitoring wells are arranged in the following transects and clusters:

Pumping station transect A

The river is channelized in the vicinity of the pumping station. The fluvial deposits on the overbanks are 2 m thick and the low-water channel is stabilized with riprap as revetment. The

pumping well is located on the landside slope of the levee near the northern side channel. A beaver dam in this side channel located 30 m upstream of the pumping station has locally increased the water level by 0.5 m. Tracer tests have shown that the bed of the side channel is clogged in the reach upstream of the beaver dam. This transect is used as a reference to represent the channelized sections of the Thur River (Table D3). The pump in the abstraction well is operated at a rate of 3.3 L/s for 1 h (pumped volume 12 m³) in the morning and 2 h in the evening (24 m³).

Forest transect B

This transect starts on a gravel bar formed after restoration of the Thur River and extends into the mature alluvial forest. As indicated in Figure D2, the overall hydraulic gradient along the transect is comparably small so that travel times of infiltrated river water may be longer than along transect A. Considering the regional hydrogeological situation, it can not be excluded that the groundwater at the north-western end of this transect consists of old groundwater rather than fresh-river infiltrate. At the south-eastern end of the transect, the morphologically active gravel bar is monitored, because we expect strong differences in water-mixing ratios of infiltrated river water to groundwater, hydrochemistry, and travel times between the two ends of the transect. As can be seen in Figure D2, the observation wells are placed much more densely on the gravel bar than within the forest. The combination of transects A and B gives the opportunity to compare bank filtration at channelized and restored sections of the Thur River with similar geological properties.

Central gravel bar cluster C

This cluster of individual monitoring wells is in the morphologically most active zone of the restored river reach. The monitoring wells are placed on a gravel bar that remains an island even at relatively high water levels. Currently, the thalweg is at the southern branch of the river, but within the time period since restoration in the year 2002, the main river course has also temporarily been north of the gravel bar. The river stage at the southern branch is about 20 cm higher than at the northern side, enforcing hyporheic flow through the gravel bar. Full inundation of the entire gravel bar occurs at 350 m³/s. Even though the surface of the gravel bar is covered by large pebbles, entrapped fines can be observed already at 10 cm depth. Because materials are mobilized during floods, the hydraulic conductivity within these active sedimentary deposits may change with time. In contrast to the other study areas, the monitoring wells are not aligned along a line, because the direction of flow through the gravel bar may change at small time scales according to different river stages, and due to

morphological changes. Locations of the monitoring wells are chosen to represent different frequencies of inundation and different morphological features (e.g., the southern branch of the river actively cuts into the sediments), whereas the slope of the gravel bar is milder at the northern side.

Downstream southern transect D

This is a comparably short transect located on the southern overbank close to the central gravel bar (Figure D2). Here, the thalweg of the river is very close to the overbank, which undergoes active erosion. We assume that clogging layers have not developed or are removed along the thalweg and thus speculate that river-water infiltration is not hindered in the vicinity of the transect D. The hydraulic gradient between the river and the southern side channel is fairly steep suggesting that the youngest infiltrate is found along the chosen transect. This transect allows us to sample very young hyporheic water at monitoring wells on the overbank that otherwise would require installations within the river.

Upstream southern transect E

This transect (E in Figure D2) exhibits the highest hydraulic gradient between the river and the side channel (Table D3) and is useful for artificial-tracer tests with limited time duration. A particular interest of such tracer experiments is to identify the direction of flow in comparison to the assumed hydraulic gradient and locations of local exfiltration into the southern side channel. We speculate that exfiltration zones are unevenly distributed forming hot spots. In comparison to the other transects and clusters, transect E includes several monitoring wells located very close to the draining southern side channel.

D.4.2 Cross-borehole geophysical surveys on monitoring-well transects

Compared to surface-based geophysical surveys, cross-borehole measurements can provide subsurface information with higher resolution at depth in regions of specific interest. Chapter 2 combines data from cross-borehole seismic and ground-penetrating radar (GPR) travel times as well as ERT measurements for a hydrogeophysical characterization of the gravel aquifer at the Widen reference site (Figure D1). GPR travel times sense variations in permittivity, which can be directly linked to porosity using petrophysical models [Lesmes and Friedman, 2005]. Combining the porosity information with electrical resistivity models from ERT measurements allows estimation of the contribution of surface conductivity, which can be linked to the amounts of clay and silt material in the ground [Linde *et al.*, 2006a]. At the

restored reach near Neuenforn, cross-borehole GPR data was acquired between the densely spaced boreholes on transects A, B and C.

D.4.3 Hydraulic surveys within the monitoring-well transects

Slug tests are applied to estimate hydraulic conductivities of aquifers by measuring the recovery of hydraulic head in monitoring wells after a forced (nearly instantaneous) change. The recorded changes in hydraulic head over time are fitted to analytical solutions. Slug tests offer quantitative information about vertical and horizontal variations in hydraulic conductivity in the vicinity of individual monitoring wells [Butler, 1998]. Compared to other techniques for hydraulic-conductivity estimation, slug tests offer advantages such as (1) low cost, (2) simplicity, (3) quick and easy application and data analysis, and (4) small support volume (less than one decimeter around the test well) that allow estimating small-scale variability of aquifer properties [Butler, 1998]. Pneumatic slug tests (injection of compressed air in a sealed monitoring well) are preferred over classic slug tests (dropping a weight into a well), because the former yield more accurate results in formations of high hydraulic conductivity [Butler, 1998].

We performed rising-head pneumatic slug tests in selected monitoring wells in transect A and B using a double-packer system together with an air-tight well-head apparatus and a small-diameter pressure transducer (Druck PDCR 35/D-8070) connected to a data logger (Campbell Scientific CR800) with an acquisition rate of 10 Hz. We followed best-practice recommendations [Zurbuchen *et al.*, 2002; Butler *et al.*, 2003] and processed our data according to Butler [1998], Butler *et al.* [2003], and McElwee and Zenner [1998] with the software AQTESOLV-Professional (www.aqtesolv.com). We applied the model of Bouwer and Rice [1976] for over-damped response data in unconfined aquifers, whereas for under-damped response data (with oscillatory behaviour), the model of Springer and Gelhar [1991] was used. In confined aquifers, we analyzed the response data with over-damped behaviour with the model of Bouwer and Rice [1976], whereas for the under-damped response data, the model of Butler [1998] was the most appropriate.

D.4.4 Instrumentation of monitoring wells

We conducted several water-sampling campaigns to monitor bank filtration. First, we sampled all monitoring wells to select locations for detailed investigation. Based on these data, we installed combined sensor units for electrical conductivity, temperature, and pressure

(DL/N70, STS AG, Switzerland; error of single measurement $\pm 2\%$ for EC, ± 0.25 K for temperature, $\pm 0.1\%$ for head) accompanied by sensor chains of electrical conductivity and temperature at different depths (e.g., TE, Decagon Devices, USA; error of single measurement $\pm 10\%$ for EC, ± 1.0 K for temperature) in the river and in selected wells. In all transects, the monitoring well nearest to the river is equipped with such sensor chains consisting of at least two – in selected monitoring wells up to five – monitoring levels over the full aquifer depth. With growing distance to the river along a transect, the number of monitored levels is reduced and successively concentrated to the topmost groundwater layer (upper meter of the aquifer). The sampling interval is 15 min which is adapted to the dynamics of the river.

Selected monitoring-wells in locations next to the river are equipped with multi-level sensing and sampling devices in a first step. In a second step, sensors are installed to continuously stream data via wireless data transfer techniques [Beutel *et al.*, 2007; Barrenetxea *et al.*, 2008], allowing real-time processing and analysis of these proxy data to enable time and depth-optimized sampling.

D.5 RESULTS

D.5.1 Geodetic surveys, bathymetry and hydraulic modeling

We calibrated and validated the hydraulic model mentioned in Section D.3 for each available DEM. Subsequently, we simulated river stages for flow conditions ranging from the minimum recorded discharge up to the one that completely inundates the island. Given the coarse grain-size distribution of the alluvial material [Pasquale *et al.*, 2011], the water-table fluctuations are expected to penetrate the gravel bar with almost no delay with respect to hydrograph dynamics. This implies quasi steady-state flow within the gravel bar. As a simple estimate, we inferred the groundwater table in the gravel bed for each point of the island (Figure D8). After having installed our monitoring wells in cluster C, we compared the interpolated heads to measured data of the monitoring wells in cluster C. Figure D8d shows this comparison for well R034, indicating a fairly high accuracy of the interpolation even under dynamic conditions (root mean-square error 80 mm). This implies that hydraulic modeling of the river at the site is not only useful to analyze fluvial hydrodynamics, but also predicts dynamics of hyporheic water tables. Additional information about hydraulic conductivities is needed to estimate hyporheic flow velocities and travel times.

D.5.2 Cross-borehole geophysical surveys

Cross-borehole GPR travel-time tomography was performed along transect A (Figure D2) to estimate relative variations in porosity (Figure D9). Radar travel-time inversion was first used to estimate the electrical-permittivity distribution, which was then transformed into estimates of porosity. These porosity estimates were obtained using the petrophysical model of *Linde et al.* [2006a] with the parameters chosen of Chapter 2 at the Widen site (see Figure D1). The porosities representing meter-scale averages vary between 16% and 23%, and a lower-porosity layer is clearly imaged in the middle of the gravel aquifer (Figure D9).

For cross-borehole GPR, it is important to have densely spaced boreholes fully penetrating the layers of interest. The ratio of borehole separation and the depth range of interest should preferably be smaller than one. The areas of interest should thus be defined on the basis of geological knowledge and surface-based geophysical measurements before installing an appropriate dense network of monitoring wells. For the processing of cross-borehole GPR data, it is essential to either have almost perfectly vertical boreholes or measure borehole deviations to obtain accurate (within a few cm) information about lateral positions of the antennas in the ground.

D.5.3 Hydraulic surveys

Figure D10 illustrates the hydraulic-conductivity distribution along transect A (Figure D2) obtained by the slug tests described in Section D.4.3. In total, 51 measurements of hydraulic conductivity K were performed in the part of transect A next to the river (5 - 30 m). They revealed less heterogeneity than commonly expected for fluvial gravel deposits. The geometric mean was 3.1×10^{-3} m/s ($\approx 10^{-2.5}$ m/s) and the variance of \log_{10} hydraulic conductivity was 0.2. These results agree with values obtained at other test sites in the Thur Valley [*Diem et al.*, 2010], indicating that our monitoring-well transects might be geologically representative for the entire Thur Valley. To obtain the vertical cross section of the hydraulic conductivity K in Figure D10, we interpolated the K -measurements by kriging assuming an anisotropy ratio of ten and a linear variogram. The lowest K -values are observed at the aquifer bottom, while higher K -values are found in the center of the aquifer (Figure D10). K -values range between 2.3×10^{-4} m/s ($\sim 10^{-3.7}$ m/s, labeled blue in Figure D10) and 7.4×10^{-3} m/s ($\sim 10^{-2.1}$ m/s, labeled red in Figure D10).

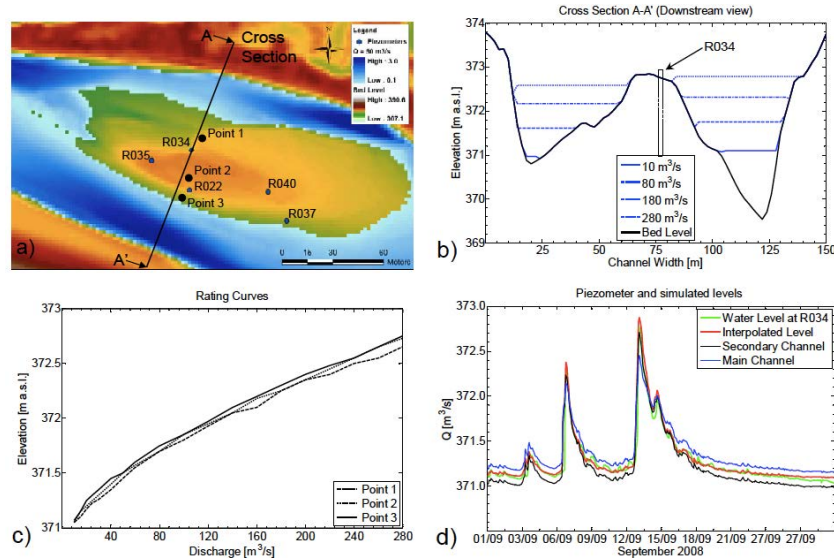


Figure D8. Cross section across the central gravel bar (transect C in Figure D2): (a) plan view; (b) profile of surface elevation (m a.s.l.) and water depth (m) as function of river discharge; (c) corresponding rating curves, (d) comparison between measured and interpolated groundwater heads in monitoring well R034.

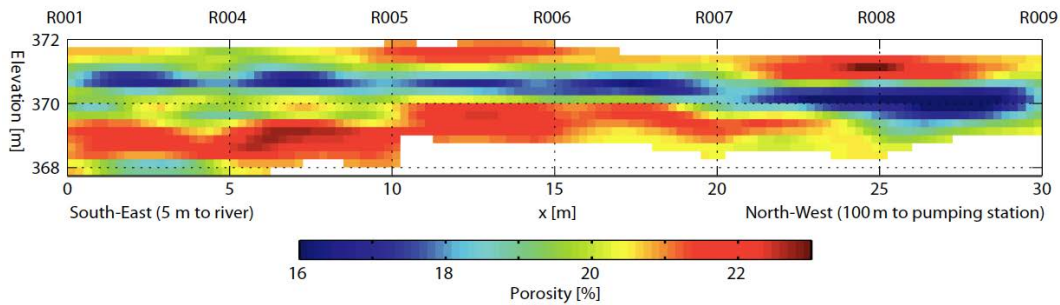


Figure D9. Porosity distribution along the pumping-station transect (transect A in Figure D2) obtained by cross-borehole georadar travel-time tomography. A continuous low-porosity layer is imaged across the entire profile between two higher-porosity subhorizontal layers. Note that the porosities represent average porosities on the m-scale and that the absolute values might be slightly down or upward biased given the uncertainty of the parameter values chosen for the petrophysical transformation.

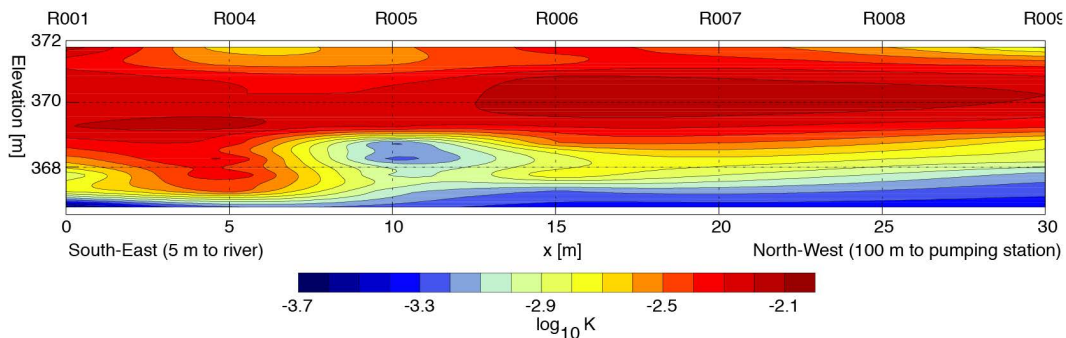


Figure D10. Hydraulic-conductivity distribution along the pumping-station transect (transect A in Figure D2) obtained by slug tests performed in different depths in monitoring wells along the transect. A continuous high hydraulic-conductivity layer is imaged in the upper aquifer, whereas the lower part of the aquifer is characterized by lower hydraulic conductivities.

D.5.4 Hydrochemical sampling and sensing

Figure D11 shows time series of the river water level (A) and electrical conductivity (B) in the Thur River and in monitoring well R042 (transect A, 15 m from the river). The figure shows a clear correspondence between electrical-conductivity (EC) signals in the river and in the monitoring well. As reported in previous studies [Cirpka *et al.*, 2007; Vogt *et al.*, 2009; Vogt *et al.*, 2010b], EC in the Thur River drops in response to precipitation in the upper catchment, which also causes high river water stages (see the correspondence of water table and low EC during flood events in Figure D11). The EC signal is propagated into the aquifer by advective-dispersive transport and is slightly modified by water-rock interactions. We analyze the time series of EC in the river and all monitoring wells equipped with EC sensors by nonparametric deconvolution [Cirpka *et al.*, 2007]. This method yields the transfer function $g(\tau)$ of EC between the river and the observation well without relying on a particular functional form, but assuming stationarity of $g(\tau)$. The transfer function may be understood as the outcome of a virtual tracer test with pulse-like injection.

The integral of the transfer function can be interpreted as the recovery rate of the EC signal, possibly quantifying the mixing ratio of fresh river-water infiltrate in the mixture with old groundwater. The normalized transfer function $p(\tau) = g(\tau) / \int_0^{\infty} g(\tau_*) d\tau_*$ is the probability density function of travel time for the transfer of EC from the river to the observation well. Figure D11c illustrates the transfer function inferred from the EC time series shown in Figure D11b. A detailed discussion of EC time series obtained at the site, including elaborations on diurnal fluctuations, is given by Vogt *et al.* [2010b].

D.6 DISCUSSION AND CONCLUSIONS

We have presented an instrumentation strategy for the assessment of bank-filtration processes in a partly restored river reach. The strategy consists of (1) preliminary surveys characterizing primarily structural properties of the river and the subsurface, (2) the design, instrumentation, and operation of monitoring-well transects, and (3) data analysis by modeling. While the studies have been performed to address water quality issues of river restoration, the present paper focuses on physical properties and processes. Particular emphasis has been given on selecting and instrumenting monitoring-well transects and clusters in the channelized and restored parts of the river reach.

The hydro-chemical properties of the infiltrating river water change during and after infiltration with a continued transformation according to its travel time in the aquifer. To

study the full range of transformation, it is important to identify locations with freshly infiltrated water and install transects of observation points that approximately follow the flowpaths. This was the major incentive of instrumenting transects A, B, and D (Figure D2), as they differ in hydraulic gradient, sampled groundwater age, and biogeochemical gradients.

In natural or restored river reaches with highly variable river morphology and dynamic flow regime, it may be impossible to identify points of pronounced infiltration and follow the direction of subsurface flow. Under such conditions, one may need to give up the idea of approximately following a water parcel. Instead, the use of monitoring-well clusters – like cluster C (Figure D2) – may become more appropriate. Enhanced erosion and deposition in restored river reaches lead to permanently changing river morphology and thus add to the complexity of maintaining continuous monitoring, and increase the related efforts and costs significantly. To protect monitoring wells in the floodplain, selected wells were constructed using a below-ground enclosure design. Several monitoring wells located on uncolonized and colonized gravel bars were frequently buried by sediments. It is therefore important to accurately locate (within a few cm) all monitoring wells in the river corridor right after installation, for example, with a high-precision differential GPS. Online sensing prevents losing complete time series acquired in such harsh environments.

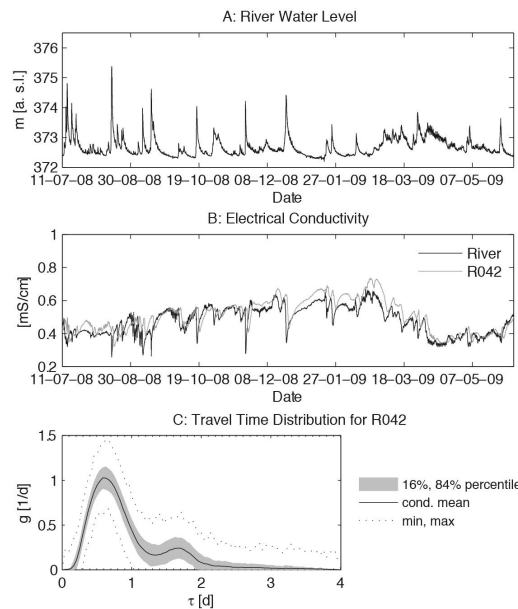


Figure D11. River water level (A) and electrical conductivity fluctuations (B) in River Thur and a near-river monitoring well (R042) in the forest transect (transect B in Figure D2). Transfer function (C) between the Thur River and monitoring well R042 obtained by deconvolution of the electrical-conductivity time series. Figure after Vogt et al. (2010a), modified.

The first results obtained at our site indicate that groundwater tables between river branches or between the river and side channels can be approximated rather well by interpolating surface-water levels, even under dynamic conditions. This implies a good hydraulic connection between surface water and groundwater. We have gained predictive capabilities with respect to groundwater levels by the calibration of a river-hydraulic model. The data needed for this model are the bathymetry of the river and side channels, the river hydrograph obtained at a river station downstream of our site, and individual river-stage or shoreline measurements at known river discharge for calibration. This procedure can be transferred to other sites with braided rivers or connected rivers and side channels.

Subtracting the estimated groundwater tables from measurements of land-surface topography yields the distance to groundwater, which may be important for the development of riparian vegetation and thus contributes to the overall ecological evaluation of river restoration. Missing ground water table dynamics in the presence of fluctuating river stages would be a clear indication of lacking connections between river and groundwater. However, synchronous river and groundwater signals alone is an insufficient indicator to quantify river-groundwater exchange (counter examples at the Thur River are given by [Vogt *et al.*, 2009]). Measurements of exchange fluxes are also needed, which are difficult to obtain [Kalbus *et al.*, 2006].

At the Thur River, travel times and mixing ratios between fresh river-water infiltrate and old groundwater can be inferred from time series of electrical conductivity [Cirpka *et al.*, 2007; Vogt *et al.*, 2009; Vogt *et al.*, 2010b]. Travel times and mixing ratios are much better indicators of river-groundwater exchange than hydraulic gradients. Travel times and hydraulic gradients are linked by hydraulic conductivity and porosity, which we have constrained in our monitoring-well transects by hydraulic and geophysical surveys. The deconvolution procedure of Cirpka *et al.* [2007], applied to infer the travel-time distributions, requires time series with several events of strong EC fluctuations. This implies a need for continuous measurements rather than individual sampling campaigns. Deployment of a sufficient number of sensors is thus crucial to gain system understanding. Extended analysis of the EC data to address changes of travel-time distributions over time will require the development of non-stationary deconvolution methods.

Field investigations in the past have often been limited by instrumentation costs and insufficient resolution of data in time and/or space. New developments in environmental sensing [Beutel *et al.*, 2007; Barrenetxea *et al.*, 2008; Trubilowicz *et al.*, 2009] reduce

monitoring network hardware and operation costs significantly and thus allow two and three-dimensional online sensing of EC, water temperature and hydraulic head with sensor units or multi-level sensor chains. Wireless data transfer reduces data losses and allows high resolution sensing of these proxy hydrological parameters at reasonable costs [Beutel *et al.*, 2007; Barrenetxea *et al.*, 2008; Nadeau *et al.*, 2009; Trubilowicz *et al.*, 2009]. Additionally, data handling can be partially automated and thereby reduce labor costs [Michel *et al.*, 2009; Wombacher and Schneider, 2010; Schneider *et al.*, 2011]. The combination of temporary deployments of such research monitoring networks (local scale, short to mid-term, problem-orientated and process- focused data sets) with governmental long-term monitoring networks (regional scale, durable design, continuous data records) is very promising.

Besides EC, we have also performed continuous monitoring of groundwater head and temperature. These data are currently under evaluation and are not discussed in the present paper. Continuous data streams of chemical parameters could potentially be of high value. Costs and stability of related sensors hinder, so far, massive deployment, so that chemical measurements at our site have been restricted to samples. The assessment of mixing ratios and travel times at individual points and of prevailing hydraulic gradients is insufficient to determine groundwater flowpaths. The latter are strongly affected by subsurface heterogeneity [e.g., Ptak and Teutsch, 1994] and may not fully coincide with hydraulic gradients. In a dynamic riparian system, hydraulic gradients and groundwater flowpaths vary in accordance to variable forcing created by fluctuations of surface-water level. This has consequences on the performance of our monitoring-well transects which were intended to follow at least approximately along flowpaths. We have oriented our monitoring-well transects in the direction of the hydraulic gradient determined from a few preliminary wells at times of low river stage. Our transects do not cover individual groundwater-flow lines at all times, but we are convinced that our strategy is superior to placing monitoring-well transects perpendicular to the direction of the river, as done in the vast majority of studies on bank filtration, hyporheic exchange, and riparian-zone mixing [Woessner, 2000].

For investigation of quifer thickness and sediment structures we have used geophysical surveying. For quantitative understanding of the groundwater flow field and associated solute transport, hydraulic parameters must be attached to the identified sedimentological structures, which we have initiated by hydraulic surveys. Boundary conditions are obtained from the river-hydraulic model and monitoring data of the river and the side channels. The ultimate goal is to integrate all available information into a 3-D groundwater flow-and-transport model

of the site that can simulate and forecast observed head and EC data in the monitoring wells. We are in the process of developing such a model. For the assessment of bank filtration, we recommend recording multi-level sensor data focusing on EC directly at river banks [Vogt *et al.*, 2010b]. The major challenges in monitoring bank filtration are (1) to choose locations with sedimentation-erosion equilibrium for monitoring-well transects, so that monitoring wells and sensors survive floods without getting eroded or covered by sediments, (2) to choose transects with a significant hydraulic gradient in groundwater, (3) to install cost-effective sensors, so that 2-D or 3-D monitoring is feasible and (4) to stream data, for example via state of the art wireless technology, so that failure or loss of a sensor does not result in a complete loss of data. Benefits of online monitoring systems are the flexible timing for sampling at specific locations and times informed by the proxy data that reflect the status of the system in the surroundings of a monitoring-well transect.

APPENDIX E: SELF-POTENTIAL INVESTIGA- TIONS IN THE THUR RIVER CORRIDOR

Published in *HESS*:

Linde, N., Doetsch, J., Jougnot, D., Genoni, O., Dürst, Y., Minsley, B. J., Vogt, T., Pasquale, N., and Luster, J., 2011. Self-potential investigations of a gravel bar in a restored river corridor, *Hydrological Earth Systems Science*, **15**, 729-742.

ABSTRACT

Self-potentials (SP) are sensitive to water fluxes and concentration gradients in both saturated and unsaturated geological media, but quantitative interpretations of SP field data may often be hindered by the superposition of different source contributions and time-varying electrode potentials. Self-potential mapping and close to two months of SP monitoring on a gravel bar were performed to investigate the origins of SP signals at a restored river section of the Thur River in northeastern Switzerland. The SP mapping and subsequent inversion of the data indicate that the SP sources are mainly located in the upper few meters in regions of soil cover rather than bare gravel. Wavelet analyses of the time-series indicate a strong, but non-linear influence of water table and water content variations, as well as rainfall intensity on the recorded SP signals. Modeling of the SP response with respect to an increase in the water table elevation and precipitation indicate that the distribution of soil properties in the vadose zone has a very strong influence. We conclude that the observed SP responses on the gravel bar are more complicated than previously proposed semi-empiric relationships between SP signals and hydraulic head or the thickness of the vadose zone. We suggest that future SP monitoring in restored river corridors should either focus on quantifying vadose zone processes by installing vertical profiles of closely spaced SP electrodes or by installing the electrodes within the river to avoid signals arising from vadose zone processes and time-varying electrochemical conditions in the vicinity of the electrodes.

E.1 INTRODUCTION

The self-potential (SP) method is a passive geophysical method, in which natural spatial and temporal variations in the electrical potential field are measured on the surface of the earth or in boreholes. The resulting SP maps and monitoring data are sensitive to flow processes in the subsurface [e.g., *Doussan et al.*, 2002; *Rizzo et al.*, 2004; *Suski et al.*, 2006], but interpretation of field measurements is challenging. First, many different phenomena (e.g., water fluxes in the vadose or saturated zone, gradients in chemical potential, or redox processes) can create SP signals and it is often unclear which source types will dominate the response at a given site. Second, accurate modeling of SP responses (to given source currents) can only be achieved when detailed knowledge about the electrical conductivity distribution is available (see Chapter 4 in *Minsley* [2007]). Third, the self-potential method is a potential field method and the inverse problem of retrieving the source-current distribution in the subsurface is plagued by non-uniqueness. Even if the electrical conductivity distribution of

the subsurface is known, there exist an infinite number of source current distributions that can explain the data equally well. This leads to a situation in which the SP method is useful on a case-by-case basis and that its applicability at a certain site can often only be reliably assessed after the data have been acquired. Interpretation is further complicated by electrode responses that are affected by temperature variations (e.g., 0.22 mVK^{-1} for the electrodes used in this study [Petiau, 2000]) and non-linear drift terms that are related to electrode design and age, as well as changing electrochemical conditions in the vicinity of the electrodes.

Despite the complications mentioned above, the SP method continues to receive considerable interest in hydrogeology as SP data are sensitive to contaminant transport [e.g., Mainault *et al.*, 2004; Revil *et al.*, 2009], redox processes [e.g., Linde and Revil, 2007], flow in saturated [e.g., Mainault *et al.*, 2008; Bolève *et al.*, 2009; Revil *et al.*, 2009] and unsaturated porous media [e.g., Thony *et al.*, 1997; Doussan *et al.*, 2002; Linde *et al.*, 2007a], flow in fractures [e.g., Wishart *et al.*, 2006], the water table elevation [e.g., Fournier, 1989; Revil *et al.*, 2003; Rizzo *et al.*, 2004], or the thickness of the vadose zone [Aubert and Yééné Atangana, 1996], etc. For example, the SP method might potentially be used to estimate water fluxes in the vadose zone [Thony *et al.*, 1997]. Such fluxes are difficult to measure in the field and are commonly inferred indirectly by differencing water content measurements over time [e.g., Vereecken *et al.*, 2008]. This richness of application areas mirrors the main limitation of the SP method; many different processes contribute to the measured response.

Self-potential source generation and the modeling of the resulting SP field are well understood under saturated conditions [Sill, 1983; Sheffer and Oldenburg, 2007]. A better understanding for multiphase conditions has developed in recent years through both theoretical and experimental work [e.g., Linde *et al.*, 2007a; Revil *et al.*, 2007; Allègre *et al.*, 2010; Jackson, 2010], but there is still room for improvements. These recent findings suggest that relationships between unsaturated water flux or the local hydraulic pressure gradient and SP gradients are more complex than suggested by Thony *et al.* [1997] and Darnet and Marquis [2004].

To decrease non-uniqueness in the interpretation of SP data, a promising approach is to treat the data as being dependent on the state of a model that describes the variations of the hydrogeological and geochemical variables of interest. This adds complexity to the problem, but makes it possible to use SP data together with other data (e.g., time-series of hydrological head and tracer concentrations) to constrain hydrological boundary conditions, hydraulic conductivity structure, or vadose zone flow properties within a hydrogeological inverse

modeling framework. This is only possible if the source contributions of different hydrological processes are accurately modeled and understood, which highlights the importance of having access to different types of hydrological and geophysical data.

A good understanding of physical processes at a given site, together with advanced signal processing and modeling, appears thus to be the only way to reliably assess the origins of the dominant contributions to the measured signals. To assess the sensitivity of SP data to hydrological processes at a restored river corridor, we performed SP mapping and monitoring on a gravel bar within a restored reach of the Thur River in northeastern Switzerland. SP monitoring in river environments is not new, for example, it has been used to study fluctuations in the water table in the vicinity of Columbia River, Washington [*Timothy Johnson*, pers. comm] and to optimize pumping rates for bank filtration at the Russian River, California [*Gasperikova et al.*, 2008], but no conclusive results have been published to date.

Our first results concern the SP mapping and subsequent inversion of these data. We then perform an exploratory analysis of SP and hydrological time-series using wavelet analysis. For suitable periods, we compare SP time-series with those of water table position, precipitation, moisture content, and temperature. We then model, for a simplified geological model, the expected response related to the two processes that are the most likely source of the observed SP variability, namely (1) fluctuations in the water table and (2) infiltration following precipitation events.

Understanding the origins of SP signals at this site is important as one could make inferences about the hydraulic diffusivity of the aquifer if the water table effect dominates or one could obtain information about soil properties if infiltration processes dominate. SP data could then be used to evaluate, by comparing the data with those acquired at neighboring unrestored sites, the effect of river restoration on hydrological subsurface processes. Another more general motivation is that better understanding of near-surface SP sources can help to remove SP signals of shallow origin when investigating deeper phenomena, such as, volcanic activity [*Friedel et al.*, 2004], earthquake precursors [*Park et al.*, 1993], or processing magnetotelluric data [*Perrier and Morat*, 2000].

E.2 METHODS

E.2.1 Thur River field site

The Thur River in northeastern Switzerland (see Figure E1) is the largest Swiss river without natural or artificial reservoirs. It is a peri-alpine tributary of the River Rhine with a catchment area of about 1750 km². River hydrology shows a typical nivo-pluvial regime. Water level and discharge variations in the Thur are characteristic of unregulated alpine rivers where neither lakes nor reservoirs attenuate the discharge. The Thur aquifer consists mainly of glacio-fluvial sandy gravels (5 - 7 m thick in our study area; average hydraulic conductivity 5×10^{-3} m/s inferred from pumping tests [Baumann *et al.*, 2009]) overlaying thick lacustrine clays that can be considered impervious. The top of the aquifer is formed by fine alluvial sediments (fine-sand with silt). Like many other rivers, the meandering Thur was channelized at the end of the 19th century for flood protection purposes and to gain arable land [Lacey, 1930; Brookes, 1988]. In an attempt to combine flood protection with ecological objectives, a more natural river environment was restored at a 2.5 km long reach of the Thur at Neunforn, starting in 2002. The effects of these restoration efforts are currently being investigated within the RECORD project [RECORD, 2011; Schneider *et al.*, 2011].

While the channelized river was practically flowing straight prior to restoration, the riverbed morphology has changed dramatically since the removal of the northern bank stabilization and overbanks in 2002 [Trush *et al.*, 2000; Soar and Thorne, 2001; Pasquale *et al.*, 2011]. This large widening forced the river to deposit its sediments in a typical alternate bar pattern [Tubino and Seminara, 1990]. By 2005, one of those gravel bars (see Figure E2a) had developed on the northern shore of the river with a surface exposure that depends strongly on the varying river discharge Q . The vegetation cover in Figure E2a indicates topographic highs that reach 1.5 m above the river level at low flow conditions. At such conditions ($Q \sim 20$ m³/s) a low-lying part with bare gravel at the surface is exposed, at intermediate flow conditions ($Q \sim 100$ m³/s; 0.8 m increase in river stage compared with low flow) this part is flooded and the exposed surface of the gravel bar consists mainly of gravel covered by up to 1 m thick recent deposits of sandy loam colonized mainly by canary reed grass (*Phalaris arundinacea*), while the entire gravel bar is flooded at high-flow conditions ($Q > 200$ m³/s; 1.4 m increase in river stage compared with low flow). This gravel bar is the focus of the SP experiments presented here.

Ten piezometers instrumented with loggers (temperature, electrical conductivity, and pressure with a sampling rate of 15 minutes) were installed on the gravel bar to investigate river-groundwater interactions [Vogt *et al.*, 2010b; Vogt *et al.*, 2010a; Schneider *et al.*, 2011]. Sensors for water content (Decagon EC-5 and EC-TM) and temperature (Decagon EC-TM) were installed at different locations at 0.1, 0.5 and 1 m depth in the soil. Data were acquired with a sample rate of 30 minutes using a Decagon EM50 data logger (Decagon Devices Inc., Pullman, WA, USA). Raw values of soil dielectric permittivity were converted to volumetric water content using specific calibration curves for the soils at the site. A complete meteorological station (Campbell Scientific) was installed to monitor micrometeorological variables [Pasquale *et al.*, 2011]. The meteorological station includes two sensors for air temperature and relative humidity with a 10 minute sampling rate (at 2.5 m and 8 m above soil level), a complete solar radiation device, two wind flow meters and an atmospheric pressure sensor. A pluviometer (OTT) with a sampling rate of 1 minute completes the station. Ground penetrating radar (GPR) and electrical resistance tomography (ERT) geophysical data have also been acquired on the gravel bar to delineate the subsurface aquifer structure [Chapter 5, Schneider *et al.*, 2011].

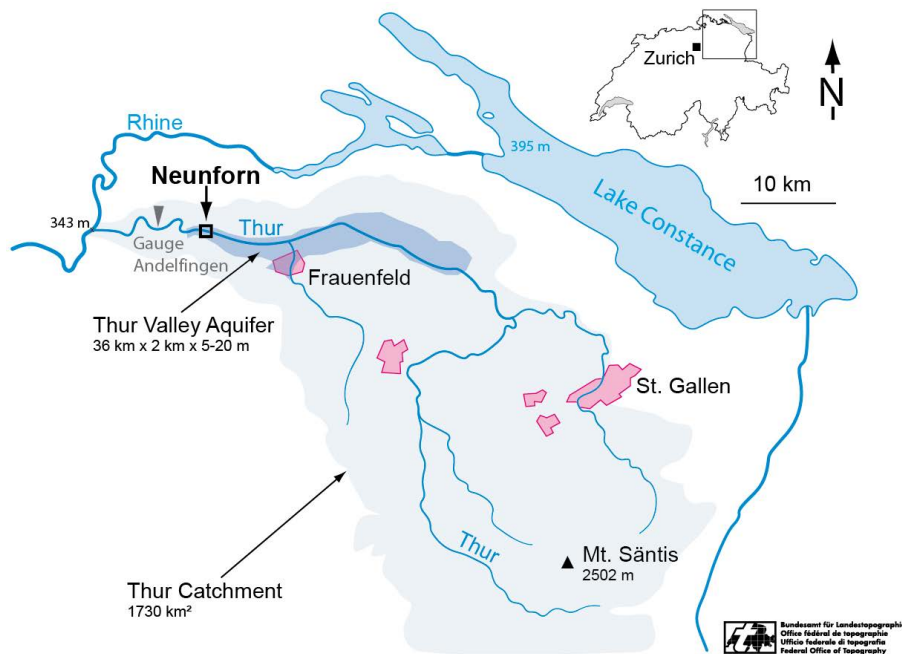


Figure E1. Location of the Thur catchment, Thur valley aquifer, and Neunforn test site in northeastern Switzerland. Modified from a figure prepared by Swisstopo (Swiss Federal Office of Topography).

E.2.2 Governing SP equations

The total electrical current density \mathbf{j} (Am^{-2}) is given by [Sill, 1983]

$$\mathbf{j} = \sigma \mathbf{E} + \mathbf{j}_s, \quad (\text{E1})$$

$$\nabla \cdot \mathbf{j} = 0, \quad (\text{E2})$$

where σ (Sm^{-1}) is the electrical conductivity, \mathbf{E} (Vm^{-1}) is the electric field $\mathbf{E} = -\nabla \phi$, ϕ (V) is the electrical potential, and \mathbf{j}_s (Am^{-2}) is the source current density. Equation E1 is a generalized Ohm's law and Equation E2 is the conservation equation in the low-frequency limit of Maxwell's equations. These two equations can be combined for any electrical conductivity distribution and boundary conditions to solve for the distribution of ϕ given knowledge of \mathbf{j}_s . The total source current density for the three dominating SP sources in hydrological applications can be described by [Revil and Linde, 2006; Arora et al., 2007]

$$\mathbf{j}_s = \bar{Q}_v \mathbf{u} - k_b T \sum_{i=1}^N \left(\frac{t_i \sigma}{q_i} \right) \nabla \ln \{i\} - \sigma \nabla E_h, \quad (\text{E3})$$

where \bar{Q}_v (Cm^{-3}) is the effective charge per unit pore volume that can be dragged by the flow of the pore water; \mathbf{u} is the Darcy velocity (m/s), k_b ($1.381 \times 10^{-23} \text{ JK}^{-1}$) is the Boltzmann constant, T (K) is the temperature, q_i (C) is the charge of ionic species i dissolved in the water, t_i (-) is the corresponding microscopic Hittorf number (i.e., the fraction of electrical current carried by species i in the water phase), $\{i\}$ is the corresponding activity, and E_h (V) is the redox potential.

The first contribution is associated with the drag of excess charge in the diffuse Gouy-Chapman layer within the electrical double layer caused by the movement of the pore water. This contribution forms the streaming current and the formulation is valid under both saturated and unsaturated conditions. The second contribution is related to chemical gradients in the pore water that gives rise to diffusion currents. The third contribution is related to redox processes that only occur for the rare conditions when a path of electronic conduction (e.g., an ore body, a metallic pipe) links parts of the subsurface with different redox potentials.

Revil and Leroy [2004] relate \bar{Q}_v at saturation to the voltage coupling coefficient at saturation C_{sat} (V Pa^{-1}) through

$$C_{sat} = - \frac{\bar{Q}_v K}{\rho_w g \sigma_{sat}}, \quad (\text{E4})$$

where K is the hydraulic conductivity (m/s), ρ_w is the density of water (kgm^{-3}), g is the acceleration of gravity (ms^{-2}), and σ_{sat} (Sm^{-1}) is the electrical conductivity of the saturated

porous media. Experimental data suggests that C_{sat} is largely controlled by the electrical conductivity of the pore water σ_w [Revil *et al.*, 2003] and laboratory measurements of aquifer material are rather straight-forward [Suski *et al.*, 2006]. Jardani *et al.* [2007] present experimental data that suggest that \bar{Q}_v decreases with increasing hydraulic conductivity. Linde *et al.* [2007a] suggested that \bar{Q}_v under unsaturated conditions should, to a first-order, scale inversely with the water saturation S_w as

$$\bar{Q}_v(S_w) = \frac{\bar{Q}_v(S_w = 1)}{S_w}. \quad (E5)$$

This parameterization is similar to the one of Waxman and Smits [1968] for a closely related parameter. This relationship is also discussed in Revil *et al.* [2007] and has been used by Jougnot *et al.* [2010].

SP measurements are performed with respect to the electrical potential of a reference electrode. The measured SP data $\varphi_i^{meas}(t)$ of electrode i at time t is given by

$$\varphi_i^{meas}(t) = (\varphi_i(t) + \varphi_i^{elec}(t)) - (\varphi_{ref}(t) + \varphi_{ref}^{elec}(t)), \quad (E6)$$

where $\varphi_i(t)$ and $\varphi_{ref}(t)$ are SP responses related to the hydraulic and/or geochemical forcing defined in Equations E1-3. The measurements will also be affected by temporal variations in electrode coupling, electrode temperature, electrode age, and geochemistry and geology in the intermediate vicinity of each electrode. These behaviors are described by $\varphi_i^{elec}(t)$ and $\varphi_{ref}^{elec}(t)$. Despite important improvements in electrode design [Petiau, 2000], these drift terms often contaminate the long-term behavior of SP monitoring signals. Common practice is to make a linear drift correction based on SP measurements performed with the two electrodes in contact with each other in the beginning and end of the monitoring period.

E.2.3 SP source current inversion

The classical SP inverse problem consists of determining the position and magnitude of SP sources that can explain the observed data within the measurement errors for a given electrical conductivity distribution, while honoring any constraints on the source distribution. The SP field can be calculated by inserting Equation E1 in Equation E2 to get

$$\nabla \cdot \sigma \nabla \varphi = s, \quad (E7)$$

where s (Am^{-3}) is a source distribution term given by $\nabla \cdot \mathbf{j}_s$ (see Equation E3). For a given conductivity distribution and boundary conditions, Equation E7 can be expressed as

$$\mathbf{K}\varphi = \mathbf{s}, \quad (E8)$$

where \mathbf{K} is a sparse linear matrix operator that contains all information about the dimensions of the model, the electrical conductivity distribution, and boundary conditions, while $\boldsymbol{\varphi}$ is the electrical potential and \mathbf{s} the source term at all model cells.

The inversion recovers a source model that minimizes the error between the measured $\boldsymbol{\varphi}^{\text{obs}}$ and predicted SP response in a least-squares sense. The objective function

$$\psi(s) = \left| \boldsymbol{\varphi}^{\text{obs}} - \mathbf{P}\mathbf{K}^\dagger \mathbf{s} \right|_2 + \lambda \left| \mathbf{W}\mathbf{s} \right|_2, \quad (\text{E9})$$

consists of a data misfit term and a model regularization term, where \mathbf{P} is a selector matrix that picks out the rows of \mathbf{K}^\dagger (i.e., the inverse of \mathbf{K}) that correspond to a SP measurement location where a potential was measured. The regularization weight λ controls the trade-off between the data misfit and the source current distribution, here quantified by the norm of the regularization operator \mathbf{W} acting on the source model.

The operator \mathbf{W} incorporates inverse sensitivity scaling information that accounts for rapidly decaying sensitivities with distance from the measurement locations. Additionally, \mathbf{W} promotes source solutions that are spatially sparse [*Portniaguine and Zhdanov, 1999; Minsley et al., 2007*]; that is, it favors solutions with the fewest number of non-zero source amplitudes while still fitting the data. This sparsity constraint is non-linear and requires an iteratively re-weighted least-squares (IRLS) inversion approach. The first iteration of the IRLS inversion corresponds to the sensitivity-weighted minimum length solution, which results in models that display very smoothly varying source current distributions even if the true source locations have a limited volumetric extent. In subsequent iterations, \mathbf{W} is updated with weights that favor models that occupy a small volume instead of being spatially smooth. We refer to *Minsley et al. [2007]* for more details about SP source current inversion. Even if not considered here, it is relatively straightforward to incorporate constraints from hydrogeological models or characterization concerning the regions in which source currents are expected to be located.

E.2.4 Wavelets

Exploratory analysis of SP field data should consider that there are many different processes that can create measurable SP signals at different temporal and spatial scales. A very useful and widely used approach to analyze non-stationary geophysical time-series is wavelet transforms [e.g., *Kumar and Fofoula-Georgiou, 1997; Torrence and Compo, 1998; Grinsted et al., 2004; Henderson et al., 2009*]. In contrast to Fourier transforms that focus on

the frequency content of a given time-series, wavelet transforms describe the temporally varying frequency content of a signal. They can also be used to evaluate how the frequency components of two different signals relate to each other over time. It appears thus that wavelet analyses could be useful to disentangle the relative contributions of the different source currents to the observed SP signals. Wavelet techniques have been used rather widely to determine the source current distribution from SP mapping surveys [e.g., *Gibert and Pessel, 2001; Saracco et al., 2004*], but not for monitoring purposes. In one of the rare wavelet applications to SP monitoring data, *Friedel et al. [2004]* analyzed data acquired at Merapi Volcano, Indonesia and found that many of the observed anomalies were associated with precipitation events.

A short description of wavelet theory is given below. We refer to *Torrence and Compo [1998]* and *Kumar and Foufoula-Georgiou [1997]* for a more detailed treatment and primary references. The wavelet used in this work is the commonly used complex valued Morlet wavelet

$$\psi_0(\eta) = \pi^{-1/4} e^{-i\omega_0\eta} e^{-\eta^2/2} \quad \omega_0 \geq 5, \quad (\text{E10})$$

where η is a non-dimensional time and ω_0 is the non-dimensional frequency. We use $\omega_0=6$ as it provides a good balance between time and frequency localization [*Grinsted et al., 2004*]. The continuous wavelet transform (CWT) of a discrete sequence x_n with a uniform time-sampling δt is defined as the convolution of x_n with a scaled and translated version of $\psi_0(\eta)$ as

$$W_n^X(s) = \sum_{n'=0}^{N-1} x_{n'} \psi^* \left[\frac{(n'-n)\delta t}{s} \right], \quad (\text{E11})$$

where (*) indicates the complex conjugate. By varying the wavelet scale s and translating along the localized time index n it is possible to construct an image of the amplitude as a function of scale (when s increases the wavelet becomes more spread out and takes only long-term behavior of x_n into account) and of how this amplitude varies with time. The wavelet in Equation E11 is normalized at each scale to have unit energy [*Torrence and Compo, 1998*]. The convolution of Equation E11 is in practice solved using Fast Fourier Transforms. The CWT has edge artifacts and it is therefore useful to define a cone of influence that identifies the regions that are sensitive to such artifacts. To assess the reliability of any features in the CWT one needs to perform a statistical test with respect to the CWT of a random process, typically red noise that can be modeled with a first order regressive process. It is then possible to test at a 5% significance level if the null hypothesis that the observed signal constitute red

noise holds. The regions in which the null hypothesis can be refuted are then highlighted in the displayed CWT.

The wavelet transform offers also the possibility to create a filtered time-series x_n^{filt} between two scales j_1 and j_2 by

$$x_n^{filt} = \frac{\delta j \sqrt{\delta t}}{C_\delta \psi_0(0)} \sum_{j=j_1}^{j=j_2} \frac{\Re\{W_n(s_j)\}}{\sqrt{s_j}}, \quad (\text{E12})$$

where $C_\delta=0.776$ is a reconstruction factor that is specific to the choice of wavelet, $\psi_0(0) = \pi / 4$, and δj is the scale sampling (12 samples for each decade is used in this study).

As $W_n^X(s)$ is complex valued, it is easier to display the real-valued wavelet power spectrum $|W_n^X(s)|^2$. To compare wavelet transforms of different time-series x_n and y_n one can calculate the cross-wavelet spectrum (WPS) as $W_n^{XY}(s) = W_n^X(s)W_n^{Y*}(s)$, where $W_n^{Y*}(s)$ is the complex conjugate of $W_n^Y(s)$ and $|W_n^{XY}(s)|$ is the corresponding cross-wavelet power. The wavelet coherence is defined as

$$\Gamma_n^{XY}(s) = \frac{|W_n^{XY}|}{\sqrt{|W_n^X(s)W_n^Y(s)|}}, \quad (\text{E13})$$

which can be seen as a localized correlation coefficient that varies between 0 and 1 in time-frequency space. Equation E13 is always 1 (see definition of $W_n^{XY}(s)$), which can be avoided when calculating the coherency by first smoothing the different contributions in time and space according to *Torrence and Webster* [1998]. This modified coherence is the preferred measure for significance testing compared with the cross-wavelet power, which can display high values due to changes in one of the time-series only [*Maraun and Kurths*, 2004].

E.3 RESULTS

E.3.1 Self-potential mapping

The SP mapping survey was carried out on March 7, 2008 using Pb-PbCl₂-NaCl electrodes, so-called Petiau electrodes [*Petiau*, 2000; PMS9000 from SDEC] and a 40 MOhm impedance voltmeter. Figure E2a indicates the area that was surveyed. Measurement profiles were oriented perpendicular to the river shore with measurements every 3 m and a profile spacing of approximately 5 m (see dots in Figure E2b). Five measurements were acquired in the vicinity of each measurement point (each reading was made after some tenths of seconds to allow stable measurements) and the median value was chosen for later processing. The

measurements were performed at approximately 5 cm depth. The total data set consisted of 246 measurement points with respect to a reference electrode located in a loamy ditch. This position was chosen to obtain good and stable electrical coupling conditions. The data were corrected for a linear drift of 2.8 mV over time using five drift measurements (i.e., the SP signal is recorded when the measurement electrode is located close to the reference electrode) acquired during the day. For further interpretation, the reference (0 V) was assigned to the position indicated in Figure E2b.

The data were detrended using linear regression in the direction of water flow and interpolated using ordinary kriging [*Deutsch and Journel, 1998*]. The kriging was performed with a spherical model that fitted the detrended experimental semi-variogram with a nugget of 3 (mV)^2 , an effective range of 18 m and a sill of 20 (mV)^2 (see *Linde et al. [2007b]* for a more detailed description of kriging of SP data). Figure E2b displays the kriged map together with the linear trend model. The vegetated region with sandy loam soils shown in Figure E2a have values in the range of -8 to -13 mV, whereas the regions in the lower-lying bare gravel have values close to 0 mV. One possibility is that the source regions are mainly located within the finer and thicker soils instead of the exposed gravel, though another possibility is that the SP sources originate from groundwater flow and aquifer heterogeneity in the gravel aquifer itself that happen to coincide with the soil boundaries seen on the surface. However, the strong SP gradients in Figure E2b indicate that the sources are at least partly located in the shallow subsurface.

A repeat survey (not shown here) was performed on March 4, 2009, which was carried out during a day when the river and groundwater level was 45 cm higher than during the previous survey. The resulting magnitudes are close to five times lower, which strongly suggest that the origin of the SP signals are more related to vadose zone processes than groundwater flow.

E.3.2 SP inversion

We use the 3-D SP source current inversion method of *Minsley [2007]* to invert our SP mapping data to determine the depths and locations of the source currents (see section 2.3). The inversion domain ($112 \times 69 \times 14 \text{ m}$) neglected topography. The top 6 m were assumed to consist of saturated gravel with a resistivity of $250 \text{ }\Omega\text{m}$, whereas the underlying clay was assumed to have a resistivity of $25 \text{ }\Omega\text{m}$ in accordance with results from ERT (Chapter 5), see Figure E5b in *Schneider et al. [2011]* for a 2-D model acquired on the gravel bar. The

discretization was 1 m in the x - and y -direction, whereas it was 0.5 and 1.0 m in the vertical direction for the gravel and clay layers, respectively. The inversion was first carried out until the model reached a mean data misfit of 1.3 mV before an additional iteration was carried out with compactness constraints.

Figure E2c and d displays the magnitudes of the source currents between 1.5 - 2 m and 3.5 - 4 m depth, respectively. They clearly indicate zones of negative source currents that approximately cover the outer part of the soil-covered region of the gravel bar. The maximum amplitudes of the source currents are found at 3 m depth. The magnitude of the source current decreases with deeper depths and is negligible at 5.5 - 6 m depth (Figure E2e). The inversion results thus indicate that the source currents are found in the shallow subsurface at locations that mainly correspond to the soil-covered part of the gravel bar. Note that the SP inversion cannot resolve the accurate depth of the sources due to the inherent non-uniqueness of the inverse problem and the simplicity of the resistivity model.

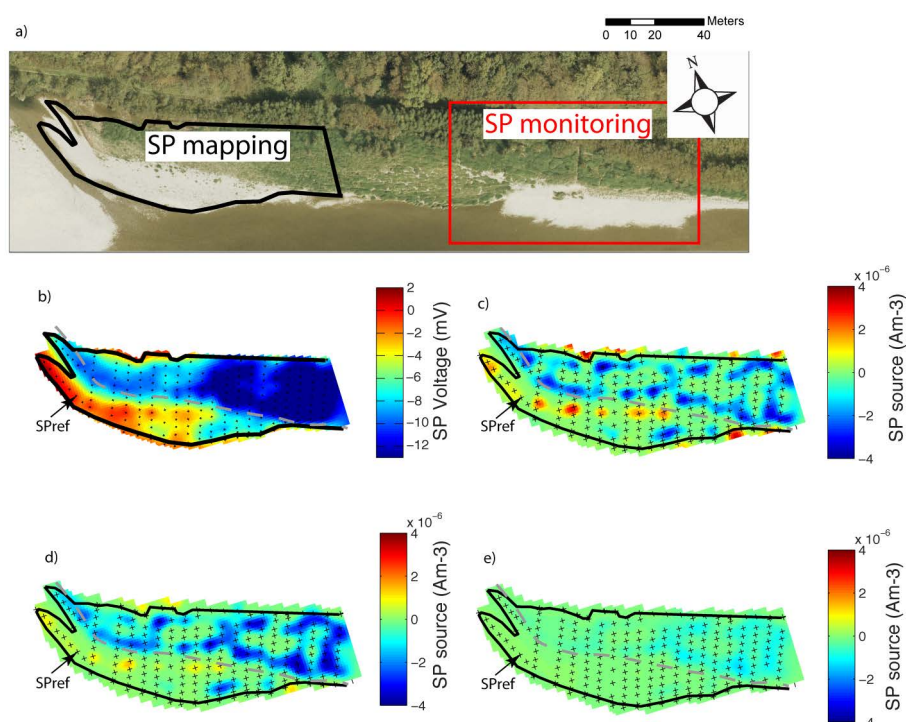


Figure E2. (a) The gravel bar at Neunforn on which SP mapping and SP monitoring (see Figure E3) was carried out. (b) The kriged SP map with measurement locations. (c-e) Source current distributions at 1.5 - 2 m, 3.5 - 4 m, and 5.5 - 6 m depth obtained from inversion. The boundaries of the gravel bar are indicated with a black solid line, whereas the gray dashed line indicate the transition between the grassy areas and the barren gravel surface.

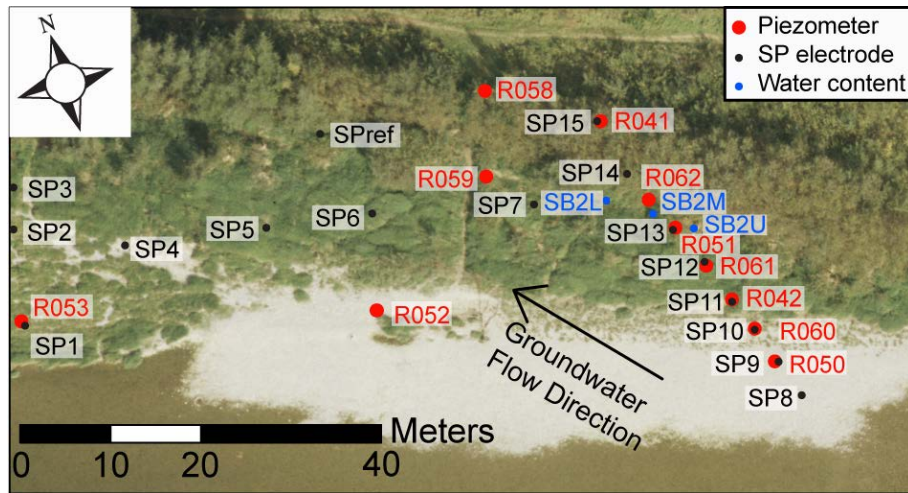


Figure E3. SP monitoring area with SP monitoring (SP1-15) and reference (SPref) electrodes, piezometers, and soil monitoring stations. The tower on which rainfall intensity was measured is located approximately 100 m away from this area.

E.3.3 SP time-series and wavelet analysis

The self-potential monitoring was performed from February 13 until April 11, 2009 in the region indicated in Figure E2a. The locations of the SP monitoring electrodes, piezometers, and soil monitoring sites (temperature and water content) are shown in Figure E3. A total of 16 Petiau electrodes were installed at 20 cm depth from the surface. A thin layer of fine sediments was added to the electrode-soil interface to improve the electrical contact and the region around the electrode was wetted before the monitoring started. The reference electrode was located in a thick loam layer. We used a Campbell Scientific Inc. CR1000 data logger that measured and stored the voltage difference between the measuring electrodes and the reference electrode every 5 seconds. A 12 V battery was used to power the CR1000. The connections between the electrodes and the data logger were achieved using isolated, but unshielded, copper wire. The data were processed by median filtering (no detrending) and sampled every 15 minutes for subsequent analysis.

Figure E4a shows time-series of rainfall intensity during the monitoring period, in which two periods of more significant rainfall occurred between days 60-70 (first rainy period) and 82-87 (second rainy period). Figure E4b shows time-series of water content at 10 cm depth (see Figure E3) with increases in water content corresponding to the rainfall periods. The hydraulic head data of Figure E4c have a delayed response to the rainfall and display some uncorrelated events that are attributed to snowmelt and rainfall upstream. The soil temperature data at 10 cm depth (Figure E4d) show that the ground was partly frozen until day 57 followed by a successive warming of the soil with daily fluctuations of a few degrees.

Selected SP data (Figure E4e) show that the main periods of SP variability correspond to the periods of rainfall. One can also observe substantial long-term variations in SP11, which is most likely related to electrode drift. No SP data were acquired in the beginning of the second rainy period as interfering ERT geophysical measurements were acquired during this period.

The WPS of the precipitation data (Figure E5a) display significant energy covering the shortest period of 30 minutes to a period of approximately two days. The WPS of the water content (Figure E5b) shows a similar pattern, but with less high-frequency content and limited response to the rainfall between days 45 and 55, possibly due to frozen ground conditions. The WPS of the hydraulic head (Figure E5c) displays energy during the two main periods of rainfall, but there is also significant energy with periods longer than a day corresponding to variations in the hydrological conditions in the upstream region of the catchment. The WPS of the soil temperature data (Figure E5d) shows only well-defined variability associated with daily fluctuations. Four different SP electrodes were chosen with WPSs that visually appear to be the most related to the state variables discussed above. The WPSs in Figure E5 of electrodes (e) SP5, (f) SP3, and (g) SP11 show that most of the higher frequency energy is found during the two rainy periods, whereas (h) SP2 has a different behavior and shows a rather significant daily variation, which is attributed to the fact that SP2 is largely insensitive to what happens during the rainy periods.

The wavelet coherencies were calculated for the (i) rainfall intensity and SP5, (j) the water content and SP3, (k) hydraulic head and SP11, and (l) temperature and SP2 following *Grinsted et al.* [2004]. The coherent events indicate in most cases time-varying phase relations. The more significant coherent periods with consistent phase relations occur for the precipitation and water content data for periods of 1 to 4 days during the two more rainy periods.

A close up of the second rainy period is shown in Figure E6. The long-period contributions of more than two weeks have been removed using Equation E12 to focus on short-term variability without superimposed long-term trends or drifts. The rainfall intensity, detrended water content, and detrended hydraulic head variations are shown in Figure E6a-c. Detrended SP time-series are shown in Figure E6d-i. It appears that (d) SP11 and (g) SP6 are very sensitive to the rainfall intensity, such that even short periods of rainfall within the rainy periods have clearly defined SP peaks. The variability in (e) SP3 shows a rather close resemblance with variations in water content, whereas (h) SP1 show more of a gradual buildup of the SP signal over time with an abrupt decrease after the end of the rainy period.

Finally, both (f) SP8 and (i) SP12 appear to be mainly correlated with the hydraulic head. The correlations observed in Figure E6 are similar to those obtained in the first rainy period (not shown). These examples indicate that the dominating SP source-generating processes can vary dramatically within a rather small monitoring area. We found no significant relationship between the degree of correlation between the SP signals and water table fluctuations as a function of the thickness of the vadoze zone (not shown here), indicating that the SP signals are likely more related to soil heterogeneity than water table dynamics.

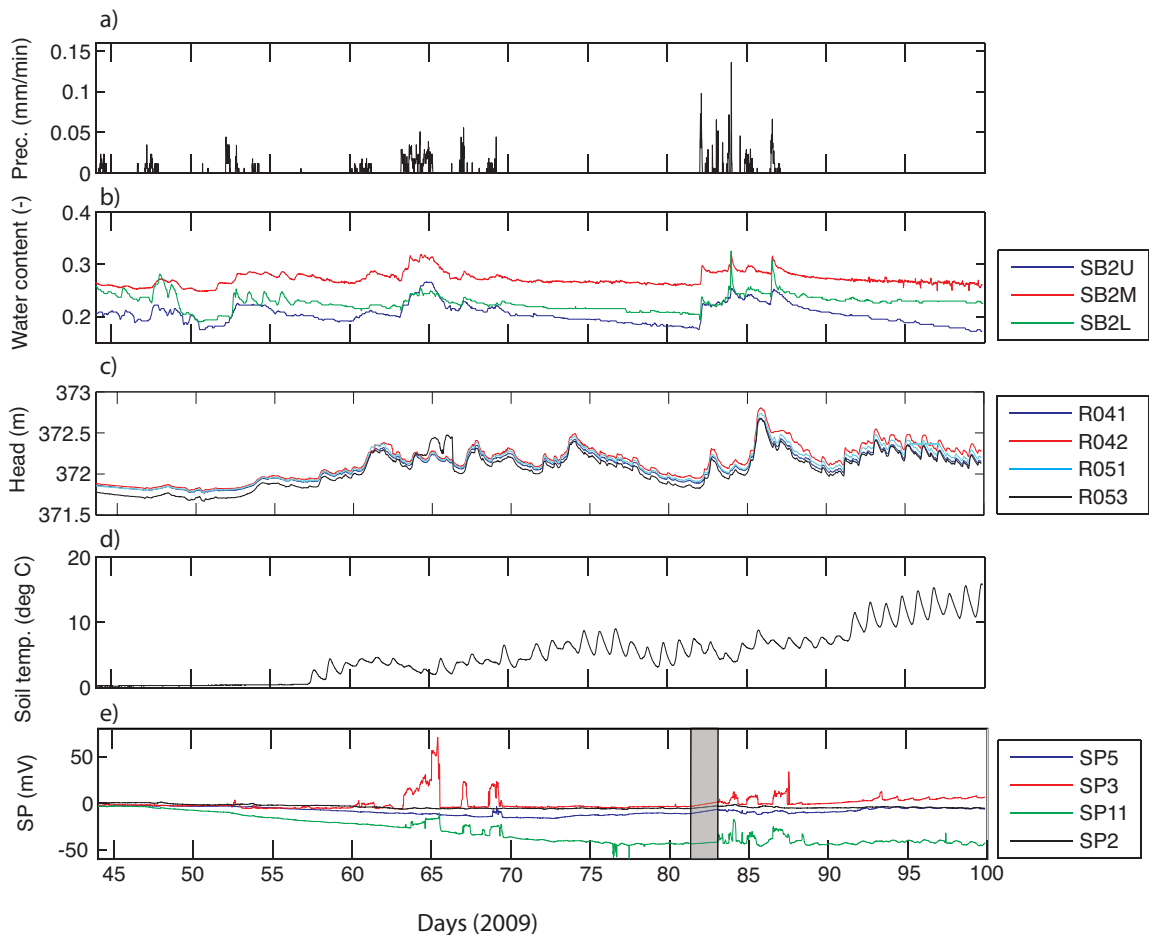


Figure E4. Time-series of (a) rainfall intensity, (b) water content at 10 cm depth (see Figure 2 for location of sensors), (c) hydraulic head, (d) soil temperature at 10 cm depth at location SB2M, and (e) SP signals from four of the SP monitoring electrodes. The gray area in (e) indicates a period when no SP data are available.

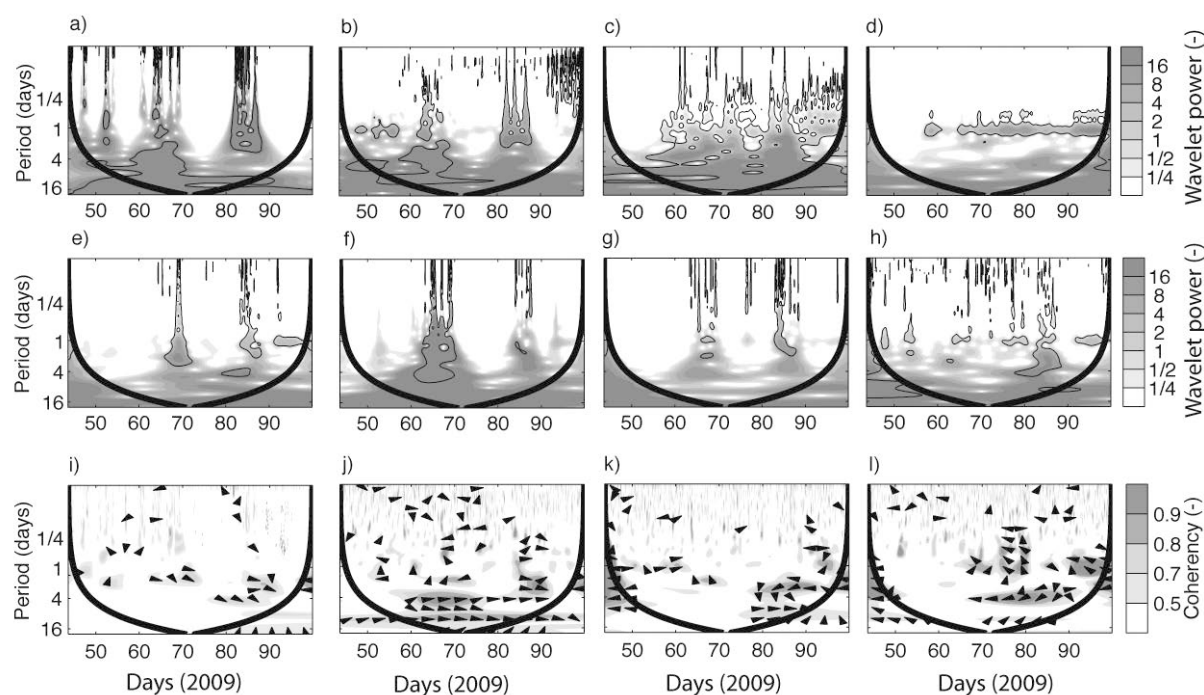


Figure E5. The wavelet power spectra for (a) rainfall intensity, (b) water content at 10 cm depth at station SB2M, (c) hydraulic head for piezometer R042, (d) soil temperature at 10 cm depth at station SB2M, (e) SP5, (f) SP3, (g) SP11, (h) SP2. The 5% significance level against red noise is shown as contour lines in a-h. Regions outside the thick solid lines (cone of influence) are increasingly affected by edge effects. Wavelet coherency between (i) rainfall intensity and SP5, (j) water content and SP3, (k) hydraulic head and SP11, (l) soil temperature and SP2. The arrows indicate the phase relation between the two time-series when the wavelet coherency is above 0.5 (in-phase when pointing right; anti-phase when pointing left; series 1 leading series 2 by 90° when pointing down).

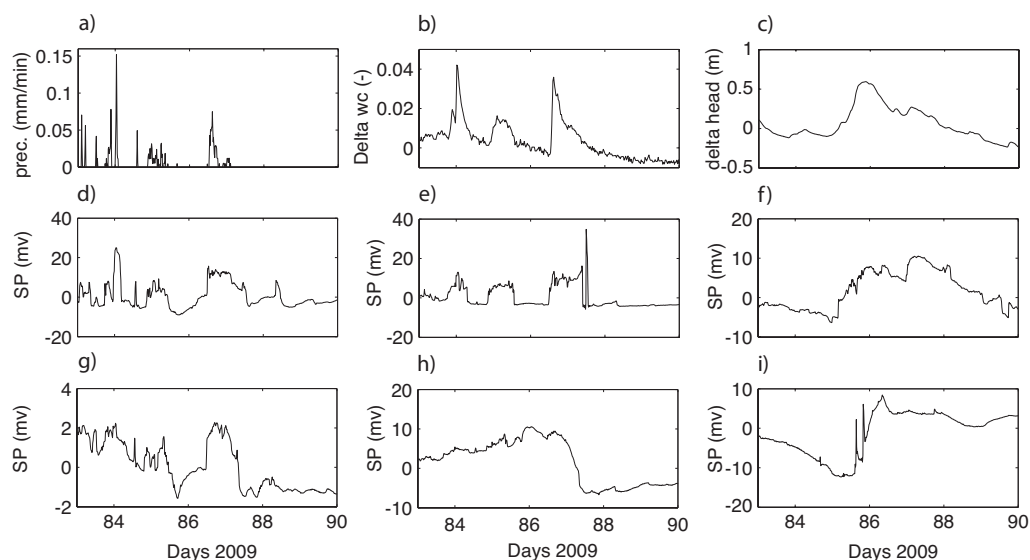


Figure E6. Filtered time-series of (a) rainfall intensity, (b) water content at 10 cm depth for station SB2M and (c) hydraulic head for piezometer R042 for time-scales less than two weeks during the major rainy period. Corresponding relative changes in the filtered SP signals are shown for (d) SP11, (e) SP3, (f) SP8, (g) SP6, (h) SP1, and (i) SP12.

E.3.4 SP modeling

An idealized geological model was created to investigate how SP signals are expected to vary with respect to a rising water table and precipitation (Figure E7). Two simulations of each type are investigated. Tests 1 and 2 simulate a water table increase with a rate of 10 cm h^{-1} during one hour from an initial level H_0 of 0.5 and 1.5 m depth, respectively, which represents a typical rate in response to a moderate precipitation event upstream. Tests 3 and 4 simulate two rainfall events with an intensity of 0.3 cm h^{-1} during 1 h with a constant water table at 0.5 m and 1.5 m depth, respectively. The simulation time is 2 hours for all tests, where the hydrological events take place during the first hour and the relaxation of the SP signal is investigated in the second hour (Figure E7b, c and d).

The model geometry (Figure E7a) consists of an upper 1 m thick layer with gravel on the left side in which we investigate variations of the SP signal, and loam on the right side, in which we have placed our reference (i.e., the electrical potential is zero). The reference is located in the loam because it is the most stable location over time and because it corresponds to the field situation. A uniform gravel aquifer is located between 1 and 9 m depth followed by a 20 m thick clay aquitard. The boundary conditions for the electrical problem is electrical insulation at all boundaries. Hydrological boundary conditions are no flow boundaries at the sides and imposed pressure at the clay-gravel aquifer interface for all simulations (Figure E7c-d). A no flow boundary at the top of the gravel is defined for the increasing water table simulations, while a prescribed flux into the gravel is prescribed for the precipitation experiment as displayed in Figure E7b. No flow boundaries are imposed on top of the loam as it is assumed that infiltration is negligible in the loam for the examples and time scales considered here. The choice of Neumann boundary conditions for the electrical and hydrogeological problems on the sides can be motivated by symmetry arguments. The aim of the modeling is to investigate the perturbation of the SP field caused by the soil heterogeneity, while modeling an essentially infinitely sized aquifer system.

The modeling is performed in 2-D using finite element calculations in COMSOL Multiphysics 3.5 with a mesh consisting of close to 50,000 triangular elements with specific mesh refinement in the unsaturated zone. The electrical resistivity of the clay is $25 \text{ } \Omega\text{m}$, whereas those of the loam and gravel are modeled by [Linde *et al.*, 2006a]

$$\sigma = \frac{1}{F} \left[S_w^n \sigma_w + (F - 1) \sigma_s \right], \quad (\text{E14})$$

with the electrical formation factor F being 12 for the gravel and 4 for the loam, Archie's saturation exponent $n=2$, the initial electrical conductivity of the groundwater was $\sigma_w=0.04$ S/m for both soils, while the electrical conductivity of the rainwater is 0.002 S/m. A surface conductivity $\sigma_s=0.002$ S/m was chosen for the loam, whereas it was assumed to be zero for the gravel.

We used the parameterization of *van Genuchten* [1980] for the relative hydraulic conductivity K_r and capillary pressure P_c functions as

$$K_r = \sqrt{S_e} \left[1 - \left(1 - S_e^{1/m} \right) \right]^2, \quad (\text{E15})$$

$$P_c = \frac{1}{\alpha} \left(S_e^{-1/m} - 1 \right)^{1-m}, \quad (\text{E16})$$

$$S_e = \frac{S_w - S_{wr}}{1 - S_{wr}}, \quad (\text{E17})$$

where S_w is the water saturation, S_e is the effective and S_{wr} is the residual water saturation, respectively, and m and α (m^{-1}) are soil-specific parameters. We used typical parameters for gravel and loam [e.g., *Carsel and Parrish*, 1988] as outlined in Table E1. The hydrological problem is solved using Richard's equation. Laboratory measurements using sediments retrieved from neighboring cores suggest that C_{sat} is -21 ± 3 mVm^{-1} for measurements performed at 20°C and with $\sigma_w=0.034$ Sm^{-1} . However, these cores were severely disturbed and it was impossible to obtain representative estimates of σ_s and K , which also indicate that our C_{sat} estimates might be biased. For the modeling, we decided instead to assume that $\bar{Q}_v(S_w = 1)$ is 0.48 Cm^{-3} for the gravel and 28 Cm^{-3} for the loam following the experimental relationship of *Jardani et al.* [2007] for a saturated medium. We use Equation E5 to model $\bar{Q}_v(S_w)$.

The SP signal for test 1 (Figure E8a) displays a positive SP signal over time that is at its maximum after 1 hour and then decreases slowly as a certain upward flow continues to occur in the vadose zone to reach hydrostatic equilibrium (Figure E8b). At a given time, the SP signal is constant with depth throughout the part of the vadose zone in which no changes in water content occurs. No SP signals (Figure E8c) occur in this region for test 2 for which the source currents at the water table are the same throughout the model. This effect occurs as the water table (Figure E8d) is located in a region of uniform geological media. These results indicate that SP signals in the unsaturated zone only occur when there are lateral contrasts in the sediments in which the water table rise or where the water content changes with time. It appears thus that any empirical relationship between water table dynamics and SP signals will

vary between electrode positions and that it might be highly nonlinear (e.g., no sensitivity at all until a contrast is reached). Heterogeneity will thus play a key role in determining the SP signals associated with water table fluctuations both in terms of determining the location and magnitude of source currents, but also in determining the electrical conductivity distribution that also strongly affects the SP magnitudes (see Equation E7).

The SP response (Figure E9a) to rainfall in test 3 indicates that infiltration creates a vertical SP gradient in the vadose zone with negative magnitudes within the vadose zone (Figure E9b). A similar SP response (Figure E9c) is shown for test 4, but with lower magnitudes. The magnitudes of the SP signals are much lower than those observed experimentally by *Doussan et al.* [2002], which can partly be attributed to different soil properties. Even if ignored here, there might be significant contributions from diffusion currents (see Equation E3) as the infiltrating rainwater has a much lower ionic content.

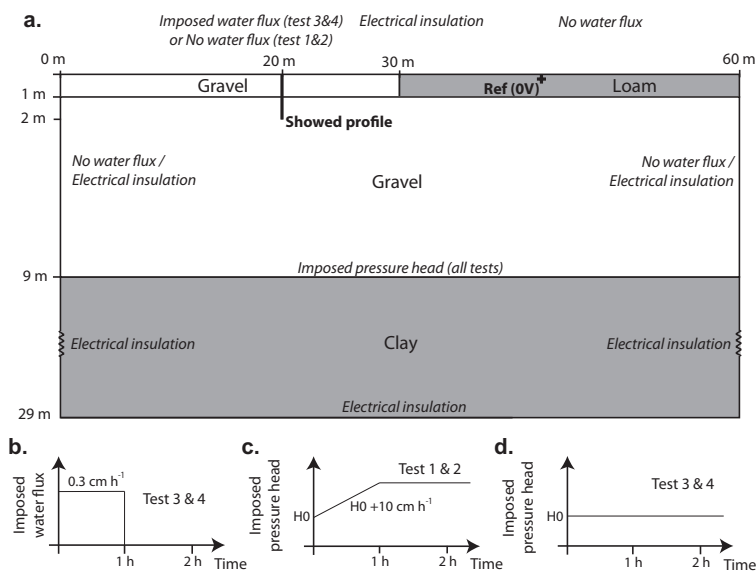


Figure E7. (a) Conceptual model used to investigate how SP signals vary with respect to variations in the water table (tests 1 and 2) and due to rainfall (tests 3 and 4) for an initial water tables and 0.5 m (tests 1 and 3) and 1.5 m (tests 2 and 4) depth. (b) Imposed infiltration rate in the gravel during tests 2 and 4. (c) Imposed groundwater level fluctuations tests (c) 1 and 2 and (d) 3 and 4, respectively.

Table E1. Hydrological parameters used for the SP modeling.

	Saturated hydraulic conductivity, K_s [m/s]	Residual saturation, S_{wr} [-]	Van Genuchten parameters	
			α [m^{-1}]	m [-]
Gravel	10^{-3}	0.18	14.5	0.63
Loam	10^{-6}	0.18	3.6	0.36

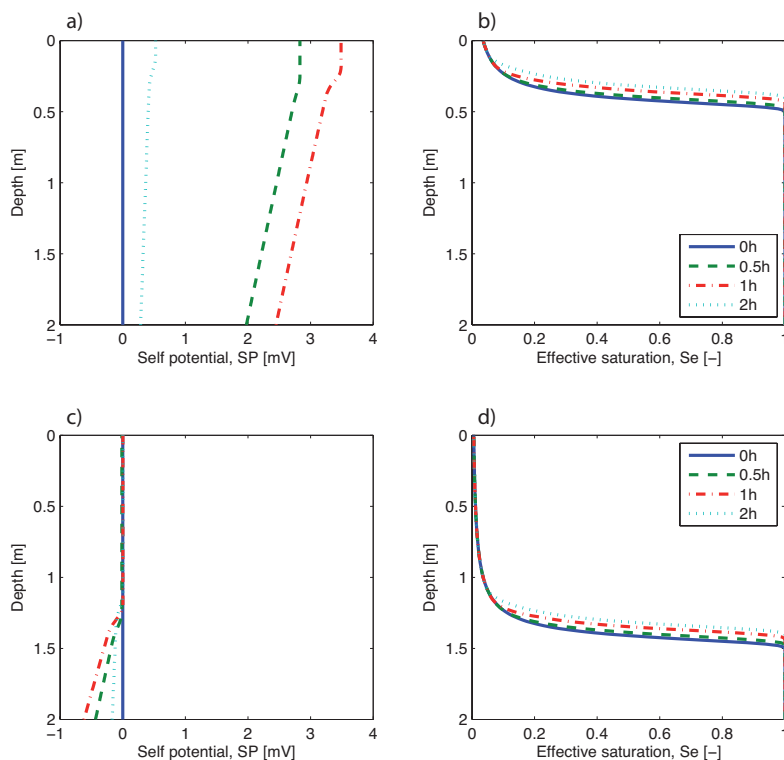


Figure E8. (a) Variation of the modeled SP signal with depth at different times for a rising water table (10 cm/h during 1 h) located at (a) 0.5-0.4 m and (c) 1.5-1.4 m depth (see Figure E7). (b) and (d) Corresponding values of the effective water saturation.

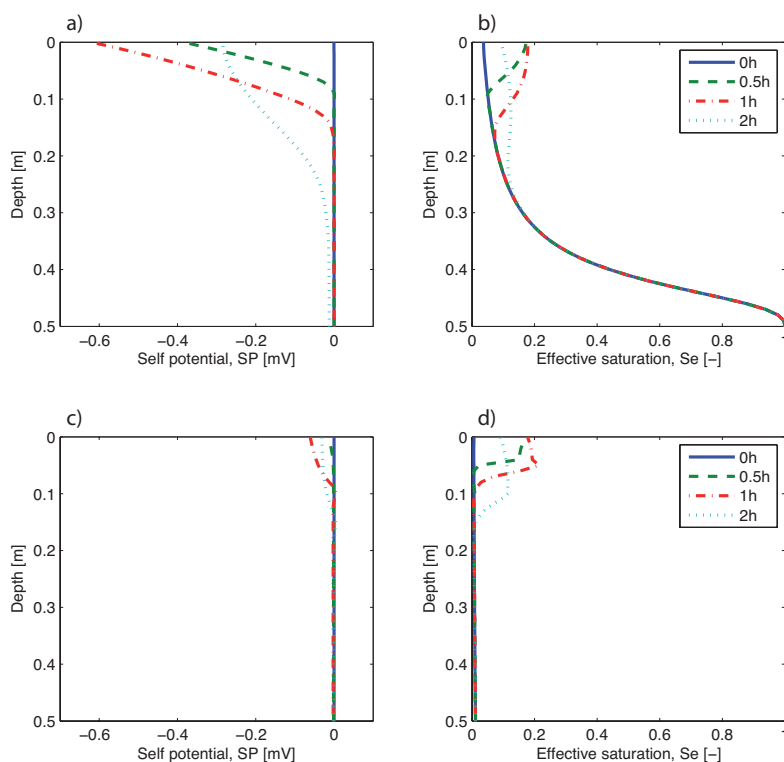


Figure E9. (a) Variation of the modeled SP signal with depth at different times for a rainfall event (3 mm/h during 1 h) with a constant water table located at (a) 0.5 m and (c) 1.5 m depth (see Figure E7). (b) and (d) Corresponding values of the effective water saturation.

E.4 DISCUSSION

Self-potential mapping makes it possible to investigate the overall SP field on the surface at high spatial resolution, but the interpretation needs to consider that contributions of SP sources located in the vadose zone might vary over short spatial and time scales. We suggest that SP mapping for hydrogeological purposes should be performed following a relatively long period (e.g., a week) of stable meteorological and hydrological conditions to minimize the effects of sources in the vadose zone.

SP monitoring can be useful to monitor vadose zone processes and to better understand the interrelations between different processes and mechanisms of SP source generation. The monitoring is however affected by long-term electrode drifts and what appears to be a high sensitivity to electrochemical conditions in the close vicinity of the electrodes and possibly wetting conditions at the electrode tip. Repeated (e.g., weekly) SP mapping with measurements in the vicinity of the monitoring electrodes might be useful to remove some of the problems with monitoring data. Even so, the data acquired in this study raise doubts about the usefulness of slowly varying (e.g., periods of weeks) natural variations in SP signals when their amplitudes are in the range of some 10 mV and electrodes are placed in the vadose zone.

That the SP method is cheap, light, and fast is often presented as making it particularly useful in regions where accessibility is limited and where limited data are available. We argue that for anything but qualitative applications it is crucial to have access to supplementary data about the geology, depth to water table, water chemistry, and meteorological conditions. It is also necessary to have a reliable model of the electrical conductivity distribution over time.

The SP time-series at the Thur River site display a non-stationary behavior with varying sensitivities to possible forcing parameters (rainfall intensity, water table, etc.). Time-series analysis with wavelets is therefore a very suitable tool to better understand casual and sometimes intermittent relationships between SP signals and other state variables.

Our results suggest that most of the SP signals on the surface of the gravel bar are related to sources in the vadose zone, which prohibit attempts to use SP signals to infer flow patterns in the aquifer. The magnitudes of the observed signals are much higher than those obtained by modeling, which is likely due to that the scaling relation $\bar{Q}_v(S_w)$ suggested in Equation E5 is too simple. Note that approaches that implicitly assume that $\bar{Q}_v(S_w) = 1$ [Perrier and Morat, 2000; Darnet and Marquis, 2004] would predict even smaller SP magnitudes for the same choice of material properties. The high sensitivity to the heterogeneity of vadose zone states and fluxes forms in our mind an important motivation for continued SP research. In fact,

measurable SP signals originating in the vadoze zone will only occur between electrodes located at the same depth in cases of differences in vertical water fluxes, lateral fluxes, or heterogeneity in electrical and soil properties. To advance understanding, we suggest that vertical profiles of SP electrodes should be installed in well-characterized and well-instrumented soils, such that more realistic modeling can be performed than what is presented here. Such time-series could allow us to understand how to infer fluxes in the vadose zone from SP measurements, which would necessitate an accurate soil-specific function to predict $\bar{Q}_v(S_w)$.

Another potentially fruitful approach would be to perform SP monitoring and mapping within river and lake systems (i.e., under saturated conditions) to investigate infiltration and exfiltration processes without having to deal with the highly complex vadose zone response while assuring good electrical coupling conditions. This would necessitate having access to not only river temperature and electrical conductivity information, but also that installations are made at locations at which deposition and erosion processes are negligible on the time-scale of the monitoring period.

It might appear surprising that the groundwater flow component to the SP signals is so low at our study site, but the reason for this is very simple. Groundwater flow is taking place in a rather thin resistive aquifer (5-7 m thick), while insignificant groundwater flow takes place in the thick electrically conductive underlying alluvial clay. SP theory [e.g., *Sill*, 1983] dictates where source currents are located within the gravel. However, the resulting SP distribution is not only dependent on the source current distribution, but also on the electrical conductivity distribution within and outside of the source region. In fact, the alluvial clay channels the electrical current, which decreases the resulting SP signal drastically compared to the case of a resistive basement. This comes naturally from the boundary condition of Maxwell's equations that state that the tangential component of the SP gradient (i.e., minus the electrical field) is equal on both sides of a boundary with different electrical properties (e.g., clay and gravel in this case). The SP signals related to groundwater flow would be about one order of magnitude more important if the aquifer was underlain by a resistive bedrock.

E.5 CONCLUSIONS

We find that wavelet transforms can be extremely useful to disentangle the temporally varying interrelations between SP monitoring signals and other state variables (e.g., rainfall intensity, soil temperature, hydraulic head, water content variations) and thus better

understand the main SP source mechanisms at a given site. At the Thur River it appears that the SP signals are mainly determined by local soil heterogeneity together with variations in water content, infiltration, and groundwater level. Contributions from groundwater flow appear to be of limited importance mainly due to the conductive underlying alluvial clay.

We suggest that future SP monitoring experiments in river environments should focus on either (1) estimating water fluxes in dedicated and well-instrumented soil profiles (several SP electrodes installed at different depths in addition to temperature and soil moisture sensors) or (2) mapping and monitoring on the river bed to avoid the influence of the spatially and temporally varying non-linear SP signals associated with vadose zone processes.

Approaches that interpret SP signals only in terms of natural water table fluctuations can only be expected to work in environments with no or very limited infiltration (i.e., dry regions, urbanized regions, or by installing plastic liners on the surface between the electrodes). Even if the understanding of self-potential signals in unsaturated media has increased in the last years, it appears that more dedicated field experiments and laboratory work with appropriate complementary data are needed before SP can be a quantitative monitoring tool of hydrological processes in river corridors.

APPENDIX F: JOINT INVERSION OF CROSSHOLE GPR AND SEISMIC TRAVELTIME DATA

Published as:

Linde, N., and Doetsch, J. A., 2010, Joint inversion of crosshole GPR and seismic traveltime data, in *Advances in near-surface seismology and ground-penetrating radar*, edited by R. D. Miller, J. H. Bradford and K. Holliger, Ch. 1, pp. 1-18, Society of Exploration Geophysicists.

ABSTRACT

Joint inversion of crosshole ground-penetrating radar and seismic data can improve model resolution and fidelity of the resultant individual models. Model coupling obtained by minimizing or penalizing some measure of structural dissimilarity between models appears to be the most versatile approach, since only weak assumptions about petrophysical relationships are required. Nevertheless, experimental results and petrophysical arguments suggest that when porosity variations are weak in saturated unconsolidated environments then radar wavespeed is approximately linearly related to seismic wavespeed. Under such circumstances, model coupling can also be achieved by incorporating cross-covariances in the model regularization. We present two case studies in which structural similarity is imposed by penalizing models for which the model cross-gradients are non-zero. The first case study demonstrates improvements in model resolution by comparing the resulting models with borehole information, whereas the second uses point-spread functions. Although, radar-seismic wavespeed crossplots are found to be very similar for the two case studies, the models plot in different portions of the graph, suggesting differences in porosity. Both examples display a close quasi-linear relationship between radar-seismic wavespeed in unconsolidated environments that is rather well described by the corresponding lower Hashin-Shtrikman bounds. We suggest that combining crossplots of the joint inversion models with Hashin-Shtrikman bounds can better constrain porosity and pore structure than individual inversion results.

F.1 INTRODUCTION

Joint inversions of geophysical data can:

1. improve model resolution and fidelity of individual models;
2. provide consistent geophysical models for interpretation, classification and petrophysical inference;
3. make it easier to identify modeling and geometrical errors by comparing the models obtained by individual and joint inversions;
4. allow hypotheses testing concerning geological structure, processes, and petrophysical relationships.

Numerous methodologies to jointly invert disparate but co-located geophysical data at different scales and for different applications have been developed and tested in the last decades [e.g., *Vozoff and Jupp, 1975; Lines et al., 1988; Tryggvason et al., 2002; Gallardo*

and Meju, 2003; Musil *et al.*, 2003; Monteiro Santos *et al.*, 2006]. Many critical choices for the development of joint and individual inversion algorithms are similar. These choices relate to model parameterization, model regularization, model and data norm, type of forward models and equation solvers, and stochastic versus deterministic frameworks. Difficulties related to weighting different data sets [e.g., Lines *et al.*, 1988] are not so different from difficulties that arise when inverting single geophysical data types (e.g., should one assume absolute or relative errors or a mixture of the two? how are actual errors estimated? etc.). Data weighting for joint inversion needs to not only consider data and modeling errors, but also sensitivity with respect to the model parameters of interest and data redundancy that arise when many data points provide very similar information. The fundamental difference between joint and individual inversion is the need to couple the models at the inversion stage.

There are basically four different approaches for doing this. The first approach is *structural*, in which it is assumed that models share one or several boundaries or that some measure of model structure is similar over given model domains [e.g., Haber and Oldenburg, 1997; Gallardo and Meju, 2003]. In the second approach models are explicitly linked with known or unknown (i.e., to be determined during the inversion) petrophysical relationships in order to create *as many inversion models as there are data sets*; one example would be the joint inversion of P- and S-wave traveltimes in which joint inversion is achieved by damping the models against a predefined V_p/V_s ratio [e.g., Tryggvason *et al.*, 2002]. For a third approach, the joint inverse problem is formulated *in terms of one inversion parameter type* only that is considered of primary importance, whereas the other data sources provide “proxy” data related to this primary inversion parameter through petrophysical relationships; typical examples in the field of hydrogeophysics would be using measurements of the hydrological state in boreholes (salinity, pressure, or water content) in response to hydrological testing together with crosshole geophysical data (also sensitive to these state variables) to invert directly for the permeability structure [e.g., Kowalsky *et al.*, 2005]. In the final approach, model parameters correspond to properties that are only indirectly related to the geophysical data at hand (i.e., no partial differential equations that describe the physical system are available); an example would be to invert for the spatially distributed electrical formation factor and surface conductivity using radar traveltimes and attenuation data; other examples could include inversion for the geochemical composition using diverse geophysical data [e.g., Chen *et al.*, 2004].

Structural approaches provide robust solutions for a wide range of application types in deterministic joint inversion. We focus here on joint inversion based on the cross-gradients constraints introduced by *Gallardo and Meju* [2003; 2004]. A number of other interesting structural approaches have been presented in the literature. For example, *Hyndman and Harris* [1996] present a traveltime inversion scheme for inverting two-dimensional zonal models using crosshole seismic traveltime data. Their technique could easily be extended to joint inversion of radar and seismic traveltime and attenuation data by assuming that all these data sets are sensitive to the same uniform zones and zonal boundaries. *Paasche and Tronicke* [2007] and *Paasche et al.* [2008] present an iterative sequential approach to invert crosshole radar traveltime and attenuation data. Their approach combines gradient-based deterministic inversion with a cluster algorithm that is used after each iteration step to classify the models in terms of a number of zones. This zonal model is used as the starting model for the next iteration step.

The examples presented here focus on the joint inversion of crosshole radar and seismic traveltimes. It would be rather straight-forward to modify the algorithm presented here to accommodate radar attenuation data [*Holliger et al.*, 2001], Fresnel volume inversion [*Vasco et al.*, 1995], full-waveform inversion [e.g., *Pratt*, 1999; *Ernst et al.*, 2007b; *Belina et al.*, 2009], or for joint inversion of surface-based seismic refraction [e.g., *Lanz et al.*, 1998] and GPR reflection data [e.g., *Bradford et al.*, 2009].

In this chapter, the joint inversion methodology is first introduced before two case-studies are presented together with a discussion about cross-property relations of seismic and radar wavespeeds. The chapter ends with discussion and conclusions.

F.2 METHOD

Joint inversion based on structural coupling using the cross-gradients constraints was introduced by *Gallardo and Meju* [2003; 2004]. This approach has been adapted and applied to a wide range of data types [*Gallardo and Meju*, 2003; 2004; *Gallardo et al.*, 2005; *Linde et al.*, 2006a; *Tryggvason and Linde*, 2006; *Gallardo*, 2007; *Gallardo and Meju*, 2007; *Linde et al.*, 2008; *Fregoso and Gallardo*, 2009; *Hu et al.*, 2009; Chapter 2]. The normalized cross-gradients function $\mathbf{t}_{qr}'(x, y, z)$ of two models \mathbf{m}_q and \mathbf{m}_r at location x, y, z is [*Linde et al.*, 2008]:

$$\mathbf{t}_{qr}'(x, y, z) = \frac{\nabla \mathbf{m}_q(x, y, z) \times \nabla \mathbf{m}_r(x, y, z)}{\|\mathbf{m}_q(x, y, z)\| \cdot \|\mathbf{m}_r(x, y, z)\|}, \quad (\text{F1})$$

where $\nabla \mathbf{m}_q(x, y, z)$ and $\nabla \mathbf{m}_r(x, y, z)$ are the gradients of models \mathbf{m}_q and \mathbf{m}_r at location x, y, z . The original definition of the cross-gradients function $t_{qr}(x, y, z)$ by *Gallardo and Meju* [2003] does not include the normalization term, which facilitates comparison of results from different applications and different joint inversion implementations. Constraints based on the cross-gradients function allows one of the models to change at a given position without requiring the other to change and it focuses on the direction of the change rather than the magnitude. The cross-gradients function is typically discretized using forward [e.g., *Gallardo and Meju*, 2003] or central differences [e.g., *Linde et al.*, 2008]. The discretized cross-gradients function based on central-differences for the y -component $t_{qr}^y(i, j, k)$ for two models \mathbf{m}_q and \mathbf{m}_r with a uniform discretization is:

$$\begin{aligned} t_{qr}^y(i, j, k) = & \frac{1}{4\Delta x \Delta z} [m_q(i, j, k+1) - m_q(i, j, k-1)] [m_r(i+1, j, k) - m_r(i-1, j, k)] \\ & - \frac{1}{4\Delta x \Delta z} [m_q(i+1, j, k) - m_q(i-1, j, k)] [m_r(i, j, k+1) - m_r(i, j, k-1)], \end{aligned} \quad (\text{F2})$$

where Δx , and Δz are the discretizations in the x - and z -directions, and indices i, j , and k indicate the corresponding indices of the model cells. *Gallardo and Meju* [2004] provide a formulation for non-uniform cell-spacings with rectangular cells.

The cross-gradients function can either be defined for the total model [*Gallardo and Meju*, 2003] or for the model update with respect to a reference model [*Tryggvason and Linde*, 2006]. The latter definition is useful when including seismic data, since there might be strong vertical trends in seismic wavespeed that dominate any effects due to small-scale variations in lithology.

The cross-gradients function is non-linear, such that it is necessary to linearize it when performing deterministic inversions. This means that an iterative approach is needed, even when solving linear forward problems (e.g., when ray-paths are assumed to be straight). Cross-gradients constraints add further non-linearity to already non-linear problems. This makes it even more important than for individual inversions to ensure a slow convergence to create final models with the least artifacts possible. The visual aspects of the joint inversion models are not very different when obtained using five or twenty iterations to achieve the target data misfit, but smaller details appear in the scatter plots of the two models and the resulting magnitude of the cross-gradients function is smaller when using many iterations. Thus, satisfactory results can be obtained using the same number of iterations as for the individual inversions, but the results are slightly improved when using more iterations, which is not a constraint for computationally benign crosshole traveltome tomography applications.

The non-linearity of the cross-gradients function makes the choice of either treating the cross-gradients as hard constraints [Gallardo and Meju, 2003; 2004] or soft constraints [Tryggvason and Linde, 2006] a matter of convenience, with no significant influence on the resulting models. Linde *et al.* [2008] suggests that the most important factor to effectively minimize the cross-gradients constraints is to ensure slow convergence (i.e., small model updates) during the inversion. Hu *et al.* [2009] solve a joint inverse problem in an iterative sequential manner in which the cross-gradients constraints are applied with respect to one model that remains fixed and one model that is updated. This approach decreases computation time and the non-linearity at each iteration step, but no comparison has been made with results obtained by simultaneous model updates. These authors also improve the convergence by using a Gauss-Newton method (i.e., second-order Taylor expansion of the objective function compared to first-order Taylor expansions in previous work).

When performing joint inversion of geophysical data with cross-gradients constraints, the objective function Φ is:

$$\Phi = \Phi_d + \Phi_m + \Phi_{CG}, \quad (\text{F3})$$

where Φ_d is a data misfit term, Φ_m is a model structure term, and Φ_{CG} is a structural dissimilarity term as defined by the cross-gradients function. Φ_d is given by

$$\Phi_d = \sum_{q=1}^Q \left[\mathbf{C}_{d,q}^{-0.5} \left(\mathbf{d}_q - \mathbf{F}_q(\mathbf{m}_q) \right) \right]_p - \Phi_d^*, \quad (\text{F4})$$

where Q is the number of data types, $\mathbf{C}_{d,q}$ is the data error covariance matrix for model q (typically assumed to be a diagonal matrix), \mathbf{d}_q are the observed data for data type q , $\mathbf{F}_q(\mathbf{m}_q)$ is the forward response of model q , and Φ_d^* refers to the pre-defined target data misfit. The forward model usually needs a finer discretization than that used for the inversion, which makes it necessary to interpolate \mathbf{m}_q on to a finer grid to solve the forward problem accurately. A key problem for any inversion strategy is to obtain an accurate representation of $\mathbf{C}_{d,q}$ and to make a good choice of Φ_d^* . This problem is not specific to joint inversion and it will not be discussed any further here.

The norm p in Equation F4 is typically 2, which assumes that a Gaussian distribution with zero mean is assumed to characterize the data noise. To decrease the sensitivity to outliers or fat tails in the data error distribution it is useful to work with approximations of the l_p -norms for the case when $p=1$ by using iteratively reweighted least squares (IRLS) [e.g., Farquharson, 2008]. The l_p -norm is given by

$$\|\mathbf{r}\|_p^p = \sum_{n=1}^N |r_n|^p, \quad (\text{F5})$$

where the entries in r_n denotes data residuals. In practice, one uses a normal least-squares inversion but with a matrix that re-weights $\mathbf{C}_{d,q}^{-0.5}$ by multiplying it with a diagonal matrix $\mathbf{R}_{d,q}$ with elements

$$R_{nn} = \sqrt{\left[p \left((r_n)^2 + \gamma^2 \right)^{p/2-1} \right]}, \quad (\text{F6})$$

where r_n is the corresponding data residual at the previous iteration. To approximate an l_1 -norm it is common to use $p = 1$ and $\gamma = 0.1$ [Farquharson, 2008]. This re-weighting yields convergence characteristics similar to those of quadratic functions, while being almost as robust to outliers as l_1 -norm inversions.

The value Φ_m is given by

$$\Phi_m = \sum_{q=1}^Q \varepsilon_q \left[\mathbf{C}_{m,q}^{-0.5} \left(\mathbf{m}_q - \mathbf{m}_q^{ref} \right) \right]_p, \quad (\text{F7})$$

where ε_q acts as a trade-off parameter between data fit and model roughness for model q (the value of ε_q takes in our implementation the same value ε for all data sources and is progressively lowered at each iteration by, for example, 10-50% until the target data misfit Φ_d^* is reached). $\mathbf{C}_{m,q}$ is the corresponding model covariance matrix, and \mathbf{m}_q^{ref} is the reference model for data type q .

The variance of $\mathbf{C}_{m,q}$ is often not known precisely and can thus be used to tune the individual inversions such that they reach the target data misfit at the same value of ε_q for each data type. We will see later that this is important to avoid too many tuning parameters when performing the joint inversion. In practice, $\mathbf{C}_{m,q}$ is often replaced by damping and smoothness constraints [Maurer *et al.*, 1998]. Damping is unsuitable for joint inversion with cross-gradients constraints, because these regularization operators have no spatial support. Instead, isotropic [Gallardo and Meju, 2003] and anisotropic [Linde *et al.*, 2006a] smoothness constraints have been used. We have found that stochastic regularization operators (see Appendix A) as introduced by Linde *et al.* [2006a] generally outperforms smoothness constraints in terms of convergence, stability, and resultant models that better correspond to complementary ground truth measurements [Linde *et al.*, 2008]. These operators are typically based on an exponential covariance function with integral scales that specify the spatial correlation in each direction. The stochastic regularization operator can either be based on geostatistical analysis of geophysical logging data [Linde *et al.*, 2006a; Linde *et al.*, 2008] or

estimated resolution properties of the inverse problem (Chapter 2). Stochastic regularization operators define a physical length scale that can be related to field conditions, such that fine-tuning is not needed when changing the model discretization from an initially coarse to a more finely discretized inversion grid. Note that if it is known that two model properties have a strong linear correlation it is also possible to make a joint inversion for these properties by including additional smoothness constraints that operate between model parameters at the same location as suggested by *Gallardo and Meju [2004]*.

Inversion results generally improve with the quality of \mathbf{m}_q^{ref} . In settings in which the largest variability occurs in the vertical direction (i.e., groundwater table, sediment-bedrock interface, sedimentary layers), it is beneficial to use average zero-offset profiles to define a one-dimensional \mathbf{m}_q^{ref} . To resolve sharper features it can help to work with IRLS mimicking l_1 -norms (defined in an analogous manner as for the data misfit in Equations F4-6) instead of the traditional l_2 -norm. Other approaches based on iterative reweighting [e.g., *Zhdanov, 2009*] may be valuable in traveltime tomography [*Ajo-Franklin et al., 2007*].

The last component Φ_{CG} in the objective function assures coupling between the models and is given by

$$\Phi_{CG} = \sum_{q=1}^Q \sum_{r>q}^R \lambda_{qr} \left[\mathbf{T}'_{qr}(\mathbf{m}_q, \mathbf{m}_r) \right]_p, \quad (\text{F8})$$

where l_{qr} is a constant weight given to the cross-gradients constraints between two model types q and r , and $\mathbf{T}'_{qr}(\mathbf{m}_q, \mathbf{m}_r)$ is a vector that consists of the estimated normalized cross-gradients function (see Equation F1) in all directions and at all locations where structural similarity is imposed. *Linde et al. [2008]* explored sensitivities related to the choice of l_{qr} . They determined that it can be chosen on the basis of trial inversions in which l_{qr} varies over several orders of magnitude with one or two values of l_{qr} for each order of magnitude. The value chosen is the one for which the mean value of $\mathbf{T}'_{qr}(\mathbf{m}_q, \mathbf{m}_r)$ is the smallest when Φ_d^* is reached. When jointly inverting three data sets, in Chapter 2 I chose to assign $l=l_{12}=l_{13}=l_{23}$. The number of constraints in Equation F8 becomes impractical in three-dimensions when jointly inverting more than three data sets. *Gallardo [2007]* presented an alternative formulation by introducing a reference gradient defined as the strongest model gradient at each location in space.

An iterative solution of the joint inversion problem is needed because (1) the forward responses typically vary non-linearly with the model (e.g., rays bend in heterogeneous media);

- (2) the cross-gradients function is non-linear, involving the product of two model gradients;
(3) IRLS and other compact regularization operators use iterative reweighting.

The estimated forward response \mathbf{d}_q^{l+1} of model \mathbf{m}_q^{l+1} at iteration $l+1$ is given by:

$$\mathbf{d}_q^{l+1} = \mathbf{F}_q(\mathbf{m}_q^l) + \mathbf{J}_q^l \Delta \mathbf{m}_q^{l+1}, \quad (\text{F9})$$

where \mathbf{J}_q^l is the Jacobian evaluated for model \mathbf{m}_q^l , $\mathbf{F}_q(\mathbf{m}_q^l)$ is the forward response of this model and $\Delta \mathbf{m}_q^l$ is a proposed model update. In traveltim tomography in which the slowness structure is represented by cells of constant slowness, the elements of the Jacobian are the ray length within each cell. Below we describe how we obtain $\Delta \mathbf{m}_q^{l+1}$.

Linearization of the cross-gradients function is given here for \mathbf{t}_y^{l+1} (see Equations F1 and F2)

$$\mathbf{t}_y^{l+1} \cong \mathbf{t}_y^l + \mathbf{B}_y^l \begin{pmatrix} \Delta \mathbf{m}_1^{l+1} \\ \Delta \mathbf{m}_2^{l+1} \end{pmatrix}, \quad (\text{F10})$$

where \mathbf{B}_y^l is the Jacobian of the normalized cross-gradients function in the y -direction (Equation F2) with respect to the model parameters. Extensions of the joint inversion framework to three or more methods are straight-forward [Gallardo, 2007; Chapter 2] but we focus here on two methods for simplicity. At each iteration, we solve the following system of equations in a least-squares sense:

$$\begin{bmatrix} \mathbf{R}_d^l (\mathbf{C}_d)^{-0.5} \mathbf{J}^l \\ \varepsilon^l \mathbf{R}_m^l \mathbf{C}_m^{-0.5} \\ \lambda \mathbf{B}_x^l \\ \lambda \mathbf{B}_y^l \\ \lambda \mathbf{B}_z^l \end{bmatrix} [\Delta \mathbf{m}^{l+1}] = \begin{bmatrix} \mathbf{R}_d^l (\mathbf{C}_d)^{-0.5} (\mathbf{d} - \mathbf{F}(\mathbf{m}^l)) \\ \varepsilon^l \mathbf{R}_m^l \mathbf{C}_m^{-0.5} (\mathbf{m}^{ref} - \mathbf{m}^l) \\ -\lambda \mathbf{t}_x^l \\ -\lambda \mathbf{t}_y^l \\ -\lambda \mathbf{t}_z^l \end{bmatrix}, \quad (\text{F11})$$

where

$$\Delta \mathbf{m}^{l+1} = \begin{bmatrix} \Delta \mathbf{m}_1^{l+1} \\ \Delta \mathbf{m}_2^{l+1} \end{bmatrix}, \quad \mathbf{m}^l = \begin{bmatrix} \mathbf{m}_1^l \\ \mathbf{m}_2^l \end{bmatrix}, \quad \mathbf{m}^{ref} = \begin{bmatrix} \mathbf{m}_1^{ref} \\ \mathbf{m}_2^{ref} \end{bmatrix},$$

$$\mathbf{d} = \begin{bmatrix} \mathbf{d}_1 \\ \mathbf{d}_2 \end{bmatrix}, \quad \mathbf{F}(\mathbf{m}^l) = \begin{bmatrix} \mathbf{F}_1(\mathbf{m}_1^l) \\ \mathbf{F}_2(\mathbf{m}_2^l) \end{bmatrix}, \quad \mathbf{J}^l = \begin{bmatrix} \mathbf{J}_1^l \\ \mathbf{J}_2^l \end{bmatrix},$$

$$\mathbf{C}_d^{-0.5} = \begin{bmatrix} w_1 \mathbf{C}_{d,1}^{-0.5} & 0 \\ 0 & w_2 \mathbf{C}_{d,2}^{-0.5} \end{bmatrix}, \quad \mathbf{C}_m^{-0.5} = \begin{bmatrix} w_1 \mathbf{C}_{m,1}^{-0.5} & 0 \\ 0 & w_2 \mathbf{C}_{m,2}^{-0.5} \end{bmatrix},$$

$$\mathbf{R}_d^l = \begin{bmatrix} \mathbf{R}_{d,1}^l & 0 \\ 0 & \mathbf{R}_{d,2}^l \end{bmatrix}, \quad \mathbf{R}_m^l = \begin{bmatrix} \mathbf{R}_{m,1}^l & 0 \\ 0 & \mathbf{R}_{m,2}^l \end{bmatrix},$$

and where w_1 and w_2 are the weights given to each data and corresponding model type in the inversion.

Recall that the weight given to the cross-gradients constraints λ is constant during the inversion and that the variances of $\mathbf{C}_{m,1}$ and $\mathbf{C}_{m,2}$ are determined from the individual inversions such that the same normalized data misfit is obtained for the same value of ε_1^l and ε_2^l . It is very important that the final models obtained by the individual and joint inversions have comparable data fit (within a few percent) to make it possible to assess the possible benefits of joint inversions. This objective explains the need for the weights w_1 and w_2 . To ensure that a similar importance is given to each model, we make the first inversions with weights w_1 and w_2 that are inversely proportional to the number of data of each data type. The weight w_2 is then manually adjusted typically in the range $\pm 30\%$ to ensure that the final models have a similar target data misfit (Chapter 2).

The resulting system of equations is stored as a sparse matrix and is, at each iteration, solved with the conjugate gradient method LSQR [Paige and Saunders, 1982], which has the advantage that the original condition number of Equation F8 is preserved. A preconditioner is applied that ensures that the l_2 -norm of each column in the left-hand side of Equation E11 is unity, which avoids unnecessary ill-conditioning [Paige and Saunders, 1982].

F.3 RESULTS

F.3.1 Oyster Case-Study

We now discuss the two-dimensional joint inversion of radar and seismic data acquired between wells S14 and M3 at the South Oyster Focus Area, Virginia [Hubbard *et al.*, 2001; Linde *et al.*, 2008]. These data sets were originally acquired to construct a permeability field to evaluate the role of heterogeneities in controlling the field-scale transport of bacteria injected for remediation purposes. The geology comprises rather coarse and high-porosity marine shoreface deposits. Radar data were acquired using a PulseEKKO 100 system with 100-MHz nominal-frequency antennae and a transmitter and receiver spacing of 0.125 m in

each borehole. Seismic data were acquired using a Geometrics Strataview seismic system, a Lawrence Berkeley National Laboratory piezoelectric source, and an ITI string of hydrophone sensors, and a 0.125 m source and sensor spacing. The source pulse had a center frequency of 4 kHz, with a bandwidth of approximately 1 - 7 kHz. From these data sets, 3248 radar and 2530 seismic traveltimes were extracted.

We used a cell-discretization of $0.125\text{ m} \times 0.125\text{ m}$ for our forward modeling $0.25\text{ m} \times 0.25\text{ m}$ for the inversion. All tomographic inversions were stopped once the target data misfits of 0.5 ns (radar) and 20 μs (seismic) were reached. Stochastic regularization based on an exponential model [see Section F.6 and *Deutsch and Journal*, 1998] with vertical and horizontal integral scales of 0.28 and 1.4 m were employed [*Hubbard et al.*, 2001]. The traveltimes and Jacobians were calculated in the high-frequency limit [*Podvin and Lecomte*, 1991; *Tryggvason and Bergman*, 2006] using `pstomo_eq` [*Tryggvason et al.*, 2002].

The individually inverted radar (Figure F1a) and seismic (Figure F1c) tomograms display predominantly layered structures with small velocity variations and overall low velocities, diagnostic of high porosity unconsolidated sediments. The joint inversion tomograms (Figure F1b and d) models display slightly more distinct boundaries between facies, but the overall structure is similar to the individually inverted results. Comparison of the cross-gradients function for the individually and jointly inverted data (Figure F1e and f) demonstrate that the joint inversion has decreased the cross-gradients function by more than two orders of magnitude. Differences between the individual and joint inversion results are best represented by scatter plots of the seismic and radar wavespeeds (Figure F1g and h). Note the much higher scatter of the individual inversion wavespeeds (Figure F1g) vis-à-vis the joint inversion values (Figure F1h).

To determine if the joint inversion models provide a better representation of subsurface architecture than the individual inversion ones, *Linde et al.* [2008] compared the models in the vicinity of the right borehole with hydraulic conductivity estimates based on flowmeter measurements and a pumping test (Figure F2a). Trends of the co-located radar wavespeed (Figure F2b) and seismic wavespeed (Figure F2c) are very similar to the hydraulic conductivity pattern. Correlation coefficients between log hydraulic conductivity and radar wavespeed are 0.72 and 0.78 for the individual and joint inversions. Corresponding values are 0.60 and 0.69 for the seismic wavespeed.

This case study demonstrates that joint inversion of crosshole radar and seismic traveltime data somewhat improves resolution compared to individual inversion, thus yielding an improved hydrogeophysical characterization of the investigation site.

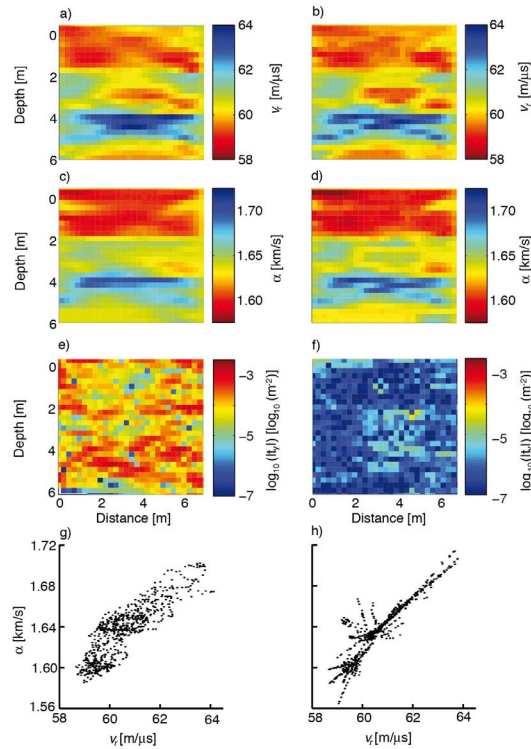


Figure F1. Radar wavespeed models from the Oyster site: (a) individual inversion with stochastic regularization; (b) joint inversion with stochastic regularization; (c) and (d) corresponding seismic wavespeed inversion results; (e) and (f) cross-gradients functions for these models; (g) and (h) scatter plots for these models. Depths are given in meters below sea level. Modified from Figure 3 in *Linde et al.* [2008].

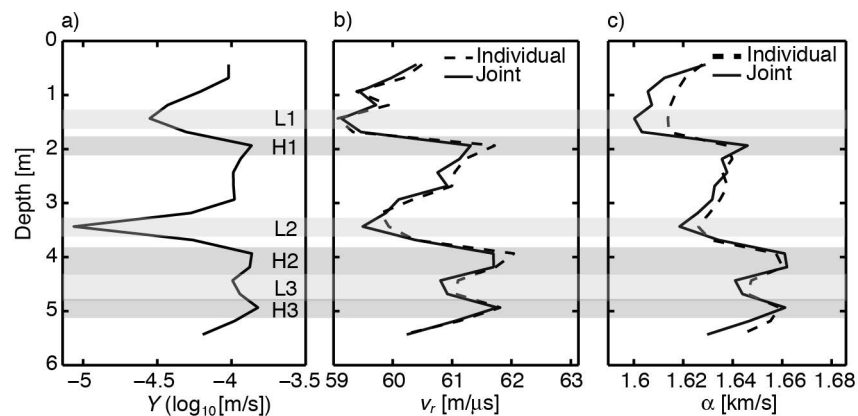


Figure F2. (a) Hydraulic conductivity data from borehole M3 at the Oyster site (located on the right side of the tomogram in Figure F1); (b) tomographic radar wavespeed models located two model cells from M3; (c) tomographic seismic wavespeed models located two model cells from M3. The dashed and solid lines in (b) and (c) represent models from the individual and joint inversion models with stochastic regularization. The shaded zones (L1-L3) and (H1-H3) are locations at which hydraulic conductivities have local minima and maxima. Modified from Figure 6 in *Linde et al.* [2008].

F.3.2 Thur River Case-Study

Our second case study involves three-dimensional joint inversion of radar and seismic traveltimes data acquired in the vicinity of the Thur River, Northern Switzerland (Chapter 2). These data sets were acquired to delineate the main hydrostratigraphic sub-units of a gravel aquifer. The resulting models will be used in an ongoing high-resolution hydrogeophysical study aiming at improving our understanding of groundwater-river water interactions in Alpine Valleys. The geology is composed of coarse gravelly river deposits with a rather wide grain-size distribution that includes small fractions of fines [Diem *et al.*, 2010].

Crosshole radar data at a 0.4 ns sampling rate were acquired using a RAMAC 250 MHz system, which at the site had a center frequency of about 100 MHz with energy in the 50-170 MHz frequency range. A sparker source was used to generate seismic waves with a center frequency of about 1 kHz, and a Geometrics GEODE system and a hydrophone streamer were used to record the seismic data at a sampling rate of 21 μ s. Borehole deviations were measured with a deviation probe using a 3-axis fluxgate magnetometer for bearing and a 3-axis accelerometer for inclination.

We inverted the crosshole radar and seismic data acquired between four boreholes located at the corners of a 5 m \times 5 m square, approximately 10 m from the Thur River. These data were acquired across all 6 planes between the four boreholes over the 6 m thick depth interval that constituted the saturated part of the aquifer. Seismic data were recorded using source and receiver spacings of 0.25 m, whereas the radar data were collected with source and receiver spacings of 0.5 m and 0.1 m, respectively. To ensure symmetric radar coverage, the source and receiver antennas were interchanged and the experiments repeated for each plane. A total of 2661 seismic and 5584 radar traveltimes could be reliably picked (radar traveltimes affected by refractions at the groundwater table were discarded). Examples of the raw data are given in Figure F3.

A cell-discretization of 0.0625 m \times 0.0625 m was employed for the forward modeling and 0.25 m \times 0.25 m for the inversion. Target data misfits corresponding to a relative error of 1% for both the radar and seismic traveltimes were estimated from reciprocal measurements. All tomographic inversions were stopped once the target misfits were reached. The stochastic regularization was based on an exponential model [see Section F.6 and *Deutsch and Journel*, 1998] with vertical and horizontal integral scale of 0.75 m and 1.5 m. This choice of weak anisotropy was made to qualitatively honor the subsurface layering seen in the borehole cores without imposing excessive lateral constraints. The integral scales were chosen in a pragmatic

manner to be comparable to the resolving capabilities of the geophysical data but smaller than the borehole spacing.

The main advantage of performing ray-based three-dimensional inversion of traveltime data at the site compared with a series of six two-dimensional inversions of the data acquired along each tomographic plane is that the regions close to the four boreholes are better resolved and that the corresponding models are internally consistent at the borehole locations. The additional constraints offered by the three-dimensional inversion in the near-borehole region also help to improve the models in-between the boreholes. Any isolated anomalies located away from the tomographic plane will neither be resolved in the two- nor in the three-dimensional inversion. The models obtained from the three-dimensional inversion in regions in-between the planes should rather be viewed as interpolations between the models along the planes using the stochastic regularization operator.

Both individual seismic (Figure F4a) and radar (Figure F4b) inversions resolve a centrally located high-velocity zone imbedded in a background of lower velocities. A very similar model was also obtained from inversion of crosshole geoelectric data; the high-velocity zone shows up as a region of low resistivity (Chapters 2 and 4). The corresponding joint inversion models (Figures 4e and f) are visually very similar to the individual inversion models, but the corresponding cross-gradients functions (Figure F4g) are 2-3 orders of magnitude smaller than for the individual inversion models (Figure F4c). In the joint inversion models it is seen that the seismic data have a rather strong influence on the resulting radar wavespeed model in the upper and lower portions of the inversion domain. This is the result of a poor GPR ray coverage in these regions, since many data were discarded due to refractions at the water table at the top and due to the highly attenuating clay at the bottom. Although the scatter plot for the individual inversion models (Figure F4d) shows a strong correspondence between the seismic and radar wavespeeds, as for the Oyster case study, the scatter plot for the joint inversion models (Figure F4h) is defined by much narrower and better defined correlations.

A useful approach for quantifying improvements in resolution is the point-spread functions (PSF), which we calculate following the approach outlined by *Alumbaugh and Newman* [2000]. A PSF can be interpreted as the spatial averaging filter that relates the true underlying model to the resulting inversion model at a specific location for a linearized solution about the final model. Normalization is important for the joint inversion case, in which the calculated PSFs are normalized with respect to the mean values of the radar and seismic slownesses. Figure F5 displays normalized PSF volumes at a central location ($x = 2.5$

m , $y = 2.5$ m, $z = 6$ m). These volumes correspond to isosurfaces for which the PSF is 33% of the largest PSF value as suggested by *Alumbaugh and Newman* [2000]. Individual inversions have similar PSFs for the radar (Figure F5a) and seismic (Figure F5b) inversion models. It is clear that the vertical resolution is much higher than the horizontal resolution. When performing joint inversion, the seismic model is at this location influenced by both the seismic (Figure F5c) and radar (Figure F5d) properties in the surroundings. Figures 5e and 5f show the corresponding regions that influence the radar model at this location. These figures demonstrate that the joint inversion may markedly improve the resolution and that the estimated model parameters (e.g., radar or seismic wavespeed) at a given point depend on both the seismic and radar wavespeed fields in the vicinity of this point. The relative resolution improvements by joint inversion are very similar for other choices of isosurfaces (e.g., 15%). Similar results were presented by *Linde et al.* [2008] for the Oyster case study.

Previous publications on joint inversions based on the cross-gradients function have employed least-squares formulations for data and model misfits. Robust inversions based on l_1 norms are appealing for applications in which the data are noisy or the geology is dominated by a few distinct boundaries, but the computational effort associated with linear programming is often prohibitive. We have investigated the perturbed Eklblom l_p norm for the model norm using IRLS with the common choice of $p = 1.0$ and $\gamma = 0.1$ (see Equation F6). Figure F6 displays vertical profiles of the seismic and radar wavespeeds obtained from the individual and joint inversions using IRLS and least-squares formulations at $x=5$ and $y=2.5$ m (see Figure F4). The largest differences appear between the joint and the individual inversions, with the joint inversion models showing somewhat more variability. The differences in radar wavespeeds between the individual and joint inversions in the upper part of the model is due to low radar ray coverage (data affected by refractions at the water table were discarded). There are relatively small differences between the joint inversion results obtained using the IRLS and least-squares model norms; the IRLS inversion results are overall more variable and less smooth. These results illustrate that the joint inversion, at least for the example considered here, have a larger impact on the final inversion results than those related to the model norm used in the inversion.

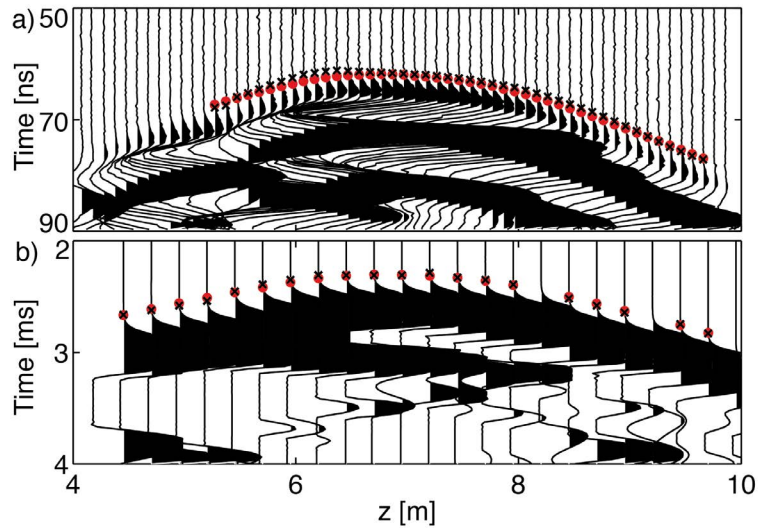


Figure F3. Typical raw (a) seismic and (b) radar source gathers for a source depth of 6.75 m. Red dots in (a) and (b) represent calculated forward responses of the final models obtained by joint inversion (see Figure F4e and f) and black crosses represent the picked first arrivals. (a) Although the seismic data were clipped, first arrivals could be reliably picked. (b) Picked first arrivals in the radar data do not include refracted waves through the unsaturated high wavespeed layer above 4 m; for the displayed source gather this means neglecting data collected above 5 m depth.

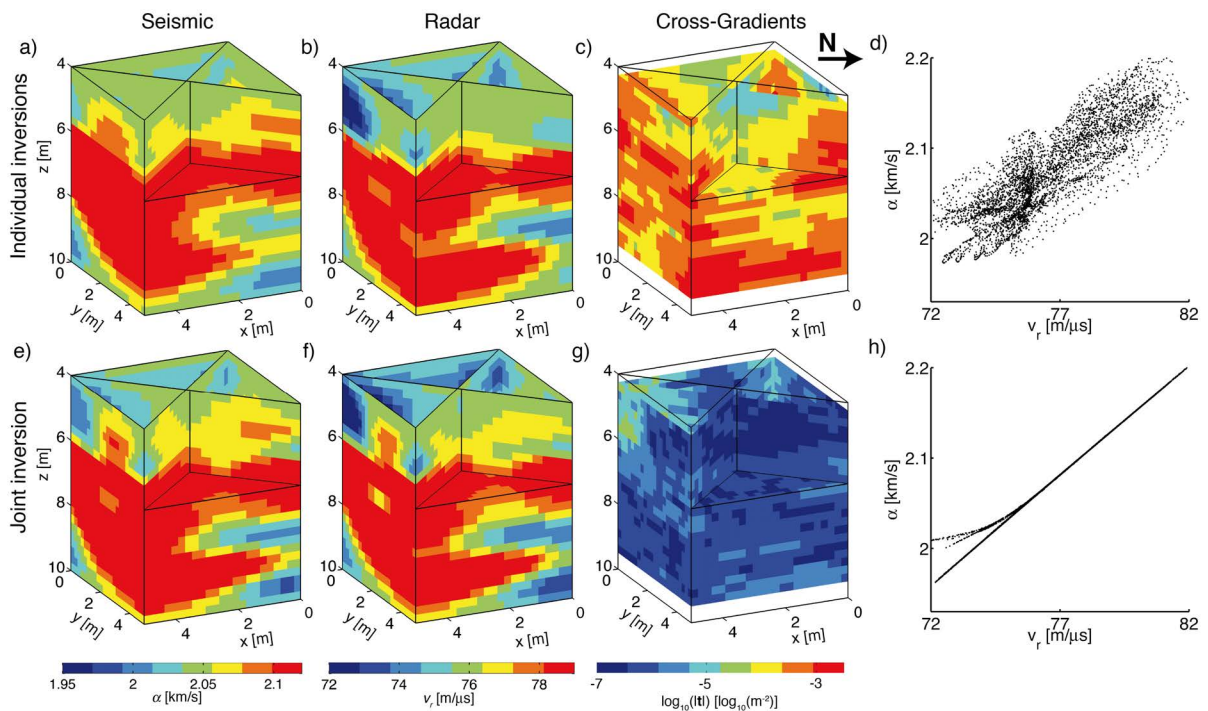


Figure F4. (a) Seismic and (b) radar wavespeed models determined from individual inversions of the Thur River site data; (e) and (f) corresponding models determined from joint inversion; (c) and (g) the cross-gradients functions for these models; (d) and (h) scatter plots for these models.

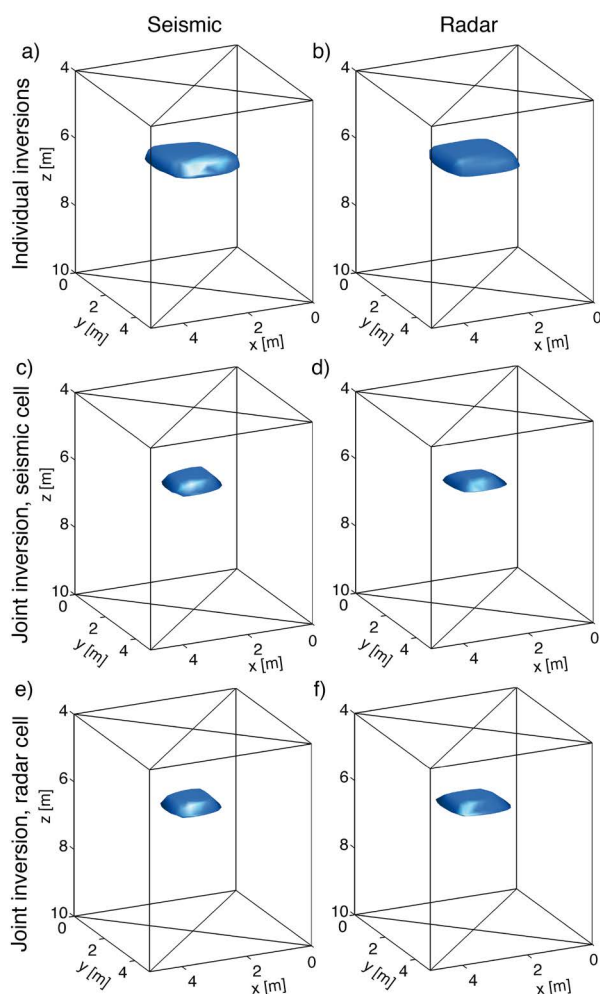


Figure F5. Normalized point-spread functions (PSFs) for the individual (a) seismic and (b) radar inversion models at location $x=2.5$ m, $y=2.5$ m, $z=6$ m for the Thur River site (see Figure 3), where the volume is the region in which the values of the PSFs are at least 33% of the values at the model cell of interest. Normalized PSFs for the seismic model obtained by joint inversion have a smaller spatial support (c), but are also influenced by the radar model (d) over a similar region. Corresponding PSFs for a radar cell showing the influence of the (e) seismic model and the (f) radar model, respectively.

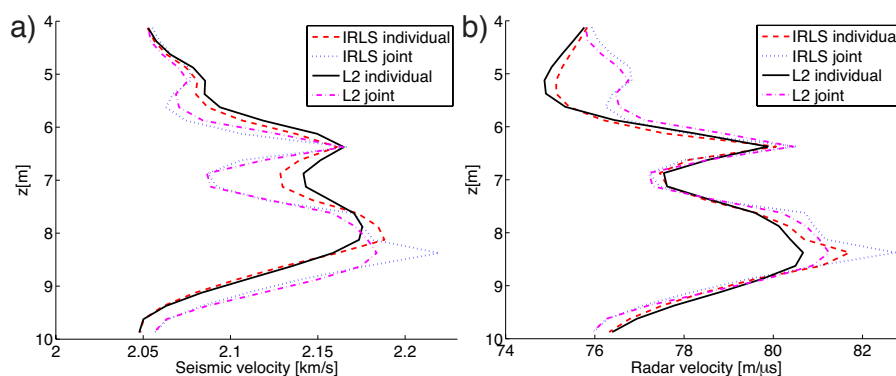


Figure F6. Comparison of (a) seismic and (b) radar wavespeed models at location $x=5.0$ m and $y=2.5$ m (see Figure 3) obtained by individual and joint iteratively reweighted least-squares (IRLS) and least-squares (L2) inversions.

F.3.3 Seismic and radar wavespeed cross-property relations

The Hashin-Shtrikman (HS) bounds [Hashin and Shtrikman, 1962; 1963] offer an appealing framework for investigating possible relationships between seismic and radar wavespeeds. Without imposing restrictive assumptions about the pore-space geometry, the HS bounds provide the tightest range of the property values a mixture of a two-phase media can take with known volume fractions f and $1-f$ and properties of each phase. The lower bounds for seismic and radar wavespeed correspond to the case in which spherical inclusions (representing the grains) are embedded in a matrix of water and the spheres are not in contact with each other. The upper bounds correspond to the case where unconnected spherical inclusions of water are imbedded in a solid matrix. *Pride et al.* [2004] argue that the lower HS bound is generally the one that is the closest to reality in sedimentary settings. Absence of a percolation threshold in most porous media, which indicates that the pore-space is connected down to very low porosities [Sen et al., 1981], supports this argument.

The lower k_{HSL} and upper k_{HSU} HS bounds for bulk modulus in water-saturated media are given by [Hashin and Shtrikman, 1963]

$$k_{\text{HSL}} = k_w + \frac{1-\phi}{\frac{1}{k_s - k_w} + \frac{3\phi}{3k_w + 4\mu_w}}, \quad (\text{F12})$$

$$k_{\text{HSU}} = k_s + \frac{\phi}{\frac{1}{k_w - k_s} + \frac{3(1-\phi)}{3k_s + 4\mu_s}}, \quad (\text{F13})$$

where ϕ is porosity, k_s and μ_s are the bulk and shear modulus of the solid, and k_w and μ_w are the corresponding values for the water phase. The lower μ_{HSL} and upper μ_{HSU} bounds for shear modulus are [Hashin and Shtrikman, 1963]

$$\mu_{\text{HSL}} = \mu_w + \frac{1-\phi}{\frac{1}{\mu_s - \mu_w} + \frac{6}{5\mu_w} \frac{(k_w + 2\mu_w)\phi}{(3k_w + 4\mu_w)}}, \quad (\text{F14})$$

$$\mu_{\text{HSU}} = \mu_s + \frac{\phi}{\frac{1}{\mu_f - \mu_s} + \frac{6}{5\mu_s} \frac{(k_s + 2\mu_s)(1-\phi)}{(3k_s + 4\mu_s)}}. \quad (\text{F15})$$

The lower and upper bounds for P-wavespeed are then given by ($\mu_w = 0$)

$$\alpha_{\text{HSL}} = \sqrt{\frac{k_{\text{HSL}}}{\rho}}, \quad (\text{F16})$$

$$\alpha_{\text{HSU}} = \sqrt{\frac{1}{\rho} \left(k_{\text{HSU}} + \frac{4}{3} \mu_{\text{HSU}} \right)}. \quad (\text{F17})$$

The lower κ_{HSL} and upper κ_{HSU} bounds for dielectric permittivity in saturated media are [e.g., Hashin and Shtrikman, 1962; Brovelli and Cassiani, 2010]

$$\kappa_{\text{HSL}} = \kappa_s + \frac{\phi}{\frac{1}{\kappa_w - \kappa_s} + \frac{1-\phi}{3\kappa_s}}, \quad (\text{F18})$$

$$\kappa_{\text{HSU}} = \kappa_w + \frac{1-\phi}{\frac{1}{\kappa_s - \kappa_w} + \frac{\phi}{3\kappa_w}}, \quad (\text{F19})$$

where κ_s and κ_w are the dielectric permittivities of the solid and the water phases. It is then possible to determine the lower v_{HSL} and upper v_{HSU} bounds for radar wavespeed using

$$v_{\text{HSL}} = \frac{c}{\sqrt{\kappa_{\text{HSU}}}}, \quad (\text{F20})$$

$$v_{\text{HSU}} = \frac{c}{\sqrt{\kappa_{\text{HSL}}}}, \quad (\text{F21})$$

where $c=3 \times 10^8$ m/s is the vacuum speed of light.

Figures 7a-b display the HS bounds for the radar and seismic wavespeed, respectively, for the case of varying ϕ with: $k_s=38$ MPa, $k_w=2.09$ GPa, $\mu_s=41.5$ GPa, $\mu_w=0$, $\kappa_s=6.5$, $\kappa_w=84$, $\rho_s=2.65$ kg·m⁻³ and $\rho_w=1000$ kg·m⁻³. These values are representative values of α -quartz [Schön, 1996] and water at 10° C [Eisenberg and Kauzmann, 1969; Fine and Millero, 1973]. The corresponding relationships between the radar and seismic wavespeeds as a function of porosity are shown in Figure F7c, together with the Oyster and Thur River scatter plots that result from the joint inversions. The scatter plots lie along or very close to the lower HS bounds. It is well-known that tomograms underestimate the variability of the real physical fields [e.g., Day-Lewis and Lane, 2004]. Because the estimated radar and seismic slownesses are based on the same inversion processes, they are approximately equally affected by this limitation. As a consequence, we expect the cross-property center points and slopes (as revealed by the scatter plots) to be more robust descriptions of the system than the tomograms themselves. For the two case studies, we conclude that the pore space is well-connected at both locations and that the Oyster site has significantly higher porosities than the Thur River site.

An example of the averaging that takes place during inversion is demonstrated in Figure F7d in which two types of estimates of porosity variations are shown. One is based on

Neutron-Neutron (NN) logs recorded in a borehole located at the center of the Thur River inversion domain ($x=2.5$ m, $y=2.5$ m) and one is based on the individual and joint inversion wavespeed models at the same location. The NN-to-porosity transform was obtained following *Barrash and Clemo* [2002], where the lowest and highest NN counts out of 18 borehole logs at the Thur River site are assigned to the highest (0.50) and lowest (0.12) expected end-member porosities for this type of sedimentary setting. Although the resulting absolute porosities obtained from this type of transform might be biased and the variability over-estimated, the relative variations with depth are expected to be well-resolved. A site-specific NN-to-porosity transform obtained by measuring the porosities on retrieved cores would have helped to improve the absolute porosity values, but no undisturbed cores could be retrieved at our site. The co-located radar and seismic wavespeeds were transformed to porosity via the lower Hashin-Shtrikman bounds using the same parameters as assumed in the construction of Figure F7a-b. Note, that the choice of $\kappa_s=6.5$ was treated as a fitting parameter to assure consistent porosity estimates from the seismic and radar joint inversion models. It is seen that the wavespeed models provide plausible and fairly tight lower bounds of porosity, but that only the main trends of porosity as defined by the NN-logs are resolved. A much better correspondence between the overall NN-derived porosity values and those obtained from the radar wavespeed model is obtained using the volume-averaging approach of *Pride* [1994].

One way to improve the models might be to include the porosity estimates defined by the NN logs into the reference model [e.g., *Yeh et al.*, 2002] or to perform full waveform inversion [*Klotzsche et al.*, 2010]. Correlation of the radar and seismic wavespeeds with the NN-determined porosities at this location is slightly improved by the joint inversion (the correlation coefficient is increased with 10-15% over the joint inversions) and the consistency between the two estimates obtained from joint inversion makes it easier to interpret the results. That the scatter plots appear on the lower HS bounds indicate that the effective porosity is rather similar to the total porosity estimated from the NN logs.

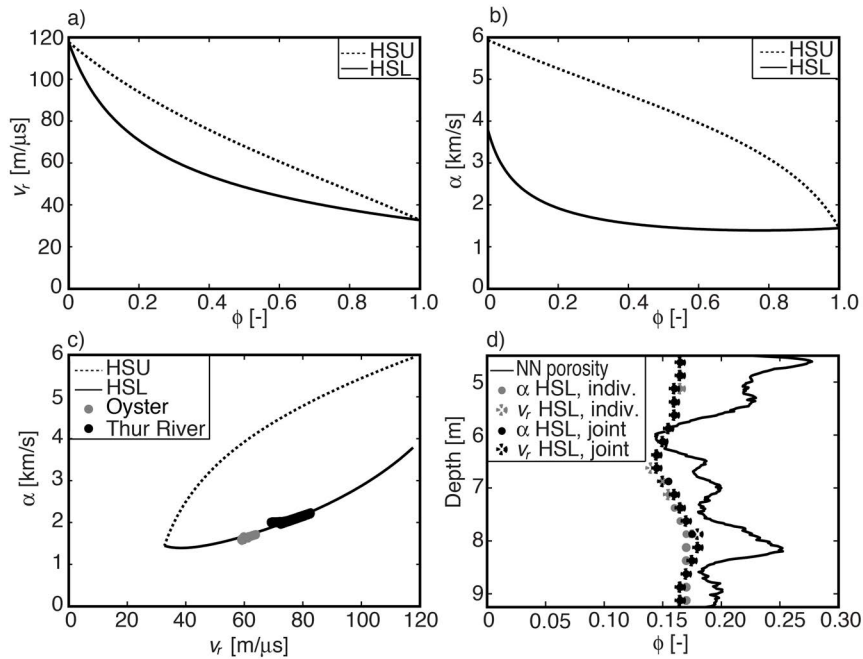


Figure F7. For the parameters described in the text: (a) Hashin-Shtrikman upper (HSU) and lower (HSL) bounds for seismic wavespeed as a function of porosity; (b) HSU and HSL bounds for radar wavespeed; (c) radar-seismic wavespeed relationships for the HSU and HSL bounds as a function of porosity together with scatter plots from the Oyster and Widen case studies; (d) porosity log derived from Neutron-Neutron data and porosity estimates obtained from radar and seismic wavespeed using the HSL bounds for the seismic and radar wavespeeds at the Thur River site.

F.4 DISCUSSION

The structural approach to joint inversion using cross-gradients constraints [Gallardo and Meju, 2003; 2004] is a maturing inversion technique that might provide internally consistent geophysical models with improved resolution compared with those obtained from individual inversions. The results presented here and elsewhere indicate that joint inversion using cross-gradients constraints may improve: (1) zonation of lithological sub-units [Gallardo and Meju, 2003; 2004; 2007; Chapter 2]; (2) ratios of physical properties [Tryggvason and Linde, 2006]; (3) petrophysical inferences [Linde *et al.*, 2006a]; (4) field-scale correlations with hydrological properties [Linde *et al.*, 2008]. These results suggest that joint inversion based on cross-gradients constraints might one day become a standard tool in diverse multi-method geophysical applications. There are nevertheless several questions that merits further attention and they are briefly discussed below.

How to justify the assumption of structural similarity for a given field application? Some knowledge about the field site is very important. An example of when the joint inversion approach is invalid would be in a heterogeneous geological media with strong gradients in

state variables (e.g., salinity) such as in a coastal setting or at a contaminated site as discussed in *Linde et al.* [2006a]. Access to geophysical logging data makes it possible to investigate structural similarity in the vertical direction at a few positions. Note that structural similarity is imposed at the resolution of the resulting models, not at the typically higher resolution of the logging data. We recommend to always perform both individual and joint inversion of given data sets. If the joint inversion fits the data to the same level as the individual inversions, if the scatter plots of the resulting models display the same main trends, and if the joint inversion models appear more distinct but that no fundamentally new structure is added, then joint inversion with cross-gradients constraints might be a valid approach. If not, it might be possible to impose structural similarity in parts of the model or to decrease the weight given to this constraint. In some cases, it might be possible to reformulate the inverse problem using, for example, time-lapse data to better constrain the properties that are expected to vary. There are many conditions when the assumption of structural similarity of model parameters is invalid and a careful analysis is needed for each new application.

What is the best discretization of the cross-gradients function? Instead of discretizing using the neighboring model cells, it might be better to define a discretization on the same scale as for the model regularization. This might further stabilize the joint inverse problem and decrease the sensitivity with respect to the model discretization.

How to determine optimal weights of the components associated with each data set in the objective function and what are the associated trade-offs? Our approach consists of first giving equal weights to each data set and then reweight until all data types can be fitted to the same error level as for the individual inversions. There are many alternative approaches, in which one could consider the resolution properties, spatial coverage, etc. It would probably be quite instructive to perform a detailed analysis of the trade-offs associated with different data types and the different components of the objective function.

How to transfer the joint inversion results to geological models and how to make robust petrophysical inferences? *Gallardo and Meju* [2003] suggested a manual lithological classification guided by the scatter plots of the different models. In Chapter 2, I developed a formalized classification scheme and performed a zonal inversion for effective petrophysical properties of each zone. A key step in all interpretations is to know what field-scale petrophysical relationships should be used to transform the models into geological or hydrogeological properties. It is useful to employ petrophysical relationships that share similar parameterizations and assumptions about the pore structure for all model types as done

here for the HS lower bounds, using a weighted average of the HS bounds [Brovelli and Cassiani, 2010], or by using volume-averaging [Linde *et al.*, 2006a]. Even if the joint inversion improves resolution, similar resolution-dependent petrophysical relationships as for individual inversions remain. A possibility is to focus on the slope of the cross-property relations that might be better resolved than the variability of each model. It would also be useful to extend the method of Day-Lewis *et al.* [2005] to this type of problems and thereby improve the determination of field-scale petrophysical relationships. One common assumption in petrophysical inference is that some properties like the dielectric permittivity of the solid phase is constant. One possibility is to relax this assumption through Monte Carlo simulations as suggested by Linde *et al.* [2006a]. This might help to better understand different possible explanations, for example, of the different slopes in the low wavespeed region of Figure F4h.

F.5 CONCLUSIONS

Joint inversion of crosshole radar and seismic traveltimes based on cross-gradients constraints using least-squares or l_1 -norm mimicking measures offers a reliable and robust methodology for improving model resolution in saturated unconsolidated media. With better resolved models, the confidence in subsequent geophysical-petrophysical analyses is increased. This inversion approach is also expected to be applicable to consolidated sedimentary environments, because porosity is the controlling factor for both radar and seismic wavespeed and the two inversion properties are expected to have similar responses to changes in the pore structure. For consolidated media, it might be useful to define a 1D reference model and to solve for the model update. No applications of joint inversion of radar and seismic data have been reported under multi-phase conditions. Such applications hold considerable promise in the vadose zone and in petroleum exploration applications, but a detailed assessment of the validity of the cross-gradients function under such conditions remains to be investigated. Similar arguments apply to surface-based data.

It is relatively straightforward to extend our joint inversion scheme to include improved forward modeling algorithms based on full-waveform or Fresnel-zone modeling approaches. Significant improvements in hydrogeophysical characterization are usually obtained by also including information about the electrical conductivity distribution obtained by incorporating radar attenuation, full-waveform modeling of radar data, or geoelectrical data in the joint inversion.

F.6 APPENDIX: STOCHASTIC REGULARIZATION OPERATORS

The model covariance matrix \mathbf{C}_m is a symmetrical Toeplitz matrix if the correlation function is stationary and the grid discretization is uniform in each direction [e.g., *Dietrich and Newsam, 1997*]. *Linde et al. [2006a]* used circulant embedding and the diagonalization theorem for circulant matrices to compute the stochastic regularization operator $\mathbf{C}_m^{-0.5}$ as described below. Their method for calculating $\mathbf{C}_m^{-0.5}$ is computationally efficient, because operations are performed on a vector instead of on a matrix.

Following *Dietrich and Newsam [1997]*, \mathbf{C}_m of a stationary process $Y(x)$ with correlation function $C(x)$ sampled on a uniform 1D mesh $\Omega = \{x_0, \dots, x_m\}$ has values $R_{qr} = r(|x_0 - x_k|)$. A model covariance matrix \mathbf{C}_m of size $m \times m$ can be circulantly embedded into a symmetric circulant matrix \mathbf{S} of size $2M \times 2M$ by assigning the following entries to the first column \mathbf{s} of \mathbf{S}

$$\begin{aligned} s_k &= r_k, & k &= 0, \dots, m, \\ s_{2M-k} &= r_k, & k &= 1, \dots, m-1, \end{aligned} \quad (\text{F22})$$

where if $M > m$ the values s_{m+1}, \dots, s_{2M-m} are arbitrary or conveniently chosen. The next column of \mathbf{S} can be obtained by shifting the first column circularly, such that the last element becomes first and all other elements are shifted forward by one, and so on. Being circulant \mathbf{S} can be decomposed by using the diagonalization theorem of circulant matrices

$$\mathbf{S} = \frac{1}{2M} \mathbf{F} \mathbf{\Lambda} \mathbf{F}^H, \quad (\text{F23})$$

where \mathbf{F} is the fast Fourier transform (FFT) matrix of size $2M$ with entries $F_{pq} = \exp(2\pi i q r / 2M)$, \mathbf{F}^H is the conjugate transpose of \mathbf{F} , and $\mathbf{\Lambda}$ is a diagonal matrix whose diagonal entries form the vector $\tilde{\mathbf{s}} = \mathbf{F} \mathbf{s}$ [e.g., *Golub and van Loan, 1996*]. The matrix \mathbf{S} is nonnegative definite if all entries of $\tilde{\mathbf{s}}$ are nonnegative. These results are extendable to two- and three dimensions [*Ranguelova, 2002*].

The matrix $\mathbf{S}^{-1/2}$ is for the one-dimensional case also circulant and its first column can be obtained as $\mathbf{F}^H \tilde{\mathbf{s}}^{-1/2}$ and the values corresponding to the first column of $\mathbf{C}_m^{-0.5}$ can be retrieved from entries 1 to m (see Equation F22), whereas all other columns of $\mathbf{C}_m^{-0.5}$ can be calculated by shifting the first column circularly. To decrease memory requirements, only elements of $\mathbf{C}_m^{-0.5}$ that are larger than 1% of the maximum value of $\mathbf{C}_m^{-0.5}$ are stored. In three dimensions, the only difference is that \mathbf{s} and $\tilde{\mathbf{s}}$ are expressed as three-dimensional arrays and that three-dimensional FFT is applied.

To ensure that S is nonnegative definite in three dimensions when using an exponential correlation function, it is necessary to choose M to be at least seven integral scales in each direction and choose s_{m+1}, \dots, s_{2M-m} to be the corresponding values of $r(l)$. The exponential covariance model used to calculate the entries R_{qr} above is for a stationary three-dimensional domain defined as

$$C(l) = ce^{-l}, \quad (\text{A3})$$

where c is the variance, e is the natural logarithm, and l is defined as

$$l = \sqrt{\left(\frac{h_x}{I_x}\right)^2 + \left(\frac{h_y}{I_y}\right)^2 + \left(\frac{h_z}{I_z}\right)^2}, \quad (\text{A4})$$

where h_x (m), h_y (m), and h_z (m) are the lags (i.e., the distances between a given pair of model parameters) in the x -, y - and z -direction, respectively, and I_x (m), I_y (m), and I_z (m) are the integral scales specified in the text for the different examples (i.e., the distance at which the correlation between model parameters is $1/e$) in the x -, y - and z -direction, respectively.

APPENDIX G: FRACTURE IMAGING USING SINGLE- AND CROSSHOLE GPR REFLECTION DATA

In press with *Journal of Applied Geophysics*:

Dorn, C., Linde, N., Doetsch, J., Le Borgne, T., and Bour, O., 2011, Fracture imaging within a granitic rock aquifer using multiple-offset single-hole and cross-hole GPR reflection data: *Journal of Applied Geophysics*, in press.

ABSTRACT

The sparsely spaced highly permeable fractures of the granitic rock aquifer at Stang-er-Brune (Brittany, France) form a well-connected fracture network of high permeability but unknown geometry. Previous work based on optical and acoustic logging together with single- and crosshole flowmeter data acquired in 3 neighboring boreholes (70-100 m deep) have identified the most important permeable fractures crossing the boreholes and their hydraulic connections. To constrain possible flow paths by estimating the geometries of known and previously unknown fractures, we have acquired, processed and interpreted multifold, single- and crosshole GPR data using 100 and 250 MHz antennas. The GPR data processing scheme consisting of time-zero corrections, scaling, bandpass filtering and F-X deconvolution, eigenvector filtering, muting, pre-stack Kirchhoff depth migration and stacking was used to differentiate fluid-filled fracture reflections from source-generated noise. The final stacked and pre-stack depth-migrated GPR sections provide high-resolution images of individual fractures (dipping 30-90°) in the surroundings (2-20 m for the 100 MHz antennas; 2-12 m for the 250 MHz antennas) of each borehole in a 2-D plane projection that are of superior quality to those obtained from single-offset sections. Most fractures previously identified from hydraulic testing can be correlated to reflections in the single-hole data. Several previously unknown major near vertical fractures have also been identified away from the boreholes.

G.1 INTRODUCTION

The hydraulic response of fractured rock aquifers is largely governed by the spatial organization of permeable fractures. Identifying and characterizing individual permeable fractures or flow paths at the local field-scale (1-100 m) is an important and largely unresolved research goal for the hydrological and geophysical research communities [*Long et al.*, 1996; *Day-Lewis et al.*, 2006]. Fractured rock masses are used worldwide, among others, for water supply purposes [e.g., *Caruthers and Smith*, 1992], as host rocks for environmentally hazardous waste [e.g., *Mair and Green*, 1981] and their characterization is necessary in rock fall prone areas [e.g., *Spillmann et al.*, 2007]. Single-hole ground penetrating radar (GPR) is a powerful technique to map potential permeable fractures and fracture zones away from boreholes and at large depths in relatively resistive rock [e.g., *Olsson et al.*, 1992; *Hollender et al.*, 1999], whereas surface GPR can be very useful down to some 10-20 m depth in sparsely fractured crystalline and metamorphic rock [*Grasmueck*,

1996]. Borehole or surface-based time-lapse GPR experiments carried out during saline tracer tests, or combined interpretations of hydraulic data and borehole or surface-based GPR may identify larger m-scale fractures that are permeable and significantly contribute to the local fluid flow [Tsoflias *et al.*; Day-Lewis *et al.*, 2003; Talley *et al.*, 2005; Day-Lewis *et al.*, 2006; Tsoflias and Becker, 2008].

Most previous work using single-hole GPR reflection data have used only one single-offset data from lower frequency antennas, such as 60 MHz, without migrating the data (see Spillmann *et al.* [2007] for an example of migrated single-offset high-frequency data). Hollender *et al.* [1999] illustrated that multiple-offset data can significantly improve the resolution of single-hole GPR sections. We expect that using high-frequency (100 and 250 MHz) multiple-offset data together with advanced processing will allow us to further improve the results of single- and crosshole GPR investigations compared with those present in the literature. We also want to investigate to what extent crosshole radar reflections complement single-hole reflection data. More importantly, the field-based results are expected to provide critical information about fractures that cannot be obtained from hydrological investigations alone.

Our field site is a well-studied hydrological research site located in a crystalline aquifer in Brittany (Stang-er-Brune, Figure G1a) in which Le Borgne *et al.* [2007] performed extensive hydrological testing and borehole logging. They concluded that the local conductive fracture network is dominated by only a few well-connected fractures (i.e. only 3-5 such fractures intersect a borehole over its entire length of ~90 m). High-resolution borehole images of the transmissive fractures show that these fractures have predominantly dip angles between 30° and 70°. The geometry of the hydrological connections between fractures is unknown. This is illustrated by apparent connections dipping up to 80° and that none of the permeable fractures appear to cross more than one borehole. The geometry of the permeable fracture network remains largely unknown as borehole data only provide detailed information in the close vicinity of the boreholes, whereas the single- and crosshole flowmeter data provide information about connections, but not their geometry [Le Borgne *et al.*, 2006].

To better understand the geometry of potential flow paths by imaging single fractures at the site, borehole GPR experiments were carried out in June 2009 to image single fractures up to some 20 m from the boreholes. We acquired multifold single- and crosshole GPR data in three boreholes (B1-B3, see Figure G1) using 100 MHz and 250 MHz antennas. This data are here used to determine the size, dip angles and to constrain the possible orientations of single

fractures, especially for those that have not been previously identified, as they do not intersect the boreholes. We expect the strongest recorded GPR reflections to originate from the major open water-filled fractures [Tsoflias and Becker, 2008] and at the ~ 40 m deep contact between mica schist and granite (Figure G1).

In this contribution, we describe the processing of data acquired in borehole B1 (single-hole) and within the borehole-plane B1-B2 (crosshole). We then present the final migrated sections including the boreholes B1-B3. The results are then interpreted together with available hydrological and borehole logging data.

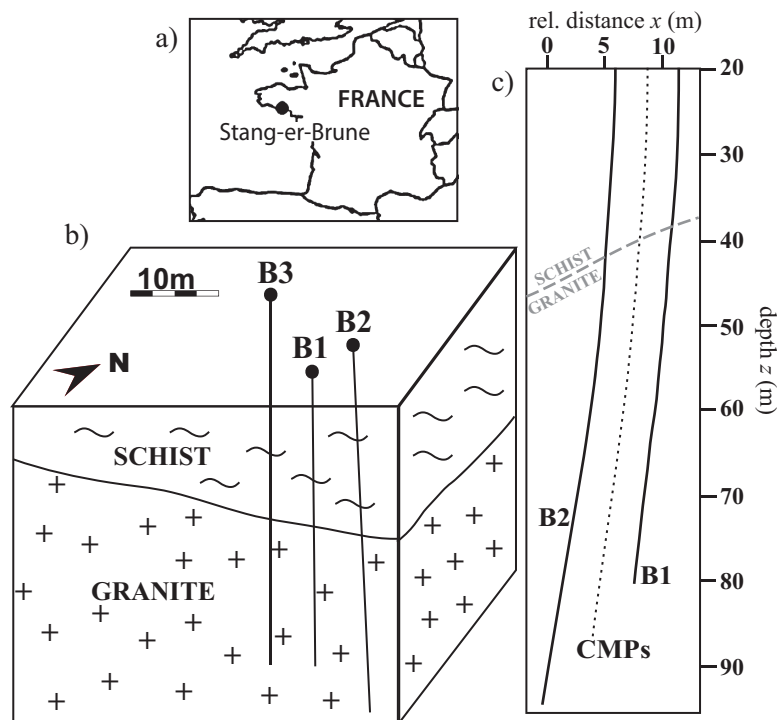


Figure G1. (a) Location of Stang-er-Brune, France. (b) Geological model of the field site showing the 30° dipping contact between mica schist and underlying granite. (c) 2-D projection of the borehole geometry of B1, B2 and cross-hole CMP (common midpoint) locations. At $z > 50$ m there is a relative dip between B1 and B2 of $\sim 3^\circ$.

G.2 GENERAL SETTING OF THE CRYSTALLINE AQUIFER

Our field-site in Brittany (Stang-er-Brune), France, is located 3 km west of the main groundwater-pumping site of Ploemeur and is part of a long-term hydrological research observatory (<http://hplus.ore.fr>). The 3 deeper boreholes installed at the site reach depths from 80 to 100 m (water table during acquisition at ~ 1.5 m depth). The borehole deviations are up to 6° from the vertical as estimated by a deviation probe using a three-axis fluxgate magnetometer for bearing and a three-axis accelerometer for inclination. This tool has an

estimated uncertainty of 0.5° , which leads to an expected standard deviation of 0.9 m in the horizontal coordinates at 100 m depth. The characterization of fractures and the geology of the site are known from borehole coring (B1) and optical, acoustic, gamma-ray and electrical geophysical logs that are discussed in detail in *Le Borgne et al.* [2007] and *Belghoul* [2007]. At a regional scale, the geology is characterized by low-porosity granite overlain by micaschists, with a contact zone dipping $\sim 30^\circ$ towards north [*Touchard*, 1999; *Le Borgne et al.*, 2006; *Ruelleu et al.*, 2010]. The contact zone is relatively complex and consists of alternating deformed granitic sheets and enclaves of micaschists, pegmatite and aplite dykes [*Ruelleu et al.*, 2010]. At the Stang-er-Brune site, we observe a part of this contact zone with micaschists in the first 30 to 40 meters overlying the Ploemeur granite. The formation is highly transmissive with overall transmissivity over the depth of each borehole varying around $10^{-3} \text{ m}^2/\text{s}$. This high transmissivity implies a strong connectivity of the permeable fractures that is probably related to the contact zone between the intrusive granite and the overlying micaschists.

G.3 MULTIFOLD DATA ACQUISITION

Single-hole GPR data were acquired in all three boreholes (B1-B3) in common offset sections using 16 (4) different transmitter-receiver separations for the employed 100 MHz (250 MHz) antennas with a depth sampling of 0.15 m (0.1 m). The antenna offsets were equally distributed in the range of 2.3-11.3 m (100 MHz antennas) and 1.8-7.8 m (250 MHz antennas). The dominant frequencies are around 70 (140) MHz for the data acquired with the 100 (250) MHz antennas.

The crosshole GPR data were acquired for all three borehole planes (B1-B2, B1-B3, B2-B3) in common transmitter gathers. The crosshole planes of B1-B2 were acquired with 250 MHz antennas, whereas 100 MHz antennas were used for B2-B3 and B1-B3. Transmitters were spaced every 0.5 m and receivers every 0.1 m resulting in nominal 30-fold data at a common-midpoint (CMP) spacing of 0.125 m. The acquired offsets were restricted to those for which reasonable signal-to-noise ratio data could still be obtained.

To protect and to center the antennas in the boreholes, we attached two self-made plastic packers to each antenna, with a slightly smaller diameter than those of the boreholes (10.5 cm). Antennas were first positioned by transforming distances along the borehole measured with a trigger wheel into depths with the help of the deviation logs. Differential GPS was used to measure the top of the borehole casings. All depths are given relative to the top of the B1

casing. Time-zero measurements were performed when changing the antenna separation (single-hole) or after measuring 40 source-gathers (crosshole).

G.4 DATA PROCESSING

Significant ringing in the 250 MHz raw data and the dominance of the direct wave at early times, together with positioning uncertainties and radar wavespeed variations, resulted in numerous processing-related challenges. The processing scheme (Table G1) addressed these issues and resulted in high-quality GPR images of the surrounding fractured rock matrix. Even if the individual processes are standard in seismic imaging [Yilmaz, 2001], it was necessary to adapt the processing and the parameters to address the specific characteristics of the borehole GPR data.

We begin the description by first explaining the progressively improved radar wavespeed and borehole trajectory estimates before we outline the specific processing schemes used for single- and crosshole data.

In the following, dips of reflectors are always given with respect to the surface assuming vertical boreholes if not mentioned differently. Note that shallow dips (relative to the surface) refer to steep dips of features relative to the subvertical borehole trajectories.

Table G1. Main processing steps of single- and crosshole GPR data.

Representative Figure	Single-hole data processing	Cross-hole data processing	Representative Figure
2a →	Static corrections AGC	Static corrections AGC	
2b →	Bandpass filter	Bandpass filter	
2c, 3a →	F-X deconvolution	F-X deconvolution	
	Eigenvector filter	Eigenvector filter	
	First-break mute	First-break mute	
3d →	Prestack depth migration	Dip-decomposition dip-moveout (includes stack)	← 7b
	Custom mute	Kirchhoff depth migration	← 7c
	CMP Stack		

G.4.1 Radar wavespeed estimation and borehole trajectory estimation

The single- and crosshole data were used together to define average radar wavespeed functions $v(z)$ and refine the estimated borehole trajectories. Isotropy of the radar wavespeed was assumed on the wavelength scale to allow for comparison of the single- and crosshole data. This assumption is reasonable as granite is an igneous rock of low porosity having negligible intrinsic anisotropy.

An initial radar wavespeed model was obtained from the single-hole data by fitting a straight line to the slope of the corrected direct wave (which travels at the wavespeed of the rock in the vicinity of the borehole) travel times vs. transmitter–receiver distances for each CMP location. This procedure allows us to avoid static errors, resulting for example from the assumption that a finite-length antenna can be represented as a point source or by neglecting the delay of the direct wave in the water filled space between the antenna and the borehole. At $z > 40$ m, the differences between the radar wavespeed functions from all three boreholes are 2.5 % on average.

The first radar wavespeed estimates were subsequently refined by traveltimes tomography. The mean of the 1-D radar wavespeed functions of each borehole pair for which tomography was carried out was used as initial and reference models in the tomography (green line in Figure G2a). The tomography was mainly carried out to improve the borehole positioning and to evaluate if the radar wavespeed estimates from the crosshole data correspond with those determined in the vertical direction (i.e., assumption of isotropy). For the tomography, we followed the inversion procedure of *Linde and Doetsch* [2010] using a stochastic regularization operator based on an exponential isotropic covariance model with integral scales of 0.5 m aiming at fitting the data to an error level of 1.0 ns. The integral scale corresponds to the distance at which the spatial correlation has decreased to $1/e$. To decrease the sensitivity to noise in the data and to image sharp radar wavespeed variations we used a formulation based on iteratively reweighted least-squares [*Farquharson*, 2008].

Initial inversions of the crosshole traveltimes in the plane B1-B2 resulted in suspiciously high radar wavespeeds at $z > 50$ m (blue line in Figure G2a) compared with the initial mean radar wavespeed function B1/B2 (green line in Figure G2a) indicating that the borehole spacing is smaller than indicated by the deviation logs. This inversion reached a final RMS error of 1.84 ns after 10 iterations. To improve the results it was necessary to correct the antenna positions in both the vertical and horizontal directions. For each transmitter gather, the receiver array was shifted vertically to minimize offset-correlated behavior in the

residuals. This correction (max. 0.5 m) was in all cases increasing with depth and helped to reduce small-scale variations in the resulting radar wavespeed models. Twisting of the antenna cables might have caused these errors.

To further constrain the distances between B1 and B2, we picked the observed prominent reflections originating from the adjacent borehole in the depth-migrated single-hole data (using the initial radar wavespeed function shown as green line in Figure G2a). We corrected for the relative borehole geometry given the shape of the picked reflector distances. To correct for significant borehole deviation errors for the other cases where we could not identify reflections from the adjacent boreholes (B2-B3 and B1-B3), we tested horizontal correction factors that linearly varied with depth until the residuals (after the first iteration) have the lowest correlation possible.

The geometrical corrections and the subsequent inversion of the B1-B2 data resulted in the tomogram shown in Figure G2b with an RMS error of 1.05 ns after 10 iterations. As expected, the traveltome tomography provides no information about individual fractures but images large-scale radar wavespeed variations and trends. The final radar wavespeed model plotted in red in Figure G2a is based on the horizontal average of the tomographic model in regions with dense ray-coverage ($z = 20$ to 80 m) and the initial model outside this region. The final radar wavespeed estimates are mostly in the range of 0.09 ± 0.002 m/ns (mica schist) to 0.12 ± 0.002 m/ns (granite). Given the small lateral variations in the tomogram (Figure G2b), it appears that the assumption of a 1-D radar wavespeed function holds well if all applied corrections prior to the inversion are correct. These 1-D radar wavespeed functions were used to migrate the single- and crosshole data.

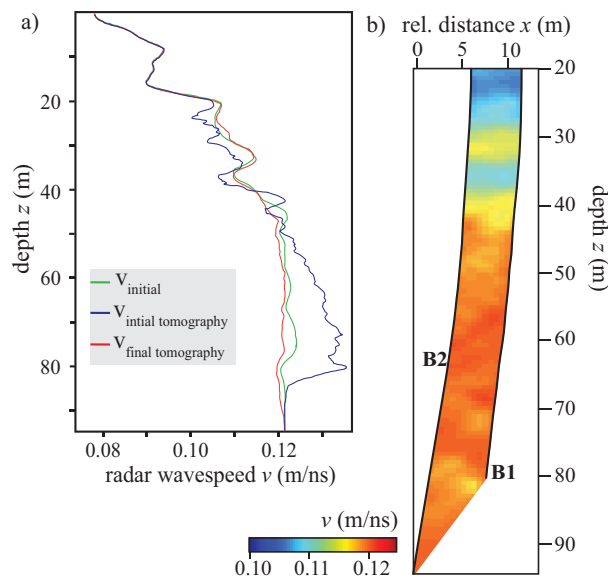


Figure G2. (a) 1-D radar wavespeed estimates for the plane B1-B2: (blue) after tomographic inversion of the cross-hole traveltimes using the initial borehole geometry and the initial radar wavespeed function (green) as starting and initial model, (red) after using the same tomographic inversion scheme but with final geometrical corrections applied. (b) Tomogram derived from first arrivals using the initial radar wavespeed function (a, green line) as starting and reference model and with final geometrical corrections.

G.4.2 Single-hole processing

Processing challenges

The GPR single-offset section (B1, 250 MHz antenna) in Figure G3a illustrates some of the data characteristics. Source-generated noise (N) or rather poor coupling within the antenna-borehole-rock system creates ringing effects parallel to the direct wave (D) but at later times. The ringing is most critical for the 250 MHz data, where it is superimposed on early reflections (R). The reflectivity pattern varies along the borehole and there is an abrupt increase in signal-to-noise ratios at approximately 40 m depth below the schist.

A general problem in single-hole GPR imaging with standard commercial omnidirectional antennas (directional borehole antennas exists [e.g., *Slob et al.*, 2010] but are not widely used) is that the orientation of the fractures cannot be determined using data from one borehole alone. The data carries no information about the direction at which a reflection wavefront arrives at the borehole. Our processing and migration is therefore carried out under the assumption that the radar wavespeed varies only in the vertical direction (1-D radar wavespeed function $v(z)$, where z is depth). We showed in Section G4.1 that the 1-D radar wavespeed assumption appears to hold well within the granite, which is of primary interest in this study as it is the host rock of the most permeable fractures.

Borehole logging data (optic and acoustic) and analysis of the retrieved core of B1 indicate that the shallowest dips of transmissive fractures are in the range of 30° (except one fracture dipping 15° [Le Borgne *et al.*, 2007]). Using migration methods to image such subhorizontal dips (steep dips with respect to the observation line) require an accurate radar wavespeed model.

Pre-stack time-domain processing

Table G1 lists the main single-trace and multi-trace filter and deconvolution tools that were applied to the single-offset data. All parameters within the processing sequence were chosen to account for the different frequency contents of the 100 and 250 MHz data.

Corrections were carried out to account for inaccuracies in the data acquisition sampling frequency [c.f. Hollender *et al.*, 1999], drifts in the time-zero and geometrical positioning errors. After appropriate scaling (Figure G3a), reflections (R) had to be enhanced and separated from the direct wave (D) and ringing noise (N), resulting in a common single-offset section as shown in Figure G3b. Bandpass filtering (30-270 MHz for the 250 MHz data, 20-130 MHz for the 100 MHz data) removed low- and high frequency noise from the data. F-X deconvolution increased reflection coherency by reducing random noise without introducing noticeable artifacts. For the 250 MHz data, an eigenvector filter was applied in a window around the direct wave to remove energy parallel to the direct wave mainly containing ringing noise (N). Residual energy that appears earlier than the direct wave is muted afterwards.

Pre-stack depth migration and stacking

Pre-stack Kirchhoff depth migration of single-offset sections provided high-quality image reflections with overlapping features and a wide dip angle range (Figure G3c). The migration radar wavespeeds used are in the range of 0.09 m/ns (mica schist) to 0.12 m/ns (granite). In Section G4.2, we describe how we estimated the radar wavespeed function.

We used a migration method that computes first arrivals through an implicit Eikonal solver. The amplitudes are neither calculated nor meaningful as the processing is based on a monopole (point) radiator, which does not correspond well with the dipole-like radiation characteristics of borehole antennas. In regions without significant radar wavespeed variations (40-100 m), subhorizontal dipping features (down to 30°) are well preserved after migration (green arrows in Figure G3c). Migration artifacts are likely to be present around $z = 40$ m (Figure G3c) since the 1-D radar wavespeed model does not account for the 30° dip angle of the mica schist-granite contact. Apart from this region, extensive comparisons of migrated

sections using a variety of radar wavespeed models indicate that the sections are free of major migration artifacts.

Stacking the migrated single-offset sections of the 100 MHz data significantly improved the quality compared to individual single-offset sections (compare Figures G4a and c). Close to the borehole, subhorizontal dipping features (e.g., $\sim 30^\circ$) are less well imaged at larger antenna offsets (see arrows in Figures G4b and c). Further away from the borehole, reflections from subhorizontal dipping features of limited extent are best recognized at larger antenna offsets (see ellipses in Figures G4b and c). The image quality increases for larger radial distance $r > \sim 8$ m by adding information from larger offset sections, but decreases for $r < \sim 6$ m. To avoid sub-optimal resolution close to the boreholes in the final image, we applied an offset-dependent top mute prior to stacking (Figure G4d); the larger the offset the longer the applied top mute.

For the 250 MHz data we stacked the three largest offset sections, since the shortest offset (1.8 m) sections were highly contaminated by ringing effects and did not contribute significantly to the stacked images. The major improvements of stacking the 250 MHz data came from the additional offset information and less from an increased signal-to-noise ratio, given that only a few offsets were used.

We do not image any features at distances $r < 2$ m because of the dominance of the direct wave at early times and its subsequent removal, which also tends to remove superimposed reflections at early times. This complicates direct comparisons with the borehole logging data.

G.4.3 Crosshole processing

Challenges

Common crosshole processing tools such as single-trace mapping techniques [Khalil *et al.*, 1993; Lazaratos *et al.*, 1995] that focus on layered structures can only handle horizontal to sub-horizontal reflectors correctly. The complex spatial distribution of fractures at the site and the crosshole acquisition geometry necessitate an approach that can accurately consider all reflector dips.

Unlike the cylindrical symmetry of the single-hole data, reflections in the crosshole sections can originate from any point on an ellipsoid around a respective CMP location (Figure G5). Some analysis is therefore needed to better understand how to migrate such data and interpret the results in terms of possible dip angle and distance ranges. For this geometry, any signal travelling between the two boreholes B1 and B2, being reflected on a 90° dipping

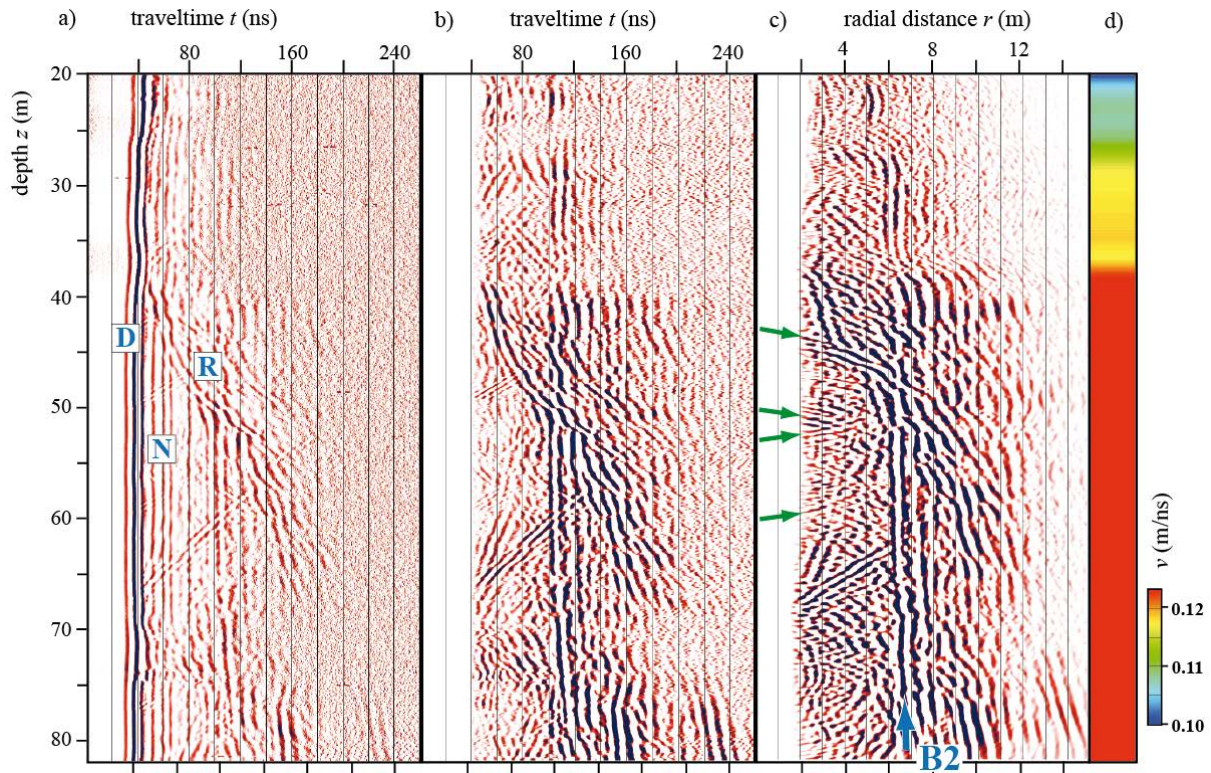


Figure G3. Results of pre-stack processing applied to a typical common-offset section of B1 (3.8 m offset, 250 MHz antennas). (a) Section with applied static corrections and an AGC of 70 ns window length. Letters indicate regions dominated by: D – direct wave; N – source-generated noise (ringing); R - reflections. (b) As in (a) but after application of bandpass filter, F-X deconvolution, eigenvector filter and custom mute (see text). (c) As in (b) but after pre-stack depth migration (the axis aspect ratio $r:z$ is 2:1). The blue arrow in (c) indicates reflections generated from the adjacent borehole B2; the green arrows refer to features discussed in the text. (d) 1-D wavespeed model for depth migration in (c).

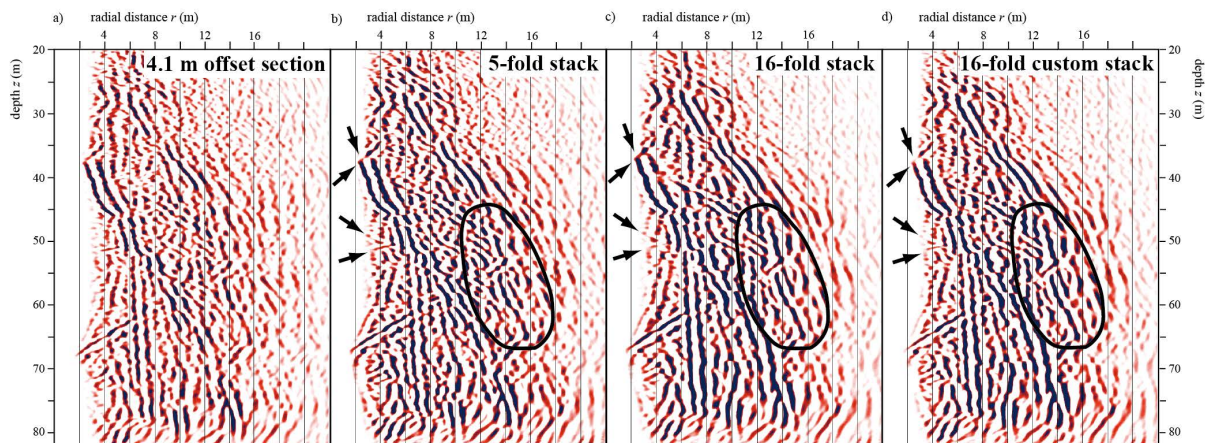


Figure G4. Illustration of the improved signal-to-noise ratios offered by stacking the migrated images of B1 (100 MHz data). (a) Single-offset section with 4.1 m antenna separation. (b) Stack of the 5 shortest antenna separations, (c) all 16 offset sections, and (d) as in (c) but with a custom mute applied for each offset section before stacking. Note that subhorizontally dipping events at small radial distances are best imaged in (b) and (d) (see arrows), whereas at larger radial distance they are best imaged in (c) and (d) (see ellipses).

plane at $y = P_y$ (Figure G5a) cannot be distinguished from any other reflection on the ellipse described by the two main axes P_x and P_y . In the depth-migrated image this plane would show up at a shorter distance $x = P_x$. A reflector plane at $y = P_y$ dipping 60° away from the borehole (see solid red lines in Figures G5a-c) is imaged in the depth-migrated section as a curved feature (see corresponding dashed red lines in Figures G5a-c).

To simulate the geometrical effects of the examples described above (90° and 60° dipping reflector), we have computed synthetic seismograms for the B1/B2 borehole geometry using *Bohlen's* [2002] 3-D viscoelastic finite difference modeling code (Figure G6). An alternative would have been to use a 3-D GPR code [e.g., *Giannopoulos*, 2005]. The use of synthetic seismograms can help to explain the GPR reflection geometry, but not the GPR amplitudes. The modeled and depth-migrated data confirms our geometrical assumption of an elliptic projection. Calculated and observed distances in the depth-migrated image fit well. Figure G6b confirm that planar features might appear curved in the migrated sections.

Due to the removal of the direct wave that strongly contaminated early reflections, the earliest reflections that are possible to image originate from an ellipse (see ellipse in Figure G5a) in a range from 2 to 4 m away from the CMP.

Processing

The pre-processing of the crosshole data was similar to that of the single-hole data (Section G.4.1) but was followed by dip decomposition DMO and depth migration (Table G1). The NMO stack (Figure G7a) performed with the dip-independent stacking wavespeeds (Figure G2a, red line), reveals some structural complexity but fails to clearly image subhorizontal dipping reflectors superimposed on subvertical features. We treated the preprocessed data with a dip-moveout (DMO) algorithm based on *Jakubowicz* [1990] that distinguishes and processes events on the basis of dip, with angles between 0° and 90° discretized into 45 different values. For each of the 45 dip angle values, the CMP gathers were NMO corrected using appropriate velocities estimated from the dip-independent wavespeeds based on standard formulas and then stacked. Finally, all 45 dip-filtered stacks were summed together to form a DMO-corrected stack (Figure G7b). Compared to the NMO stack, the DMO process improved signal-to-noise ratios throughout the section and conflicting dips are better imaged (see rectangles in Figures G7a and b). Other tested DMO algorithms did not sufficiently image subhorizontal dips (e.g., common-offset F-K DMO).

The migrated section (Figure G7c) was obtained by a post-stack Kirchhoff depth migration for steep dips (in this context *steep* refers to dips with respect to the observation

line, Table G1) using the same implicit eikonal solver as for the single-hole data. This allowed us to obtain images that were free of major artifacts. We decided to use partial pre-stack migration followed by post-stack depth migration because it showed the least migration artifacts in comparison with pre-stack-migration schemes performed on the modeled crosshole seismograms (see also Figure G6).

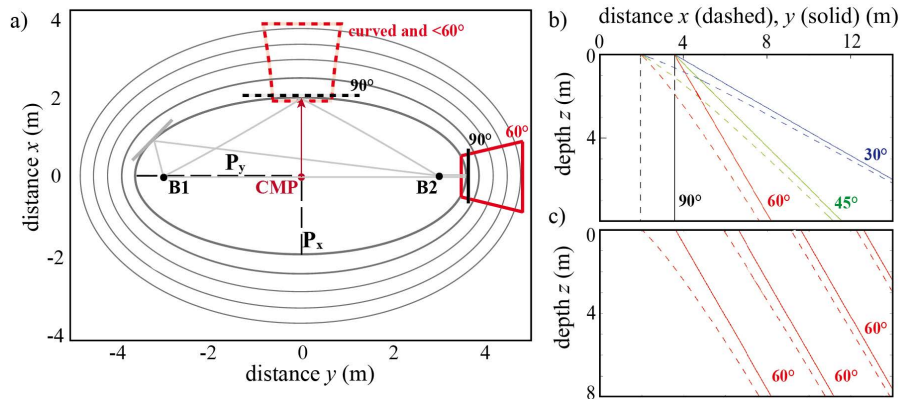


Figure G5. (a) 2-D-schematic of elliptic distance projection in cross-hole reflection imaging showing boreholes B1 and B2 from a bird's eye view. A 90° dipping reflector at a distance $x = P_x$ in the depth-migrated GPR image can originate from anywhere on an ellipse described by the two main axes P_x and P_y surrounding the CMP. (b) and (c) Dip and distance representations in the depth migrated images. The solid lines describe tangential reflector planes striking perpendicular to the inter-borehole plane and dipping at angles 30° , 45° , 60° and 90° (see solid lines in (a) of both 90° and 60° dipping planes). The dashed lines describe how they would appear in a depth-migrated image (see dashed lines in (a) of plane representations).

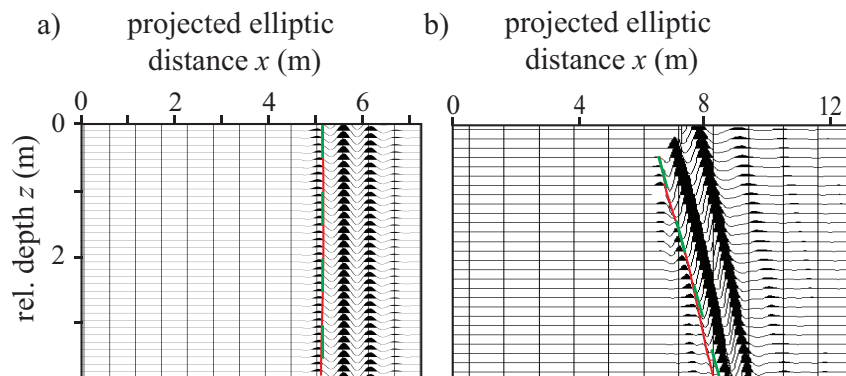


Figure G6. (a) Modelled depth-migrated seismic data for a borehole geometry as in Fig. 5a and a 90° dipping reflector plane at $y = 5.9$ m away from the CMP. The picked (red line) and predicted distances (green line) are both $x = 5.1$ m. (b) As for (a), but for a modelled reflector plane dipping 60° away from the surface.

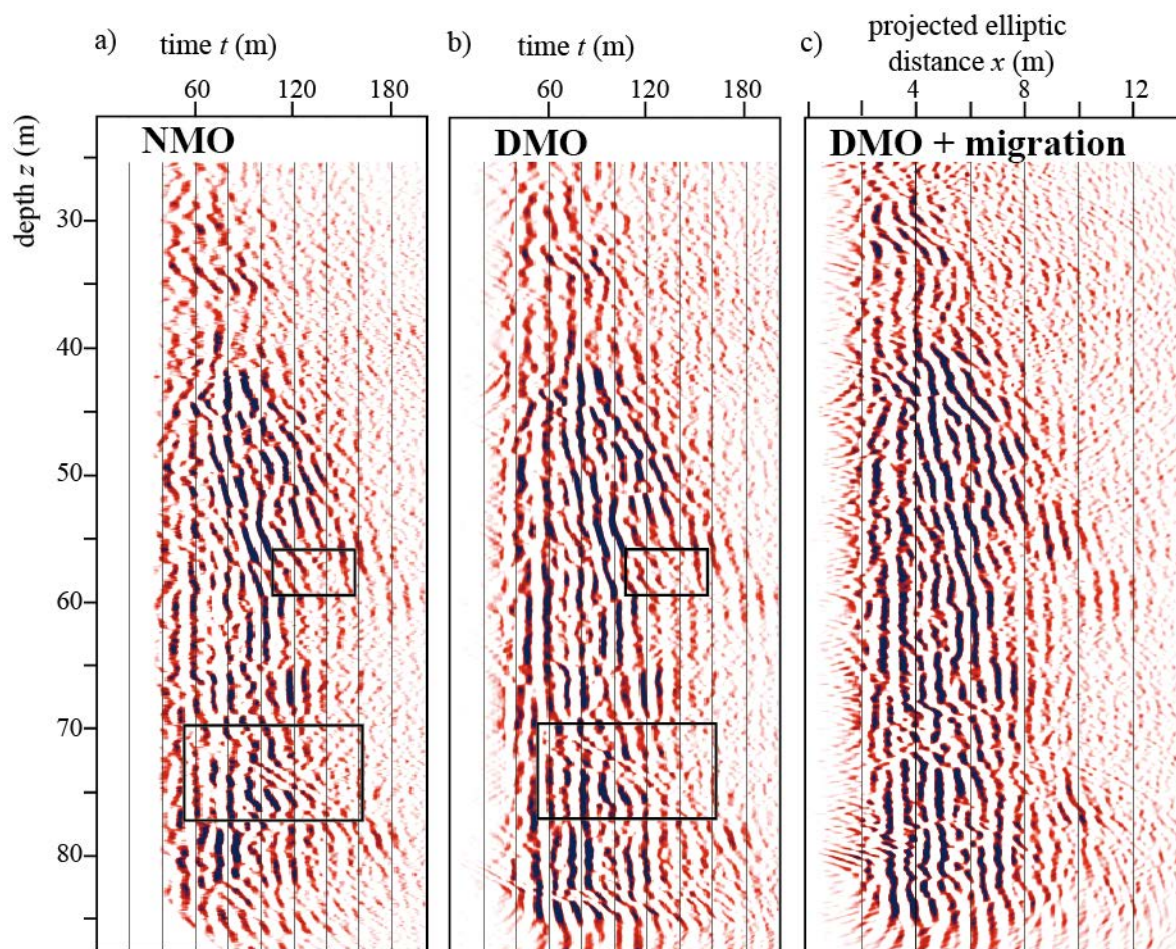


Figure G7. Post-stack processed cross-hole section for B1-B2. (a) NMO stack, (b) dip-decomposition DMO stack and (c) post-stack Kirchhoff depth-migrated version of (b) based on radar wavespeed model shown in Figure G2a (red line). Black rectangles refer to features discussed in the text.

G.5 RESULTS

G.5.1 Single-hole GPR images

The final stacked and migrated sections of B1-B3 show several linear reflections (dipping 30-90°) located at 2-14 m and 2-20 m radial distance for the 250 MHz (Figure G8) and 100 MHz (Figure G9) data. These reflections are expected to mainly originate from individual fractures and fracture zones. The sections obtained from the 100 and 250 MHz antennas are comparable as most prominent features in the 250 MHz section are also represented in the 100 MHz section. The higher resolution of the 250 MHz data at $r < 8$ m allows more structural details to be imaged, especially for subhorizontal dipping features. The change from low to high reflectivity at $z = 38$ m in B1 ($z = 42$ m in B2, $z = 35$ m in B3) is related to the higher attenuation in the more conductive overlying mica schist compared to the granite.

The prominent sub-vertical reflections at $r \approx 6$ m (arrows B2 and B1 in Figures G8 and G9) correspond to the neighboring borehole. Identical reflector planes can be recognized in both B1 and B2 GPR sections as having similar dips and corresponding depth ranges. We can also distinguish reflections originating from outside the borehole plane B1-B2 from reflections generated between the boreholes. Reflections originate from outside the plane B1-B2 if the imaged reflections have similar dip angle and dip direction for both single-hole sections (see A1 in Figure G8). Reflections originate from within the borehole plane if they have similar dips but the dip direction appears different comparing both single-hole sections (see A2 in Figure G8).

A series of transmissive fractures previously identified at their intersection with the boreholes and characterized through flowmeter tests and optical logging [*Le Borgne et al.*, 2007] can be correlated to reflections in the GPR sections (blue letters in Figures G8 and G9) based on their dips and extrapolated intersection points given positioning errors of up to 4%. Fractures that could not be correlated to GPR reflections either lie in the mica schist (B1-1) where signal-to-noise ratios are low, have a nearly horizontal dip and hence cannot lead to direct reflections (B1-4 in Figure G8a: probable phase shift on reflections due to B1-4) or have a too small spatial extent to be seen at $r > 2$ m (B3-2 and B2-2 are only seen up to $r = 4$ m in Figure G8 but are not clearly seen in the 100 MHz data in Figure G9). A number of hitherto unknown prominent subvertical features can be seen that do not cross the boreholes. As an example there is a larger fracture zone (A3) dipping $\sim 70^\circ$ that is crossing the sections B1 and B2 at $r = 2$ -10 m.

G.5.2 Crosshole GPR images

The final stacked and migrated crosshole sections (Figure G10) image several features relative to the corresponding CMP locations (for position see Figure G1c for B1-B2 plane). The signal attenuation is much lower at $z > \sim 38$ m at which the surrounding rock matrix consist of high-resistive granite. Most features are linear dipping 30 - 90° , some curved features are shown at $x < \sim 8$ m that can be attributed to the elliptic symmetry. Most prominent reflections are subvertical (A3-A7 in Figure G10).

It is difficult to confidently correlate reflections in the crosshole image to those identified in the borehole logs since the reflections are imaged as originating away from the crosshole midpoints. It appears still that certain prominent subvertical reflections seen in the single-hole data can be related to reflections in the crosshole sections (for example A3 in Figures G8-10).

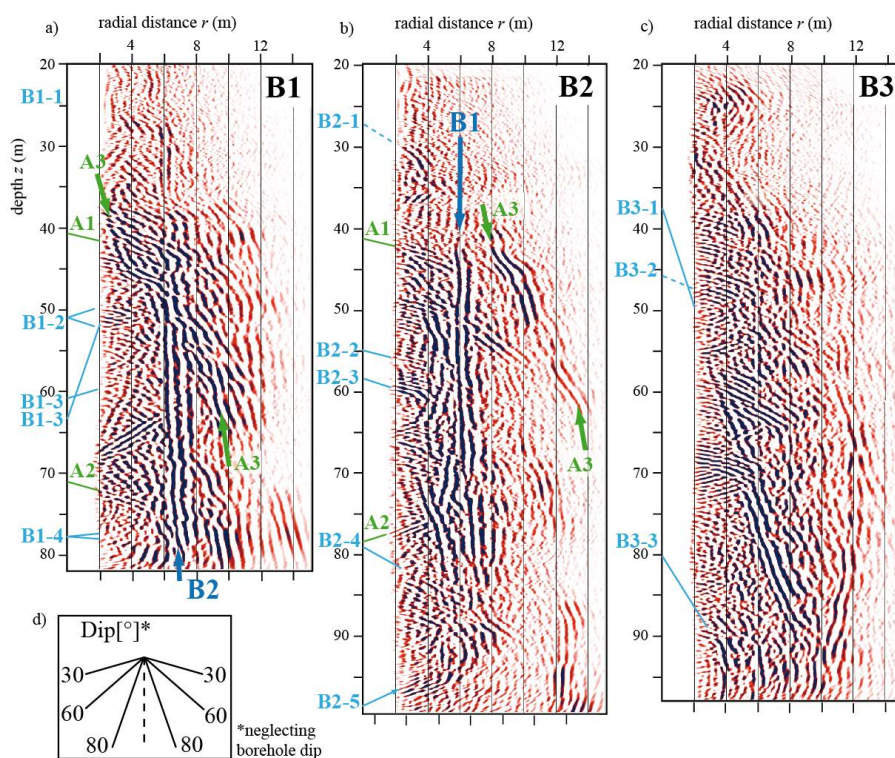


Figure G8. Processed and pre-stack depth-migrated single-hole GPR data acquired with the 250 MHz antenna in (a) B1, (b) B2, and (c) B3. Blue letters refer to transmissive fractures observed in the boreholes from optical logs and flowmeter tests [Le Borgne *et al.*, 2007], green letters refer to additional features discussed in the text. The radial distance r indicates distances away from the respective boreholes. Note the lack of information at $r < 2$ m due to the direct wave removal. (d) Dip angles corresponding to the axis aspect ratio $r:z$ of 2:1. Note that a given dip (0 - 90°) can be imaged with two different dip directions (e.g., A2).

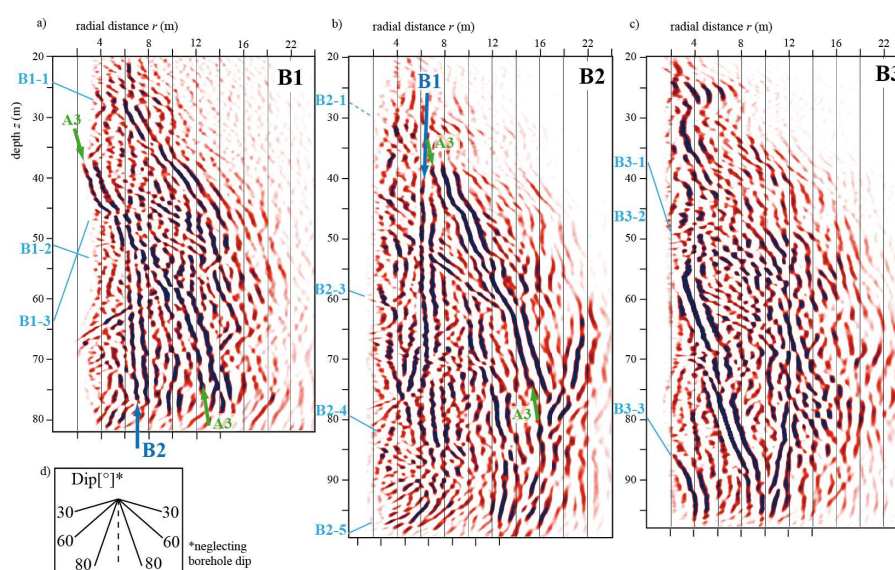


Figure G9. The same borehole sections as in Figure G8 but for the processed and pre-stack depth-migrated GPR data that were acquired with the 100 MHz antenna. Section (a) is identical to Figure G4d.

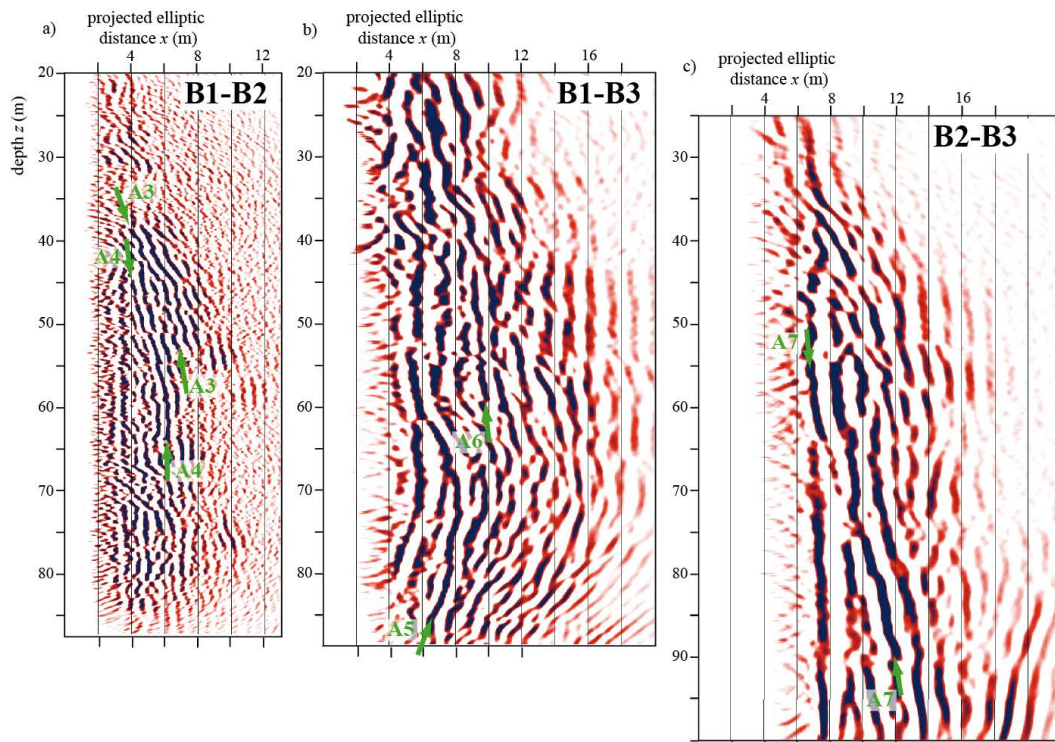


Figure G10. Processed and migrated cross-hole GPR sections of (a) B1-B2 (250 MHz), (b) B1-B3 (100 MHz), and (c) B2-B3 (100 MHz). A3-A7 refer to features discussed in the text. The projected elliptic distances x are relative to the CMP locations as shown for B1-B2 in Figure G1c. The axis aspect ratio $x:z$ is 2:1. Note the lack of information at $x < \sim 2$ m due to the direct wave removal. Note also that dipping individual fractures that are expected to be linear show up as curved features in accordance with Figure G5b and c.

G.6 DISCUSSION

Multiple-offset data acquisition together with a tailored pre-processing and pre-stack migration made it possible to correlate most transmissive fractures observed in flowmeter and optical televiewer data [Le Borgne *et al.*, 2007] with reflectors observed in the single-hole reflection data (Figures G8 and G9). In fact, a total of 10 out of 11 transmissive fractures in the granite could be correlated with reflectors. These reflections appear as (sub-) linear features in the final processed and migrated images. Reflectors crossing the boreholes were best identified by first picking reflectors from the migrated 250 MHz data (Figure G9) followed by verification that these reflectors are visible on individual unmigrated time-sections. The dip angles of the reflectors and those observed in the boreholes were allowed to have a mismatch of up to 10° as fractures/reflectors that appear linear on the scale of the fracture might locally (i.e., where they cross the boreholes) show larger deviations in the dip angle as evidenced at outcrops of similar patterns on the coastline 5 km away. Most transmissive fractures can be correlated with reflectors, but there are also certain reflectors

that appear to cross the boreholes that are unrelated to the previously identified permeable fractures. One important result is that we can associate a length scale to previously identified transmissive fractures.

The migrated single-hole (Figures G8 and G9) and crosshole (Figure G10) data image several prominent fractures or fracture zones with lengths exceeding 40 m. Only one of those (B3-1 in Figures G8c and G9c) appears to cross the borehole. It is important to note that the anisotropic radiation/reception patterns of the antennas make subvertical dipping features in the single- and crosshole data more prominent compared to shallow ones because the electric dipole source has its orientation in the vertical direction. Furthermore, imaging limitations at large distances away from the boreholes make it impossible to trace the full length of the more subhorizontal dipping reflectors. It is possible that the previously unknown subvertical fracture zones play an important role in (1) establishing the hydraulic connections observed and (2) providing sustained yield during pumping. This interpretation is supported by *Le Borgne et al.* [2007] who demonstrate that none of the identified permeable fractures appear to cross more than one borehole. Furthermore, steady-state conditions are established almost instantaneously at this site, which indicates a well-connected fracture network extending over a large scale. Some of these major reflectors can be imaged from different boreholes and with the crosshole data (Figures G8-10). Consider A3, as it is imaged in both B1 and B2 single-hole data, and in the B1-B2 crosshole data, it is possible to better constrain its location [e.g., *Olsson et al.*, 1992; *Spillmann et al.*, 2007].

Saline tracer tests monitored with single-hole GPR data will in the future be analyzed to test the conceptual model invoked above. It is also expected that such experiments will decrease the inherent uncertainty caused by projecting 3-D data into 2-D as the injection point is known.

G.7 CONCLUSIONS

GPR is one of few geophysical methods that are capable of imaging individual millimeter wide fractures away from boreholes. We have processed and interpreted multiple-offset single- and crosshole GPR data acquired in a granitic rock aquifer. The multiple-offset acquisition not only increased the CMP fold, but also made it possible to image fractures with limited extents and dip angles for which reflections are only visible within a certain offset-range. Our processing scheme allowed us to separate useful reflections from unwanted signals to obtain high-resolution images. Key processing steps included time-zero and geometrical

corrections, eigenvector filtering to remove direct wave and ringing effects, careful top muting and migration, and accurate radar wavespeed estimation and borehole positioning by a combined analysis of single- and crosshole data. The migration (using pre-stack depth migration or DMO-corrections followed by depth migration) was able to handle subhorizontal dips and provided images that were free of major artifacts. The superposition of reflections necessitate a combined interpretation considering both unmigrated and migrated data.

The final GPR sections image a number of reflectors with dips in the range of 30-90° at radial distances of 2-20 m and spatial extents of more than the first Fresnel-zone (2 m at $r = 20$ m down to 0.6 m at $r = 2$ m). Reflections from a certain reflector can be observed if a normal-vector to the reflector exists which crosses the borehole. We observe the highest resolution in the vicinity of the borehole when using the 250 MHz data, whereas the 100 MHz data are very useful in imaging major subvertical features away from the borehole. These mostly linear reflections are interpreted as mainly corresponding to fractures, but are also due to other boreholes and the contact zone between mica schist and granite. Ten out of eleven known transmissive fractures in the granite can be correlated to reflections. By identifying the same reflectors in different borehole GPR sections, we can reduce the inherent 360° circular uncertainty of single-hole data and elliptical uncertainty of crosshole data to some extent. The dip direction of identified fractures remains underdetermined because the three boreholes do not form a triangular prism at depth, but rather lie on a common plane. Prominent sub-vertical reflectors image previously unknown fractures (they do not intersect the boreholes) with lengths exceeding 40 m that may play a key role in determining the flow geometry at the site.

REFERENCES

- Acworth, R. I., and Dasey, G. R., 2003. Mapping of the hyporheic zone around a tidal creek using a combination of borehole logging, borehole electrical tomography and cross-creek electrical imaging, New South Wales, Australia, *Hydrogeology Journal*, **11**, 368-377.
- Ajo-Franklin, J. B., Minsley, B. J., and Daley, T. M., 2007. Applying compactness constraints to differential travelt ime tomography, *Geophysics*, **72**, R67-R75.
- al Hagrey, S. A., and Müller, C., 2000. GPR study of pore water content and salinity in sand, *Geophysical Prospecting*, **48**, 63-85.
- Allègre, V., Jouniaux, L., Lehmann, F., and Sailhac, P., 2010. Streaming potential dependence on water-content in Fontainebleau sand, *Geophysical Journal International*, **182**, 1248-1266.
- Alumbaugh, D., Chang, P. Y., Paprocki, L., Brainard, J. R., Glass, R. J., and Rautman, C. A., 2002. Estimating moisture contents in the vadose zone using cross-borehole ground penetrating radar: A study of accuracy and repeatability, *Water Resources Research*, **38**, 1309.
- Alumbaugh, D. L., and Newman, G. A., 2000. Image appraisal for 2-D and 3-D electromagnetic inversion, *Geophysics*, **65**, 1455-1467.
- Annan, A. P., 2005. GPR Methods for Hydrogeological Studies, in *Hydrogeophysics*, edited by Y. Rubin and S. S. Hubbard, pp. 185-213, Springer Netherlands.
- Archie, G. E., 1942. The electrical resistivity log as an aid in determining some reservoir characteristics, *Transactions of the American institute of Mining, Metallurgical and Petroleum Engineers*, **146**, 54-62.
- Arora, T., Linde, N., Revil, A., and Castermant, J., 2007. Non-intrusive characterization of the redox potential of landfill leachate plumes from self-potential data, *Journal of Contaminant Hydrology*, **92**, 274-292.
- Aubert, M., and Yééné Atangana, Q., 1996. Self-potential method in hydrogeological exploration of volcanic areas, *Ground Water*, **34**, 1010-1016.
- Avseth, P., Mukerji, T., Jørstad, A., Mavko, G., and Veggeland, T., 2001. Seismic reservoir mapping from 3-D AVO in a North Sea turbidite system, *Geophysics*, **66**, 1157-1176.
- BAFU, 2010. Hydrologischer Atlas der Schweiz, *Bundeamt für Umwelt, Bern, Switzerland*.
- Barrash, W., and Clemo, T., 2002. Hierarchical geostatistics and multifacies systems: Boise Hydrogeophysical Research Site, Boise, Idaho, *Water Resources Research*, **38**, 1196.
- Barrenetxea, G., Ingelrest, F., Schaefer, G., and Vetterli, M., 2008. The hitchhiker's guide to successful wireless sensor network deployments, *Sensys'08: Proceedings of the 6th Acm Conference on Embedded Networked Sensor Systems*, 43-56.
- Battin, T. J., and Sengschmitt, D., 1999. Linking sediment biofilms, hydrodynamics, and river bed clogging: Evidence from a large river, *Microbial Ecology*, **37**, 185-196.

- Baumann, M., Jordan, P., Hoehn, E., and Geisser, H., 2009. Ein neues Grundwassermodell für das Thurtal, *Mitteilungen der Thurgauischen Naturforschenden Gesellschaft*, **63**.
- Bedrosian, P. A., Maercklin, N., Weckmann, U., Bartov, Y., Ryberg, T., and Ritter, O., 2007. Lithology-derived structure classification from the joint interpretation of magnetotelluric and seismic models, *Geophysical Journal International*, **170**, 737-748.
- Bélanger, C., Giroux, B., Gloaguen, E., and Lefebvre, R., 2010. GPR, ERT and CPT data integration for high resolution aquifer modeling, *13th International Conference on GPR*, 1-6.
- Belghoul, A., 2007. *Caractérisation pétrophysique et hydrodynamique du socle cristallin*: PhD thesis, University of Montpellier.
- Belina, F. A., Ernst, J. R., and Holliger, K., 2009. Inversion of crosshole seismic data in heterogeneous environments: Comparison of waveform and ray-based approaches, *Journal of Applied Geophysics*, **68**, 85-94.
- Bencala, K. E., 1984. Interactions of solutes and streambed sediment 2. A dynamic analysis of coupled hydrologic and chemical processes that determine solute transport, *Water Resources Research*, **20**, 1804-1814.
- Beres, M., Green, A., Huggenberger, P., and Horstmeyer, H., 1995. Mapping the architecture of glaciofluvial sediments with 3-dimensional georadar, *Geology*, **23**, 1087-1090.
- Beres, M., Huggenberger, P., Green, A. G., and Horstmeyer, H., 1999. Using two- and three-dimensional georadar methods to characterize glaciofluvial architecture, *Sedimentary Geology*, **129**, 1-24.
- Bernhardt, E. S., Palmer, M. A., Allan, J. D., Alexander, G., Barnas, K., et al., 2005. Ecology - Synthesizing US river restoration efforts, *Science*, **308**, 636-637.
- Beutel, J., Dyer, M., Lim, R., Plessl, C., Wohrle, M., et al., 2007. Automated wireless sensor network testing, *INSS 07: Proceedings of the Fourth International Conference on Networked Sensing Systems*, 303-303.
- Beven, K., and Binley, A., 1992. The future of distributed models - model calibration and uncertainty prediction, *Hydrological Processes*, **6**, 279-298.
- Bing, Z., and Greenhalgh, S. A., 1998a. A damping method for the computation of the 2.5-D Green's function for arbitrary acoustic media, *Geophysical Journal International*, **133**, 111-120.
- Bing, Z., and Greenhalgh, S. A., 1998b. Crosshole acoustic velocity imaging with full-waveform spectral data: 2.5-D numerical simulations, *Exploration Geophysics*, **29**, 680-684.
- Bing, Z., and Greenhalgh, S. A., 2000. Cross-hole resistivity tomography using different electrode configurations, *Geophysical Prospecting*, **48**, 887-912.
- Binley, A., Winship, P., Middleton, R., Pokar, M., and West, J., 2001. High-resolution characterization of vadose zone dynamics using cross-borehole radar, *Water Resources Research*, **37**, 2639-2652.
- Binley, A., Winship, P., West, L. J., Pokar, M., and Middleton, R., 2002a. Seasonal variation of moisture content in unsaturated sandstone inferred from borehole radar and resistivity profiles, *Journal of Hydrology*, **267**, 160-172.

-
- Binley, A., Cassiani, G., Middleton, R., and Winship, P., 2002b. Vadose zone flow model parameterisation using cross-borehole radar and resistivity imaging, *Journal of Hydrology*, **267**, 147-159.
- Binley, A., Cassiani, G., and Deiana, R., 2010. Hydrogeophysics: Opportunities and challenges, *Bollettino di Geofisica Teorica ed Applicata*, **51**, 267-284.
- Birchak, J. R., Gardner, C. G., Hipp, J. E., and Victor, J. M., 1974. High dielectric constant microwave probes for sensing soil moisture, *Proceedings of the IEEE*, **62**, 93-98.
- Bleistein, N., 1986. 2-1/2 dimensional inplane wave-propagation, *Geophysical Prospecting*, **34**, 686-703.
- Blome, M., Maurer, H. R., and Schmidt, K., 2009. Advances in three-dimensional geoelectric forward solver techniques, *Geophysical Journal International*, **176**, 740-752.
- Blome, M., Maurer, H., and Greenhalgh, S., 2011. Geoelectric experimental design - Efficient acquisition and exploitation of complete pole-bipole data sets, *Geophysics*, **76**, F15-F26.
- Boggs, J. M., and Adams, E. E., 1992. Field study of dispersion in a heterogeneous aquifer: 4. Investigation of adsorption and sampling bias, *Water Resources Research*, **28**, 3325-3336.
- Boggs, J. M., Young, S. C., Beard, L. M., Gelhar, L. W., Rehfeldt, K. R., and Adams, E. E., 1992. Field-study of dispersion in a heterogeneous aquifer: 1. Overview and site description, *Water Resources Research*, **28**, 3281-3291.
- Bohlen, T., 2002. Parallel 3-D viscoelastic finite difference seismic modelling, *Computers & Geosciences*, **28**, 887-899.
- Bolève, A., Revil, A., Janod, F., Mattiuzzo, J. L., and Fry, J. J., 2009. Preferential fluid flow pathways in embankment dams imaged by self-potential tomography, *Near Surface Geophysics*, **7**, 447-462.
- Bosma, T. N. P., Balleman, E. M. W., Hoekstra, N. K., teWelscher, R. A. G., Smeenk, J. G. M. M., et al., 1996. Biotransformation of organics in soil columns and an infiltration area, *Ground Water*, **34**, 49-56.
- Bouman, C. A., 1997. Cluster: An unsupervised algorithm for modeling Gaussian mixtures, <http://www.ece.purdue.edu/~bouman>.
- Bourg, A. C. M., and Bertin, C., 1993. Biogeochemical processes during the infiltration of river water into an alluvial aquifer, *Environmental Science & Technology*, **27**, 661-666.
- Bouwer, H., and Rice, R. C., 1976. Slug test for determining hydraulic conductivity of unconfined aquifers with completely or partially penetrating wells, *Water Resources Research*, **12**, 423-428.
- Bowling, J. C., Rodriguez, A. B., Harry, D. L., and Zheng, C., 2005. Delineating alluvial aquifer heterogeneity using resistivity and GPR data, *Ground Water*, **43**, 890-903.
- Bowling, J. C., Harry, D. L., Rodriguez, A. B., and Zheng, C., 2007. Integrated geophysical and geological investigation of a heterogeneous fluvial aquifer in Columbus Mississippi, *Journal of Applied Geophysics*, **62**, 58-73.
-

- Bradford, J. H., Clement, W. P., and Barrash, W., 2009. Estimating porosity with ground-penetrating radar reflection tomography: A controlled 3-D experiment at the Boise Hydrogeophysical Research Site, *Water Resources Research*, **45**, W00D26.
- Brookes, A., 1988. *Channelized rivers: Prospectives for environmental management*, John Wiley and Sons, Chichester, UK.
- Brovelli, A., and Cassiani, G., 2010. A combination of the Hashin-Shtrikman bounds aimed at modelling electrical conductivity and permittivity of variably saturated porous media, *Geophysical Journal International*, **180**, 225-237.
- Brunke, M., and Gonser, T., 1997. The ecological significance of exchange processes between rivers and groundwater, *Freshwater Biology*, **37**, 1-33.
- Butler, A. P., Mathias, S. A., Gallagher, A. J., Peach, D. W., and Williams, A. T., 2009. Analysis of flow processes in fractured chalk under pumped and ambient conditions (UK), *Hydrogeology Journal*, **17**, 1849-1858.
- Butler, J. J., 1998. *The design, performance and analysis of slug tests*, Lewis, Boca Raton.
- Butler, J. J., Garnett, E. J., and Healey, J. M., 2003. Analysis of slug tests in formations of high hydraulic conductivity, *Ground Water*, **41**, 620-630.
- BUWAL, 2004. *Wegleitung Grundwasserschutz, Bundesamt für Umwelt, Wald und Landschaft, Bern, Switzerland.*
- Carcione, J. M., Ursin, B., and Nordskog, J. I., 2007. Cross-property relations between electrical conductivity and the seismic velocity of rocks, *Geophysics*, **72**, E193-E204.
- Cardenas, M. B., Wilson, J. L., and Zlotnik, V. A., 2004. Impact of heterogeneity, bed forms, and stream curvature on subchannel hyporheic exchange, *Water Resources Research*, **40**, W08307.
- Cardenas, M. B., and Markowski, M. S., 2011. Geoelectrical imaging of hyporheic exchange and mixing of river water and groundwater in a large regulated river, *Environmental Science & Technology*, **45**, 1407-1411.
- Carsel, R. F., and Parrish, R. S., 1988. Developing joint probability-distributions of soil-water retention characteristics, *Water Resources Research*, **24**, 755-769.
- Caruthers, R. M., and Smith, I. F., 1992. The use of ground electrical survey methods for siting water-supply boreholes in shallow crystalline basement terrains, in *Hydrogeology of Crystalline Basement Aquifers in Africa*, edited by E. P. Wright and W. G. Burgess, pp. 203-220, Geological Society Special Publication.
- Cassiani, G., Bruno, V., Villa, A., Fusi, N., and Binley, A. M., 2006. A saline trace test monitored via time-lapse surface electrical resistivity tomography, *Journal of Applied Geophysics*, **59**, 244-259.
- Chambers, J. E., Wilkinson, P. B., Weller, A. L., Meldrum, P. I., Gilvy, R. D., and Caunt, S., 2007. Mineshaft imaging using surface and crosshole 3D electrical resistivity tomography: A case history from the East Pennine Coalfield, UK, *Journal of Applied Geophysics*, **62**, 324-337.
- Chen, J. S., Hubbard, S., Rubin, Y., Murray, C., Roden, E., and Majer, E., 2004. Geochemical characterization using geophysical data and Markov Chain Monte Carlo methods: A case

-
- study at the South Oyster bacterial transport site in Virginia, *Water Resources Research*, **40**, W12412.
- Cirpka, O. A., Fienen, M. N., Hofer, M., Hoehn, E., Tessarini, A., et al., 2007. Analyzing bank filtration by deconvoluting time series of electric conductivity, *Ground Water*, **45**, 318-328.
- Claerbout, J. F., and Muir, F., 1973. Robust modeling with erratic data, *Geophysics*, **38**, 826-844.
- Constantz, J., Cox, M. H., and Su, G. W., 2003. Comparison of heat and bromide as ground water tracers near streams, *Ground Water*, **41**, 647-656.
- Constantz, J., 2008. Heat as a tracer to determine streambed water exchanges, *Water Resources Research*, **44**, W00D10.
- Coscia, I., Marescot, L., Maurer, H., Greenhalgh, S., and Linde, N., 2008. Experimental design for crosshole electrical resistivity tomography data sets, *14th Annual European Meeting of Environmental and Engineering Geophysics, EAGE*.
- Coscia, I., Greenhalgh, S., Linde, N., Green, A., Günther, T., et al., 2010. A multi-borehole 3-D ERT monitoring system for aquifer characterization using river flood events as a natural tracer, *16th Annual European Meeting of Environmental and Engineering Geophysics, EAGE*.
- Coscia, I., Greenhalgh, S. A., Linde, N., Doetsch, J., Marescot, L., et al., 2011a. 3D crosshole ERT for aquifer characterization and monitoring of infiltrating river water, *Geophysics*, **76**, G49-G59.
- Coscia, I., Linde, N., Greenhalgh, S., Günther, T., and Green, A., 2011b. A deconvolution approach to correct time-lapse 3D ERT data and improve imaging of natural aquifer dynamics, *Water Resources Research*, under review.
- Crook, N., Binley, A., Knight, R., Robinson, D. A., Zarnetske, J., and Haggerty, R., 2008. Electrical resistivity imaging of the architecture of substream sediments, *Water Resources Research*, **44**, W00D13.
- Daily, W., and Owen, E., 1991. Cross-borehole resistivity tomography, *Geophysics*, **56**, 1228-1235.
- Daily, W., Ramirez, A., Labrecque, D., and Nitao, J., 1992. Electrical resistivity tomography of vadose water movement, *Water Resources Research*, **28**, 1429-1442.
- Daily, W., and Ramirez, A., 1995. Electrical-resistance tomography during in-situ trichloroethylene remediation at the savanna river site, *Journal of Applied Geophysics*, **33**, 239-249.
- Daily, W., Ramirez, A., Binley, A., and LaBrecque, D., 2005. Electrical resistance tomography — theory and practice, in *Near surface geophysics*, edited by D. K. Butler, pp. 525-550, SEG.
- Daniels, J. J., Allred, B., Binley, A., Labrecque, D., and Alumbaugh, D., 2005. Hydrogeophysical case studies in the vadose zone, in *Hydrogeophysics*, edited by Y. Rubin and S. S. Hubbard, pp. 413-440, Springer.
- Darling, T., 2005. *Well logging and formation evaluation*, Elsevier.
- Darnet, M., and Marquis, G., 2004. Modelling streaming potential (SP) signals induced by water movement in the vadose zone, *Journal of Hydrology*, **285**, 114-124.
- Day-Lewis, F. D., Lane, J. W., Jr., Harris, J. M., and Gorelick, S. M., 2003. Time-lapse imaging of saline-tracer transport in fractured rock using difference-attenuation radar tomography, *Water Resources Research*, **39**, 1290.
-

- Day-Lewis, F. D., and Lane, J. W., 2004. Assessing the resolution-dependent utility of tomograms for geostatistics, *Geophysical Research Letters*, **31**, L07503.
- Day-Lewis, F. D., Singha, K., and Binley, A. M., 2005. Applying petrophysical models to radar travel time and electrical resistivity tomograms: Resolution-dependent limitations, *Journal of Geophysical Research-Solid Earth*, **110**, B08206.
- Day-Lewis, F. D., Lane, J. W., and Gorelick, S. M., 2006. Combined interpretation of radar, hydraulic, and tracer data from a fractured-rock aquifer near Mirror Lake, New Hampshire, USA, *Hydrogeology Journal*, **14**, 1-14.
- Day-Lewis, F. D., Chen, Y., and Singha, K., 2007. Moment inference from tomograms, *Geophysical Research Letters*, **34**, L22404.
- de Franco, R., Biella, G., Tosi, L., Teatini, P., Lozej, A., et al., 2009. Monitoring the saltwater intrusion by time lapse electrical resistivity tomography: The Chioggia test site (Venice Lagoon, Italy), *Journal of Applied Geophysics*, **69**, 117-130.
- Deiana, R., Cassiani, G., Kemna, A., Villa, A., Bruno, V., and Bagliani, A., 2007. An experiment of non-invasive characterization of the vadose zone via water injection and cross-hole time-lapse geophysical monitoring, *Near Surface Geophysics*, **5**, 183-194.
- Dempster, A. P., Laird, N. M., and Rubin, D. B., 1977. Maximum likelihood from incomplete data via the EM algorithm, *Journal of the Royal Statistical Society, Series B (Methodological)*, **39**, 1-38.
- Deutsch, C. V., and Journel, A. G., 1998. *GSLIB: Geostatistical software library and user's guide*, 2. edition ed., Oxford Univ. Press, New York, 2. edition.
- Diem, S., Vogt, T., and Hoehn, E., 2010. Räumliche Charakterisierung der hydraulischen Leitfähigkeit in alluvialen Schotter-Grundwasserleitern: Ein Methodenvergleich, *Grundwasser*, **15**, 241-251.
- Dietrich, C. R., and Newsam, G. N., 1997. Fast and exact simulation of stationary Gaussian processes through circulant embedding of the covariance matrix, *Siam Journal on Scientific Computing*, **18**, 1088-1107.
- Dogan, M., Van Dam, R. L., Bohling, G. C., Butler, J. J., Jr., and Hyndman, D. W., 2011. Hydrostratigraphic analysis of the MADE site with full-resolution GPR and direct-push hydraulic profiling, *Geophysical Research Letters*, **38**, L06405.
- Dorn, C., Linde, N., Le Borgne, T., Bour, O., and Baron, L., 2011. Single-hole GPR reflection imaging of solute transport in a granitic aquifer, *Geophysical Research Letters*, **38**, L08401.
- Doussan, C., Jouniaux, L., and Thony, J. L., 2002. Variations of self-potential and unsaturated water flow with time in sandy loam and clay loam soils, *Journal of Hydrology*, **267**, 173-185.
- EC, 2000. Directive 2000/60/EC of the European Parliament and of the council establishing a framework for community action in the field of water policy, *Official Journal of the European Community*, **L327**, 1-72.
- Eckert, P., Lamberts, R., and Wagner, C., 2008. The impact of climate change on drinking water supply by riverbank filtration, *Water Science Technology*, **8**, 319-324.

-
- Edmaier, K., Burlando, P., and Perona, P., 2011. Mechanisms of vegetation uprooting by flow in alluvial non-cohesive sediment, *Hydrology and Earth Systems Science Discussion*, **8**, 1365-1398.
- Eisenberg, D., and Kauzmann, W., 1969. *The structure and properties of water*, Oxford University Press.
- Ellis, R. G., and Oldenburg, D. W., 1994. Applied geophysical inversion, *Geophysical Journal International*, **116**, 5-11.
- Eppstein, M. J., and Dougherty, D. E., 1998. Optimal 3-D traveltime tomography, *Geophysics*, **63**, 1053-1061.
- Ernst, J. R., Maurer, H., Green, A. G., and Holliger, K., 2007a. Full-waveform inversion of crosshole radar data based on 2-D finite-difference time-domain solutions of Maxwell's equations, *Ieee Transactions on Geoscience and Remote Sensing*, **45**, 2807-2828.
- Ernst, J. R., Green, A. G., Maurer, H., and Holliger, K., 2007b. Application of a new 2D time-domain full-waveform inversion scheme to crosshole radar data, *Geophysics*, **72**, J53-J64.
- Ernst, J. R., 2007. *2-D finite-difference time-domain full-waveform inversion of crosshole georadar data*: PhD thesis, ETH Zurich.
- Farquharson, C. G., 2008. Constructing piecewise-constant models in multidimensional minimum-structure inversions, *Geophysics*, **73**, K1-K9.
- Favetto, A., Pomposiello, C., Booker, J., and Rossello, E. A., 2007. Magnetotelluric inversion constrained by seismic data in the Tucuman basin (Andean foothills, 27 degrees S, NW Argentina), *Journal of Geophysical Research - Solid Earth*, **112**, B09104.
- Fine, R. A., and Millero, F. J., 1973. Compressibility of water as a function of temperature and pressure, *Journal of Chemical Physics*, **59**, 5529-5536.
- Fleckenstein, J. H., Niswonger, R. G., and Fogg, G. E., 2006. River-aquifer interactions, geologic heterogeneity, and low-flow management, *Ground Water*, **44**, 837-852.
- Fournier, C., 1989. Spontaneous potentials and resistivity surveys applied to hydrogeology in a volcanic area - case-history of the Chaîne-Des-Puys (Puy-De-Dome, France), *Geophysical Prospecting*, **37**, 647-668.
- Fregoso, E., and Gallardo, L. A., 2009. Cross-gradients joint 3D inversion with applications to gravity and magnetic data, *Geophysics*, **74**, L31-L42.
- French, H., and Binley, A., 2004. Snowmelt infiltration: Monitoring temporal and spatial variability using time-lapse electrical resistivity, *Journal of Hydrology*, **297**, 174-186.
- Friedel, S., 2003. Resolution, stability and efficiency of resistivity tomography estimated from a generalized inverse approach, *Geophysical Journal International*, **153**, 305-316.
- Friedel, S., Byrdina, S., Jacobs, F., and Zimmer, M., 2004. Self-potential and ground temperature at Merapi volcano prior to its crisis in the rainy season of 2000-2001, *Journal of Volcanology and Geothermal Research*, **134**, 149-168.
- Füchtenbauer, H., 1988. *Sedimente und Sedimentgesteine: Sandsteine*, 4 ed., Schweizerbart, Stuttgart.
- Gallardo, L. A., and Meju, M. A., 2003. Characterization of heterogeneous near-surface materials by joint 2D inversion of dc resistivity and seismic data, *Geophysical Research Letters*, **30**, 1658.
-

- Gallardo, L. A., and Meju, M. A., 2004. Joint two-dimensional DC resistivity and seismic travel time inversion with cross-gradients constraints, *Journal of Geophysical Research - Solid Earth*, **109**, B03311.
- Gallardo, L. A., Meju, M. A., and Pérez-Flores, M. A., 2005. A quadratic programming approach for joint image reconstruction: Mathematical and geophysical examples, *Inverse Problems*, **21**, 435-452.
- Gallardo, L. A., 2007. Multiple cross-gradient joint inversion for geospectral imaging, *Geophysical Research Letters*, **34**, L19301.
- Gallardo, L. A., and Meju, M. A., 2007. Joint two-dimensional cross-gradient imaging of magnetotelluric and seismic traveltimes data for structural and lithological classification, *Geophysical Journal International*, **169**, 1261-1272.
- Gallardo, L. A., and Meju, M. A., 2011. Structure-Coupled Multiphysics Imaging in Geophysical Sciences, *Reviews of Geophysics*, **49**, RG1003.
- Garambois, S., Senechal, P., and Perroud, H., 2002. On the use of combined geophysical methods to assess water content and water conductivity of near-surface formations, *Journal of Hydrology*, **259**, 32-48.
- Gasperikova, E., Zhang, Y., and Hubbard, S., 2008. Using self potential and multiphase flow modeling to optimize groundwater pumping, *EOS Transactions AGU*, *89*(53).
- Giannopoulos, A., 2005. Modelling ground penetrating radar by GprMax, *Construction and Building Materials*, **19**, 755-762.
- Gibert, D., and Pessel, M., 2001. Identification of sources of potential fields with the continuous wavelet transform: Application to self-potential profiles, *Geophysical Research Letters*, **28**, 1863-1866.
- Golub, G. H., and van Loan, C. F., 1996. *Matrix computations*, Johns Hopkins University Press.
- Gooseff, M. N., Anderson, J. K., Wondzell, S. M., LaNier, J., and Haggerty, R., 2005. A modelling study of hyporheic exchange pattern and the sequence, size, and spacing of stream bedforms in mountain stream networks, Oregon, USA, *Hydrological Processes*, **19**, 2915-2929.
- Grasmueck, M., 1996. 3-D ground-penetrating radar applied to fracture imaging in gneiss, *Geophysics*, **61**, 1050-1064.
- Grinsted, A., Moore, J. C., and Jevrejeva, S., 2004. Application of the cross wavelet transform and wavelet coherence to geophysical time series, *Nonlinear Processes in Geophysics*, **11**, 561-566.
- GschG, 1991. Gewässerschutzgesetz, *Bundesgesetz über den Schutz der Gewässer, Schweiz*, **814.20**, 30.
- GSchV, 1998. Gewässerschutzverordnung, *Bundesgesetz über den Schutz der Gewässer, Schweiz*, **814.201**, 60.
- Günther, T., 2004. *Inversion methods and resolution analysis for the 2D/3D reconstruction of resistivity structures from DC measurements*, Ph.D. thesis thesis: TU Bergakademie Freiberg.

-
- Günther, T., and Rücker, C., 2006. A general approach for introducing information into inversion and examples from dc resistivity inversion, in *14th Annual European Meeting of Environmental and Engineering Geophysics*, edited, p. P039, EAGE.
- Günther, T., Rücker, C., and Spitzer, K., 2006. Three-dimensional modelling and inversion of dc resistivity data incorporating topography - II. Inversion, *Geophysical Journal International*, **166**, 506-517.
- Günther, T., and Rücker, C., 2009. Advanced inversion strategies using a new geophysical inversion and modelling library, *15th Annual European Meeting of Environmental and Engineering Geophysics*, EAGE.
- Haber, E., and Oldenburg, D., 1997. Joint inversion: A structural approach, *Inverse Problems*, **13**, 63-77.
- Harbaugh, A. W., 2005. MODFLOW-2005, The U.S. Geological Survey modular ground-water model—the ground-water flow process, in *Book 6. Modeling techniques*, Ch. 16.
- Harvey, J. W., and Bencala, K. E., 1993. The effect of streambed topography on surface-subsurface water exchange in mountain catchments, *Water Resources Research*, **29**, 89-98.
- Hashin, Z., and Shtrikman, S., 1962. A variational approach to theory of effective magnetic permeability of multiphase materials, *Journal of Applied Physics*, **33**, 3125-&.
- Hashin, Z., and Shtrikman, S., 1963. A variational approach to the theory of the elastic behaviour of multiphase materials, *Journal of the Mechanics and Physics of Solids*, **11**, 127-140.
- Hatch, C. E., Fisher, A. T., Revenaugh, J. S., Constantz, J., and Ruehl, C., 2006. Quantifying surface water-groundwater interactions using time series analysis of streambed thermal records: Method development, *Water Resources Research*, **42**, W10410.
- Hauck, C., 2002. Frozen ground monitoring using DC resistivity tomography, *Geophysical Research Letters*, **29**, 2016.
- Hayley, K., Bentley, L. R., and Gharibi, M., 2009. Time-lapse electrical resistivity monitoring of salt-affected soil and groundwater, *Water Resources Research*, **45**.
- Heinz, J., Kleineidam, S., Teutsch, G., and Aigner, T., 2003. Heterogeneity patterns of quaternary glaciofluvial gravel bodies (SW-Germany): Application to hydrogeology, *Sedimentary Geology*, **158**, 1-23.
- Henderson, R. D., Day-Lewis, F. D., and Harvey, C. F., 2009. Investigation of aquifer-estuary interaction using wavelet analysis of fiber-optic temperature data, *Geophysical Research Letters*, **36**, L06403.
- Hiscock, K. M., and Grischek, T., 2002. Attenuation of groundwater pollution by bank filtration, *Journal of Hydrology*, **266**, 139-144.
- Hoehn, E., and Cirpka, O. A., 2006. Assessing residence times of hyporheic ground water in two alluvial flood plains of the Southern Alps using water temperature and tracers, *Hydrology and Earth System Sciences*, **10**, 553-563.
- Hoehn, E., and Scholtis, A., 2011. Exchange between a river and groundwater, assessed with hydrochemical data, *Hydrology and Earth System Sciences*, **15**, 983-988.

- Hollender, F., Tillard, S., and Corin, L., 1999. Multifold borehole radar acquisition and processing, *Geophysical Prospecting*, **47**, 1077-1090.
- Holliger, K., Musil, M., and Maurer, H. R., 2001. Ray-based amplitude tomography for crosshole georadar data: A numerical assessment, *Journal of Applied Geophysics*, **47**, 285-298.
- Hu, W. Y., Abubakar, A., and Habashy, T. M., 2009. Joint electromagnetic and seismic inversion using structural constraints, *Geophysics*, **74**, R99-R109.
- Hubbard, S., and Linde, N., 2011. Hydrogeophysics, in *Treatise on water*, edited by P. Wilderer, Ch. 43, Elsevier.
- Hubbard, S. S., Rubin, Y., and Majer, E., 1999. Spatial correlation structure estimation using geophysical and hydrogeological data, *Water Resources Research*, **35**, 1809-1825.
- Hubbard, S. S., Chen, J. S., Peterson, J., Majer, E. L., Williams, K. H., et al., 2001. Hydrogeological characterization of the South Oyster Bacterial Transport Site using geophysical data, *Water Resources Research*, **37**, 2431-2456.
- Huggenberger, P., 1993. Radar facies: Recognition of facies patterns and heterogeneities within Pleistocene Rhine gravels, NE Switzerland, *Geological Society, London, Special Publications*, **75**, 163-176.
- Huggenberger, P., Hoehn, E., Beschta, R., and Woessner, W., 1998. Abiotic aspects of channels and floodplains in riparian ecology, *Freshwater Biology*, **40**, 407-425.
- Hyndman, D. W., and Gorelick, S. M., 1996. Estimating lithologic and transport properties in three dimensions using seismic and tracer data: The Kesterson aquifer, *Water Resources Research*, **32**, 2659-2670.
- Hyndman, D. W., and Harris, J. M., 1996. Traveltime inversion for the geometry of aquifer lithologies, *Geophysics*, **61**, 1728-1737.
- Jackson, M. D., 2010. Multiphase electrokinetic coupling: Insights into the impact of fluid and charge distribution at the pore scale from a bundle of capillary tubes model, *Journal of Geophysical Research-Solid Earth*, **115**, B07206.
- Jacobs, L. A., Vongunten, H. R., Keil, R., and Kuslys, M., 1988. Geochemical changes along a river-groundwater infiltration flow path - Glattfelden, Switzerland, *Geochimica Et Cosmochimica Acta*, **52**, 2693-2706.
- Jakubowicz, H., 1990. A simple efficient method of dip-moveout correction, *Geophysical Prospecting*, **38**, 221-245.
- Jardani, A., Revil, A., Boleve, A., Crespy, A., Dupont, J. P., et al., 2007. Tomography of the Darcy velocity from self-potential measurements, *Geophysical Research Letters*, **34**, L24403.
- Jayawickreme, D. H., Van Dam, R. L., and Hyndman, D. W., 2008. Subsurface imaging of vegetation, climate, and root-zone moisture interactions, *Geophysical Research Letters*, **35**, L18404.
- Jegen, M. D., Hobbs, R. W., Tarits, P., and Chave, A., 2009. Joint inversion of marine magnetotelluric and gravity data incorporating seismic constraints: Preliminary results of sub-basalt imaging off the Faroe Shelf, *Earth and Planetary Science Letters*, **282**, 47-55.

-
- Jougnot, D., Ghorbani, A., Revil, A., Leroy, P., and Cosenza, P., 2010. Spectral induced polarization of partially saturated clay-rocks: A mechanistic approach, *Geophysical Journal International*, **180**, 210-224.
- Jung, H. K., Min, D. J., Lee, H. S., Oh, S., and Chung, H., 2009. Negative apparent resistivity in dipole-dipole electrical surveys, *Exploration Geophysics*, **40**, 33-40.
- Kalbus, E., Reinstorf, F., and Schirmer, M., 2006. Measuring methods for groundwater - surface water interactions: A review, *Hydrology and Earth System Sciences*, **10**, 873-887.
- Kalbus, E., Schmidt, C., Molson, J. W., Reinstorf, F., and Schirmer, M., 2009. Influence of aquifer and streambed heterogeneity on the distribution of groundwater discharge, *Hydrology and Earth System Sciences*, **13**, 69-77.
- Keery, J., Binley, A., Crook, N., and Smith, J. W. N., 2007. Temporal and spatial variability of groundwater-surface water fluxes: Development and application of an analytical method using temperature time series, *Journal of Hydrology*, **336**, 1-16.
- Keller, G. V., and Frischknecht, F., 1966. *Electrical methods in geophysical prospecting*, Pergamon.
- Kemna, A., Kulesa, B., and Vereecken, H., 2002. Imaging and characterisation of subsurface solute transport using electrical resistivity tomography (ERT) and equivalent transport models, *Journal of Hydrology*, **267**, 125-146.
- Khalil, A. A., Stewart, R. R., and Henley, D. C., 1993. Full-wave-form processing and interpretation of kilohertz cross-well seismic data, *Geophysics*, **58**, 1248-1256.
- Kipfer, R., Aeschbach-Hertig, W., Peeters, F., and Stute, M., 2002. Noble gases in lakes and ground waters, *Noble Gases in Geochemistry and Cosmochemistry*, **47**, 615-700.
- Klotzsche, A., van der Kruk, J., Meles, G. A., Doetsch, J., Maurer, H., and Linde, N., 2010. Full-waveform inversion of cross-hole ground-penetrating radar data to characterize a gravel aquifer close to the Thur River, Switzerland, *Near Surface Geophysics*, **8**, 635-649.
- Knight, R. J., and Nur, A., 1987. The dielectric-constant of sandstones, 60 Khz to 4 Mhz, *Geophysics*, **52**, 644-654.
- Koch, K., Wenninger, J., Uhlenbrook, S., and Bonell, M., 2009. Joint interpretation of hydrological and geophysical data: Electrical resistivity tomography results from a process hydrological research site in the Black Forest Mountains, Germany, *Hydrological Processes*, **23**, 1501-1513.
- Kondolf, G. M., 1998. Lessons learned from river restoration projects in California, *Aquatic Conservation-Marine and Freshwater Ecosystems*, **8**, 39-52.
- Kosinski, W. K., and Kelly, W. E., 1981. Geoelectric soundings for predicting aquifer properties, *Ground Water*, **19**, 163-171.
- Kowalsky, M. B., Finsterle, S., Peterson, J., Hubbard, S., Rubin, Y., et al., 2005. Estimation of field-scale soil hydraulic and dielectric parameters through joint inversion of GPR and hydrological data, *Water Resources Research*, **41**, W11425.
- Krautblatter, M., Verleysdonk, S., Flores-Orozco, A., and Kemna, A., 2010. Temperature-calibrated imaging of seasonal changes in permafrost rock walls by quantitative electrical resistivity
-

- tomography (Zugspitze, German/Austrian Alps), *Journal of Geophysical Research-Earth Surface*, **115**, F02003.
- Kruse, S., Grasmueck, M., Weiss, M., and Viggiano, D., 2006. Sinkhole structure imaging in covered Karst terrain, *Geophysical Research Letters*, **33**, L16405.
- Kumar, P., and Foufoula-Georgiou, E., 1997. Wavelet analysis for geophysical applications, *Reviews of Geophysics*, **35**, 385-412.
- Kuras, O., Pritchard, J. D., Meldrum, P. I., Chambers, J. E., Wilkinson, P. B., et al., 2009. Monitoring hydraulic processes with automated time-lapse electrical resistivity tomography (ALERT), *Comptes Rendus Geoscience*, **341**, 868-885.
- Kuroda, S., Takeuchi, M., and Kim, H. J., 2007. Full-waveform inversion algorithm for interpreting crosshole radar data: A theoretical approach, *Geosciences Journal*, **11**, 211-217.
- LaBrecque, D. J., Ramirez, A. L., Daily, W. D., Binley, A. M., and Schima, S. A., 1996a. ERT monitoring on environmental remediation processes, *Measurement Science & Technology*, **7**, 375-383.
- LaBrecque, D. J., Miletto, M., Daily, W., Ramirez, A., and Owen, E., 1996b. The effects of noise on Occam's inversion of resistivity tomography data, *Geophysics*, **61**, 538-548.
- LaBrecque, D. J., and Yang, X., 2001. Difference inversion of ERT data: A fast inversion method for 3-D in situ monitoring, *Journal of Environmental and Engineering Geophysics*, **6**, 83-89.
- Lacey, G., 1930. Stable channel in alluvium, *Proceedings of the Institution of Civil Engineers*, **229**, 259-292.
- Lane, J. W., Day-Lewis, F. D., and Casey, C. C., 2006. Geophysical monitoring of a field-scale biostimulation pilot project, *Ground Water*, **44**, 430-443.
- Langevin, C. D., Thorne, D. T., Jr., Dausman, A. M., Sukip, M. C., and Guo, W., 2008. SEAWAT version 4: A computer program for simulation of multi-species solute and heat transport, in *USGS Techniques and Methods Book 6*, Ch. A22.
- Langevin, C. D., 2009. SEAWAT: A computer program for simulation of variable-density groundwater flow and multi-species solute and heat transport, *U.S. Geological Survey*, Fact Sheet 2009-3047.
- Lanz, E., Boerner, D. E., Maurer, H., and Green, A., 1998. Landfill delineation and characterization using electrical, electromagnetic and magnetic methods, *Journal of Environmental and Engineering Geophysics*, **3**, 185-196.
- Lazaratos, S. K., Harris, J. M., Rector, J. W., and Vanschaack, M., 1995. High-resolution crosswell imaging of a west texas carbonate reservoir 4. Reflection imaging, *Geophysics*, **60**, 702-711.
- Le Borgne, T., Bour, O., Paillet, F. L., and Caudal, J. P., 2006. Assessment of preferential flow path connectivity, and hydraulic properties at single-borehole and cross-borehole scales in a fractured aquifer, *Journal of Hydrology*, **328**, 347-359.
- Le Borgne, T., Bour, O., Riley, M. S., Gouze, P., Pezard, P. A., et al., 2007. Comparison of alternative methodologies for identifying and characterizing preferential flow paths in heterogeneous aquifers, *Journal of Hydrology*, **345**, 134-148.

- Leonard, B. P., 1991. The ULTIMATE conservative difference scheme applied to unsteady one-dimensional advection, *Computer Methods in Applied Mechanics and Engineering*, **88**, 17-74.
- Lesmes, D. P., and Friedman, S. P., 2005. Relationships between the electrical and hydrogeological properties of rocks and soils, in *Hydrogeophysics*, edited by Y. Rubin and S. S. Hubbard, pp. 87-128, Springer.
- Li, S. H., Unsworth, M. J., Booker, J. R., Wei, W. B., Tan, H. D., and Jones, A. G., 2003. Partial melt or aqueous fluid in the mid-crust of Southern Tibet? Constraints from INDEPTH magnetotelluric data, *Geophysical Journal International*, **153**, 289-304.
- Linde, N., Binley, A., Tryggvason, A., Pedersen, L. B., and Revil, A., 2006a. Improved hydrogeophysical characterization using joint inversion of cross-hole electrical resistance and ground-penetrating radar traveltime data, *Water Resources Research*, **42**, W12404.
- Linde, N., Finsterle, S., and Hubbard, S., 2006b. Inversion of tracer test data using tomographic constraints, *Water Resources Research*, **42**, W04410.
- Linde, N., Jougnot, D., Revil, A., Matthäi, S. K., Arora, T., et al., 2007a. Streaming current generation in two-phase flow conditions, *Geophysical Research Letters*, **34**, L03306.
- Linde, N., and Revil, A., 2007. Inverting self-potential data for redox potentials of contaminant plumes, *Geophysical Research Letters*, **34**, L14302.
- Linde, N., Revil, A., Bolève, A., Dagès, C., Castermant, J., et al., 2007b. Estimation of the water table throughout a catchment using self-potential and piezometric data in a Bayesian framework, *Journal of Hydrology*, **334**, 88-98.
- Linde, N., Tryggvason, A., Peterson, J. E., and Hubbard, S. S., 2008. Joint inversion of crosshole radar and seismic traveltimes acquired at the South Oyster Bacterial Transport Site, *Geophysics*, **73**, G29-G37.
- Linde, N., and Doetsch, J. A., 2010. Joint inversion of crosshole GPR and seismic traveltime data, in *Advances in near-surface seismology and ground-penetrating radar*, edited by R. D. Miller, J. H. Bradford and K. Holliger, Ch. 1, pp. 1-18, Society of Exploration Geophysicists.
- Linde, N., Doetsch, J., Jougnot, D., Genoni, O., Dürst, Y., et al., 2011. Self-potential investigations of a gravel bar in a restored river corridor, *Hydrology and Earth System Sciences*, **15**, 729-742.
- Lines, L. R., Schultz, A. K., and Treitel, S., 1988. Cooperative inversion of geophysical data, *Geophysics*, **53**, 8-20.
- Loke, M. H., and Barker, R. D., 1996. Practical techniques for 3D resistivity surveys and data inversion, *Geophysical Prospecting*, **44**, 499-523.
- Long, J. C. S., Aydin, A., Brown, S. R., Einstein, H. H., Hestir, K., et al., 1996. *Rock fracture and fluid flow: Contemporary understanding and applications*, National Academy Press, Washington, DC.
- Looms, M. C., Jensen, K. H., Binley, A., and Nielsen, L., 2008. Monitoring unsaturated flow and transport using cross-borehole geophysical methods, *Vadose Zone Journal*, **7**, 227.
- Lowry, T., Allen, M. B., and Shive, P. N., 1989. Singularity removal: A refinement of resistivity modeling techniques, *Geophysics*, **54**, 766-774.

- Lunt, I. A., Bridge, J. S., and Tye, R. S., 2004. A quantitative three-dimensional depositional model of gravelly braided rivers, *Sedimentology*, **51**, 1155-1155.
- Maineult, A., Bernabe, Y., and Ackerer, P., 2004. Electrical response of flow, diffusion, and advection in a laboratory sand box, *Vadose Zone Journal*, **3**, 1180-1192.
- Maineult, A., Bernabe, Y., and Ackerer, P., 2005. Detection of advected concentration and pH fronts from self-potential measurements, *Journal of Geophysical Research-Solid Earth*, **110**, B11205.
- Maineult, A., Strobach, E., and Renner, J., 2008. Self-potential signals induced by periodic pumping tests, *Journal of Geophysical Research-Solid Earth*, **113**, B01203.
- Mair, J. A., and Green, A. G., 1981. High-resolution seismic-reflection profiles reveal fracture-zones within a homogeneous granite batholith, *Nature*, **294**, 439-442.
- Maraun, D., and Kurths, J., 2004. Cross wavelet analysis: Significance testing and pitfalls, *Nonlinear Processes in Geophysics*, **11**, 505-514.
- Marescot, L., Rigobert, S., P. Lopes, S., Lagabrielle, R., and Chapellier, D., 2006. A general approach for DC apparent resistivity evaluation on arbitrarily shaped 3D structures, *Journal of Applied Geophysics*, **60**, 55-67.
- Maurer, H., Holliger, K., and Boerner, D. E., 1998. Stochastic regularization: Smoothness or similarity?, *Geophysical Research Letters*, **25**, 2889-2892.
- Maurer, H., and Musil, M., 2004. Effects and removal of systematic errors in crosshole georadar attenuation tomography, *Journal of Applied Geophysics*, **55**, 261-270.
- Maurer, H., and Friedel, S., 2006. Outer-space sensitivities in geoelectrical tomography, *Geophysics*, **71**, G93-G96.
- Maurer, H., Friedel, S., and Jaeggi, D., 2009. Characterization of a coastal aquifer using seismic and geoelectric borehole methods, *Near Surface Geophysics*, **7**, 353-366.
- Mazac, O., Kelly, W. E., and Landa, I., 1987. Surface geoelectrics for groundwater pollution and protection studies, *Journal of Hydrology*, **93**, 277-294.
- McClymont, A. F., Green, A. G., Streich, R., Horstmeyer, H., Tronicke, J., et al., 2008. Visualization of active faults using geometric attributes of 3D GPR data: An example from the Alpine Fault Zone, New Zealand, *Geophysics*, **73**, B11-B23.
- McElwee, C. D., and Zenner, M. A., 1998. A nonlinear model for analysis of slug-test data, *Water Resources Research*, **34**, 55-66.
- Meles, G. A., Van der Kruk, J., Greenhalgh, S. A., Ernst, J. R., Maurer, H., and Green, A. G., 2010. A new vector waveform inversion algorithm for simultaneous updating of conductivity and permittivity parameters from combination crosshole/borehole-to-surface GPR data, *Ieee Transactions on Geoscience and Remote Sensing*, **48**, 3391-3407.
- Merkli, B., 1975. *Untersuchungen über Mechanismen und Kinetik der Elimination von Bakterien und Viren im Grundwasser*: ETH Zurich.
- Miall, A. D., 1995. Description and interpretation of fluvial deposits - A critical perspective, *Sedimentology*, **42**, 379-384.

-
- Michel, S., Salehi, A., Luo, L., Dawes, N., Aberer, K., et al., 2009. Environmental monitoring 2.0, *Icde: 2009 Ieee 25th International Conference on Data Engineering, Vols. 1-3*, 1507-1510.
- Michot, D., Benderitter, Y., Dorigny, A., Nicoullaud, B., King, D., and Tabbagh, A., 2003. Spatial and temporal monitoring of soil water content with an irrigated corn crop cover using surface electrical resistivity tomography, *Water Resources Research*, **39**, 1138.
- Miller, C. R., Routh, P. S., Brosten, T. R., and McNamara, J. P., 2008. Application of time-lapse ERT imaging to watershed characterization, *Geophysics*, **73**, G7-G17.
- Minsley, B. J., 2007. *Modeling and inversion of self-potential data*: PhD thesis, Massachusetts Institute of Technology.
- Minsley, B. J., Sogade, J., and Morgan, F. D., 2007. Three-dimensional source inversion of self-potential data, *Journal of Geophysical Research*, **112**.
- Mitchell, T. M., 1997. *Machine learning*, McGraw-Hill, New York.
- Monego, M., Cassiani, G., Deiana, R., Putti, M., Passadore, G., and Altissimo, L., 2010. A tracer test in a shallow heterogeneous aquifer monitored via time-lapse surface electrical resistivity tomography, *Geophysics*, **75**, WA61-WA73.
- Monteiro Santos, F. A., Sultan, S. A., Represas, P., and El Sorady, A. L., 2006. Joint inversion of gravity and geoelectrical data for groundwater and structural investigation: Application to the northwestern part of Sinai, Egypt, *Geophysical Journal International*, **165**, 705-718.
- Mora, P., 1987. Nonlinear two-dimensional elastic inversion of multioffset seismic data, *Geophysics*, **52**, 1211-1228.
- Müller, K., Vanderborght, J., Englert, A., Kemna, A., Huisman, J. A., et al., 2010. Imaging and characterization of solute transport during two tracer tests in a shallow aquifer using electrical resistivity tomography and multilevel groundwater samplers, *Water Resources Research*, **46**, W03502.
- Musil, M., Maurer, H. R., and Green, A. G., 2003. Discrete tomography and joint inversion for loosely connected or unconnected physical properties: Application to crosshole seismic and georadar data sets, *Geophysical Journal International*, **153**, 389-402.
- Nadeau, D. F., Brutsaert, W., Parlange, M. B., Bou-Zeid, E., Barrenetxea, G., et al., 2009. Estimation of urban sensible heat flux using a dense wireless network of observations, *Environmental Fluid Mechanics*, **9**, 635-653.
- Nimmer, R. E., Osiensky, J. L., Binley, A. M., Sprenke, K. F., and Williams, B. C., 2007. Electrical resistivity imaging of conductive plume dilution in fractured rock, *Hydrogeology Journal*, **15**, 877-890.
- Nimmer, R. E., Osiensky, J. L., Binley, A. M., and Williams, B. C., 2008. Three-dimensional effects causing artifacts in two-dimensional, cross-borehole, electrical imaging, *Journal of Hydrology*, **359**, 59-70.
- Nyquist, J. E., Freyer, P. A., and Toran, L., 2008. Stream bottom resistivity tomography to map ground water discharge, *Ground Water*, **46**, 561-569.

- Ogilvy, R. D., Meldrum, P. I., Kuras, O., Wilkinson, P. B., Chambers, J. E., et al., 2009. Automated monitoring of coastal aquifers with electrical resistivity tomography, *Near Surface Geophysics*, **7**, 367-375.
- Oldenburg, D. W., and Li, Y. G., 1999. Estimating depth of investigation in dc resistivity and IP surveys, *Geophysics*, **64**, 403-416.
- Olsson, O., Falk, L., Forslund, O., Lundmark, L., and Sandberg, E., 1992. Borehole radar applied to the characterization of hydraulically conductive fracture-zones in crystalline rock, *Geophysical Prospecting*, **40**, 109-142.
- Oreskes, N., Shrader-Frechette, K., and Belitz, K., 1994. Verification, validation, and confirmation of numerical models in the earth sciences, *Science*, **263**, 641-646.
- Orghidan, T., 1959. Ein neuer Lebensraum des unterirdischen Wassers: der hyporheische Biotop, *Arch. Hydrobiol.*, **55**, 392-414.
- Osiensky, J. L., Nimmer, R., and Binley, A. M., 2004. Borehole cylindrical noise during hole-surface and hole-hole resistivity measurements, *Journal of Hydrology*, **289**, 78-94.
- Paasche, H., Tronicke, J., Holliger, K., Green, A. G., and Maurer, H., 2006. Integration of diverse physical-property models: Subsurface zonation and petrophysical parameter estimation based on fuzzy c-means cluster analyses, *Geophysics*, **71**, H33-H44.
- Paasche, H., and Tronicke, J., 2007. Cooperative inversion of 2D geophysical data sets: A zonal approach based on fuzzy c-means cluster analysis, *Geophysics*, **72**, A35-A39.
- Paasche, H., Wendrich, A., Tronicke, J., and Trela, C., 2008. Detecting voids in masonry by cooperatively inverting P-wave and georadar traveltimes, *Journal of Geophysics and Engineering*, **5**, 256-267.
- Paige, C. C., and Saunders, M. A., 1982. LSQR: An algorithm for sparse linear equations and sparse least squares, *ACM Transactions on Mathematical Software*, **8**, 43-71.
- Palmer, M. A., Bernhardt, E. S., Allan, J. D., Lake, P. S., Alexander, G., et al., 2005. Standards for ecologically successful river restoration, *Journal of Applied Ecology*, **42**, 208-217.
- Park, S. K., Johnston, M. J. S., Madden, T. R., Morgan, F. D., and Morrison, H. F., 1993. Electromagnetic precursors to earthquakes in the ULF band - a review of observations and mechanisms, *Reviews of Geophysics*, **31**, 117-132.
- Parker, R. L., 1984. The inverse problem of resistivity sounding, *Geophysics*, **49**, 2143-2158.
- Pasquale, N., Perona, P., Schneider, P., Shrestha, J., Wombacher, A., and Burlando, P., 2011. Modern comprehensive approach to monitor the morphodynamic evolution of a restored river corridor, *Hydrology and Earth System Sciences*, **15**, 1197-1212.
- Perrier, F., and Morat, P., 2000. Characterization of electrical daily variations induced by capillary flow in the non-saturated zone, *Pure and Applied Geophysics*, **157**, 785-810.
- Petiau, G., 2000. Second generation of lead-lead chloride electrodes for geophysical applications, *Pure and Applied Geophysics*, **157**, 357-382.
- Podvin, P., and Lecomte, I., 1991. Finite difference computation of traveltimes in very contrasted velocity models: A massively parallel approach and its associated tools, *Geophysical Journal International*, **105**, 271-284.

-
- Pollock, D., and Cirpka, O. A., 2010. Fully coupled hydrogeophysical inversion of synthetic salt tracer experiments, *Water Resources Research*, **46**, W07501.
- Portniaguine, O., and Zhdanov, M. S., 1999. Focusing geophysical inversion images, *Geophysics*, **64**, 874-887.
- Pratt, R. G., 1999. Seismic waveform inversion in the frequency domain, part 1: Theory and verification in a physical scale model, *Geophysics*, **64**, 888-901.
- Pratt, R. G., and Shipp, R. M., 1999. Seismic waveform inversion in the frequency domain, part 2: Fault delineation in sediments using crosshole data, *Geophysics*, **64**, 902-914.
- Pride, S., 1994. Governing equations for the coupled electromagnetics and acoustics of porous-media, *Physical Review B*, **50**, 15678-15696.
- Pride, S. R., Berryman, J. G., and Harris, J. M., 2004. Seismic attenuation due to wave-induced flow, *Journal of Geophysical Research-Solid Earth*, **109**, B01201.
- Pruess, K., Oldenburg, C. M., and Moridis, G. J., 1999. TOUGH2 user's guide version 2, Rep. LBNL--43134, 204 pp, Lawrence Berkeley National Laboratory.
- Ptak, T., and Teutsch, G., 1994. Forced and natural gradient tracer tests in a highly heterogeneous porous aquifer - instrumentation and measurements, *Journal of Hydrology*, **159**, 79-104.
- Ramirez, A., Daily, W., Labrecque, D., Owen, E., and Chesnut, D., 1993. Monitoring an underground steam injection process using electrical-resistance tomography, *Water Resources Research*, **29**, 73-87.
- Ranguelova, E. B., 2002. *Segmentation of textured images on three-dimensional lattices*: PhD thesis, University of Dublin.
- RECORD, 2011. Assessment and modeling of coupled ecological and hydrological dynamics in the restored corridor of the river, *Competence Center Environment and Sustainability*, <http://www.cces.ethz.ch/projects/nature/Record>.
- Regli, C., Rauber, M., and Huggenberger, P., 2003. Analysis of aquifer heterogeneity within a well capture zone, comparison of model data with field experiments: A case study from the river Wiese, Switzerland, *Aquatic Sciences*, **65**, 111-128.
- Revil, A., Cathles, L. M., Losh, S., and Nunn, J. A., 1998. Electrical conductivity in shaly sands with geophysical applications, *Journal of Geophysical Research - Solid Earth*, **103**, 23925-23936.
- Revil, A., and Cathles, L. M., 1999. Permeability of shaly sands, *Water Resources Research*, **35**, 651-662.
- Revil, A., Naudet, V., Nouzaret, J., and Pessel, M., 2003. Principles of electrography applied to self-potential electrokinetic sources and hydrogeological applications, *Water Resources Research*, **39**, 1114.
- Revil, A., and Leroy, P., 2004. Constitutive equations for ionic transport in porous shales, *Journal of Geophysical Research-Solid Earth*, **109**, B03208.
- Revil, A., and Linde, N., 2006. Chemico-electromechanical coupling in microporous media, *Journal of Colloid and Interface Science*, **302**, 682-694.
- Revil, A., Linde, N., Cerepi, A., Jougnot, D., Matthai, S., and Finsterle, S., 2007. Electrokinetic coupling in unsaturated porous media, *Journal of Colloid and Interface Science*, **313**, 315-327.
-

- Revil, A., Trolard, F., Bourrie, G., Castermant, J., Jardani, A., and Mendonca, C. A., 2009. Ionic contribution to the self-potential signals associated with a redox front, *Journal of Contaminant Hydrology*, **109**, 27-39.
- Rizzo, E., Suski, B., Revil, A., Straface, S., and Troisi, S., 2004. Self-potential signals associated with pumping tests experiments, *Journal of Geophysical Research-Solid Earth*, **109**, B10203.
- Robinson, D. A., Binley, A., Crook, N., Day-Lewis, F. D., Ferre, T. P. A., et al., 2008. Advancing process-based watershed hydrological research using near-surface geophysics: A vision for, and review of, electrical and magnetic geophysical methods, *Hydrological Processes*, **22**, 3604-3635.
- Rubin, Y., and Hubbard, S. S. (Eds.), 2005. *Hydrogeophysics*, Springer, Dordrecht, The Netherlands.
- Rücker, C., Günther, T., and Spitzer, K., 2006. Three-dimensional modelling and inversion of dc resistivity data incorporating topography - I. Modelling, *Geophysical Journal International*, **166**, 495-505.
- Ruelleu, S., Moreau, F., Bour, O., Gapais, D., and Martelet, G., 2010. Impact of gently dipping discontinuities on basement aquifer recharge: An example from Ploemeur (Brittany, France), *Journal of Applied Geophysics*, **70**, 161-168.
- Samaritani, E., Shrestha, J., Fournier, B., Frossard, E., Gillet, F., et al., 2011. Heterogeneity of soil carbon pools and fluxes in a channelized and a restored floodplain section (Thur River, Switzerland), *Hydrology and Earth System Sciences Discussions*, **8**, 1059-1091.
- Sambridge, M., Braun, J., and McQueen, H., 1995. Geophysical parametrization and interpolation of irregular data using natural neighbors, *Geophysical Journal International*, **122**, 837-857.
- Sandberg, S. K., Slater, L. D., and Versteeg, R., 2002. An integrated geophysical investigation of the hydrogeology of an anisotropic unconfined aquifer, *Journal of Hydrology*, **267**, 227-243.
- Saracco, G., Labazuy, P., and Moreau, F., 2004. Localization of self-potential sources in volcano-electric effect with complex continuous wavelet transform and electrical tomography methods for an active volcano, *Geophysical Research Letters*, **31**, L12610.
- Schälchli, U., 1992. The clogging of coarse gravel river beds by fine sediment, *Hydrobiologia*, **235-236**, 189-197.
- Schälchli, U., 2008. Geschiebehaushalt im Thurgebiet, *Wasser Energie Luft*, **100**, 23-28.
- Schäppi, B., Perona, P., Schneider, P., and Burlando, P., 2010. Integrating river cross section measurements with digital terrain models for improved flow modelling applications, *Computers & Geosciences*, **36**, 707-716.
- Scheibe, T. D., and Chien, Y. J., 2003. An evaluation of conditioning data for solute transport prediction, *Ground Water*, **41**, 128-141.
- Schmidt, C., Bayer-Raich, M., and Schirmer, M., 2006. Characterization of spatial heterogeneity of groundwater-stream water interactions using multiple depth streambed temperature measurements at the reach scale, *Hydrology and Earth System Sciences*, **10**, 849-859.
- Schmidt, C., Conant, B., Bayer-Raich, M., and Schirmer, M., 2007. Evaluation and field-scale application of an analytical method to quantify groundwater discharge using mapped streambed temperatures, *Journal of Hydrology*, **347**, 292-307.

- Schneider, P., Vogt, T., Schirmer, M., Doetsch, J., Linde, N., et al., 2011. Towards improved instrumentation for assessing river-groundwater interactions in a restored river corridor, *Hydrology and Earth System Sciences*, **15**, 2531-2549.
- Schön, J. H., 1996. *Physical properties of rocks: Fundamentals and principles of petrophysics*, Elsevier Science Publishing Company, Inc.
- Schulmeister, M. K., Butler, J. J., Healey, J. M., Zheng, L., Wysocki, D. A., and McCall, G. W., 2003. Direct-push electrical conductivity logging for high-resolution hydrostratigraphic characterization, *Ground Water Monitoring and Remediation*, **23**, 52-62.
- Schwarzenbach, R. P., and Westall, J., 1981. Transport of non-polar organic-compounds from surface-water to groundwater - Laboratory sorption studies, *Environmental Science & Technology*, **15**, 1360-1367.
- Schwarzenbach, R. P., Giger, W., Hoehn, E., and Schneider, J. K., 1983. Behavior of organic-compounds during infiltration of river water to groundwater - Field studies, *Environmental Science & Technology*, **17**, 472-479.
- Schwarzenbach, R. P., Escher, B. I., Fenner, K., Hofstetter, T. B., Johnson, C. A., et al., 2006. The challenge of micropollutants in aquatic systems, *Science*, **313**, 1072-1077.
- Seiz, G., and Foppa, N., 2007. Nationales Klima-Beobachtungssystem (GCOS Schweiz), *Bundesamt für Meteorologie und Klimatologie, MeteoSchweiz und ProClim, Bern, Switzerland*.
- Selker, J. S., Thevenaz, L., Huwald, H., Mallet, A., Luxemburg, W., et al., 2006. Distributed fiber-optic temperature sensing for hydrologic systems, *Water Resources Research*, **42**, W12202.
- Sen, P. N., Scala, C., and Cohen, M. H., 1981. A self-similar model for sedimentary-rocks with application to the dielectric-constant of fused glass-beads, *Geophysics*, **46**, 781-795.
- Shankar, V., Eckert, P., Ojha, C. S. P., and König, C. M., 2009. Transient three-dimensional modeling of riverbank filtration at Grind well field, Germany, *Hydrogeology Journal*, **17**, 321-326.
- Sheffer, M. R., and Oldenburg, D. W., 2007. Three-dimensional modelling of streaming potential, *Geophysical Journal International*, **169**, 839-848.
- Sill, W. R., 1983. Self-potential modeling from primary flows, *Geophysics*, **48**, 76-86.
- Silliman, S. E., and Booth, D. F., 1993. Analysis of time-series measurements of sediment temperature for identification of gaining vs losing portions of Juday-Creek, Indiana, *Journal of Hydrology*, **146**, 131-148.
- Singha, K., and Gorelick, S. M., 2005. Saline tracer visualized with three-dimensional electrical resistivity tomography: Field-scale spatial moment analysis, *Water Resources Research*, **41**, W05023.
- Sjödahl, P., Dahlin, T., and Johansson, S., 2009. Embankment dam seepage evaluation from resistivity monitoring data, *Near Surface Geophysics*, **7**, 463-474.
- Slater, L., and Sandberg, S. K., 2000. Resistivity and induced polarization monitoring of salt transport under natural hydraulic gradients, *Geophysics*, **65**, 408-420.
- Slater, L., Binley, A. M., Daily, W., and Johnson, R., 2000. Cross-hole electrical imaging of a controlled saline tracer injection, *Journal of Applied Geophysics*, **44**, 85-102.

- Slater, L., and Binley, A., 2006. Synthetic and field-based electrical imaging of a zerovalent iron barrier: Implications for monitoring long-term barrier performance, *Geophysics*, **71**, B129-B137.
- Slob, E., Sato, M., and Olhoeft, G., 2010. Surface and borehole ground-penetrating-radar developments, *Geophysics*, **75**, A103-A120.
- Smith, D. G., and Jol, H. M., 1992. Ground-penetrating radar investigation of a Lake Bonneville delta, Provo level, Brigham City, Utah, *Geology*, **20**, 1083-1086.
- Soar, P. J., and Thorne, C. R., 2001. *Channel restoration design for meandering rivers*, U.S. Army Engineer Research and Development Center, Vicksburg, Miss.
- Spillmann, T., Maurer, H., Willenberg, H., Evans, K. F., Heincke, B., and Green, A. G., 2007. Characterization of an unstable rock mass based on borehole logs and diverse borehole radar data, *Journal of Applied Geophysics*, **61**, 16-38.
- Springer, R. K., and Gelhar, L. W., 1991. Characterization of large-scale aquifer heterogeneity in glacial outwash by analysis of slug tests with oscillatory response, *US Geological Survey, Cape Cod*, Report 91-4034.
- Stanford, J. A., and Ward, J. V., 1988. The hyporheic habitat of river ecosystems, *Nature*, **335**, 64-66.
- Stanford, J. A., and Ward, J. V., 1993. An ecosystem perspective of alluvial rivers - connectivity and the hyporheic corridor, *Journal of the North American Benthological Society*, **12**, 48-60.
- Stauffer, F., and Dracos, T., 1986. Experimental and numerical study of water and solute infiltration in layered porous-media, *Journal of Hydrology*, **84**, 9-34.
- Storey, R. G., Howard, K. W. F., and Williams, D. D., 2003. Factors controlling riffle-scale hyporheic exchange flows and their seasonal changes in a gaining stream: A three-dimensional groundwater flow model, *Water Resources Research*, **39**, 1034.
- Streich, R., van der Kruk, J., and Green, A. G., 2006. Three-dimensional multicomponent georadar imaging of sedimentary structures, *Near Surface Geophysics*, **4**, 39-48.
- Streich, R., and van der Kruk, J., 2007a. Accurate imaging of multicomponent GPR data based on exact radiation patterns, *Ieee Transactions on Geoscience and Remote Sensing*, **45**, 93-103.
- Streich, R., and van der Kruk, J., 2007b. Characterizing a GPR antenna system by near-field electric field measurements, *Geophysics*, **72**, A51-A55.
- Stummer, P., Maurer, H., and Green, A. G., 2004. Experimental design: Electrical resistivity data sets that provide optimum subsurface information, *Geophysics*, **69**, 120-139.
- Suski, B., Revil, A., Titov, K., Konosavsky, P., Voltz, M., et al., 2006. Monitoring of an infiltration experiment using the self-potential method, *Water Resources Research*, **42**, W08418.
- SVGW, 2004. Jahrbuch 2003/2004, *SVGW, Zürich*.
- SVGW, 2007. Empfehlungen – Revitalisierung im Einflussbereich von Trinkwasserfassungen, *Zürich, Switzerland*.
- Talley, J., Baker, G. S., Becker, M. W., and Beyrle, N., 2005. Four dimensional mapping of tracer channelization in subhorizontal bedrock fractures using surface ground penetrating radar, *Geophysical Research Letters*, **32**, L04401.

-
- Tarantola, A., 1984a. Inversion of seismic-reflection data in the acoustic approximation, *Geophysics*, **49**, 1259-1266.
- Tarantola, A., 1984b. Linearized inversion of seismic-reflection data, *Geophysical Prospecting*, **32**, 998-1015.
- Tarantola, A., 1986. A strategy for nonlinear elastic inversion of seismic-reflection data, *Geophysics*, **51**, 1893-1903.
- Thony, J. L., Morat, P., Vachaud, G., and LeMouel, J. L., 1997. Field characterization of the relationship between electrical potential gradients and soil water flux, *Comptes Rendus De L'Academie Des Sciences*, **325**, 317-321.
- Topp, G. C., Davis, J. L., and Annan, A. P., 1980. Electromagnetic determination of soil-water content - Measurements in coaxial transmission-lines, *Water Resources Research*, **16**, 574-582.
- Topp, G. C., Davis, J. L., and Annan, A. P., 1982. Electromagnetic determination of soil-water content using TDR 2. Evaluation of installation and configuration of parallel transmission-lines, *Soil Science Society of America Journal*, **46**, 678-684.
- Torrence, C., and Compo, G. P., 1998. A practical guide to wavelet analysis, *Bulletin of the American Meteorological Society*, **79**, 61-78.
- Touchard, F., 1999. *Caractérisation hydrogéologique d'un aquifère en socle fracture. Site de Ploëmeur (Morbihan)*: PhD thesis, University of Rennes I.
- Trefry, M. G., and Muffels, C., 2007. Feflow: A finite-element ground water flow and transport modeling tool, *Ground Water*, **45**, 525-528.
- Triska, F. J., Kennedy, V. C., Avanzino, R. J., Zellweger, G. W., and Bencala, K. E., 1989. Retention and transport of nutrients in a 3rd-order stream in Northwestern California - hyporheic processes, *Ecology*, **70**, 1893-1905.
- Triska, F. J., Duff, J. H., and Avanzino, R. J., 1993a. Patterns of hydrological exchange and nutrient transformation in the hyporheic zone of a gravel-bottom stream - examining terrestrial aquatic linkages, *Freshwater Biology*, **29**, 259-274.
- Triska, F. J., Duff, J. H., and Avanzino, R. J., 1993b. The role of water exchange between a stream channel and its hyporheic zone in nitrogen cycling at the terrestrial aquatic interface, *Hydrobiologia*, **251**, 167-184.
- Tronicke, J., Dietrich, P., Wahlig, U., and Appel, E., 2002. Integrating surface georadar and crosshole radar tomography: A validation experiment in braided stream deposits, *Geophysics*, **67**, 1516-1523.
- Tronicke, J., and Holliger, K., 2004. Effects of gas- and water-filled boreholes on the amplitudes of crosshole georadar data as inferred from experimental evidence, *Geophysics*, **69**, 1255-1260.
- Tronicke, J., Holliger, K., Barrash, W., and Knoll, M. D., 2004. Multivariate analysis of cross-hole georadar velocity and attenuation tomograms for aquifer zonation, *Water Resources Research*, **40**, W01519.
- Trubilowicz, J., Cai, K., and Weiler, M., 2009. Viability of motes for hydrological measurement, *Water Resources Research*, **45**, W00D22.
-

- Trush, W. J., McBain, S. M., and Leopold, L. B., 2000. Attributes of an alluvial river and their relation to water policy and management, *Proceedings of the National Academy of Sciences of the United States of America*, **97**, 11858-11863.
- Tryggvason, A., Rögnvaldsson, S. T., and Flóvenz, Ó. G., 2002. Three-dimensional imaging of the P- and S-wave velocity structure and earthquake locations beneath Southwest Iceland, *Geophysical Journal International*, **151**, 848-866.
- Tryggvason, A., and Linde, N., 2006. Local earthquake (LE) tomography with joint inversion for P- and S-wave velocities using structural constraints, *Geophysical Research Letters*, **33**, L07303.
- Tryggvason, A., and Bergman, B., 2006. A travelttime reciprocity discrepancy in the Podvin & Lecomte time3d finite difference algorithm, *Geophysical Journal International*, **165**, 432-435.
- Tsoflias, G. P., Halihan, T., and Sharp, J. M., 2001. Monitoring pumping test response in a fractured aquifer using ground-penetrating radar, *Water Resources Research*, **37**, 1221-1229.
- Tsoflias, G. P., and Becker, M. W., 2008. Ground-penetrating-radar response to fracture-fluid salinity: Why lower frequencies are favorable for resolving salinity changes, *Geophysics*, **73**, J25-J30.
- Tubino, M., and Seminara, G., 1990. Free forced interactions in developing meanders and suppression of free bars, *Journal of Fluid Mechanics*, **214**, 131-159.
- Tufenkji, N., Ryan, J. N., and Elimelech, M., 2002. The promise of bank filtration, *Environmental Science & Technology*, **36**, 422A-428A.
- Turesson, A., 2006. Water content and porosity estimated from ground-penetrating radar and resistivity, *Journal of Applied Geophysics*, **58**, 99-111.
- van Genuchten, M. T., 1980. A closed-form equation for predicting the hydraulic conductivity of unsaturated soils, *Soil Science Society of America Journal*, **44**, 892-898.
- Vasco, D. W., Peterson, J. E., and Majer, E. L., 1995. Beyond ray tomography - Wavepaths and fresnel volumes, *Geophysics*, **60**, 1790-1804.
- Vereecken, H., Binley, A., Cassiani, G., Revil, A., and Titov, K. (Eds.), 2006. *Applied hydrogeophysics*, Springer, Dordrecht, The Netherlands.
- Vereecken, H., Huisman, J. A., Bogaen, H., Vanderborght, J., Vrugt, J. A., and Hopmans, J. W., 2008. On the value of soil moisture measurements in vadose zone hydrology: A review, *Water Resources Research*, **44**, W00D06.
- Vogt, T., Hoehn, E., Schneider, P., and Cirpka, O. A., 2009. Untersuchung der Flusswasserinfiltration in voralpinen Schottern mittels Zeitreihenanalyse, *Grundwasser*, **14**, 179-194.
- Vogt, T., Schneider, P., Hahn-Woernle, L., and Cirpka, O. A., 2010a. Estimation of seepage rates in a losing stream by means of fiber-optic high-resolution vertical temperature profiling, *Journal of Hydrology*, **380**, 154-164.
- Vogt, T., Hoehn, E., Schneider, P., Freund, A., Schirmer, M., and Cirpka, O. A., 2010b. Fluctuations of electrical conductivity as a natural tracer for bank filtration in a losing stream, *Advances in Water Resources*, **33**, 1296-1308.
- von Gunten, H. R., Karametaxas, G., and Keil, R., 1994. Chemical Processes in Infiltrated Riverbed Sediments, *Environmental Science & Technology*, **28**, 2087-2093.

-
- von Gunten, U., and Zobrist, J., 1993. Biogeochemical changes in groundwater-infiltration systems - column studies, *Geochimica Et Cosmochimica Acta*, **57**, 3895-3906.
- Vozoff, K., and Jupp, D. L. B., 1975. Joint inversion of geophysical data, *Geophysical Journal of the Royal Astronomical Society*, **42**, 977-991.
- Ward, A. S., Gooseff, M. N., and Singha, K., 2010. Imaging hyporheic zone solute transport using electrical resistivity, *Hydrological Processes*, **24**, 948-953.
- Ward, J. V., 1989. The four-dimensional nature of lotic ecosystems, *Journal of the North American Benthological Society*, **8**, 2-8.
- Watanabe, T., Nihei, K. T., Nakagawa, S., and Myer, L. R., 2004. Viscoacoustic wave form inversion of transmission data for velocity and attenuation, *Journal of the Acoustical Society of America*, **115**, 3059-3067.
- Waxman, M. H., and Smits, L. J. M., 1968. Electrical Conductivities in Oil-Bearing Shaly Sands, *Society of Petroleum Engineers Journal*, **8**, 107.
- West, L. J., Handley, K., Huang, Y., and Pokar, M., 2003. Radar frequency dielectric dispersion in sandstone: Implications for determination of moisture and clay content, *Water Resources Research*, **39**, 1026.
- Western, A. W., Grayson, R. B., and Blöschl, G., 2002. Scaling of soil moisture: A hydrologic perspective, *Annual Review of Earth and Planetary Sciences*, **30**, 149-180.
- Wilkinson, P. B., Meldrum, P. I., Kuras, O., Chambers, J. E., Holyoake, S. J., and Ogilvy, R. D., 2010. High-resolution electrical resistivity tomography monitoring of a tracer test in a confined aquifer, *Journal of Applied Geophysics*, **70**, 268-276.
- Winship, P., Binley, A., and Gomez, D., 2006. Flow and transport in the unsaturated Sherwood Sandstone: Characterization using cross-borehole geophysical methods, *Fluid Flow and Solute Movement in Sandstones: The Onshore UK Permo-Triassic Red Bed Sequence*, **263**, 219-231.
- Wishart, D. N., Slater, L. D., and Gates, A. E., 2006. Self potential improves characterization of hydraulically-active fractures from azimuthal geoelectrical measurements, *Geophysical Research Letters*, **33**, L17314.
- Woessner, W. W., 2000. Stream and fluvial plain ground water interactions: Rescaling hydrogeologic thought, *Ground Water*, **38**, 423-429.
- Wombacher, A., and Schneider, P., 2010. Observation centric sensor data model, *Technical Report TR-CTIT-10-13, University of Twente, Enschede*, ISSN 1381-3625.
- Woolsey, S., Capelli, F., Gonser, T., Hoehn, E., Hostmann, M., et al., 2007. A strategy to assess river restoration success, *Freshwater Biology*, **52**, 752-769.
- Worthington, P. F., 1993. The uses and abuses of the archie equations 1. The formation factor porosity relationship, *Journal of Applied Geophysics*, **30**, 215-228.
- Wriedt, G., and Rode, M., 2006. Modelling nitrate transport and turnover in a lowland catchment system, *Journal of Hydrology*, **328**, 157-176.
- Wroblicky, G. J., Campana, M. E., Valett, H. M., and Dahm, C. N., 1998. Seasonal variation in surface-subsurface water exchange and lateral hyporheic area of two stream-aquifer systems, *Water Resources Research*, **34**, 317-328.
-

- Yeh, T. C. J., Liu, S., Glass, R. J., Baker, K., Brainard, J. R., et al., 2002. A geostatistically based inverse model for electrical resistivity surveys and its applications to vadose zone hydrology, *Water Resources Research*, **38**, 1278.
- Yeh, T. C. J., Lee, C. H., Hsu, K. C., Illman, W. A., Barrash, W., et al., 2008. A view toward the future of subsurface characterization: CAT scanning groundwater basins, *Water Resources Research*, **44**, W03301.
- Yilmaz, Ö., 2001. *Seismic data processing*, Society of Exploration Geophysicists, Tulsa, USA.
- Zhang, J., and Morgan, F. D., 1997. Joint Seismic and Electrical Tomography, *Proceedings of the Symposium on the Application of Geophysics to Engineering and Environmental Problems*, 391-396.
- Zhdanov, M. S., 2009. New advances in regularized inversion of gravity and electromagnetic data, *Geophysical Prospecting*, **57**, 463-478.
- Zhou, B., and Greenhalgh, S. A., 2003. Crosshole seismic inversion with normalized full-waveform amplitude data, *Geophysics*, **68**, 1320-1330.
- Zonge, K., Wynn, J., and Urquhart, S., 2005. Resistivity, induced polarization, and complex resistivity, in *Near Surface Geophysics*, edited by D. K. Butler, pp. 265-300, SEG.
- Zurbuchen, B. R., Zlotnik, V. A., and Butler, J. J., 2002. Dynamic interpretation of slug tests in highly permeable aquifers, *Water Resources Research*, **38**, 1025.

ACKNOWLEDGMENTS

Many thanks to all the great people at ETH and elsewhere, whom I had the privilege to meet and work with, and who supported me during the course of my thesis.

Foremost, I would like to express my deep gratitude to Niklas Linde, who introduced me to the world of hydrogeophysics, ensured a red thread through my thesis, and cared about every detail in my projects. Although physically located in Lausanne, he was very present at any time through various communication channels, and his response times and quality of feedback were unprecedented!

My Doktorvater Alan Green provided invaluable advice about scientific writing, and his insights and feedback greatly improved my work. His endless energy and enthusiasm helped to inspire me and get me involved with projects beyond my own.

I would like to thank Stewart Greenhalgh for sharing his encyclopedic knowledge about geophysics, and for prompt and valuable feedback at any time. Thanks also to Thomas Günther for discussions about ERT and his technical support, and to Andrew Binley for insights into hydrogeology.

The time (in and outside the office) and many discussions about Geophysics, life and the universe with Ilaria Coscia were very enriching. I will keep them as good memories. I am also indebted to the members of the AUG & friends group and I will remember the great time spent together with you!

It was a great pleasure working and socializing with the other PhDs in the RECORD project. I especially enjoyed the field work and collaboration with Tobias Vogt. I will keep the field days at the Thur River as good memories and although the weather wasn't always pleasant, I could always count on field and any other type of assistance from Alain, Alastair, Anna, Arthur, Baptiste, Caro, Christoph, Edgar, Franz, Giovanni, Hansruedi, Heinrich, Ilaria, Jan, Jan, Jakob, Jochen, Jürg, Kaspar, Laurent, Ludwig, Marian, Mark, Martha, Mirco, Miro, Niklas, Oliver, Philipp, Priska, Sandro, Simeon, Stefan, Stefano², Stewart, Thomas, and Yolanda. Many thanks also to the people that shared the adventures to various glaciers, Brittany, New Zealand, and Botswana with me.

Finally, thanks to Linda for sharing everything with me and for giving me some of her endless power and determination. Last, but far from least, a special mention to my parents, brothers, and sister who supported me from the distance.

CURRICULUM VITAE

PERSONAL

Name: Joseph Andreas Doetsch
Date of Birth: 25 August 1981
Place of Birth: Frankfurt/Main, Germany
Citizenship: German

EDUCATION

10.2007 – 2011 PhD Student at the Institute of Geophysics, ETH Zurich, Switzerland
10.2005 – 09.2007 *Diploma (Master of Science) in Physics*, ETH Zurich, Switzerland
08.2004 – 08.2005 *Master of Science in Physics*, Uppsala University, Sweden
10.2002 – 07.2004 *Vordiplom in Physics*, Heidelberg University, Germany
08.1988 – 07.2001 *Abitur*, Rudolf-Steiner-Schule Dietzenbach, Germany

JOURNALS AND BOOKS

2006

Oswald, B., Doetsch, J., and Roth, K., 2006. A new computational technique for processing transmission-line measurements to determine dispersive dielectric properties, *Geophysics*, **71**, K31-K35.

2010

Carpentier, S. F. A., Horstmeyer, H., Green, A. G., Doetsch, J., and Coscia, I., 2010. Semiautomated suppression of above-surface diffractions in GPR data, *Geophysics*, **75**, J43-J50.

Doetsch, J., Linde, N., and Binley, A., 2010. Structural joint inversion of time-lapse crosshole ERT and GPR traveltimes data, *Geophysical Research Letters*, **37**, L24404.

Doetsch, J., Linde, N., Coscia, I., Greenhalgh, S. A., and Green, A. G., 2010. Zonation for 3D aquifer characterization based on joint inversions of multimethod crosshole geophysical data, *Geophysics*, **75**, G53-G64.

Doetsch, J. A., Coscia, I., Greenhalgh, S., Linde, N., Green, A., and Günther, T., 2010. The borehole-fluid effect in electrical resistivity imaging, *Geophysics*, **75**, F107-F114.

Klotzsche, A., van der Kruk, J., Meles, G. A., Doetsch, J., Maurer, H., and Linde, N., 2010. Full-waveform inversion of cross-hole ground-penetrating radar data to characterize a gravel aquifer close to the Thur River, Switzerland, *Near Surface Geophysics*, **8**, 635-649.

Linde, N., and Doetsch, J. A., 2010. Joint Inversion of Crosshole GPR and Seismic Traveltime Data, in *Advances in Near-surface Seismology and Ground-penetrating Radar*, edited by R. D. Miller, J. H. Bradford and K. Holliger, Ch. 1, pp. 1-18, Society of Exploration Geophysicists.

Linde, N., Coscia, I., Doetsch, J. A., Greenhalgh, S. A., Vogt, T., Schneider, P., Green, A. G., 2010. Hydrogeophysical studies in unrestored and restored river corridors of the Thur River, Switzerland, *First Break*, **28**, 69-75.

2011

Brauchler, R., Doetsch, J., Dietrich, P., and Sauter, M., 2011. Derivation of site-specific relationships between hydraulic parameters and p-wave velocities based on hydraulic and seismic tomography, *under revision for Water Resources Research*.

Carpentier, S., Green, A., Doetsch, J., Dorn, C., Kaiser, A.E., Campbell, F.M., Horstmeyer, H., Finnemore, M., 2011. Recent deformation of Quaternary sediments in the northwest Canterbury Plains of New Zealand as inferred from GPR images and shallow P-wave velocity tomograms, *Journal of Applied Geophysics*, in Press.

Carpentier, S.F.A., Green, A.G., Langridge, R., Boschetti, S., Doetsch, J., Abächerli, A.N., Horstmeyer, H., and Finnemore, M., 2011. Flower structures and Riedel shears at a stepover zone along the Alpine Fault (New Zealand) inferred from 2D and 3D GPR images, *under review with Journal of Geophysical Research - Solid Earth*.

Coscia, I., Greenhalgh, S. A., Linde, N., Doetsch, J., Marescot, L., et al., 2011. 3D crosshole ERT for aquifer characterization and monitoring of infiltrating river water, *Geophysics*, **76**, G49-G59.

Doetsch, J., Linde, N., Pessognelli, M., Green, A. G., and Günther, T., 2011. Constraining 3-D electrical resistance tomography with GPR data for improved aquifer characterization, *Journal of Applied Geophysics*, in press.

Doetsch, J., Linde, N., Vogt, T., Binley, B., and Green, A.G., 2011. Imaging and quantifying salt tracer transport in a riparian groundwater system by means of 3-D ERT monitoring, *under revision for Water Resources Research*.

Dorn, C., Linde, N., Doetsch, J., Le Borgne, T., and Bour, O., 2011. Fracture imaging within a granitic rock aquifer using multiple-offset single-hole and cross-hole GPR reflection data, *Journal of Applied Geophysics*, in Press.

Linde, N., Doetsch, J., Jougnot, D., Genoni, O., Dürst, Y., Minsley, B. J., Vogt, T., Pasquale, N., Luster, J., 2011. Self-potential investigations of a gravel bar in a restored river corridor, *Hydrology and Earth System Sciences*, **15**, 729-742.

Schneider, P., Vogt, T., Schirmer, M., Doetsch, J. A., Linde, N., Pasquale, N., Perona, P., Cirpka, O. A., 2011. Towards improved instrumentation for assessing river-groundwater interactions in a restored river corridor, *Hydrology and Earth System Sciences*, **15**, 2531-2549.

SCIENTIFIC AWARDS

- Young Scientists Outstanding Poster Paper Award 2009 of the European Geosciences Union (Hydrology Section).
- “Best Poster Award” at the summer school on "Flow and Transport in Porous and Fractured media", Corsica, August 2010.
- EAGE “Best of Near Surface 2010” award, with an invitation to present the work at SAGEEP 2011 conference in Charleston, South Carolina.